Title	Geometry effect in the fatigue behaviour of microscale 316L stainless steel specimens
Author(s)	Donnelly, Evin
Publication Date	2012-06-07
Item record	http://hdl.handle.net/10379/3029

NUI Galway
OÉ Gaillimh

Geometry effect in the fatigue behaviour of microscale 316L stainless steel specimens

by

Evin Donnelly

B.E., University of Limerick, 1999.

A thesis submitted to the National University of Ireland
as fulfilment of the requirements for the Degree of Doctor of Philosophy

Department of Mechanical and Biomedical Engineering
National University of Ireland, Galway

June 2012

Supervisor of Research:	Dr. Mark Bruzzi
Director of Research:	Prof. Peter McHugh

ABSTRACT

Advances in engineering fabrication technology permit the manufacture of microscale components and devices. These tiny products are used in a wide range of applications, from medical devices to smart phones. There are occasions when the speed with which these new fabrication technologies are developed outpaces the scientific research that seeks to understand the behaviour of microscale components. The behaviour of traditional engineering material is generally expressed in terms that relate to bulk material. However, it is known that bulk material behaviour does not apply at the microscale and that the physical characteristics of tiny components are modified by size effects. These size effects influence every aspect of a material's behaviour; mechanical, electrical and thermal properties all differ from the properties normally associated with a particular material.

This thesis focuses on the microscale fatigue properties of 316L stainless steel. This material is commonly used in microscale medical devices such as stents, which, once implanted, are subjected to hundreds of millions of fatigue cycles.

Fatigue testing was carried out on 50 μm, 75 μm, 100 μm and 150 μm 316L specimens. A size effect was shown to exist in the fatigue performance of the 50 μm specimens. In order to determine the cause of this size effect, the outer surfaces and fracture surfaces of failed test specimens were examined using a scanning electron microscope. These SEM studies suggested that the process of strain localization was occurring and was most pronounced in the 50 μm specimens. The surface roughness of the test specimens was measured using white light interferometry and this confirmed the SEM observation. Finally, finite element models, designed to approximately represent the grain structure and the anisotropic material behaviour of the grains were developed. These models shed further light on the process of strain localization. Taken as a whole, the thesis shows that a size effect exists in the microscale fatigue behaviour of stainless steel, and that this size effect is caused by the process of strain localization.

Acknowledgements

I am grateful to Enterprise Ireland for financial support of this work as part of the Development of Software for Small Scale Implanted Metallic Structures (DESIMS) research programme and to NUI Galway for providing a world class research facility in the form of the NCBES.

I wish to thank the following people, who during my time in NUI Galway, educated and entertained in sometimes unequal measures. Thomas Connolley provided great assistance during the early years, and also a lesson in dedication. Mark Bruzzi, my supervisor, who provided direction and offered useful advice, which I appreciated, but did not always act on. Peter McHugh provided great academic assistance and kept the show on the road. Sean Leen arrived late in the process, but had an immediate impact by lighting the proverbial fire. Noel, Frank, Brendan, Jen, Suzanne, John, Bruce, Pat McG, Karen, Adam, Ailish, Linda, Kevin, Pat McD, Mags, Daniel, Helen and many more provided the entertainment aspect of my time in NUI Galway. NUI Galway BC, the rowing club, my crews and the Corrib provided a life apart from the university. Tony, who reminded me many times that completing my PhD is well worth the effort. My parents, Liam and Kay, who supported and cajoled and Caitriona, who has not known a time without this PhD, but reminded me many times that “there are no problems, only solutions”.

I would also like to thank my colleagues at Medtronic, Frank, Cahal and Christy for continuing to educate and entertain.

Table of Contents

10. Conclusions

INTRODUCTION

1.1. Background

Advances in micro-manufacturing techniques have allowed for the development of micron-sized components, devices and machines. Products on this scale are manufactured from a range of materials, by several different methods. They are used in a wide variety of applications where they offer a cost saving and performance improvement over traditional components, and also where special size requirements must be met. The products are generally of two types:

1. Micro-electro-mechanical systems (MEMS) and
2. Micro-scale medical devices.

Figure 1.1 shows an example of a MEMS device. Micro-electro-mechanical systems (MEMS) incorporate mechanical and electronic elements and are known collectively as micro-electro-mechanical systems. Figure 1.2 shows an example of a medical device whose structural components exist in the range of less than 100 microns. A range of metal micron-scale devices, used for the treatment of human pathological conditions and generally known as implantable medical devices are also products of micro-scale engineering processes.

Commonly used MEMS devices include the accelerometer, used to detect changes in acceleration and an integral part of the vehicle airbag deployment mechanism. The accelerometer in the Apple iPhone allows the device to switch between landscape and portrait views depending upon tilt angle. Other MEMS devices include the piezoelectric crystal based ink-dispensing system of ink jet printers and miniature pressure sensors used in a range of everyday applications.

Microelectronics components are an integral part of all modern-day computer systems. Chipsets, which provide the computing power for all PCs, are composed of silicon and in modern devices, thousands of kilometres of ultrathin Cu wire. Advancements in chip power are achieved by fitting ever more computing capability, in the form of Cu wires, on an ever shrinking package. Micro and nanoscale engineering methods are not new in this industry and many of the current generation MEMS are fabricated using technology that has been developed for IC fabrication.

There are also many modern implantable medical devices with components that are micron-sized. Examples include products such as the stent, the vena cava filter, guide-wires for catheters and pacemaker leads, among others. Some of these devices are deployed within the confines of occluded human arteries and must therefore have a low crossing profile. The individual struts of these devices may be no more that 100 μm wide by 60 μm thick.

MEMS are manufactured from a range of materials, including silicon, polymers, and metals. Many operational MEMS devices are manufactured from silicon ($Si0_2$) using Integrated Circuit fabrication techniques. The devices can be combined with layers of metals of various types (Al, Cu, Au, Ag) through deposition processes such as sputter coating, electroplating, and vapour deposition. The structural component of implantable medical devices is generally produced from one of the following alloys: 316LVM stainless steel, MP35N, Cobalt Chromium, or Nitinol. These materials are selected because of their advantageous material properties and biocompatibility.

Integrated Circuit (IC) manufacturing techniques borrowed from the electronics industry have proven to be very successful in generating entire silicon-based MEMS devices. Polymer MEMS devices are typically manufactured by micro-extrusion, embossing and stereolithography processes. Metal-based MEMS devices, on the other hand, are typically manufactured by micro-forming techniques, or metal deposition techniques such as electroplating, evaporation, and sputtering processes. Polymers are also an important MEMS material, as polymer devices can be produced in large numbers, cheaply, and are suited to single-use applications where disposability is required. The range of technologies used to manufacture these devices is diverse, and under continual refinement. In many cases, the methods used to manufacture MEMS and medical devices are refinements of existing methods. Refinement is required due to the existence of size effects that prohibit the direct transfer of a manufacturing method from the macro-scale to the micro-scale [1.1]. Micron-scale laser cutting is commonly used in the medical device industry to produce vascular stents from 316LVM stainless steel, Cobalt Chromium or Nitinol tubing. Laser cut components usually require electropolishing to produce the smooth surface required for implantable medical devices to avoid injury.

Microdevices are designed for a range of applications, the nature of which determines the operating requirements for the device. The components of micro turbines, such as those under development at MIT and Gatech [1.2], will be subjected to heat, centrifugal forces and associated creep and fatigue from cyclic loading. Micro-fluidic devices will be subjected to temperature variations, pressure variations and fluid effects which will create a fatigue type loading situation [1.3]. Integrated circuit components such as microwires will experience thermal cycling which may cause fatigue failure at joints and solder points [1.4]. Medical devices such as the vascular stent will experience an initial super yield, high strain upon deployment, followed by pulmonary induced cyclic loading in a physiologic environment [1.5]. Such a device must withstand at least ten years service or four hundred million load cycles without failure [1.6].

Electrostatic effects can also affect device performance should components “stick” to one another if the device is operating in an electrostatically charged environment or becomes so charged during operation. The components of microscale devices are so small that momentum of the component itself may not be sufficient to overcome this force of attraction.

1.2. Size effects

Micro devices are typically of a scale such that factors which can be largely ignored at the macrolevel can change the material behaviour considerably at the micron level. For example, chemical effects such as oxide layer formation can result in increased yield strength and fatigue life in Cu microwires [1.7] and Al thin films [1.8]. Such a change in the composition of the component should be taken into consideration for devices made of such materials and operating in an environment where oxidation is likely to take place. Other chemical effects may have a deleterious effect on material behaviour, again this effect must be characterised for proper design and operation of the device when the surface constitutes a significant portion of the component size.

Microscale components and MEMS fabricated from silicon can experience an improvement in fatigue life due to the small component size and consequent reduction in surface defect size and quantity. This is a phenomenon generally associated with brittle components and is a most useful characteristic from the point of view of MEMS performance. A reduction in ductility of polycrystalline material due to a reduction in the number of active slip systems has also been observed in microscale components. Therefore, the various material characteristics of microscale devices must be established through mechanical testing of actual components or of test specimens of a similar texture, grain size, scale and fabrication method as the proposed components.

MEMS and medical devices are created to serve a multitude of purposes. As with all machines or devices, the purpose for which they are designed determines the selection of materials, processing route, component size and any special properties to enhance material performance, such as increasing its resistance to fatigue crack initiation and growth, to chemical attack etc. However, at such small size scales, changing any one of above parameters will result in a change in material behaviour that could influence device performance.

Given a particular geometry, processing route and composition of a metal, it is necessary to determine the associated material characteristics such as Young's modulus, yield point, hardening rate, ultimate strength, fracture strain and fatigue life.

Mechanical testing of microscale components is not an easy task. In general, standard mechanical test equipment is not suitable for testing microscale components due to the operating range and resolution of load and displacement transducers and the design of gripping members.

At the very least, very sensitive load cells, displacement transducers and specially designed grips capable of holding delicate microspecimens, must be fitted to bench mounted mechanical testers. In some cases, where very thin specimens are investigated, highly sensitive equipment such as Atomic Force Microscopy systems [1.9] and nanoindenters [1.8] must be used for static and dynamic testing. Such systems are capable of measuring nanoscale forces and deflections.

Microscale test specimens are designed to elucidate both material properties and deformation and failure mechanisms. The various material characteristics of microscale devices must be established through mechanical testing of actual machine or device components or of test specimens of a similar texture, grain size, scale and fabrication method as the proposed components. This requires development of novel test methods and test specimens. By their very nature, microscale test specimens (an example of which is shown in Figure 1.3) are difficult to handle without causing deformation and damage prior to testing.

1.3. Coronary Heart Disease and Minimally Invasive Medical Devices

Coronary Heart Disease is responsible for the deaths of as many as one in three people in the developed world. It is estimated that as many as 62,000,000 Americans have at least one form of cardiovascular disease [1.10]. The human and economic consequences of such a prevalent disease are considerable and the demand for treatment methods has created a multi-billion euro industry, a substantial portion of which is located in the west of Ireland.

The disease is a progressive condition; as one ages, a fat-like substance, atheromatous plaque, is deposited on the inner walls of the coronary arteries [1.11]. The consequent narrowing and hardening of the arteries is known as atherosclerosis, and results in a reduction of elasticity and hence blood flow to the muscles of the heart. If the condition is severe, the heart muscle tissue becomes infarcted (cell death caused due to inadequate blood supply). This loss of tissue and associated heart function is irrecoverable. However, advances in medical knowledge, and in minimally and non-invasive treatment and inspection techniques have improved significantly the prognosis of individuals affected by the disease, if detected in time.

It has been known for decades that atherosclerosis begins in youth and develops throughout the lifetime of the affected individual. A revelatory 1953 study on the coronary arteries of young (average age of 22 years) Korean war casualties by three US army pathologists [1.12] highlighted both the high frequency and advanced state of the disease in the subjects. Since that time, much work has been done on the identification of risk factors that may be measured or observed in the young and are linked with coronary heart disease in later life [1.13]. Such risk factors may be used as a predictive tool for determining an individual’s potential susceptibility to the disease, and a lifelong treatment process aimed at preventing coronary heart disease may begin at a young age.

However, such forward looking inspection systems have not been established as routine in the health services of the developed world, and consequently, the requirement is created for treatment methods that may be applied in later life when the problem has developed.

Heavily stenosed coronary arteries were initially treated with a technique known as coronary artery bypass surgery. In this procedure, a section from a healthy artery or vein from elsewhere in the body is grafted onto a coronary artery, bypassing the blocked region of the vessel and restoring blood flow to the heart. This is a highly invasive procedure, from which it may take months to recover.

In the late seventies, a German physician, Andreas Gruentzig, developed the concept of using a balloon to expand the blocked region of a coronary artery, thus restoring vessel patency. Greuntzig aimed to attach the balloon to a catheter in a modification of a process that had been developed by another physician, Charles Dotter [1.14].

This minimally invasive procedure is known as Percutaneous Transluminal Balloon Angioplasty (PTCA) and Greuntzig’s first successful operation on a human using a balloon catheter took place in Zurich in 1977. Though generally successful, complications associated with this technique, namely abrupt vessel closure and restenosis (reblocking) of the affected vessel meant that further refinement was required.

1.4. The Stent

In the mid- 1980s, an American physician, Dr. Richard Schatz, conceived of the idea to prop open blocked coronary arteries with a spring-like metal device known as a "stent". In doing so, Dr. Schatz created a device that revolutionized both the area of interventional cardiology and the medical device industry.

As the name suggests, a balloon expandable stent is deployed when the balloon on which it is mounted is inflated. An example of a balloon expanded stent is shown in Figure 1.4. These stents were typically manufactured from stainless steel, because of its biocompatibility, and remain open once the yield point of the metal has been exceeded. The extent to which the stent is deployed is dependent upon the inflation pressure of the balloon, and many cardiologists deploy the stents to a diameter greater than that required to insure adequate vessel patency in order to account for elastic recoil of the device [1.15]. Complications associated with Percutaneous Transluminal Coronary Angioplasty, namely, acute vessel closure and a restenosis of the target vessel requiring recanalization, necessitated the development of the vascular stent. Comparative studies [1.16, 1.17] of balloon angioplasty alone and balloon angioplasty with coronary stenting revealed that there was a reduction in the number of repeat revascularisation procedures required with stenting, a greater immediate increase in lumen diameter and a reduction in the levels of restenosis at 6-month follow up. The use of stents represented a significant improvement in outcomes in comparison to straight balloon angioplasty, so much so that by 2002, up to 80% of coronary angioplasty procedures carried out in 30 European countries were accompanied by stenting (this compares with 50% in 1996) [1.18, 1.19].

However, the move to bare metal stents was only partially successful. While the serious problem of acute vessel closure was resolved, the issue of restenosis of the vessel remained. The rates of restenosis, while lower than those for straight balloon angioplasty, were still in the order of 20 – 30% [1.18, 1.19]. The reasons for this restenosis of the artery are complex and not completely understood, but are generally attributed to a hyperplasic response to stent induced intimal injury [1.20], where the stent cuts through the endothelium (the innermost layer of the artery) and into the smooth muscle tissue of the intima. Figure 1.5 shows a schematic sketch of the basic anatomy of the artery. Inflammation associated with this injury can cause cell growth to an extent that reduces the diameter of the lumen by 50%. This represents the standard definition for angiographic restenosis, and the level at which remedial intervention is recommended. This process is known as neointimal hyperplasia. Severe hyperplasia can quickly reverse the benefits of stenting and return the artery to a state where a repeat procedure is required [1.21].

It is worth noting that the type of restenosis that occurs with a stent implantation (in-stent restenosis) differs from that associated with a standard PTCA procedure [1.16, 1.17]. In PTCA, restenosis is due largely to negative vessel remodelling, where the adventitia becomes enlarged as a result of damage to the medial layer and to the adventitia itself. This leads to vessel contraction and shrinkage of the lumen diameter. In-stent restenosis is due to the formation of new smooth-muscle cells, growing from the compromised intima, around the stent and into the lumen. This difference is important from the viewpoint of selecting treatment methods. The frequency and severity of restenosis and the associated requirement for vessel revascularization necessitated further development of the technology. Such a development came in the form of the drug-eluting stent. When combined with restenosis-inhibiting drugs, the stent becomes a site-specific drug delivery vehicle and is ideally suited to combating in-stent-restenosis. This third generation device was achieved by coating the stent with a drug-infused polymer. The polymer serves a dual-purpose. Firstly, it attaches the drug to the stent. Secondly, it controls the release rate or "elution" rate of the drug into the adjacent arterial tissue. Two forms of drug have been approved by the U.S. Food and Drugs Administration for use in this technology; the immuno-suppressant drug, Sirolimus, and a cancer treatment drug, Paclitaxel. The drugs act to prevent restenosis through different mechanisms. Clinical trials comparing drug-eluting stents (both sirolimus and paclitaxel eluting stents) directly against bare–metal stents [1.22, 1.23] have shown that significantly lower levels of neointimal hyperplasia exist in DES treated vasculature at six month, eight month, twelve month and eighteen month angiographic follow-up. Also, the need for revascularization procedures was effectively eliminated.

1.5. New and emerging stent technologies

The stent solution has been applied to many problems in the human body and stent designs differ depending upon their application. Where significant and repeated bending is expected, such as in the supra femoral artery (SFA) of the leg, super elastic nitinol stents are used to restore vessel patency and provide suitable fatigue life. Stents form the basis of products used to treat various types of aneurysms such as the Abdominal Aortic Aneurysm or AAA. An example of such a device is shown in Figure 1.6. Here, a wire frame, again of nitinol, is covered in a polyester sheath. The frame provides radial force which anchors the device and maintains patency, and the sheath diverts blood flow away from the aneurysm. The latest coronary stents, both bare metal and drug eluting are made from a range of materials including 316L stainless steel, MP35N and cobalt chromium. The design of these stents is constantly evolving in order to maintain competitive advantage and achieve reductions in manufacturing costs.

An emerging and innovative application of the stent is in the form of minimally invasive heart valve replacement therapies. The device frame provides the usual radial force and anchoring elements. As shown in Figure 1.7, frames are either balloon expandable and made from 316L stainless steel (Edwards Sapien) or self-expanding and of superelastic nitinol (Medtronic CoreValve). In addition, a bioprosthetic leaflet, of bovine or porcine pericardium is attached to the inside of the frame. These devices are delivered to the heart in a minimally invasive manner, and current technology provides for the replacement of aortic and pulmonary valves. While these heart valves deviate significantly from the original stent concept, they are nonetheless, a form of stent.

A common element of all the above devices is that each in turn pushes the boundaries of current device design knowledge and understanding of material behaviour. A problem not previously treated in a minimally invasive manner poses new challenges and provides a new set of design requirements. Implicit in the design of a successful product is a complete understanding of the problem to be addressed, the operating environment and the various elements of the proposed solution. First among these is a well developed understanding of the mechanical behaviour of the various materials from which the device will be made.

However, it is not sufficient to rely exclusively on existing knowledge of material behaviour obtained from testing samples significantly larger than the micro-scale samples in question for medical device applications. The behaviour of the selected materials must be characterised anew, with test specimens of the same material, size, and processing route as the critical elements of the proposed frame design. Material performance should be characterized under a range of loading conditions, including conditions that describe relevant physiologic loads. This is necessary in order to take account of any size effects and process-related artefacts which can cause behaviour to deviate significantly from bulk material behaviour.

Stent-based therapies are becoming ever more ambitious, aiming to provide treatment for problems in more tortuous vessels with more complex loading conditions. The use of stents to treat cerebral blockages and aneurysms requires further miniaturization below the size of the smallest currently available vascular stents. The small scale of these devices is such that a range of size-related phenomena, not associated with macroscale devices, must be considered. These effects, known simply as “size effects”, relate to all aspects of material behaviour at the micron-scale. The consequences of these size effects must be accounted for during device design, manufacturing and operation. Of general interest in this project are the mechanical size effects associated with metals, and in particular those associated with 316LVM stainless steel.

As component size is reduced, size effects become apparent regardless of material type. In brittle materials, where fracture is related to the number and size of flaws, reducing component size can significantly improve ultimate tensile strength [1.17], where there is a lower probability of finding a critical flaw in a very small specimen. At very small sizes, because of the large surface area to volume ratio, surface effects such as electrostatics, surface tension and oxidation may influence, to a much greater extent, material and component behaviour. Size effects in metals are generally attributable to the granular structure of the metal. At the microstructural level, metals are composed of grains as illustrated by a scanning electron microscope (SEM) image of a 316L steel sample shown in Figure 1.8. The grain size varies considerably depending on processing route, and is a tightly controlled parameter during the manufacturing process. Deformation within grains results due to slip in defined directions on defined planes. Therefore the deformation behaviour of a grain in a given direction is dependent upon the loading direction with respect to the grain orientation. As grains are randomly orientated within a metal, each one deforms to a different extent at a local level when the structure as a whole is subjected to a given load. For most metal components, the grain size is so small relative to the size of the component that its effect on component performance is negligible, i.e. no deformation within a single grain, resulting from a preferential slip orientation, dominates the overall component behaviour.

In these situations, engineers generally consider the component to be composed of a homogeneous material and hence isotropic in its behaviour. Associated design calculations and finite element modelling work reflect this assumption. However, as schematically illustrated in Figure 1.9, where the grain size is of the order of the component size, a different approach must be adopted. At size scales where the grain size and the specimen size are of the same order, the orientation of individual grains has a significant effect on component behaviour. The resulting deviation from expected material behaviour with diminution in specimen size is known as a “size effect” and can be attributed to a reduction in the level of constraint experienced by the individual grains and a consequent increase in granular compliance to external loading. A series of tensile tests [1.24] carried out on electropolished 316L stainless steel struts within the size range of 60 – 500 μm established that a size effect does exist and has the effect of reducing the strain to failure for smaller specimens. Designers of micron-sized products should, therefore, be aware of such material behaviour.

The existence of a size effect under tensile loading raises the question as to whether a similar effect exists under conditions of fatigue loading at a similar size scale. Again, this is directly applicable to a medical device such as a stent, which undergoes an initial tensile load upon deployment and subsequent cyclic loading (albeit at much reduced strain amplitude) for the working life of device. Should such a size effect exist, standard fatigue resistance prediction tools such as the Goodman method could potentially produce nonconservative estimates of safe working loads, which could result in fractures of devices *in-vivo.*

1.6. Objectives and scope of project

The objective of this work is to establish if a size effect exists in the fatigue behaviour of 316L stainless steel struts of sizes comparable to those used within cardiovascular stents. This is to be achieved by fatigue testing micron-sized 316L stainless steel test specimens of varying widths, laser cut from industry standard, annealed, seamless tubing and electropolished to achieve medical device quality finish. Fatigue testing will mimic the effects of stent deployment by applying a high initial strain amplitude, followed by a maximum of ten million tension-tension cycles at lower strain amplitude under conditions of load control. Strut widths of 150, 100, 75 and 50µm with a constant wall thickness of 60µm will be investigated. Stress-life curves will be generated from the output of the fatigue tests allowing the assessment of whether a size effect manifests itself as a reduced endurance limit for specimens of smaller sizes and what mechanisms exists to explain such a size-effect.

In this thesis, a literature review is conducted in Chapter 2 exploring size effects in the mechanical behaviour of microscale components. Chapter 3 describes the finite element modelling that was carried out in order to determine the operating stress range for vascular stents. Chapter 4 details the material and methods associated with the fatigue testing of microscale 316L test specimens. The results of the fatigue testing of the microscale specimens are described in Chapter 5. Chapter 6 considers the surface analysis that was carried out on the fatigue test specimens. The development of a micromechanical finite element modelling methodology is dealt with in Chapter 7, while the output of these models is presented in Chapter 8. The work is discussed in chapter 9 and conclusions are presented in Chapter 10.

References

[1.1] Vollertsen, F., Schulze Niehoff, H and Hu, Z. (2006) State of the art in micro forming. *Int J Mach tool Manu*, Vol. 46, Issue 11, pp. 1172-1179

[1.2] http://web.mit.edu/newsoffice/2006/microengines.html

[1.3] http://en.wikipedia.org/wiki/Microfluidics

[1.4] Qiang, Y., Shiratori, M. (1997) Fatigue-strength prediction of microeclectronics solder joints under thermal cyclic loading. *Eng. & Mater. Sci.*, Vol. 20, Issue 3, pp. 266-273

[1.5] Dumoulin, C. and Cochelin, B. (2000) Mechanical behaviour of balloon-expandable stents, *J. Biomech.*, Vol. 33, 1461-1470

[1.6] Guidance for Industry and FDA staff (2010) – Non-Clinical Engineering Tests and Recommended Labeling for Intravascular Stents and Associated Delivery Systems. FDA, Centre for Devices and Radiological Health, Section IV-B-11

[1.7] Khatibi, G., Betzwar-Kotwas, A., Groger, V. and Weiss, B. (2005) A study of the mechanical and fatigue properties of metallic microwires. *Fatigue Fract. Engng Mater. Stuct.* Vol. 28, pp. 723-733

[1.8] Son, D., Jeong, J.H., and Kwon, D., (2003) Film-thickness considerations in microcantilever-beam test in measuring mechanical properties of metal thin film. *Thin Solid Films* Vol. 437, 182-187

[1.9] Nilsson, S. G., Sarwe, E-L. and Montelius, L. (2003) Fabrication and mechanical characterization of ultrashort nanocantilevers. *Appl Phys Lett.* Vol. 83, 990–992

[1.10] American Heart Association, (2002) Heart and Stroke Statistical Update. Dallas, Tex. *Amer Heart Assoc*

[1.11] Tortora, G., (2002) Principles of the Human Anatomy, John Wiley & Sons. 9th Ed., pp. 408-410

[1.12] Enos W.F., Holmes R.H., Beyer J. (1986), Landmark article, July 18, 1953: (1953) Coronary disease among United States soldiers killed in action in Korea: Preliminary report. *J Amer Med Assoc,* Vol. 256 (20) : 2859-2862

[1.13] Li, S., Chen, W., Srinivasan, S.R., Bond, M.G., Tang, R., Urbina, E. M., Berenson, G.S., (2003) Childhood Cardiovascular Risk Factors and Carotid Vascular Changes in Adulthood - The Bogalusa Heart Study. *J Amer Med Assoc*, Vol. 290 (17), 2271-2276

[1.14] Mueller, R.l., Sanborn, T.A., (1995) The history of interventional cardiology: cardiac catheterization, angioplasty and related interventions, *Am Heart J*, Vol. 129 (1): 146-172

[1.15] M.A. Costa, M. Sabate, I.P. Kay and P. de Feyter, (2000) “Three-dimensional intravascular ultrasonic volumetric quantification of stent recoil and neointimal formation of two new generation tubular stents”, *Am. J. Cardiol*., Vol. 85, pp. 135-139

[1.16] Serruys, P.W., de Jaegere, P., Kiemeneij, F., Macaya, C., Rutsch, W., Heyndrickx, G., Emanuelsson, H., Marco, J., Legrand, V., Materne, P., Belardi, J., Sigwart, U., Colombo, A., Goy, J.J., van den Heuvel, P., Delcan, J., and Morel, M-A. (1994) A comparison of balloon-expandable-stent implantation with balloon andioplasty in patients with coronary artery disease: Benestent Study Group, *N Engl J Med*., Vol. 331, pp. 489-495

[1.17] Fischman, D.L., Leon, M.B., Baim, D.S., Schatz, R.A., Savage, M.P., Penn, I. Detre, K., Veltri, L., Ricci, D., Nobuyoshi, M., Cleman, M., Heuser, R., Almond, D., Teirstein, P.S., David Fish R., Colombo, A., Brinker, J., Moses, J., Shaknovich, A., Hirshfeld, J., Bailey, S., Ellis, S., Rake, R., and Goldberg, S. (1994) “A randomized comparison of coronary artery-stent placement and balloon angioplasty in the treatment of coronary artery disease” *N Engl J Med*. Vol. 331 pp. 496-501

[1.18] Togni et al, (2004) Percutaneous coronary interventions in Europe 1992-2001, *European Heart Journal*. 25, 1208-1213

[1.19] Maier et al, (2001) The European registry of cardiac catheter interventions 1996, *European Heart Journal*. Vol. 22, pp.373-377.

[1.20] Hoffmann, R., Mintz, G.S., Haager, P., K., Bozoglu,, T., Grube, E., Gross, M., Beythien, C., Mudra, H., vom Dahl, J. and Hanrath, P., (2002) Relation of stent design and stent surface material to subsequent in-stent intimal hyperplasia in coronary arteries determined by intravascular ultrasound, *Am. J. Cardiol.*, Vol. 89(12) pp.1360-1364

[1.14] Schwartz et al (1998) Artery Size, Neointima, and Remodeling, Time for some Standards, *J Am Coll Cardiol*. Vol. 32, pp.2087-2094

[1.15] Vishnevetsky et al (2004) Sirolimus-eluting coronary stent, *Am J Health-Syst Pharm*. Vol. 61, pp.449-456

[1.16] Nawarskas et al (2005) Paclitaxel-eluting stents in coronary artery disease, *Am J Health-Syst Pharm*. Vol. 62, pp.2241-2251

[1.17] Murphy, B.P., Savage, P., McHugh, P.E., Quinn, D.F. (2003) The stress-strain behaviour of coronary stents struts is size dependent. *Annals Biomed. Engng*. Vol. 31, pp. 686-691

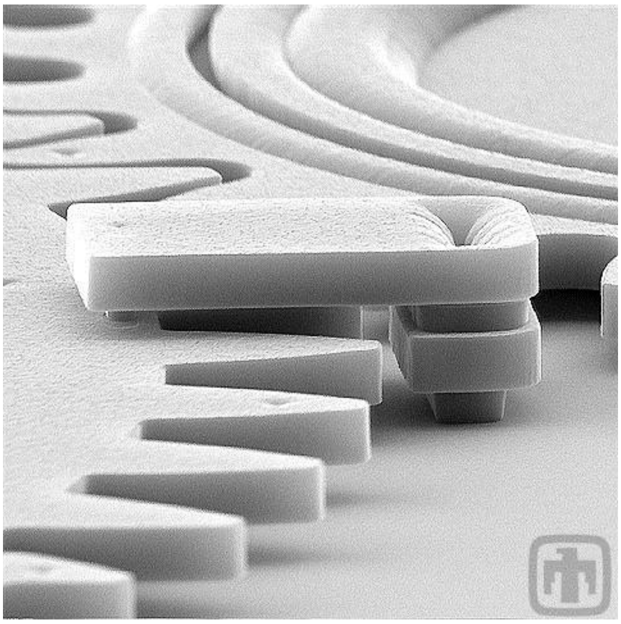

Figure 1.1. Gear train of a micro engine. The gear teeth are about the size of a red blood cell. Sandia National Laboratories, SUMMiTTM Technologies, www.mems.sandia.gov

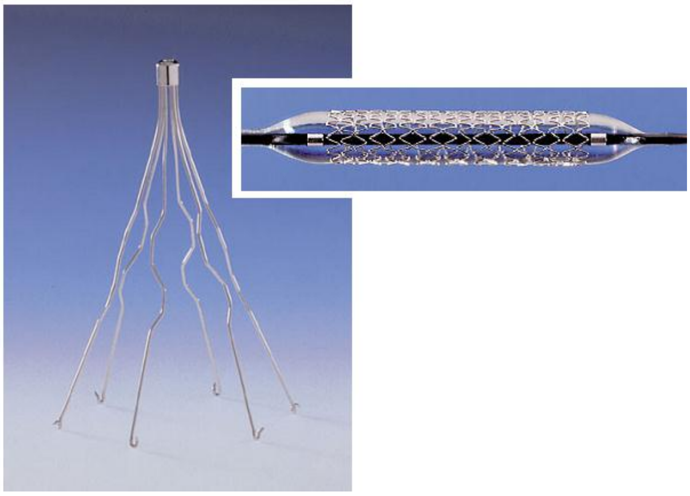

Figure 1.2. Boston Scientific Greenfield ® Vena Cava Filter (L) and Medtronic S7 ® vascular stent (R). In the undeployed state, the diameter of both devices is approximately 1.5mm.

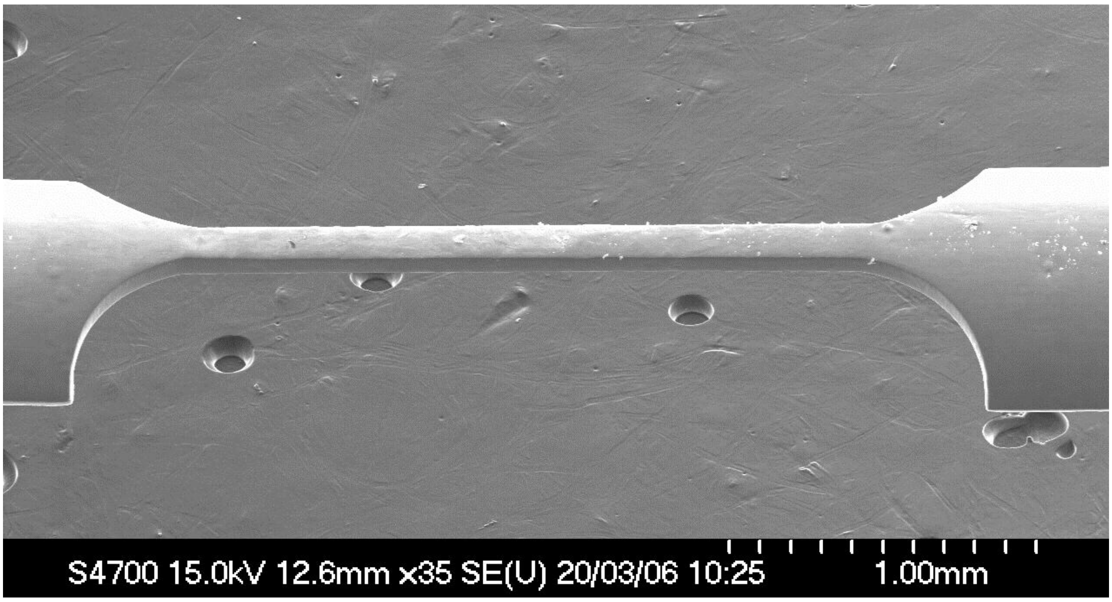

Figure 1.3. Image of microtest specimen

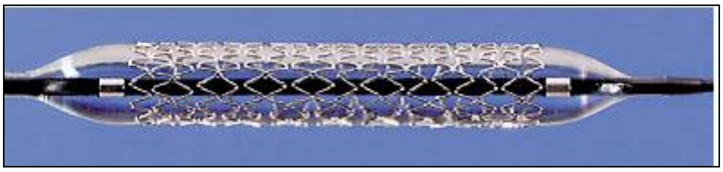

Figure 1.4. Bare metal stent on an inflated balloon. The angiogram markers are clearly visible on the catheter. The markers assist in stent positioning.

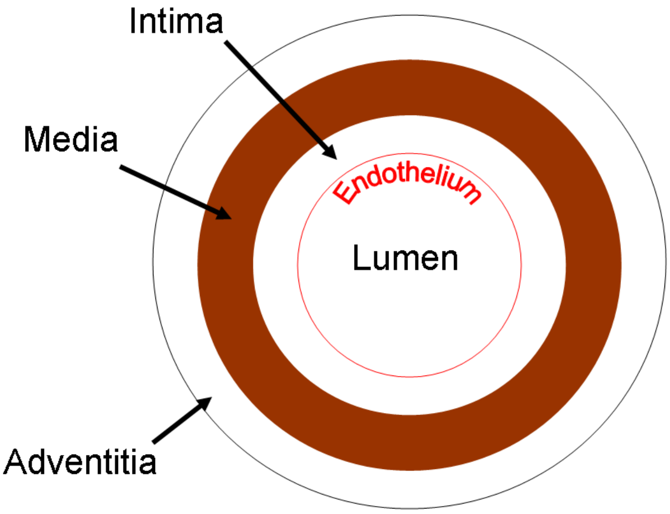

Figure 1.5. The basic structure of an artery.

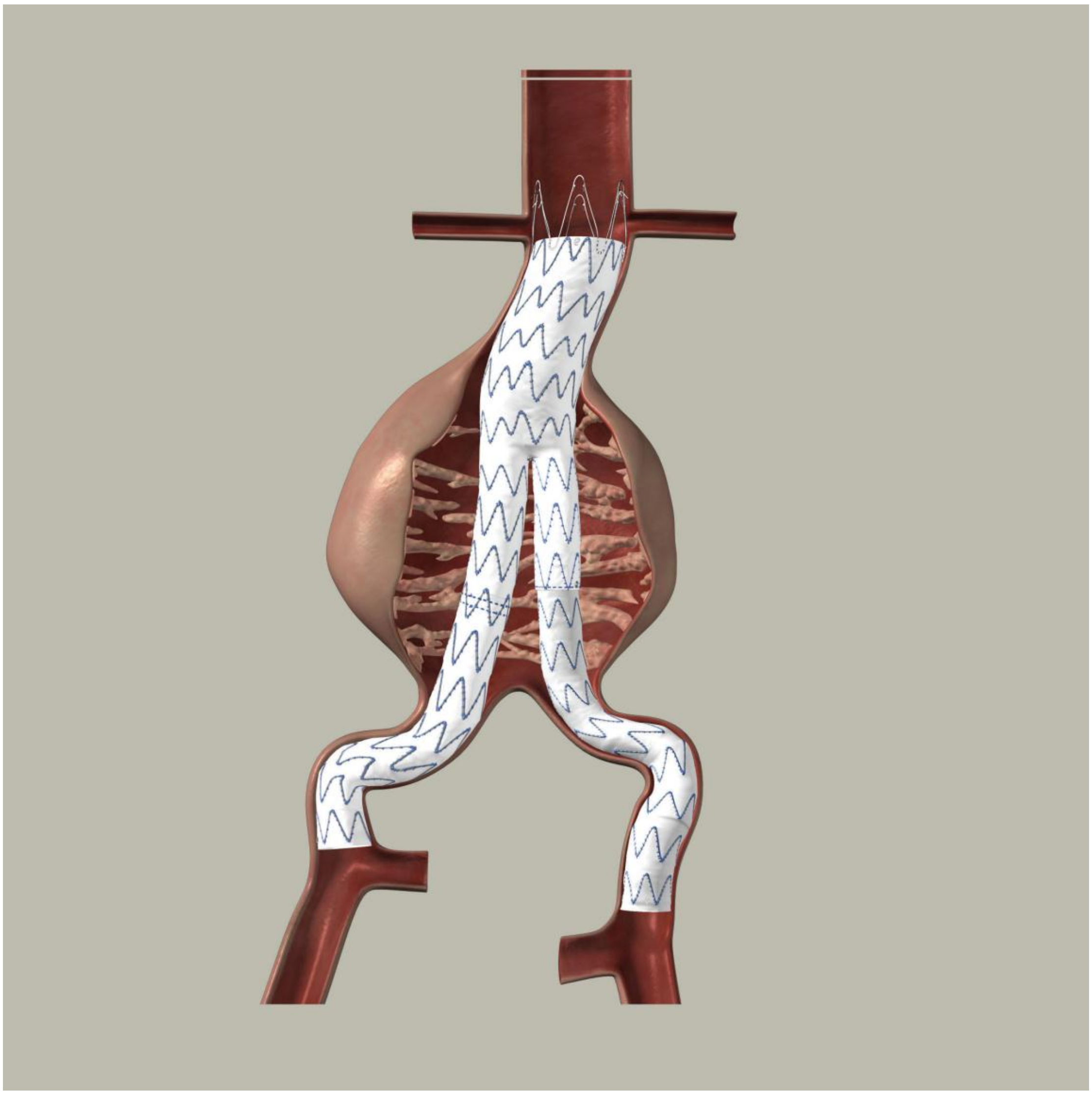

Figure 1.6. The Endurant AAA Stent Graft creates a new path for blood flow through the aorta, reducing pressure on the aneurysm and the risk of rupture.
Courtesy Medtronic, Inc

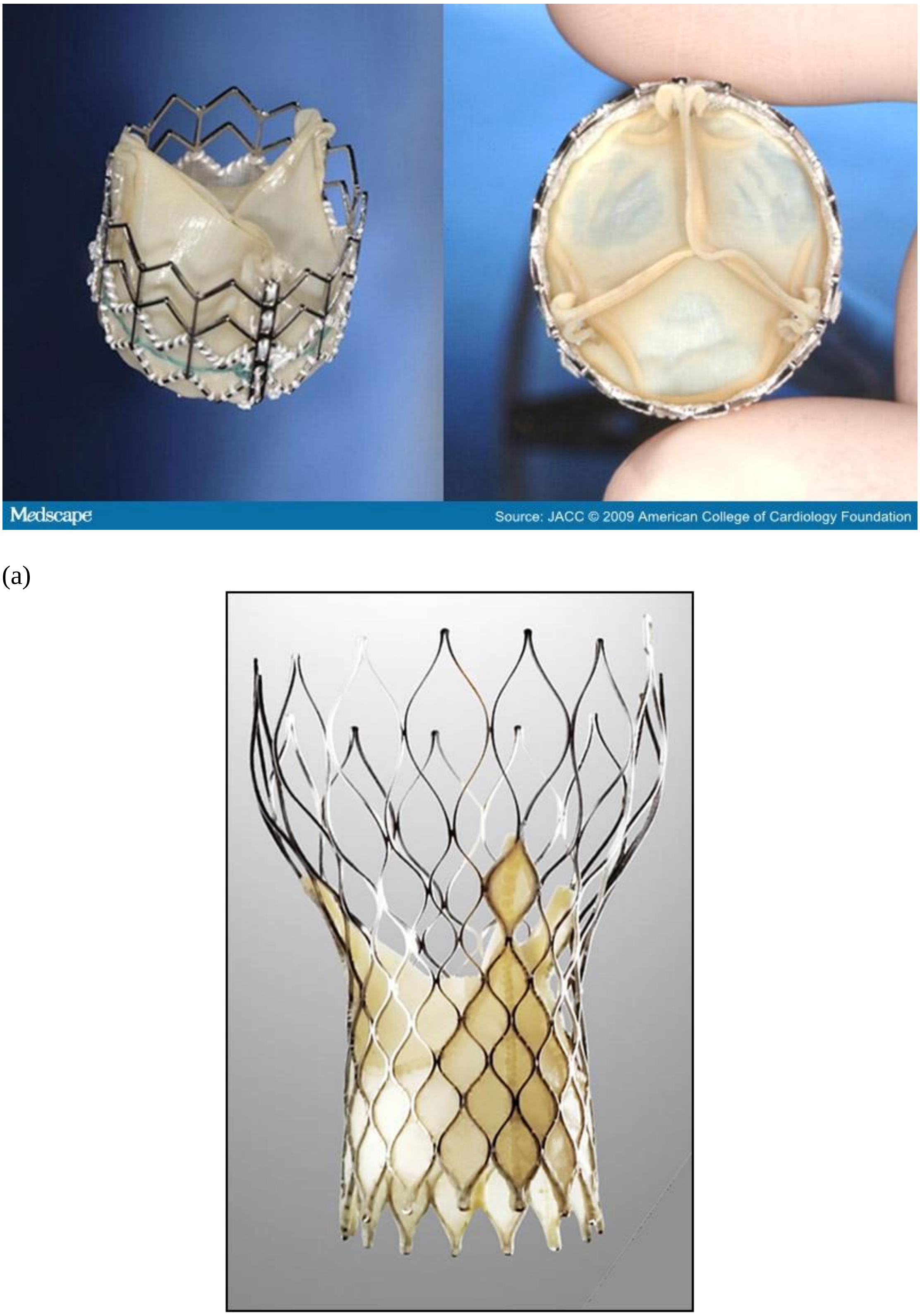

Source: JACC © 2009 American College of Cardiology Foundation

(a)

(b)

Figure 1.7. Aortic heart valve replacement therapies (a) Edwards ‘Sapien’ device with bovine pericardial tissue leaflets and balloon expandable stainless steel stent (b) Medtronic’s ‘CoreValve’ with porcine pericardial leaflets and a superelastic nitinol stent.

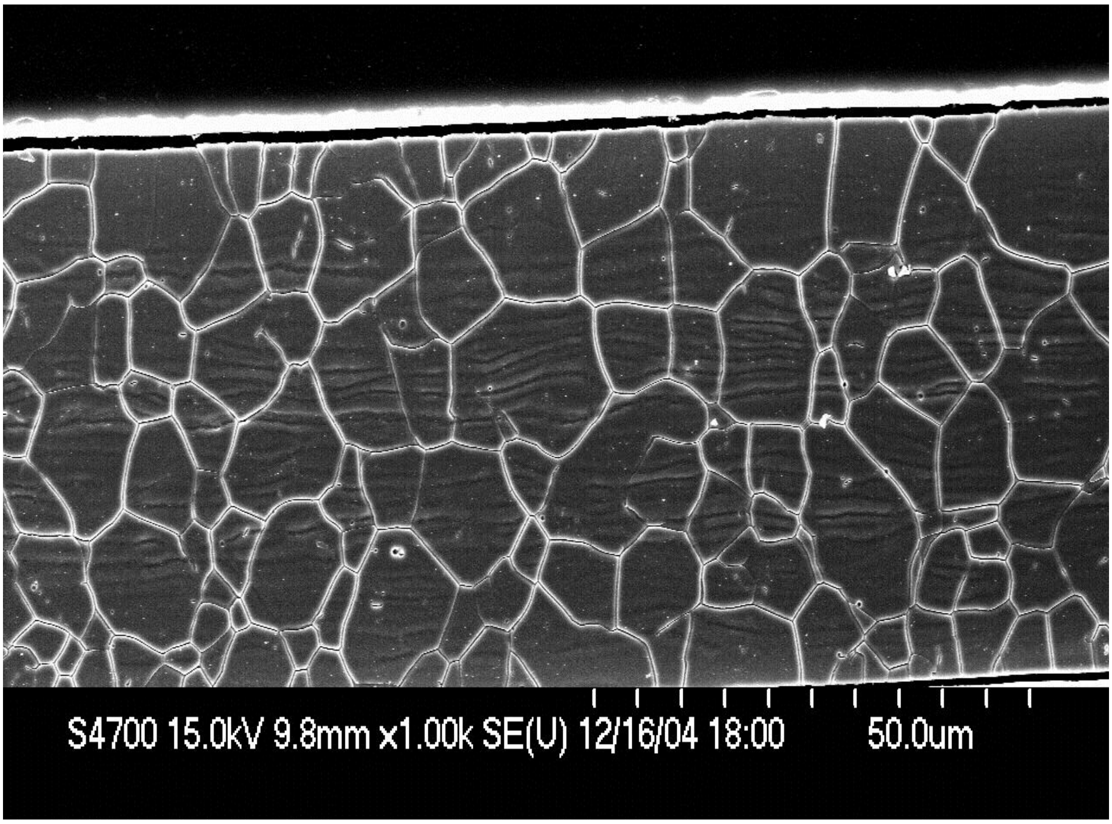

Figure 1.8. SEM micrograph of etched stainless steel strut showing the grain structure.

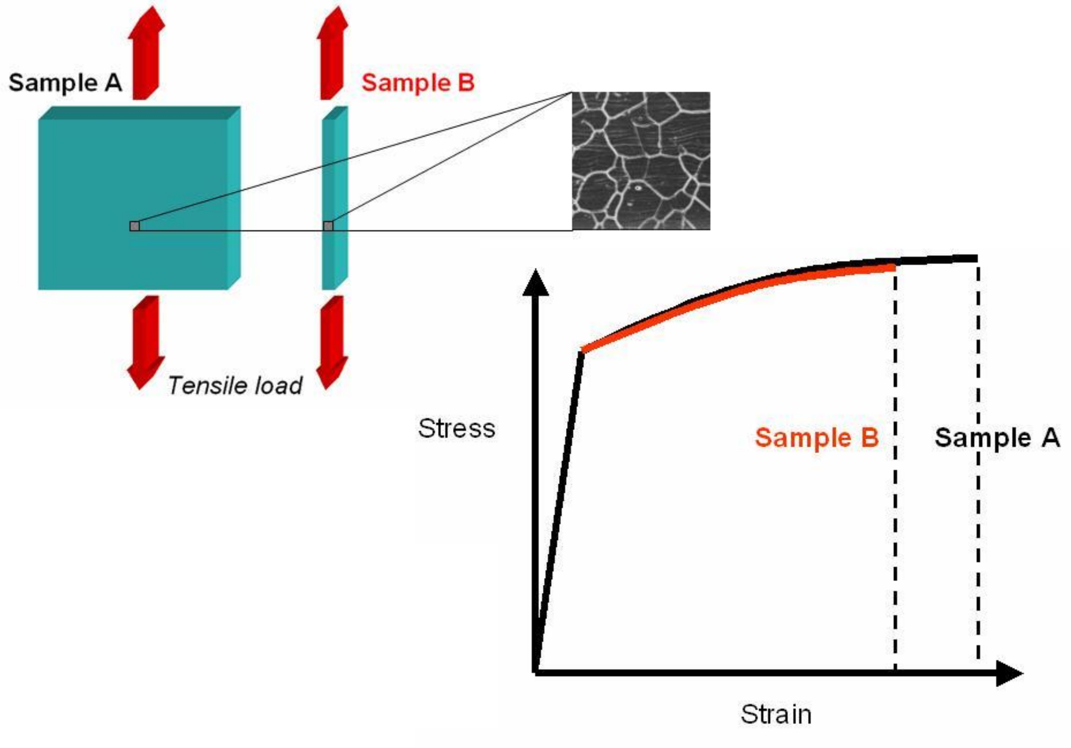

Figure 1.9. Reduction in specimen size and corresponding reduction in uniform plastic strain on application of tensile load

LITERATURE REVIEW

2.1. A brief history of fatigue

The mechanism of failure through cyclic loading became an issue in the early stages of the industrial revolution. Metal components replaced those made from natural materials and the requirements of industry ensured that these components experienced sufficient numbers of load cycles for fatigue failure to occur. The history of fatigue, [2.1] begins in 1837 in the Clausthal mines in Germany. A civil servant by the name of W.A.J. Albert with responsibility for the mines published the first known fatigue test results. Conveyor chains had failed in the mines and Albert developed a test machine that replicated in-service loads and performed testing on the chains in order to determine the cause of failure. His interpretation of the results of the fatigue testing led him to invent the wire rope. As early as 1853 French engineers were operating a “safe life” design approach with the axles of horse-drawn mail coaches specifying that axles be replaced at 60,000km. In 1843, W.J.M Rankine, a British railway engineer, recognised the distinctive characteristics of fatigue failures and noted the dangers of stress concentrations in machine components. The term “fatigue” was first mentioned by Englishman Braithwaite in 1854. He employed the term exclusively to refer to cracking of metals under cyclic loading. In his paper, Braithwaite describes service failures of a whole range of industrial equipment. A. Wöhler carried out extensive work (1858-1870) characterizing the fatigue life of railway axles. He observed that the strength of steel axles subjected to cyclic loading was appreciably lower than the static strength. His work led to the characterization of fatigue behaviour in terms of stress amplitude – life (S – N) curves and to the concept of the endurance limit. In 1864, W. Fairbarn, working for the British Board of Trade, concluded that wrought iron girders subjected to cyclic stresses with a maximum of only one-third of the ultimate strength would fail. Bauschinger (1886) observed that the elastic limit of metals differs between forward and reverse loading. Ewing and Rosenhain (1900) and Ewing and Humfrey (1903) published optical micrographs showing fatigue-induced slip bands on the surface of polished iron specimens. These slip bands were observed to deepen with fatigue cycling, intrusions and extrusions were formed, and eventually a crack developed. An understanding of the fundamental mechanisms contributing to fatigue had been developed. Up to the early 1900s, work on fatigue dealt with failures due to the application of cyclic loads, or mechanical fatigue. From the 1900s on, researchers became aware of and began to examine among others, fretting fatigue, thermomechanical fatigue, creep fatigue and corrosion fatigue. By 1920, fatigue had evolved into a major field of study and the pace of developments accelerated. Damage accumulation models were developed by Palmgren (1924) and Miner (1945), notch effects were examined by Neuber (1946) and statistical theories of the strength of materials were proposed by Weibull (1939). Coffin and Manson (1954) independently proposed an empirical relationship between the number of cycles to failure and the plastic strain amplitude. Inglis (1913) and Griffith (1921) developed methods for analyzing brittle fracture and Irwin (1957) in his work on crack tip stress singularities extended this field of fracture analysis to cover fatigue failure in metals. This new field, linear elastic fracture mechanics, related Irwin’s stress intensity factor to the increment of cyclic crack growth. Paris (1961) made a further important contribution to this field through the introduction of the Paris law (or Paris-Erdogan law). This law provides a relationship between crack size and the remaining number of cycles to failure.

2.1.1. Different approaches to fatigue

2.1.1.1 Total life approach

In this classical approach, the total number of cycles required to produce fatigue failure in smooth test specimens under laboratory conditions is estimated under controlled stress or strain amplitudes. The total life, N_f, is therefore comprised of the initiation phase, $N_{i,}$ and the propagation phase, $N_{p,}$ where:

$$N_f = N_i + N_p \tag{2.1}$$

2.1.1.2 Defect tolerant approach

As the name suggests, the approach assumes that all engineering components are inherently flawed. The working life of the component is then calculated as the number of cycles required to propagate the largest flaw to some critical size. The size is determined by the fracture toughness of the material, the limit load for the component and the permissible compliance change. The prediction of crack growth rates relies on empirical crack-growth laws based on fracture mechanics.

2.2. A Statistical Theory of the Strength of Materials

In 1939, Weibull [2.2] proposed that there exists a statistical theory for the strength of materials. As the size of a component increases so too does the likelihood that a critically large flaw is present in the structure. This explains why the fatigue limit decreases as specimen size increases. The theory is traditionally applied to components of a size where bulk material properties apply [2.3] but it seems that it may also apply at the microscale. In his work on MEMS, Park et al [2.4] investigated the tensile and fatigue performance of 1 μm thick, 50, 100 and 150 μm wide Al-3%Ti films. He attributed a decrease in the fatigue life of the larger volume 150μm films to a weakest link mechanism, with the probability of a weak link increasing with material volume. If a larger specimen has lower fatigue strength than a smaller one of the same material, then the weakest link theory may be used as an explanation, regardless of scale.

2.3. Fatigue in foils and films

Investigating the mechanical behaviour of micro and nano-scale components is not a facile task. The test specimens are too small and delicate for standard mechanical characterization equipment to be of any use. The resolution of force and displacement sensors can be too low; the grips are far too large, and in some cases, physical manipulation of the specimens is not possible as they are simply too small to see. Testing these tiny specimens requires the researcher to be both inventive and thorough in pursuit of his or her test objectives.

From a fatigue stand point, micron and nano-scale component testing poses many challenges. Crack growth studies are rare due to the small size of specimens and are generally restricted to fatigue studies that produce through-thickness cracks in foils and films. It is easier to characterize fatigue life in terms of stress-life or strain-life, or to measure number of cycles to failure (N_f) or the number required to produce a pre-determined change in specimen compliance. Alic and Asimov [2.5] qualitatively describe tensile and fatigue crack propagation rates and deformation mechanisms in wrought metallic foils of Cu, 70:30 brass and Tantalum. Foil thicknesses of 25– 50.8 μm were investigated, with one grain through the thickness. Short central slits orientated perpendicular to the loading direction acted as crack initiators. The brass foils were fatigued at near-yield and above yield conditions, and in 25 μm thick foils, crack propagation occurred by coalescence of voids formed. For 50.8 μm thick brass foils, low stress cycling produced planar areas on the fracture surface. As shown in figure 2.1, flat or planar fracture surfaces indicate a transition from plane stress to plane-strain conditions. The Tantalum foil showed a tendency for crack growth to occur below the yield stress and this fatigue crack growth occurred by void coalescence. Under certain conditions, plane-strain type cracking was observed; starting from the centrally located through thickness slit and transitioning to a knife-edge like shear mechanism (figure 2.1). This transition from a planar fracture surface to a knife-edge type fracture surface is associated with a change from plane strain to plane stress (figure 2.1). The size of crack tip plastic zone was of the order of the foil thickness at the transition point. A transition from plane-strain to plane-stress with decreasing foil thickness may offer an explanation for changes in crack growth and fracture behaviour. This correlates with fracture surface behaviour. Hadrboletz [2.6, 2.7] performed crack growth studies on wrought Cu, Al, Mo foils and electrodeposited Cu foil, with thicknesses ranging from 20 to 250 μm. Crack growth rates and thresholds were measured. The crack initiated from through-thickness slits in the centre of 20 μm wide foil samples at a frequency 20kHz and a R-ratio of -1. For the Cu foils, thinner wrought foils showed crack arrests associated with grain boundaries. This is similar to typical short crack growth behaviour. For foils less than 70 μm thick, ductile fracture occurred with knife edge rupture and there was a threshold stress intensity range dependence on thickness as described in figure 2.2. As previously noted [2.5], there occurred a transition from plane strain to plane stress with decreasing foil thickness with the crack tip plastic zone becoming similar in size to the foil thickness.

It has been observed that there is a decrease in crack growth threshold and ductility with decreasing foil thickness. On thicker foils dimpling could be observed. Bao & McEvilly [2.9] carried out studies on steel and aluminium of two thicknesses, 300 μm and 6360 μm. Plane strain crack growth was continuous and occurred on a cycle-by-cycle basis. The process of fatigue crack growth in plane stress was discontinuous in nature and slower. This was attributed to crack closure effects.

Takashimi [2.10] measured fatigue crack growth rates and fracture toughness in nickel-phosphorus thin films. Cantilever beam specimens measuring 10x12x50 μm^3 were prepared with Focussed Ion Beam milling. The fatigue specimens were prenotched to a depth of 3 μm. Crack growth rates calculated from striation spacing and a load ratio effect was identified. These effects were generally attributed to crack closure. Failure occurred within 1000 cycles indicating crack initiation dominated fatigue lives.

Judelewicz [2.8, 2.11] relying on natural crack initiation (rather than a precrack approach) used 100 μm Cu foil with grain sizes of 20-15 μm and testing under R=0, at 70 or 700 Hz. Cumulative plastic deformation was measured with an optical extensometer and showed cyclic hardening and saturation at low-stress amplitudes and continued cyclic hardening at high-stress amplitudes. Knife-edge rupture occurred and was due to cumulative damage and necking rather than crack growth. There was a significant size effect in 20 μm and 100 μm thick foils with a grain diameter of 100 μm, with the fatigue life of 20 μm foils being up to thirty times greater than the fatigue life of the 100 μm foil.

Hong and Weil (71) [2.11] compared the stress-controlled low cycle fatigue behaviour of a 25 μm thick electrodeposited (ED) Cu foil with a 33 μm thick Cu wrought foil. Stress-life data fitted the Basquin equation. There was no significant difference between wrought thin foil and bulk Cu but the electrodeposited foils had higher fatigue limit than the wrought foils. This corresponded to a higher yield stress and UTS for the electrodeposited foils. The difference was attributed to higher dislocation and twin densities and smaller grain size. However, the ED foils had a lower fracture strain and necked down to failure.

Merchant [2.13] performed strain controlled bending tests on wrought and electrodeposited 12-35 μm thick Cu foils and considered the effect of foil thickness and microstructure. Electrodeposited foils were manufactured to have equiaxed grains. It was found that the number of cycles to failure for a fixed strain range increased with decreasing foil thickness and fatigue life was further improved by annealing the foils. Wrought foils had pancake grains approximately 7-12 μm long and 1-2 μm wide resulting in an observed anisotropy in fatigue. For foils less than 10 μm thick, with one through-thickness grain or amorphous in structure, it was found that dislocations can slip out at the surface and interactions with surface oxide can affect mechanical properties. Schwaiger *et al.* [2.14] studied the effect of film thickness on fatigue behaviour. Thinner films had increased fatigue resistance. For all films below 1.5 μm thickness, there was a critical stress amplitude below which no fatigue damage occurred, regardless of mean stress. This was attributed to the fact that thinner films are below the thickness and grain size necessary for persistent slip band formation, so fatigue cannot occur. It was shown that the fatigue strength scaled with the yield strength.

The studies mentioned above all investigated foil / film samples rather than 3D structures with section aspect ratios closer to one (or of the same order). The LIGA (an acronym of **Li**thographie, **G**alvanoformung, **A**bformung or lithography, electroplating and molding) process provides a means of producing such 3D structures which are more representative of components, such as stent struts, than foils and films. This process allows for the fabrication of structures with an aspect ratio as high as 100:1. Allameh *et al.* [2.15] performed fatigue testing on 3D LIGA Ni specimens of 70 μm and 270 μm thickness of similar microstructure. The 70 μm thick specimens were found to have a longer fatigue life and a higher endurance limit (260 MPa) relative to the 270 μm thick structure (195 MPa). The increased endurance limit was due to the higher strength of the 70 μm samples and was determined to be 0.35 times the UTS which is typical for FCC metals.

In a similar study, Boyce *et al.* [2.16] tested LIGA nickel accelerometer components and observed an endurance limit of 0.37 times the UTS. It was also commented that size effects are not expected when many grains span component. Also, Saotome *et al.* [2.17] tested a Ni micro spring 0.95 mm high, 0.85 mm wide and 0.05 mm thick and also observed that the endurance limit was approximately 0.3 times the UTS. Improving static strength can be expected to improve fatigue performance.

2.4. Fatigue testing of wires

Small diameter wires are used in many biomedical applications; hence, wire fatigue is of interest to the field of biomedical engineering. Coquillet *et al.* [2.18] tested 18-10 stainless steel orthodontic wire of 2 mm diameter and considered effects of composition and processing. Wires experienced increased fatigue strength and endurance ratio with up to 20% cold work. A surface roughness effect was observed, with electropolishing contributing to an improvement in fatigue strength. Cracks were observed to initiate at surface defects, inclusions and persistent slip bands (PSBs).

Scheiner *et al.* [2.19] investigated size effects in Co-Cr wires used in heart pacemakers and intramuscular electrodes. It was observed that for multi-stranded wires, smaller individual strands gave an improved fatigue life for the cable.

Hildebrand [2.20] tested wires of cold drawn MP35N in rotating bending tests at R = -1 and observed that fatigue strength decreases for decreasing wire diameter which is contrary to conventional theory. While the UTS was not the same for wires of different diameter, this alone could not explain the difference. Bradley *et al.* [2.21, 2.22] offered an explanation. In work on MP35N, the cause of the size effect was attributed to the presence in the wire of 10 μm cubic TiN particles. The smaller the wire diameter, the greater the effect of a TiN particle. Better control of alloy chemistry and melt practice reduced Ti and nitrogen pickup and hence improved significantly the fatigue properties of the MP35N wire.

Nakai [2.23] fatigue tested 1 mm diameter pure iron and aluminium rods. The rods were electropolished to give minimum diameters of 200, 300 and 600 μm with a grain size of 25 μm for the Al and 20 μm for the Fe samples. In both materials, scatter in fatigue results was large relative to results from testing the bulk material. For Al, the scatter increased and fatigue life decreased as the rod diameter decreased. The effect was smaller for Fe.

2. 5. Yield Strength and Tensile Strength

In 2002, Haque *et al.* [2.24] reported a yield stress of 330 MPa for 200 nm aluminium films, much greater than the 10 MPa value for bulk high purity aluminium. In work on gold and aluminium films, Son *et al.* [2.25] observed an increase in yield stress with decreasing film thickness and discussed how yield stress is influenced by grain size and surface defects. The yield stress of the gold films followed the Hall-Petch relationship:

$$\sigma_{yield} = \sigma_i + kd^{\frac{1}{2}} \tag{2.2}$$

which relates the strength of a material to grain size, the smaller the grain size the higher the yield stress. σ_{yield} is the yield stress, σ_i the friction stress representing overall resistance to dislocation motion, k is a factor representing the hardening contribution of grain boundaries and d is the grain diameter. The trend for aluminium films was not represented by Hall-Petch but when the relationship was modified to take account of the additional resistance offered by a native oxide layer, a much better fit was obtained.

An increase in yield stress with decreasing film thickness was also reported by Schwaiger *et al.* [2.14] in work on 0.2 - 1.5 μm thick silver films deposited on SiO_2. All films had through thickness grains of a similar size (0.84 - 1.01 μm) and texture. The increase in yield strength was not attributed to grain size or film texture, but instead to film thickness effects.

Khatibi *et al.* [2.26] also reported an increase in yield strength with decreasing diameter for 10, 20, 50 and 125 μm diameter copper wire. Wires had single grains extending across the diameter and grain boundaries perpendicular to wire axis. A Hall-Petch relationship was followed. The UTS also decreased with decreasing wire diameter, with the exception of 10 μm wire which showed increased tensile strength and a higher work hardening rate with serrated flow. Microstructural analysis revealed non-uniform deformation in adjacent grains and single slip deformation, increasing with decreasing wire diameter. The serrated flow and increased yield strength of the 10 μm wire was due to dislocation pile-ups breaking through a surface oxide.

In a review of the properties of nanocrystalline materials, Baker *et al.* [2.27] concluded that classical scaling laws for strength and stiffness were not grossly violated in pure, fully dense materials with grains sizes down to 20 nm. Stiffness was reported to remain fairly constant and yield strength increased on a Hall-Petch plot. Below 20 nm, strength levelled off and stiffness decreased. With very small grains it seems reasonable to assume that properties will approach those of amorphous materials. Artz *et al.* [2.28] conclude that Hall-Petch must break down for very fine grained material as a clear limit is defined by the fact that at least one dislocation loop must fit inside the grain. For nanocrystalline copper, Hall-Petch breaks down at a grain size of around 50nm. For micron and nano-sized components, purity and density have a significant bearing on the material behaviour. At this small scale, defects such as inclusions, impurities and voids will alter the deformation and fracture mechanisms. In addition to Hall-Petch, oxide thickness and film texture and film thickness related size effects exist, resulting in an increase in yield strength above bulk values as size decreases [2.14, 2.24, 2.25, 2.26]. Studying size effects in thin wire and films requires careful characterization of microstructure. Grains may not be equiaxed so surface characterization of grains/ in-plane measurements, may not be sufficient. Grains may be through thickness, and residual stresses may affect results. Artz *et al.* [2.28] reviewed mechanisms of size effects. In general, there is a grain size and film thickness dependence of mechanical strength though it is not clear if Hall-Petch applies in all cases.

2.6. Ductility

Murphy *et al.* [2.29] investigated the existence of size effects in 316L stainless steel vascular stents. A typical stent strut is 100 μm thick, with an average grain size of approximately 25 µm for stainless steel stents. Struts were cut from medical-grade stainless steel tubing and electropolished. Strut widths ranged from 60 - 500 µm with 85 µm wall thickness. Tensile testing showed a significant reduction in plastic strain with decreasing strut width. The strain at necking of the 500 µm struts (~50%) was over twice that of the 60 µm struts. In another study, Rooein *et al.* [2.30] compared the tensile properties of 100 µm wall thickness 316L hypotubes with that of tubing ground down to 60 µm. A reduction in elongation from 33 to 24% was found. Also, Hadrboletz and Klein [2.7, 2.7] found a ductility-related size effect during tensile testing of copper, molybdenum and aluminium foils, with thinner foils having lower failure strains. Weiss *et al.* [2.31], in a comparison of the mechanical properties of two austenitic stainless steels (316L and AHNS) found a significant reduction in elongation for 100 µm diameter wires relative to bulk material. Khatibi *et al.* [2.26] in testing on copper wires of up to 125 µm diameter also found that the UTS decreased with decreasing wire diameter.

For 316L, the critical grain size to specimen width ratio below which a ductility related size effect arises was found to be 1/10 [2.31], for copper the ratio is about 1/4 [2.26, 2.29] and for aluminium alloys the ratio is 1/3 to 1/5 times the average grain diameter.

As the studies mentioned above indicate, there is a reduction in ductility with a reduction in size for crystalline metals. As the specimen size approaches the grain size, strain localization is increased and the overall ductility is decreased. The critical grain diameter to specimen width ratio ranges from 1/4 to 1/10. A true ductility size effect can be observed in samples with through thickness grains. Other factors such as aspect ratio [2.32], texture and the presence of defects can also reduce ductility [2.6, 2.7]. In foils one or two grains thick, the number of active slip systems is reduced, particularly if the foil is textured. This results in a reduction in ductility.

2.7. Size effects in 316L stainless steel

Care must be taken in inferring bulk material properties from tests on very small specimens. Size effects in steels have been thoroughly researched by various groups associated with the nuclear industry [2.32, 2.33]. Small samples of material are routinely removed from a reactor vessel in order to monitor the condition of the vessel. It is obvious that in applications such as this, size effects that are introduced by using small-scale test coupons must be identified (if they exist) and characterized. Kohno *et al.* [2.33] working on modified 316L austenitic stainless steel, found a thickness dependence, affecting yield point and yield strength. For ferrous alloys, the critical thickness is about 6-10 times the grain diameter. Thinner specimens have lower yield stress and UTS and failure strains decreased significantly below a critical aspect ratio of ~ 0.2.

Weiss *et al.* [2.31] carried out a comparison of the mechanical properties of two austenitic stainless steels (316L and AHNS). AHNS is a low nickel, high nitrogen content CrMnMoN steel, which is suited to medical device applications. In addition to the axial tensile tests on bulk material and wires of 100 μm diameter, mentioned above, the fatigue characteristics of coronary stents made of both materials were also evaluated within a commercial fatigue tester. Stents were cycled in a physiological solution for 50 million cycles at a frequency of 45Hz. For the wires, grain orientation mapping due to plastic deformation was measured with an electron back-scatter diffraction (EBSD) technique and demonstrated that deformation is concentrated in only a few, or just one, grain. Post-expansion of the stents of both materials showed regions of high deformation, with characteristic features such a slip lines on the surface. For the 10 μm grains in 316L stents, high dislocation densities near grain boundaries were apparent, with particularly high concentrations occurring at the intrados and extrados of the plastic hinge. After cyclic loading of the 316L material, it was found that a dislocation cell network occurs (evaluated by transmission electron microscopy), and progressive cycling caused dislocations to move in various directions along different slip systems. This rearrangement served to reduce dislocation concentrations. For the 316L, it was observed that because of the small sample size/grain size ratio, deformation behaviour comparable to single crystal behaviour occurred. The effect was less pronounced in the larger grain (100 μm) AHNS steel.

Wiersma *et al.* [2.34] also investigated size effects in microscopic 316L components with one to ten grains through the thickness. Tube and strut specimens with different notch geometries were fatigue tested at R=0.1 for two million cycles and the associated fatigue limits were determined. These results were compared with simple continuum mechanics predictions of the fatigue limits. Microscopic specimens were observed to have very flat S-N curves with low fatigue thresholds for notched specimens. The low thresholds (relative to macroscopic specimens) were attributed to a lack of crack closure due to the small thickness of the specimens. A size dependent, quasi-brittle, failure mechanism was also proposed. Grain boundaries are known to impede the growth of fatigue cracks and for microscale components, the fatigue limit is therefore often associated with the stress required to penetrate the grain boundary. As Figure 2.3 shows, for cracks growing through large grains, once the associated grain boundary has been penetrated, the remaining cross-section will be significantly reduced. This leads to rapid crack growth and failure in a lower number of cycles than a situation where the first grain is relatively small.

2.8. Size effects associated with strain gradients

The flow strength of a metal depends upon both strain and gradients of strain and hardening is due to a combination of and interaction between different types of dislocations including geometrically necessary dislocations (GNDs) [2.35]. GNDs describe a form of dislocation that arise when a metal is deformed in a non-uniform manner. In general, the smaller the length scale over which the plastic deformation occurs, the more pronounced the strain gradient and the density of GNDs. The size effect associated with a strain gradient is therefore one where the flow strength increases as the size is reduced. This effect is observed when the size is of the order of several microns or less. The GNDs do not contribute directly to plastic strain, but increase the work hardening of a material by impeding the motion of what are termed statistically stored dislocations. Figure 2.4 illustrates the concept of necessary dislocations being generated under an indenter during a hardness test. As the indenter moves into the metal, the deformed material is pushed into the substrate and is accommodated in the form or dislocations [2.36]. In summary, where non-uniform plastic deformation takes place, plasticity is accommodated by dislocations which move so as to relax a stress (statistically stored dislocations) and dislocations which position themselves so as to describe curvature (geometrically necessary dislocations).

2.9. Ratchetting

A behaviour known as “ratchetting” has been observed to occur in 316L stainless steel with the application of asymmetrical cyclic loads [2.37 - 2.41]. Ratchetting is defined as an acculumation of plastic strain in one direction during cyclic loading and it can occur in part or all of a structure [2.37]. Ratchetting results in a translation of the hysteresis during cyclic loading [2.38] and is a secondary plastic strain accumulation oa a cycle by cycle basis which is dependent upon the hardening or softening characteristics of an alloy and the load conditions (non-zero mean stress being and asymmetrical cyclic stressing) [2.39]. It is difficult to separate mechanistically the phenomena of fatigue and ratchetting; this can be done if ratchetting is defined as the accumulation or plastic strain while fatigue is the initiation, propagation and growth of a crack. Ratchetting contributes to the level of plastic strain in a component and consequently accelerates the development of fatigue cracks [2.37].

Ratchetting strain can be defined as:

$$\varepsilon_r = \frac{1}{2}(\varepsilon_{max} + \varepsilon_{min}) \qquad (2.3)$$

Where ε_{max} is the maximum axial strain in each cycle and ε_{min} is the minimum axial strain. The ratchetting strain rate is defined as the increment of ratchetting strain ε_r in each cycle and is denoted $\frac{d\varepsilon_r}{dN}$ [2.39]. Gaudin & Feaugas [2.38] observed that as the mean stress increases, the rate of ratchetting decreases and conversely, for a given maximum stress, as the mean stress decreases, the rate of ratchetting increases [2.40].

Factor influencing ratchetting behaviour include the shakedown limit of a material. Elastic shakedown occurs when cyclic loads induce plastic flow in ductile materials. If the residual stresses induced in the component during early cycling are ewual to or greater than the stresses induced by continued application of the load, then a closed cycle of entirely elastic deformation occurs. There is a limiting value of applied load below which there is no continual accumulation of plastic strain during cyclic straining. This is known as the “shakedown limit”. Ratchetting can be prevented by keeping the applied stress lower than the material’s shakedown limit [2.40].

2.10. Conclusions

On examination of the literature, as described above, several mechanical size effects have been identified:

- As film thickness is reduced, there is a transition from plane strain to plane stress; this may offer an explanation for changes in crack growth and fracture behaviour. Figure 2.1 shows plane stress and plane strain type fracture surfaces. Plane stress generally involves knife edge fracture (fig 2.3(a)), with the mechanism of crack propagation generally involving void nucleation and growth ahead of the crack tip. Knife edge rupture is observed in foils with through thickness grains [2.5, 2.7]. On the other hand, plane strain fracture surfaces are generally planar, or have a section which is flat, and crack growth occurs (figure 2.3(b)).
- Crack growth thresholds and ductility decrease with decreases in foil thickness.
- In foils consisting of one or two through thickness grains, the number of active slip systems is reduced, particularly if the foil is textured. Therefore there is a consequent reduction in ductility.
- For Cu, thinner wrought foils have shown crack arrests associated with grain boundaries [2.6, 2.7]. This is similar to typical short crack growth behaviour.
- A load ratio effect has been identified. These effects have been generally attributed to crack closure.

- Higher fatigue limits found in thin samples generally corresponds to higher yield stress and UTS [2.11]
- The number of cycles to failure for a fixed strain range has been found to increase with decreasing foil thickness and fatigue life has been further improved by annealing the foils. [2.13]
- For very thin films, (below 1.5μm thickness) it has been found that there is a critical stress amplitude below which no fatigue damage occurred, regardless of mean stress [2.14]. This was attributed to the fact that thinner films are below the thickness and grain size necessary for persistent slip band formation, so fatigue cannot occur.
- The endurance limit has been found to be approximately 0.3 times the UTS, which is typical for FCC metals [2.15, 2.16, 2.17]. Increasing the static strength can be expected to improve the fatigue performance.
- In addition to the Hall-Petch relationship, oxide thickness, specimen texture and specimen thickness related size effects exist, resulting in increases in yield strength above bulk values as the specimen size decreases [2.24, 2.25, 2.26, 2.27]
- Strain gradient effects in micron-scale component can also produce size effects. This size effect increases the work hardening of a metal [2.35, 2.36].

Figures

Fracture surface profiles

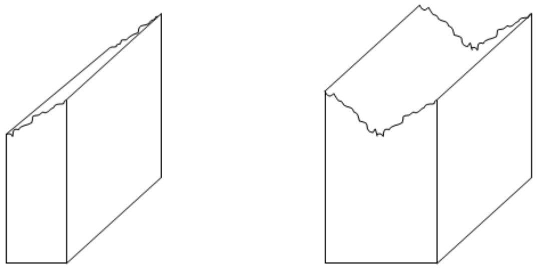

(a) Plane stress – knife edge rupture

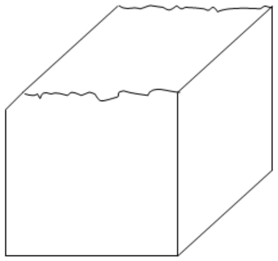

(b) Plane strain – shear lip with flat fracture surface

Figure 2.1. Plane stress and plane strain fracture surface profiles

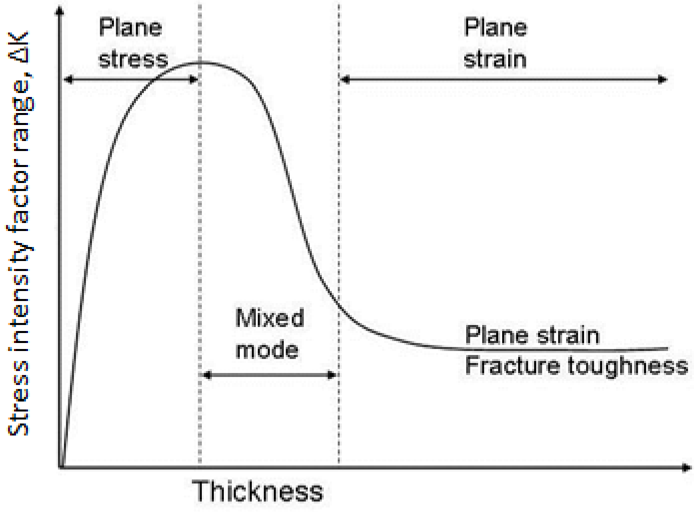

Figure 2.2. Plane stress and plane strain fracture toughness variation

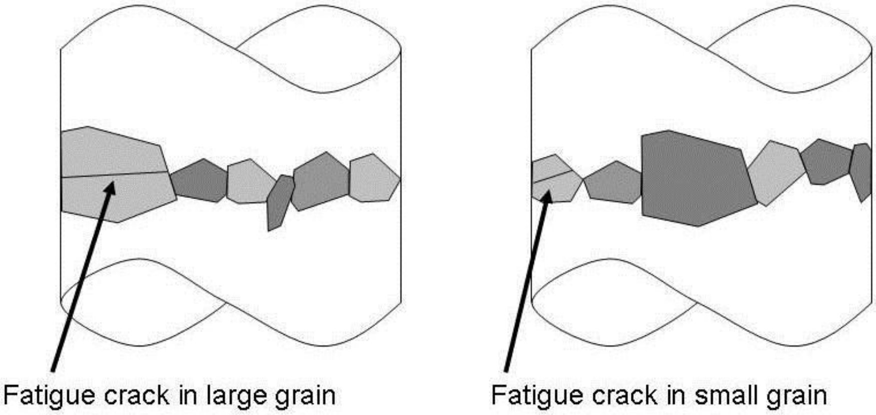

Figure 2.3. Fatigue crack propagating through large grain and small grain in microscopic components (from [2.34]).

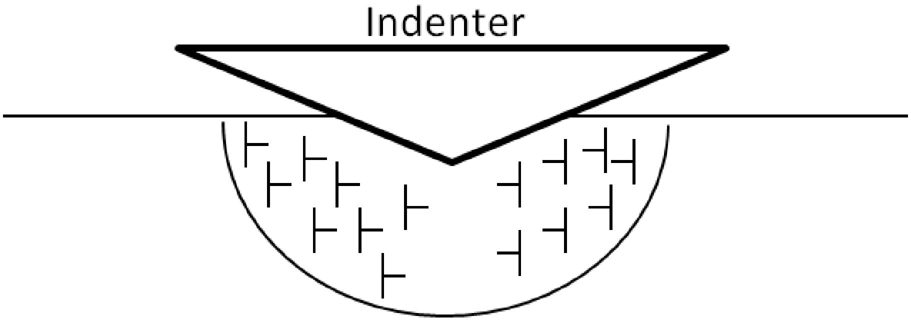

Figure 2.4. Geometrically necessary dislocations caused by the non-uniform deformation of a material during indentation.

References

[2.1] Schütz, W., (1996) A history of fatigue, *Engng Fract. Mech.*, Vol. 54, no. 2, 263-300

[2.2] Weibull, W., (1939) A Statistical Theory of the Strength of Materials, Ingeniörs Vetenskpas Akademiens Handlingar No. 151 Generalstabens Litografisky Anstalts Förlag, Stockholm

[2.3] Makkonen, M., (2000) Statistical size effect in the fatigue limit of steel, *Int. J. Fat.*, 23, 395-402

[2.4] Park, J.-H., Myung, M.S. and Kim, Y.-J., (2008), Sensors and Actuators A, 147, 561-569

[2.5] Alic, J.A. and Asimov, R.M., (1974) Growth of tensile and fatigue cracks in metal foils. *Engng Fract. Mech.* 6, 223-230

[2.6] Klein, M., Hadrboletz, A., Weiss, B. and Khatibi, G., (2001) The 'size effect' on the stress-strain, fatigue and fracture properties of thin metallic foils, *Mater. Sci. Engng* A319-A321, 924-928

[2.7] Hadrboletz, A., Weiss, B. and Khatibi, G. (2001) Fatigue and fracture properties of thin metallic foils. *Int. J. Fract.* 109, 69-89

[2.8] Judelewicz, M., (1993) Cyclic deformation of 100μm thin polycrystalline foils. *Scr. Metall. Mater.* 29, 1463-1466

[2.9] Bao, H. and McEvily, A.J., On plane-stress, plane-strain interactions in fatigue crack growth, *Int. J. Fatigue*, Vol. 20, No. 6, pp.441

[2.10] Takashimi, K. and Higo. Y. (2005) Fatigue and fracture of a Ni-P amorphous alloy thin film on the micrometer scale. *Fatigue Fract. Eng mater. Struct.* 28, 703-710

[2.11] Judelewicz, M., Künzi, H.U., Merk, N. and Ilschner, B. (1994) Microstructural development during fatigue of copper foils 20-100μm thick. *Mater. Sci. Engng* A186, 135-142

[2.12] Hong, S. and Weil, R. (1996) Low cycle fatigue of thin copper foils. *Thin solid Films.* 283, 175-181.

[2.13] Merchant, H.D., Minor, M.G. and Liu, Y.L., (1999). Mechanical fatigue of thin copper foil. *J. Electron. Mater.* 28, 998-1007.

[2.14] Schwaiger, R. and Kraft, O., (2003) Size effect in the fatigue behaviour of thin Ag films. *Acta Mater.* 51, 195-206.

[2.15] Allameh, S.M., Lou, J., Kavishe, F., Buchheit and T., Soboyejo, W.O. (2004) An investigation of fatigue in LIGA Ni MEMS thin films. *Mater Sci. Engng* A371, 256-266

[2.16] Boyce, B.L., Michael, J.R. and Kotula, P.G.., (2004) fatigue of metallic microdevices and the role of fatigue-induced surface oxides. *Acta Mater.* 52, 1609-1619

[2.17] Saotome, Y., Yokote, S., Okamoto, T. and Kinuta, S. (2003) Design and in-situ mechanical testing system for probe card (UV-LIGA-Ni microspring. *In: Proceedings of IEEE 16th International conference on Micromechanical systems*, pp. 670-673.

[2.18] Coquillet, B., Vincent, L. and Guiraldenq, P. (1979) Influence of cold working on fatigue behaviour of stainless steels used for prosthesis: application to study of wires with small sections. *J. Biomed. Mater. Res.* 13, 657-668

[2.19] Scheiner, A., Mortimer, J.T. and Kircher, T.P., (1991) A study of fatigue properties of small diameter wires used in intramuscular electrodes. *J. Biomed. Mater. Res.* 25, 589-608

[2.20] Hildebrand, L.B., Schmidt, J. A., Prentice, J.K. and Stotts, L.J. (1999) Quantitative, low cycle, crack initiation testing of fine wires and CENELEC standard pacing coil. *J. Biomed. Mater.* Res. 48, 251-257

[2.21] Bradley, D., Kay, L., Lippard, H. and Stephenson, T. (2003) Optimization of melt chemistry and properties of 35cobalt-35nickel-20chromium-10molybdenum alloy medical grade wire. *In: Proceedings of Conference on Materials and Processes for Medical Devices*, Anaheim, CA., USA, ASM international, pp. 301-307

[2.22] Bradley, D. and Kay, L. (2004) Optimizing fatigue resistance of medical wire. *Medical Device Technol. Sept.*, 10-11

[2.23] Nakai, Y., Hashimoto, A. and Taketani, A. (2005) Development of fatigue test method and size effect of fatigue strength in metallic thin wires. *J. Soc. Mater. Sci. Japan.* 54, 284-289.

[2.24] Haque, M.A. and Saif, M.T.A., (2002) In-situ tensile testing of nano-scale specimens in SEM and TEM. *Exper. Mechan.* 42, 123-128.

[2.25] Son, D., Jeong, J.H., and Kwon, D., (2003) Film-thickness considerations in microcantilever-beam test in measuring mechanical properties of metal thin film. *Thin Solid Films* 437, 182-187

[2.26] Khatibi, G., Betzwar-Kotwas, A., Groger, V. and Weiss, B. (2005) A study of the mechanical and fatigue properties of metallic microwires. *Fatigue Fract. Eng Mater. Stuct.* 28, 723-733

[2.27] Baker, S.P., (2001) Plastic deformation and strength of materials in small dimensions. *Mater. Sci. Engng* A319-A321, 16-23.

[2.28] Artz, E., (1998) Size effects in materials due to microstructural and dimensional constraints: a comparative review. *Acta Mater.* 46, 5611-5626

[2.29] Murphy, B.P., Savage, P., McHugh, P.E., Quinn, D.F. (2003) The stress-strain behaviour of coronary stents struts is size dependent. *Annals Biomed. Engng* 31, 686-691

[2.30] Rooein, M., Fariabi, S., Selvaduray, G. and Callol, J. (2003) Investigation of the structure-property-processing relationships of 316L stainless steel tubing. *In: Proceedings of Conference on Materials and Processes for Medical Devices*, Anaheim, California, USA. ASM International. pp. 48-53.

[2.31] Weiss, S., Meissner, A. and Fischer, A. (2009) Microstructural changes within similar coronary stents produced from two different austenitic steels. *Journal of the Mechanical Behaviour of Biomedical Materials*, 2, 210-216

[2.32] Kohno, Y., Kohyama, A., Hamilton, M.L., Hirose, T., Katoh, Y. and Garner, F.,A. (2000) Specimen size effects on the tensile properties of JPCA and JFMS. *J. of Nucl. Mater.* 283-287, 1014-1017

[2.33] Hirose, T., Sakasegawa, H., Kohyama, A., Katoh, Y., Tanigawa, H. (2000) Effect of specimen size on fatigue properties of reduced activation ferritic/martensitic steels. *J.of Nuc. Mater.*283-287, 1018-1022

[2.34] Wiersma, S., Taylor, D. (2005) Fatigue of materials used in microscopic components. *Fatigue Fract. Engng Mater. Struct.* 28, 1153-1160

[2.35] Fleck, N.A., Hutchinson, J.W., (1997) Strain Gradient Plasticity. *Advances in Applied mechanics*, Volume 33

[2.36] Gao, H., Huang, Y.. (2003) Geometrically necessary dislocation and size-dependent plasticity. *Scripta Materilia*, Vol. 48, Issue 2, 113-118

[2.37] Weiß, E., Postberg, B., Nicak, T., Rudolph, J., (2004) Simulation of ratchetting and low cycle fatigue. *Int. J. Pres. Ves Pip.* Volume 81, issue 3, 235-242

[2.38] Gaudin, C., Feaugas, X., (2003) Cyclic creep process in AISI 316L stainless steel in terms of dislocation patterns and internal stresses. *Acta Materilia*, Volume 52, Issue 10, 3097-3110

[2.39] Kang, G.Z., Li, Y.G., Zhang, J., Sun, Y.F., Gao, Q., (2004) Uniaxial ratchetting and failure behaviour of two steels. *Theor. Appl. Fract. Mech.* Volume 43, Issue 2, 199-209

[2.40] Feaugas, X., Gaudin, C., (2003) Ratchetting process in the stainless steel AISI 316L at 300K: an experimental investigation. *Int. J. Plas.*, Volume 20, issues 4-2, 643-662

[2.41] Suresh, S., (2004) Fatigue of Materials, *Cambridge University Press*, 2nd Ed.

MACROMECHANICAL STENT MODELLING

3.1. Introduction

Balloon expandable vascular stents are deployed within stenosed arterial lesions and are then subjected to hundreds of millions of cycles of pulsatile loading due to the beating of the heart. Deployment involves inflating the balloon and plastically deforming the stent until the required diameter is obtained. This plastic deformation induces static stresses in the stent, which will remain for the lifetime of the device and the pulsatile loading induces additional cyclic stresses within the device. In order to determine these stresses, finite element models of the unit cells of geometrically different, commercially available balloon expandable stents have been created, and deployment and elastic recoil have been simulated. In this chapter the residual stresses associated with deployment and recoil are compared for the various stent geometries, and the maximum, minimum, and mean stresses induced in the stent due to systolic/diastolic pressure are evaluated with a view to establishing appropriate initial stress states for fatigue loading for the test specimens.

3.2. Finite element modelling

There are various approaches to developing finite element models of vascular stents. For example Etave *et al*. [3.1] modelled the deployment of a 3D unit cell subjected to internal radial pressure and Migliavacca *et al*. [3.2] modelled the deployment of an entire 3D stent subjected to internal radial pressure. Several authors have attempted to quantify the stresses induced in the atherosclerotic lesion as a result of the stenting process. By developing constitutive equations that describe the behaviour of the plaque tissue system, Liang *et al.* [3.3] and Lally *et al.* [3.4] were able to evaluate the stresses at the stent–artery interface. An actual stent is typically comprised of, but not limited to, four to six unit cells in the circumferential direction, and from six to eighteen in the axial direction, depending on stent length. The geometric configuration of a particular stent and the associated surface area has been shown to influence the rates of intimal hyperplasia in coronary arteries [3.5]. Figure 3.1 shows such a stent. The 2D unit cell approach, in which the smallest repeating structure of the stent is identified and discretized, is adopted in the work presented here as shown in figure 3.2. As the unit cell generally describes only one-sixth of the circumference of a stent, and as the radial thickness of the stent is small relative to the outer diameter, a 2D model may approximately describe it. This 2D unit cell approach has been previously used successfully in McGarry *et al*, [3.6]. Because of the simplicity and the significant computational efficiency associated with the 2D unit cell approach (less than one hundredth of the time for a full 3D analysis), it is adopted here as a platform for efficient comparison of different stent designs. It is acknowledged that the 2D unit cell approach is an approximation of the full 3D situation. However, the unit cell method, incorporating periodic boundary conditions and achieving stresses within the structure by applying a predetermined strain, has been shown to produce results similar to 3D models [3.7].

3.2.1 Validation of 2D modelling approach

In order to further validate this statement, the expansion and recoil of a complete 3D finite element model of the Abbott Opencell® stent (also known as the BioDivYsio Opencell® stent) was simulated. The stent was expanded to a maximum deployment diameter of 3.6mm, matching the intended deployment diameter of the unit cell. This allowed direct comparison of the results obtained with 3D and 2D models of the same stent type. For the purposes of this comparison, expansion of the 3D stent model was achieved in a straightforward manner by applying a radial displacement to the inner surface of the stent, resulting in uniform deployment to the required diameter as shown in figure 3.3. For the 2D model, eight-noded, full integration, quadrilateral elements were used and for the 3D model 8-noded hexahedral elements were used. The stainless steel material behaviour was described with an elastic-plastic material curve and hardening through the use of an isotropic hardening model. The yield point of the material occurs at 200GPa. The results in Table 3.1 show that on the whole, the order of magnitude of the results is in general agreement. However, the unit cell method gives a greater and consequently a more conservative estimation of device performance than a complete 3D model, in particular in relation to the important design considerations of radial recoil and maximum post-recoil stress. On this basis it can be concluded that the 2D approach is acceptable for simple and efficient comparison of different stent designs. Focusing on some specifics of the 2D to 3D comparison, there is a difference between the maximum post-recoil stress in the 2D unit cell and the maximum post-recoil stress in the 3D model (475MPa in 2D vs. 375MPa in 3D). There is also a difference in radial recoil between both model types. Both factors are related, and the reason for the difference can be attributed in a significant part to the method used to deploy the 3D stent model. A radial displacement boundary condition is applied to the inner surface of the entire stent, thus forcing the stent geometry to assume the shape of an almost perfect cylinder upon deployment. In reality, with balloon inflation, the constituent parts that make up the stent would deform in a manner determined by the geometry of the device, with most of the deformation constrained to the plastic hinges, and the stent would assume a more angular appearance (when viewed along its axis). The additional components of strain introduced by the deployment method used here are responsible for lower maximum post-recoil stresses and the more diffuse stress pattern in the 3D model as shown in figure 3.4(a). Figure 3.4(b) shows that, in contrast, a more localised pattern of stress distribution exists within the unit cell of the 2D model, where strain is confined to the plastic hinges to a greater degree. These observations further support the appropriateness of the 2D unit cell approach.

3.2.2 2D stent unit cell models

The five 2D finite element stent models presented in this chapter were generated using MSC Patran® 2000 as a preprocessor and ABAQUS® 6.4 as processor and post-processor. Certain geometries were extracted from the Handbook of Coronary Stents [3.8]. The models are 2D unit cell representations of the 316L stainless steel stents, modelled with generalized plane-strain elements and assuming rate-independent elastic-plastic material behaviour with a von Mises yield criterion. The strut thicknesses for the various stent types are included in the models as an out-of-plane thickness. However in the 2D plane model framework, where there is no out-of-plane bending, this thickness has no effect on the stress and strain distributions, or consequently, the predicted recoil and foreshortening, etc. that result from the simulations. For comparison purposes, plane stress elements were also used, and results were not significantly different from those obtained with generalized plane strain elements.

In order to validate the mesh density used in the analyses, a mesh dependency study was carried out using the Abbott Opencell stent geometry. An identical analysis to that which produced the results included here was performed with a four-fold increase in mesh density. Figure 3.5 shows both mesh densities. No notable difference in the results was observed. All stents were expanded from their initial state to a diameter of 3.6mm (the required diameter of 3.0mm multiplied by a correction factor of 1.2 [3.9] to compensate for radial recoil and compressive arterial forces) and then allowed to recoil elastically. The stent models were of the:

- BioDivYsio/Abbott Opencell®,
- Medtronic AVE S7®,
- Guidant Multilink Pixel®,
- Medtronic GFX2®, and the
- Coroflex Delta® coronary stents.

Both eight-noded quadrilateral and six-noded triangular elements were used in the meshes. Unit cell finite element meshes for these models are shown in figure 3.6. For the stents, the representative deployment process was modelled by applying periodic boundary conditions to the unit cell and by using four load steps to achieve expansion, recoil and pulsatile distortions (maximum pressure and minimum pressure).

With reference to figure 3.7, in the first step, the unit cell (using the Abbott Opencell ® stent for example) was subjected to a positive displacement in the vertical direction. In the second step, this displacement was removed, allowing the unit cell to recoil elastically. In the third and fourth steps two further displacements were imposed upon the unit cell. Step three mimics the change in diameter of the stent due to systole, and step four mimics the change in diameter of the stent upon diastole. The cross sectional area of the lumen of the coronary artery changes by approximately 5% between systole and diastole [3.3, 3.10]. It was assumed for the purpose of this analysis that the changes in lumen diameter due to systole/diastole are transferred directly to the stent, with the post-recoil stent diameter as the mean diameter value. These steps permit calculation of Radial recoil, Longitudinal recoil and

Foreshortening [3.2] and generate the distribution of von Mises stress in the expanded stent. The maximum stresses induced by the pulsatile displacements were evaluated.

Periodic boundary conditions on the unit cell ensure translational symmetry and that the deformation of one unit cell accurately represents the deformation of many interconnected cells in the plane. Figure 3.7 illustrates how these boundary conditions are applied, taking the Abbott Opencell® stent as an example. As well as preventing rigid body motion and rotation, it is necessary to use the *EQUATION function in ABAQUS® to enforce periodic behaviour on the unit cell by defining linear, multi-point constraint equations. An example of such an equation, relating the displacement of individual nodes in node sets 3 and 2 (as defined in Figure 3.7), is of the form:

$$U_1^{\mathrm{A}} - U_1^{\mathrm{B}} = U_1^{\mathrm{C}} - U_1^{\mathrm{D}} \qquad (3.1)$$

where U_1^{A} is displacement of node A in the 1-direction (horizontal direction) and similarly for nodes B, C and D. This equation is used to maintain parallelism of edges that would be joined in a larger structure of repeated unit cells; it keeps distance *d*, shown in figure 3.7, the same for all corresponding nodes and thus maintains parallel edges. All the unit cell geometries use constraints of this form. In addition, in some cases the following constraint is used:

$$U_1^{\mathrm{A}} - U_1^{\mathrm{B}} = 0 \qquad (3.2)$$

which ensures that the distance *d* remains the same for each individual set of corresponding nodes, forcing edges to maintain the same profile, but they may not necessarily be parallel.

3.3. Stent mechanical performance

The five stent geometries investigated are compared under the following criteria:

- Radial recoil which is defined as the difference between the loaded and unloaded stent radius divided by the loaded stent radius.
- Longitudinal recoil, which is defined as the difference between the loaded and unloaded stent length divided by the loaded stent length.
- Foreshortening, which is defined as the difference between the original undeformed stent length and the loaded stent length divided by the original length.
- Distribution of von Mises stress in the expanded stent.
- Maximum stress and minimum stress due to changes in arterial diameter.

Clinical studies [3.11, 3.12] have shown that more complete stent expansion is associated with both larger initial and late luminal diameters. It is therefore necessary to know to what degree the stent will recoil on deflation of the balloon. This elastic radial recoil can be compensated for by over-expanding the stent, typically by a factor of between 1.1 and 1.2 times the required diameter [3.9]. The degree of foreshortening at different diameters must be known, as the stent must comfortably cover the arterial lesion when deployed. The stress distribution within the stent is also of interest, as regions of high stress will have a bearing on the fatigue life of the device.

3.4. Results

The finite element models determined the change in stress state of the various stent designs upon recoil. An example is provided in figures 3.8(a) – (d) where it is possible to see this change of stress state. It is clear from the finite element model of the Abbott Opencell® stent shown in Figure 3.8 that plastic deformation is located primarily in the plastic hinges. These hinges are an integral part of the stent design, localising plastic deformation and facilitating the opening of the unit cells. The interconnecting struts undergo little, if any deformation. The "S" shaped members in this particular design are included in order to enhance the flexibility of the stent as it is being guided through an artery and hence are not subjected to any appreciable stresses in a simple tension model such as this. All stent models investigated in this work exhibit similar behaviour. Plastic deformation is restricted to the plastic hinges, while the interconnecting struts are subjected to little, if any plastic deformation during deployment. The post-deployment characteristics of the various stents are detailed in Table 3.2. Table 3.3 lists the maximum stresses in the various stents. These values were used to establishing appropriate initial stress states for fatigue loading of the 316L test specimens.

3.5. Discussion

The data presented in Table 3.2 shows that for most of the characteristics examined, there is no significant difference between the stent models. Manufacturer's data [3.8] has been included where available. Radial recoil at a deployment diameter of 3.6mm is in the order of 2.5%. This resulted in post-recoil diameters of between 3.4mm and 3.5mm, indicating that a compensation factor of 1.2 is excessive. However, the *in-vivo* situation is more complicated than the situation modelled here, and direct comparisons are not possible. The 2D modelling method represents a simplistic approximation of both the in-vivo scenario and the mechanical behaviour of the stent. The effect of atherosclerotic plaque and pulsatile loading is described by a displacement. The stent geometry is greatly simplified. The material model will also introduce a level of inaccuracy, particularly in relation to accurate prediction of recoil.

The Guidant Multilink stent has a slightly higher recoil value at 4%. This stent has the largest unexpanded diameter of the five stents modelled, and this higher level of recoil may be due to the fact that a greater proportion of the initial deployment is made up of elastic deformation. Consequently, the level of radial recoil is higher. It is interesting to note that the longitudinal recoil associated with the models examined here, both 2D and 3D, is in the order of 0.1%, a very low value, and not one which will cause a physician any concern.

The stent foreshortening values vary quite considerably, related to the geometric configuration of the unit cell. If the unit cell features “straight” elements or elements that are designed to accommodate bending or twisting of the device during insertion (such as the Abbott Opencell), then the foreshortening values are lower when compared with stent designs that do not include these elements (GFX2 stent).

The maximum post-deployment stress values are in the order of 500MPa, though it should be noted that both Medtronic stent types have higher values at over 600 MPa. It would appear from the stent designs examined here that higher stresses are generated in conjoined plastic hinges, such as those used in the Medtronic devices, than in stand alone plastic hinges. This is due to the fact that the plastic deformation of two hinges is localised in an area that would normally be reserved for the plastic deformation of one hinge. Increasing the number of unit cells per circumference may circumvent this as, as this will serve to reduce the average amount of plastic deformation experienced per plastic hinge, and consequently will reduce the localised maximum stress experienced by the device.

The finite element method serves a useful purpose in identifying these areas of high stress, as it is in these regions that fatigue damage is most likely to initiate. In these analyses, systolic and diastolic diametric changes cycle evenly about the post-recoil stent diameter. It is interesting to note that based on the direct transfer of luminal cross sectional area changes to the stent, the stress induced in the device upon systole is less than the maximum stress experienced by the stent upon deployment and is within the elastic limits of the device. Therefore, the stent will be cycling within its elastic range under systolic pressure. However, this is not the case with the stresses induced by diastole. Some reverse plasticity occurs in the inner radius of the plastic hinges. Should such a scenario occur in reality, it is a possibility that the stent would at some stage fail due to the propagation of a fatigue crack which initiated at a defect or persistent slip band within one of these plastic hinges. It must be borne in mind that the artery itself may not be capable of inducing the stresses within the stent which would cause this localized reverse plasticity. If plasticity is not induced in the material of the stent, it or its corollary must occur in the artery, and this may be reflected indirectly by the high levels of restenosis [3.13], which occur with bare metal stents. The chosen method, 2D unit cell with linear displacements, does not permit modelling of stent–artery interaction; the physiological arterial displacements due to pulsatile flow are applied directly to the stent unit cell. In reality, it is unlikely that a diseased artery will undergo the normal pulsatile diametric changes or that the displacements the artery does undergo will be transferred entirely to the stent. Therefore, in the cases presented here, the simulated effect of arterial behaviour is exaggerated. However, the model does present a conservative analysis of artery induced strains in a stent, and as such, may provide a worst case scenario for estimating mean stresses for the fatigue testing of such devices.

The 2D modelling method discussed here is a simple and effective tool for evaluating the design of these devices. Models may be created in a matter of hours and the analyses take only minutes to simulate. Several design variations may be evaluated quickly and cost effectively in terms of computational time. However, there are limitations to the use of this particular modelling technique when compared to a full three-dimensional model such as that by Migliavacca *et al*. [3.14], and the analyses carried out here do not permit identification of a generally superior stent design. As the expansion of the unit cell is achieved by displacing sections of the model and not by applying a radial pressure, it is not possible to describe the relationship between pressure and expansion ratio, or even expansion rates using rate dependent material data. Also, the discrete nature of the unit cell will not describe "dog boning," where the ends of the stent open before the main body of the stent (due to less constraint) giving the device an initial dog bone shape. Any conclusive statement on the efficacy of a particular stent design would have to include a biological assessment of the device performance, i.e. its propensity to promote or arrest restenosis. Such detail is beyond the scope of this work.

3.6. The stress range of interest

The residual stresses associated with deployment and recoil were compared for the various stent geometries, with a view to establishing appropriate initial stress states for fatigue loading for the test specimens. Five different stent types were investigated and the results of interest are presented in Table 3.3. Based on these results and bearing in mind the size range of the test specimens, it was decided to investigate stresses in the range of 350 to 600MPa.

Note: This chapter was published in a more complete form as [3.15].

Table 3.1. Comparison of Radial recoil, Longitudinal recoil, Foreshortening, and Maximum post-recoil stress in 2D and 3D models at a deployment diameter of 3.6mm.

Abbott Opencell®	**Radial Recoil**	**Longitudinal Recoil**	**Foreshortening**	**Maximum post-recoil stress**
2D unit cell	2.6%	-0.1%	1.8% Manufacturers's Data 1% at 3mm radius	475 MPa
3D full	1.5%	-0.1%	2%	375 MPa

Table 3.2. Stent Mechanical Performance; manufacturer's data included where available.

Stent Type	**Radial Recoil**	**Longitudinal Recoil**	**Foreshortening**
Abbott opencell®	2.6% Manufacturer's Data – 1% at 4mm diameter	-0.1%	1.8% Manufacturer's Data – 1% at 3mm diameter
Guidant Multilink®	4% Manufacturer's Data – 1.4%	-0.1%	0.1%
Medtronic Ave S7®	3%	-0.1%	0.5%
Medtronic GFX2®	2.5%	-0.1%	4%
Coroflex®	2.3% Manufacturer's Data – 4-5%	-0.2%	5% Manufacturer's Data 1-3%

Table 3.3. Operating tensile stresses for cardiovascular stents.

Stent Type	**Maximum stress post recoil [MPa]**	**Maximum arterial induced stress [MPa]**
Abbott Opencell ®	475	700
Guidant Multilink ®	520	460
Medtronic S7 ®	610	640
Medtronic GFX2 ®	620	660
Coroflex ®	450	575

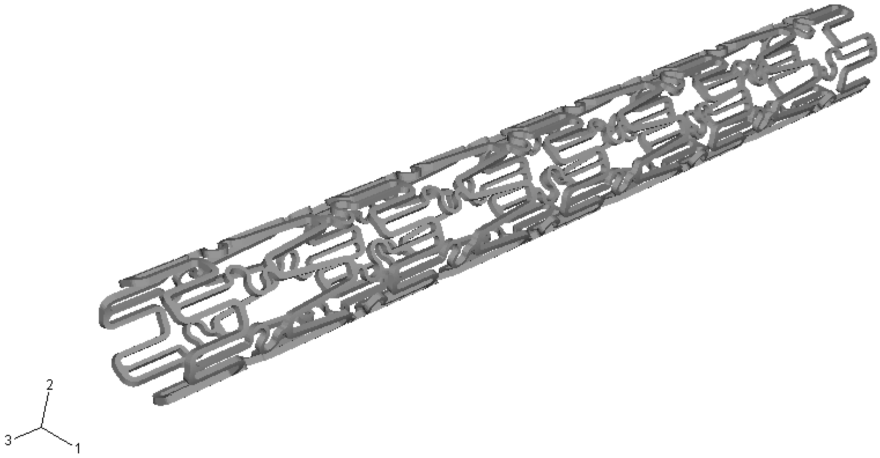

Figure 3.1. Balloon expandable stent in undeployed condition. This stent measures 1.5mm in outer diameter and 15mm in length. The radial thickness of the stent struts is 0.094mm.

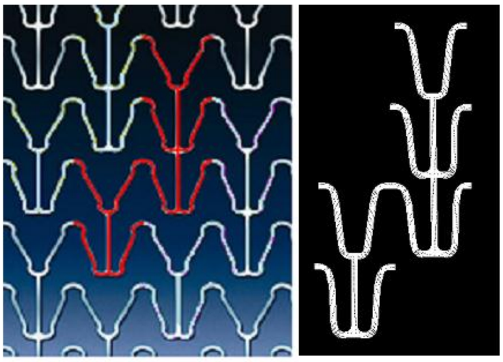

Figure 3.2. Smallest repeating structure of stent (highlighted on left hand side) and a 2D finite model of that structure (on right hand side).

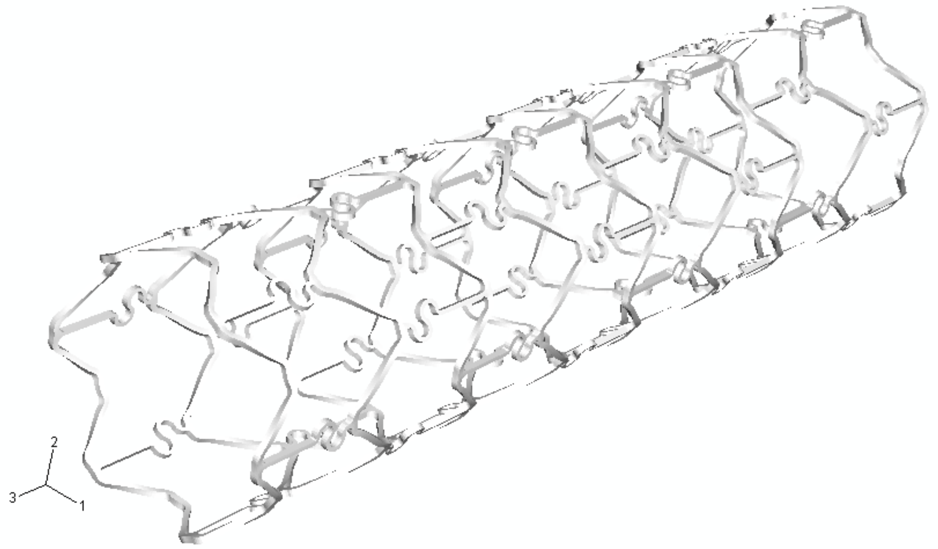

Figure 3.3. Balloon expandable stent in deployed condition. This has been expanded to a diameter of 3.6mm using displacement boundary conditions.

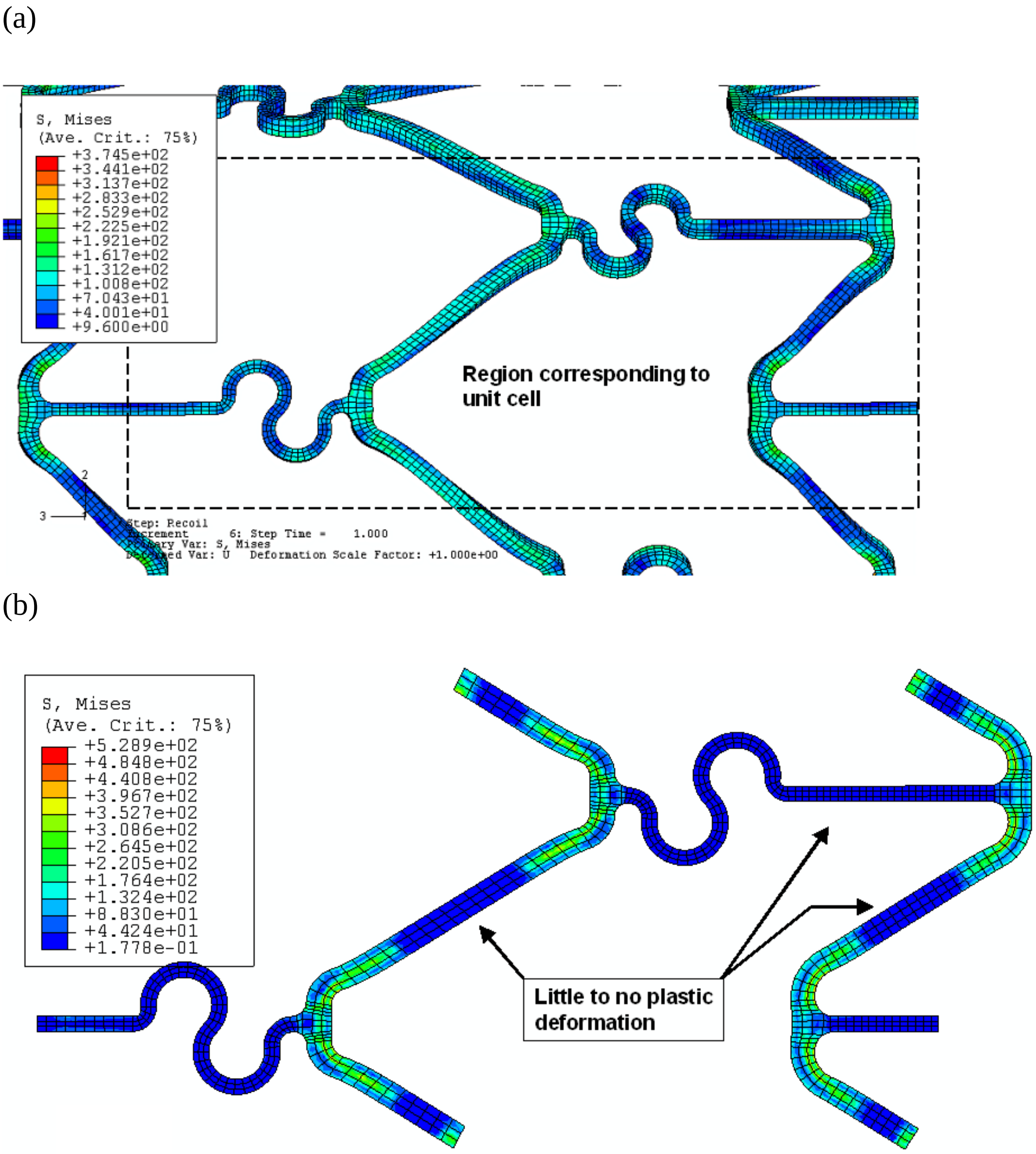

Figure 3.4. (a) Stress distribution within the 3D stent model. A “unit cell” region corresponding to the 2D model unit cell is highlighted. (b) Stress distribution within the unit cell of the 2D stent model. Note the areas of little or no plastic deformation. The units of stress are MPa.

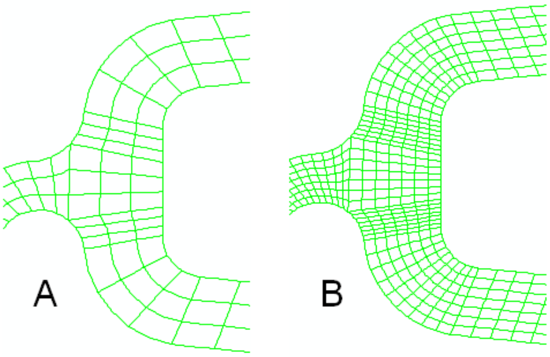

Figure 3.5. Mesh dependency study. Mesh B is four times more dense than mesh A.

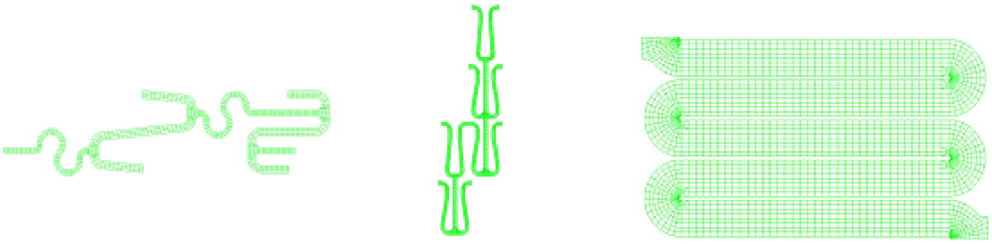

Abbott Opencell® Medtronic AVE S7® Guidant Multilink®

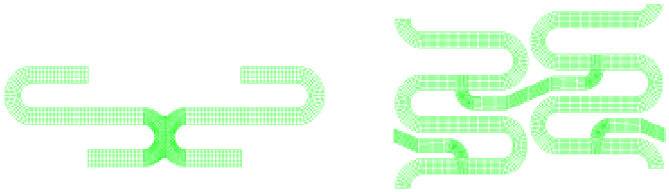

Medtronic GFX2® Coroflex®

Figure 3.6. Finite element models of the unit cells of five different stent types. Unit cells are not to scale.

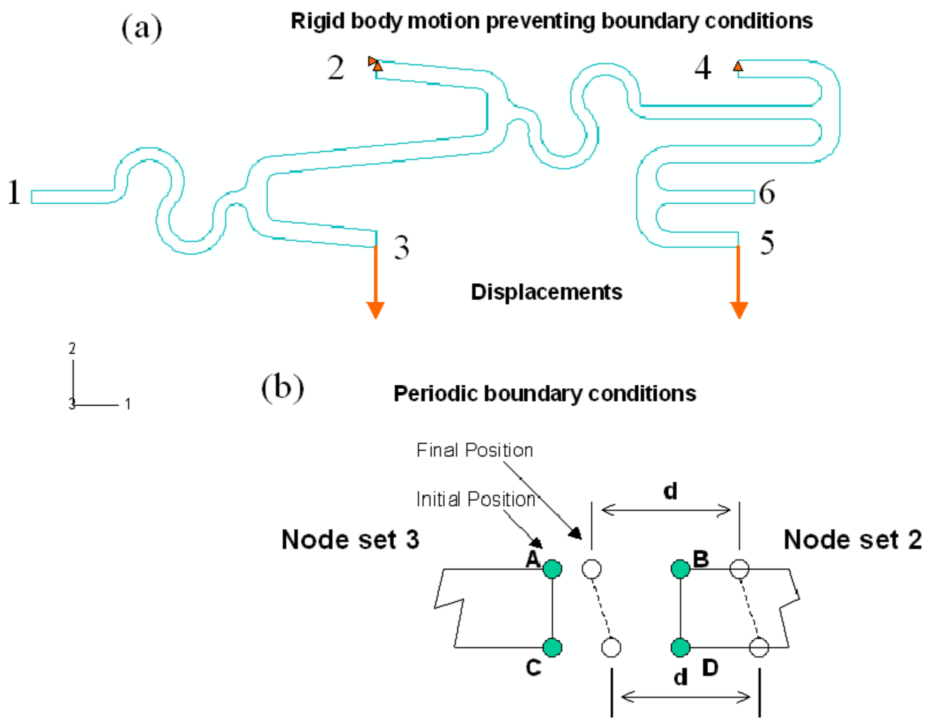

Figure 3.7. Application of periodic boundary conditions. Numbers indicate node sets to which periodicity constraints are applied, and in each case the node set contains all nodes on the associated edge. (a) Abbott Opencell® unit cell showing the boundary conditions applied to simulate stent expansion. Triangles indicate fixed boundary constraints and arrows indicate applied displacements. (b) Detail of the node set 2-node set 3 connectivity, highlighting nodes A, B, C and D to be constrained to ensure periodicity. This form of periodic constraint is also applied to node sets 1 and 6 and also to sets 4 and 5.

(a)

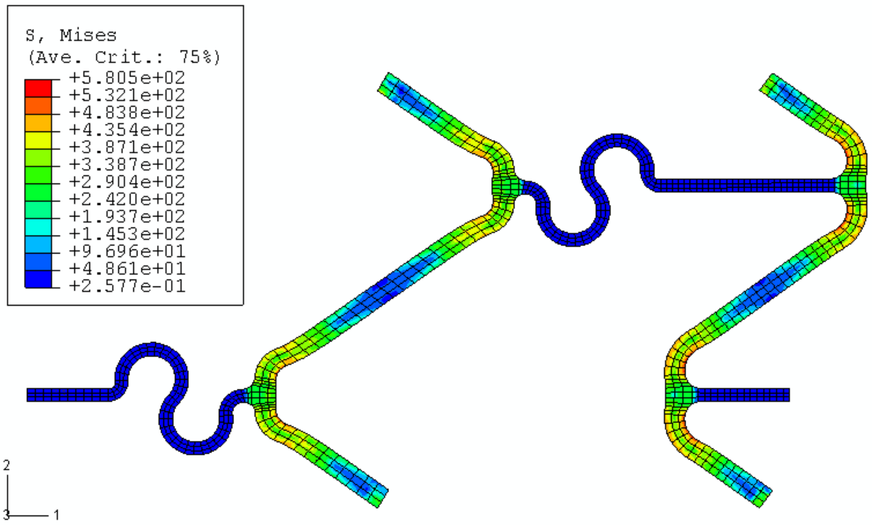
S, Mises
(Ave. Crit.: 75%)
+5.805e+02
+5.321e+02
+4.838e+02
+4.354e+02
+3.871e+02
+3.387e+02
+2.904e+02
+2.420e+02
+1.937e+02
+1.453e+02
+9.696e+01
+4.861e+01
+2.577e-01
2
3
1

(b)

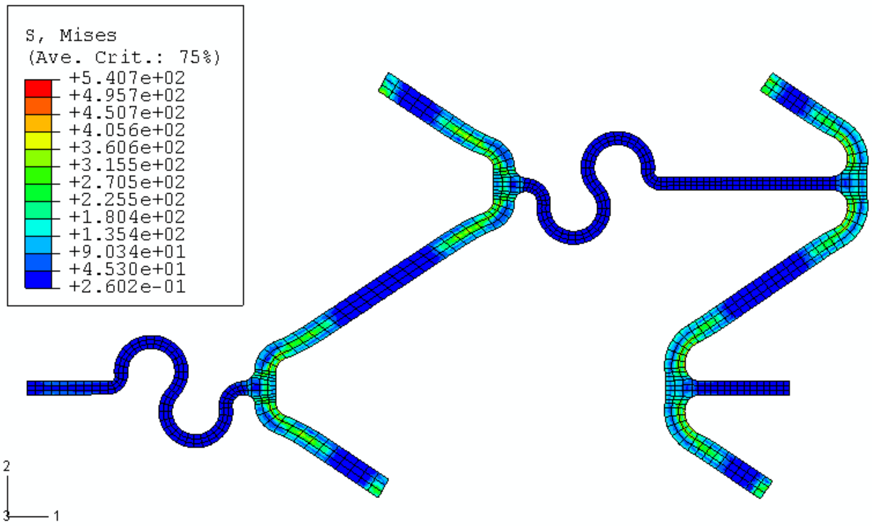
S, Mises
(Ave. Crit.: 75%)
+5.407e+02
+4.957e+02
+4.507e+02
+4.056e+02
+3.606e+02
+3.155e+02
+2.705e+02
+2.255e+02
+1.804e+02
+1.354e+02
+9.034e+01
+4.530e+01
+2.602e-01
2
3
1

(c)

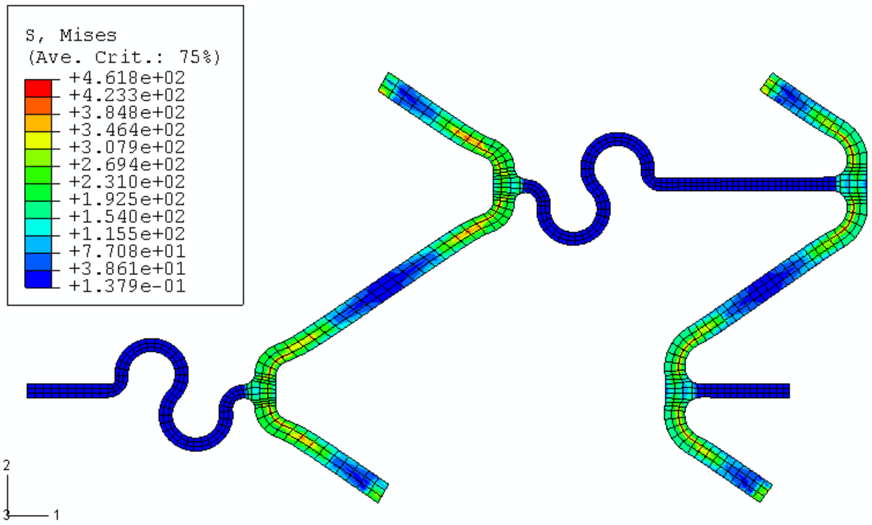

(d)

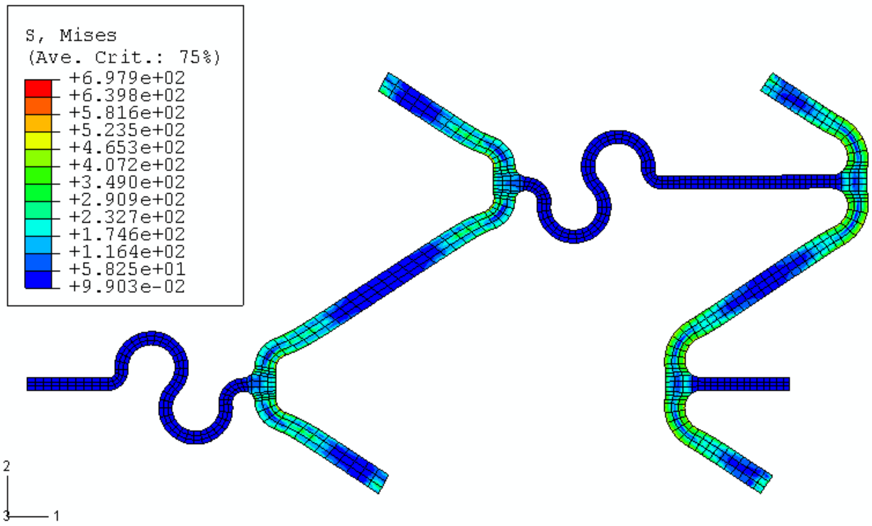

Figure 3.8. (a) Deployed Abbott Opencell ® stent, (b) stent following recoil,(c) stent following systole, and (d) stent following diastole. The units of stress are in MPa.

References

[3.1] Etave, F., Finet, G., Boivin, M., Boyer, J.C., Rioufol, G. and Thollet, G. (2001) Mechanical Properties of coronary stents determined by using finite element analysis, *J. Biomech*., Vol. 34, 1065-1075 [3.2]

[3.2] Migliavacca, F., Petrini, L., Colombe, M., Auricchio, F. and Pietrabissa, R. (2002) Mechanical behaviour of coronary stents investigated through the finite element method, *J. Biomech.*, Vol. 35, 803-811

[3.3] Liang, D.K.; Yang, D.Z.; Qi, M. and Wang, W.Q. (2005) Finite element analysis of the implantation of a balloon-expandable stent in a stenosed artery, *International Journal of Cardiology*, Vol 104, 314-318

[3.4] Lally, C., Dolan, F. and Prendergast, P.J. (2005) Cardiovascular stent design and vessel stresses: a finite element analysis, *Journal of Biomechanics*, Vol. 38, 1574-1581

[3.5] Hoffmann, R., Mintz, G.S., Haager, P., K., Bozoglu,, T., Grube, E., Gross, M., Beythien, C., Mudra, H., vom Dahl, J. and Hanrath, P., Relation of stent design and stent surface material to subsequent in-stent intimal hyperplasia in coronary arteries determined by intravascular ultrasound, *Am. J. Cardiol.*, Vol. 89, issue 12, 1360-1364

[3.6] McGarry, J.P., O'Donnell, B. P., McHugh, P.E., and McGarry, J.G. (2004) Analysis of the mechanical performance of a cardiovascular stent design based on micromechanical modelling, *Computational Materials Science*, Vol. 31, 421-438

[3.7] Dumoulin, C. and Cochelin, B. (2000) Mechanical behaviour of balloon-expandable stents, *J. Biomech.*, Vol. 33, 1461-1470

[3.8] Serruys, P.W. and Rensing, B.J., Handbook of Coronary Stents, 4th Edition, *Martin Dunitz Press*

[3.9] Costa, M.A., Sabate, M., Kay, I.P. and de Feyter, P. (2000) Three-Dimensional Intravascular Ultrasonic Volumetric Quantification of Stent Recoil and Neointimal Formation of Two New Generation Tubular Stents, *Am. J. Cardiol.*, Vol. 85, 135-139

[3.10] Guyton, A.C. and Hall, J.E. (2006) Textbook of Medical Physiology, Elsevier Saunders, 11th Ed., 103-115

[3.11] Fischman, D.l., Leon, M.B., Baim, D.S., Schatz, R.A., Savage, M.P., Penn, I., Detre, K., Veltri, L., Ricci, D., Nobuyoshi, M., Cleman, M., Heuser, R., Almond, D., Teirstein, P.S., Fish, R.D., Colombo, A., Brinker, J., Moses, J., Shaknovich, A., Hirschfeld, J., Bailey, S., Ellis, S., Rake, R. and Goldberg, S. (1994) A Randomised Comparison of Coronary-Stent Placement and Balloon Angioplasty in the Treatment of Coronary Artery Disease, *N. Engl. J. Med.*, Vol. 331, 496-501

[3.12] Serruys, P.W., de Jaegere, P., Kiemeneij, F., Macaya C., Rutsch, W., Heyndrickx, G., Emanuelsson, H., Marco, J., Legrand, V., Materne, P., Belardi, J., Sijwart, U., Colombo. A., Goy, J., van den Heuvel, P., Delcan, J. and Morel, M. (1994) A comparison of balloon-expandable-stent implantation with balloon angioplasty in patients with coronary artery disease, *N. Engl. J. Med.*, Vol. 331, 489-495

[3.13] Kastrati, A., Mehilli, J., Dirschinger, J., Pache, J., Ulm, H., Schülen, H., Seyfarth, M., Schmitt, C., Blasini, R., Neumann, F.J., and Schömig, A. (2001) Restenosis after Coronary Placement of Various Stent Types. *Am. J. Cardiol.*, Vol. 87, 34-39

[3.14] Migliavacca, F., Petrini, L., Montanari, V., Quagliana, I., Auricchio, F. and Dubini, G. (2005) A predictive study of the mechanical behaviour of coronary stents by computer modeling, *Medical Engineering & Physics* Vol. 27, 13-18

[3.15] Donnelly, E.W., Bruzzi, M.S., Connolley, T. and McHugh, P.E. (2007) Finite element comparisons of performance related characteristics of balloon expandable stents. *Computer methods in Biomechanics and Biomedical Engineering*, 10:2, 103 - 110

EXPERIMENTAL MATERIALS AND METHODS

4.1. Introduction

The objective of this thesis is to establish if a mechanical size effect exists in the fatigue behaviour of microscale 316L stainless steel struts. Fatigue testing is performed on four different sizes of stainless steel test specimens for this investigation. The specimens are laser cut from annealed 316L stainless steel tubing and electropolished to produce a smooth outer surface in a process similar to that used in the manufacture of vascular stents. The tube outer diameter is 1.5 mm with a wall thickness of 0.06 mm. The size variation is achieved by varying the width of the test specimens. Strut widths of 50 µm, 75 µm, 100 µm and 150 µm are investigated, with a constant gauge length. The test specimens are designed so as to protect the fragile gauge length during pre-test handling and mounting into the fatigue tester.

4.2. Processing methods and material

4.2.1. General

Tubing can be produced by several processes and can be classified as seamless or welded. Extrusion and cold-drawing processes produce seamless tubing. Welded tubing is formed from sheet metal that is rolled and welded by hot-forming, fusion or electric welding; the tubing is then re-drawn to improve dimensional accuracy and surface finish. Extrusion through a die produces seamless tubing with tolerances close to those obtained by cold-drawing. Tubes made by hot-forming processes such as extrusion or piercing and rolling are often finished by cold-drawing. Plug drawing is suitable for producing stent tubing as it results in greater dimensional accuracy and surface finish than tube sinking or moving mandrel drawing. In plug drawing, the tube is drawn over a fixed or a floating plug. A reduction in area of 30 % can be achieved with fixed plug cold-drawing and 45 % with a floating plug cold-drawing [4.1, 4.2]. Seamless tubing is the preferred form of tubing for stent and implantable device use as it produces tubing with good concentricity and consistent wall thickness. Also, welding processes can introduce defects into the tube wall with the associated risk of corrosion and embrittlement [4.2]

4.2.2. Annealing

While process annealing is commonly applied to heavily cold worked materials in order to remove internal stresses and increase ductility, it may not necessarily be applied to metals destined for use in medical devices. It can be advantageous to use cold worked tubing during stent manufacture as the hardness imparted by the cold-work process can protect the tube from handling damage. As well as increasing ductility and achieving a desirable microstructure, post laser-cutting annealing can also serve to remove laser induced residual stress.

4.2.3. 316L/LVM Stainless steel

316L is a nonferromagnetic, austenitic stainless steel. It is well suited for use in balloon expandable stents and medical devices in general. It is biocompatible, corrosion resistant and it offers good radial strength, good fatigue resistance and high stiffness. In recent times, it has been superseded somewhat by materials such as MP35N and Co-Cr alloys as the material of choice for balloon expandable devices. These materials are stronger and more dense than 316L so it is possible to reduce strut size and still retain sufficient radial strength and radiopacity. However, 316L can still be considered as the default stent material. Certain new-to-market devices, such as the balloon expandable Edward’s Sapien aortic heart valve replacement device continue to use 316L.

316LVM is a unique nomenclature used by Fort Wayne Metals Inc. referring to the vacuum melt processing (VM). This stainless steel is initially electric-arc melted. The purity and homogeneity are then refined by vacuum arc remelting (VAR). This process yields a more uniform chemistry with reduced void and contaminant content. The chemical composition of 316L/316LVM is shown in Table 4.1 and a more complete description of the material is included in Appendix I.

4.3. Test specimen design

The most common use of microscale 316L components is in the medical industry with the material being used in either tubular or wire form to produce a range of *in-vivo* medical devices such as stents, embolism filters, guide wires and pace maker wires. The production methods used for such devices are a mixture of laser cutting, welding and electropolishing for tube-based stents, wire based stents are braided and welded. Guide wires are cold worked and annealed to achieve the required balance of stiffness and strength. Depending on the condition of the as-received tubes and wires and upon the subsequent processing steps involved in making a particular device, an annealing step may be incorporated to relieve process induced internal stresses and to achieve a desired grain size.

4.3.1. 316LVM laser cut tube specimens

Fatigue test specimens were produced from 316LVM medical grade seamless stainless steel hypotube supplied by Sandvik Precitube and produced from Fort Wayne Metals 316LVM stainless steel. Figure 1.3 shows the specimens which were laser cut and electropolished by Creganna Medical Devices (www.creganna.com). As the specimens are all produced from the same tubing, any texture-related effect may be assumed to affect all specimens equally. The texture itself was not investigated. Specimen design was influenced by the tensile testing samples used by Murphy *et al*. [4.3]. Figure 4.1 shows the support struts which are set back from the test region so that they may be cut and removed without damaging the gauge length once the specimen has been aligned and gripped. A range of four different specimen sizes were produced and tested. The specimen strut dimensions are given in Table 4.2. Two variations of the tube-based specimens were produced. As shown in Figure 4.1, a gauge length of 4 mm was initially tested, these samples being referred to by the code CREG_#_50/75/100/150, where the numerals refer to the specimen width. Difficulties were encountered in producing straight and parallel edge gauge lengths as the 4mm gauge length is very long relative to its thickness (150 µm at its maximum). A further modification was incorporated, whereby the gauge length was reduced to 2 mm. These samples were referred to by the code CREGII_#_50/75/100/150. This modification improved manufacturability, reduced the reject count, and made the removal of the support struts without damaging the gauge length an easier task. The tube samples were expensive, with each sample costing approximately €100. Materal data sheets for 316LVM are attached in Appendix A.

4.4. Fatigue test system

An Enduratec ELectroForce® (ELF®) 3200 System was selected for fatigue testing. As shown in Figure 4.2, the system is comprised of a tabletop mounted test unit, a power supply, a Linear Voltage Displacement Transducer Conditioning Module, a PCI electronics box and the PC-based WinTest ® Digital Control System. Data generated during the test is stored on the PC hard drive. Load frame specifications are listed in Table 4.3. The ELF 3200 is an advanced form of voice coil linear motor technology. Typical voice coil systems are limited in their operation by the heat generated in the coils. As the coils are moving, this energy is not easily removed with the result that the maximum force generated by these systems is low. Enduratec ® and Bose ® Corporation created a new system of linear actuation known as the moving magnet motor. In this system the magnet moves and the coils are stationary. As the coils are fixed, they can be cooled much more effectively than coils in a traditional voice coil system, thus allowing for much higher force generation.

In its simplest form, the method of operation is based on the fact that oppositely charged magnets attract and similarly charged magnets repel one another. The flux generated in the stationary electro-magnets when a current passes through the coils interacts with the flux of the permanent magnets. This causes them to react with a force, the direction of which is determined by the polarity of the electro-magnet flux. The higher the current in the coils, the greater the reaction force of the permanent magnet. However, at high currents, resistive losses in the coils result in heating of the coils and surrounding components. The maximum force that may be generated by such systems is limited by the ability to keep the temperature of the system within a favourable range for proper operation. In the case of the ELF ® 3200, the maximum force achievable is ±450 N. The permanent magnet must also be suspended within the electro-magnet. As Figure 4.3 shows, in the Enduratec system, this has been achieved by attaching the magnet at both ends to flexural members. These members are wide and thin so that, while providing very little resistance to movement in the desired direction, they prevent the magnet from moving in other, undesired directions. They are made of a fatigue resistant stainless steel. The maximum linear displacement achievable with the ELF ® is 12.5 mm (±6 mm). The permanent magnets are made of Neodymium Iron Boron and its high energy product (ten times that of normal ferritic magnets) results in a low inertia moving portion of the motor capable of acceleration in the order of 150 Gs. The low moving mass permits a wide range of velocities, frequencies and amplitudes with a high degree of correspondence between the input signal and the output signal.

The wide range of dynamic performance and high fidelity of such advanced linear motion systems make them suitable for the fatigue testing of microscale specimens by allowing for accurate position or load control and precise waveform mapping at a range of frequencies. The Wintest ® control software also allows for a wide range of test types and data capture methods.

4.5. Investigating the size effect

As the samples were all produced from the same tube type (OD 1500 µm, ID 1380 µm), specimen thickness was determined by the wall thickness of the tube and remained constant at a nominal 60 µm. The size effect was investigated by varying the width of the samples; samples of 50 µm, 75 µm, 100 µm, and 150 µm widths were investigated. Figure 4.4 shows the cross-sectional shapes investigated. Balloon expandable stents are generally created from a single tube; therefore the thickness of the struts remains constant, whilst the width of the struts varies according to the stent geometry. Stents of ever smaller strut widths are also being created for peripheral vascular applications, where the diameter of the blood vessel is less than that of a coronary artery (normally 3-4 mm). The test specimens were designed to capture this variation in width with constant thickness. The investigation carried out here characterises the variation in fatigue life as a function of specimen width (aspect ratio).

4.5.1. Cross sectional area (CSA) evaluation

The strut area used to calculate the load necessary to achieve a particular maximum stress value was an averaged value. Samples are tested within a stress range determined by the maximum stress and the R-ratio. In order to perform such tests on a load control system it is necessary to know the cross sectional area of the strut. Table 4.4 shows an example of the measurements supplied by Creganna Medical Devices. Three width and thickness measurements were supplied for each test specimen along its length along with an indication regarding the suitability of the specimen for testing. The area of a strut was calculated by multiplying the average of the three width measurements and the average of the three thickness measurements.

4.5.2. Establishing the stress range of interest

The stress range of interest was established through finite element modelling of various cardiovascular stent geometries. This is described in detail in section 3.5 of Chapter 3.

4.5.3. Specimen manipulation and test limitations

In its pre-test configuration, i.e. with the support struts intact, a specimen may be more easily handled without causing damage to the gauge length. Once the support struts have been removed, additional manipulation will almost certainly damage the gauge length and render it useless for further testing. This places limitations on the types of tests that may be performed. It is not possible to perform stop-start type tests, where a certain number of cycles are accumulated; the specimen is removed and is inspected in some manner, and is subsequently reinserted into the test frame for further fatigue cycling. The information generated by the load and displacement sensors is therefore the only information available that relates to events that occur during the period of the test. All other information and measurements relating to the test specimens were gathered before or after the test. The experimental set up protocol is attached in Appendix B.

4.5.4. Fixturing

Specimens were laser cut from tubes of 1.5 mm diameter. Each specimen length was 40mm. While the diameter is small, it was still possible to handle the specimens manually and without the aid of tweezers or microscopes. The support struts ensured that, if handled with care, no damage would occur to the delicate gauge length of the specimen. Figure 4.5 shows the orientation of the test specimen in the Enduratec titanium fatigue grips. A 1.35 mm diameter steel pin was inserted into either end of the tube in order to prevent the tube being crushed as the grips were tightened. Carefully alignment of the specimen within the grips is important in order to ensure that only axial loads are applied. Appendix B gives a detailed procedure of the fixturing method.

4.5.5. Fatigue testing

The test protocol was developed in order to establish if a variation in fatigue life existed within the range of specimen sizes investigated. The stresses of interest were established through finite element modelling of vascular stents (Chapter 4); therefore, tests were carried out within the general range of relevant stresses using load control. A frequency of 60 Hz was selected in order to accelerate the fatigue testing of the specimens. A series of preliminary tests established that a high fidelity (good mapping of the selected waveform, and accurate load reversals) was achieved at 60 Hz.

An R-ratio (ratio of minimum stress to maximum stress) of 0.5 was selected, resulting in a tension-tension type test. The test specimens were very delicate and could not withstand compressive loads without buckling. Given that under-loads of the specified minimum load can occur, particularly during ramp up at test start, it was necessary to select an R-ratio (0.5) where this could occur without causing the sample to buckle. The maximum stress ranged from 350 to 600 MPa, generally in increments of 25 MPa. Tests were run in this range of stresses in order to populate stress-life (S-N) curves for the four different sample geometries. However, not all samples were tested at all maximum stresses, for example, the larger 150 and 100 µm samples were not tested at the lowest stress ranges as runout could effectively be guaranteed. The smaller 75 and 50 µm samples were not tested at the highest stress ranges as failure occurred so quickly as to render the test almost useless in terms of providing information. Sample cost determined that such test were not worthwhile. A ramp up period, where 10,000 cycles were accumulated at a frequency 20 Hz before increasing to 60 Hz for the remainder of the test was included for the 50 µm samples in order to improve control during the ramp-up to the maximum load.

Test runout was set at 10,000,000 cycles. This was considered a reasonable number of cycles given the number of specimens that had to be tested, and an acceptable number of cycles for a high cycle fatigue test. At a frequency of 60 Hz, a test takes approximately two days to complete.

4.5.6. Data acquisition

Two forms of data recording were used:

- High frequency data recording for the first 4000 cycles of test. This captures early life failures in great detail and is termed “timed data” or .tdf data.

- Lower frequency data recording for duration of test, termed peak/valley file data or .pvf data. This data shows the history of plastic strain accumulation in specimens at failure or runout.

The timed data method blindly records data points at a frequency and for a duration determined by the user, while peak/valley recording is activated by a user-configured trigger mechanism. Generally two points are recorded, one peak value and one valley value at a frequency determined by the user. The .tdf files are created in order to get a better understanding of early life failures. It is not feasible to use the peak valley files for this purpose, as this method does not allow the scan rates to be altered after test start. The data files would be huge if peak/valley scanning were to occur for the duration of the test at the intervals necessary to accumulate sufficient data for investigation of early life failures. A combination of both methods was used in this work.

4.5.6.1. Timed Data File configuration

Timed data recording was configured to provide continuous scanning for a period of 200 seconds, with 1024 scanpoints per second and to provide sufficient data for complete reconstruction of the fatigue test up to 12,000 cycles at 60 Hz, or 4000 cycles at 20 Hz. Figure 4.6 shows a typical timed data file output. Should failure occur, a trigger is activated which stops cycle and data logging immediately.

4.5.6.2. Peak/Valley Data Files

Peak/Valley data files records data for the duration of the test beyond the ‘timed data’ generated. A scan is conducted every 500 cycles throughout the life of the test producing a plot such as that shown in Figure 4.7.

4.6. Fatigue test data and size effect

Fatigue testing the different width specimens at a range of stresses was designed to expose an endurance limit related size effect. In the case of specimens that runout or fail after an appreciable number of cycles, the peak/valley data provides information on the evolution of plastic strain within those samples. Where samples undergo early life failure, the timed data provides information on the nature of that failure.

References

[4.1] Dieter, G.E. (2001) Mechanical Metallurgy, McGraw-Hill, London.

[4.2] Poncin, P. (2003) Stent Tubing: Understanding the desired Attributes. *In: Proceedings of Materials and Medical Devices Conference*. ASM International, Materials Park, OH, USA

[4.3] Murphy, B.P., Savage, P., McHugh, P.E., Quinn, D.F. (2003) The stress-strain behaviour of coronary stents struts is size dependent. *Annals Biomed. Engng* 31, 686-691

[4.4] Wintest ® Software manual, pg. 3-2

Table 4.1
Chemical composition (nominal) % of 316L / 316LVM by weight

Element	**316L/316LVM**
Chromium (Cr)	**17.5**
Nickel (Ni)	**14**
Molybdenum (Mo)	**2.8**
Manganese (Mn)	**1.7**
Silicon (Si)	**0.6**
Copper (Cu) Max	**0.10**
Nitrogen (N) Max	**0.10**
Carbon (C) Max	**0.025**
Phosphorus (P) Max	**0.025**
Sulphur (S) Max	**0.003**
Iron (FE)	**Balance**

Table 4.2
Size range of Creganna laser cut specimens

Batch	**Labels**	**Gauge Length (µm)**	**Nominal Strut Thickness (µm)**	**Nominal Strut Width (µm)**
Creganna Batch 1	CREG_#_50	4000	60	50
	CREG_#_75	4000	60	75
	CREG_#_100	4000	60	100
	CREG_#_150	4000	60	150
Creganna Batch 2	CREGII_#_50	2000	60	50
	CREGII_#_75	2000	60	75
	CREGII_#_100	2000	60	100
	CREGII_#_150	2000	60	150

Table 4.3
Enduratec ELF 3200 specifications

Parameter	**Specification**
Force range	mN to ±450 N
Static force range	±320 N
Range of displacement	12.5 mm
Maximum frequency	400 Hz
Support column Spacing	406 mm
Test space	
Vertical test space	0-450 mm
Load cell to back of column	305 mm
Load frame dimensions	
Width	495 mm
Depth	483 mm
Height	813 mm
Load frame weight	80 kg

Table 4.4
Example of a table with strut measurements for 75um tube-based specimens

		width				thickness			reject
1	width	0.084	0.088	0.085	thickness	0.057	0.057	0.059	
2	width	0.083	0.088	0.089	thickness	0.054	0.056	0.053	
3	width	0.105	0.106	0.103	thickness	0.078	0.081	0.08	out of spec
4	width	0.079	0.075	0.074	thickness	0.051	0.053	0.049	strut damage
5	width	0.071	0.072	0.078	thickness	0.05	0.053	0.055	
6	width	0.08	0.084	0.083	thickness	0.06	0.061	0.059	
7	width	0.076	0.078	0.08	thickness	0.057	0.055	0.057	
8	width	0.085	0.081	0.085	thickness	0.057	0.056	0.055	
9	width	0.079	0.079	0.078	thickness	0.056	0.058	0.059	
10	width	0.079	0.08	0.079	thickness	0.061	0.059	0.063	
11	width	0.078	0.079	0.079	thickness	0.06	0.059	0.057	
12	width	0.084	0.082	0.081	thickness	0.058	0.054	0.051	

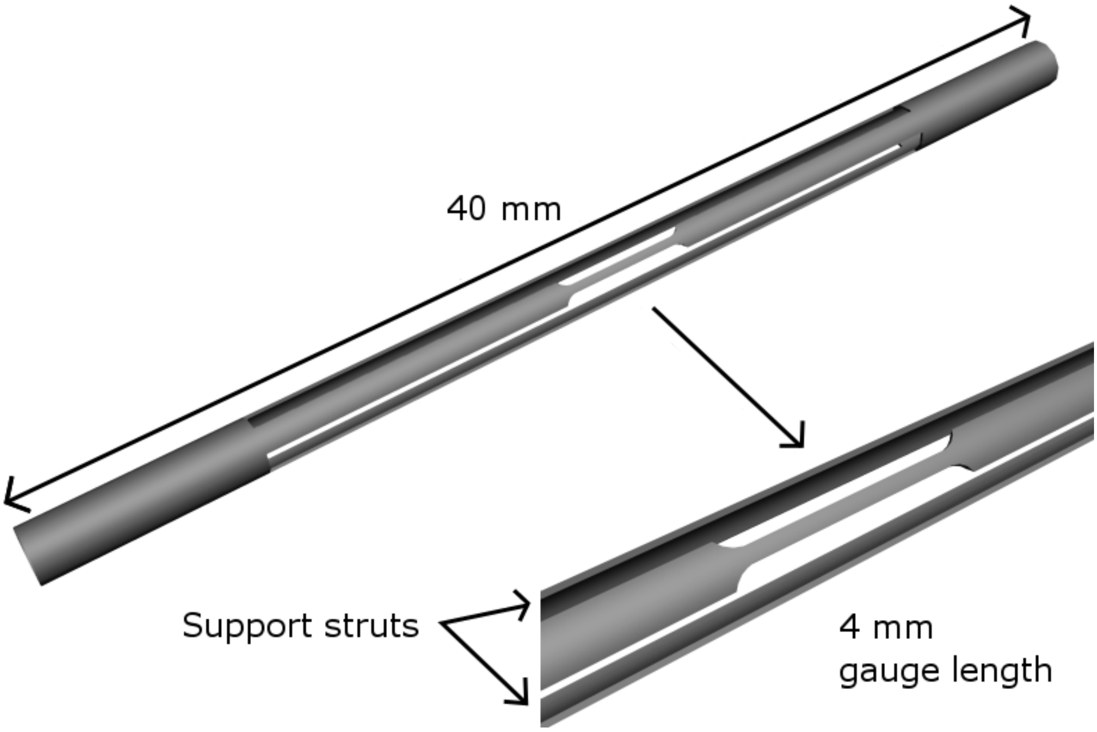

Figure 4.1. Laser cut tube fatigue specimen. Outer tube diameter nominally 1500 µm, inner tube diameter nominally 1380 µm.

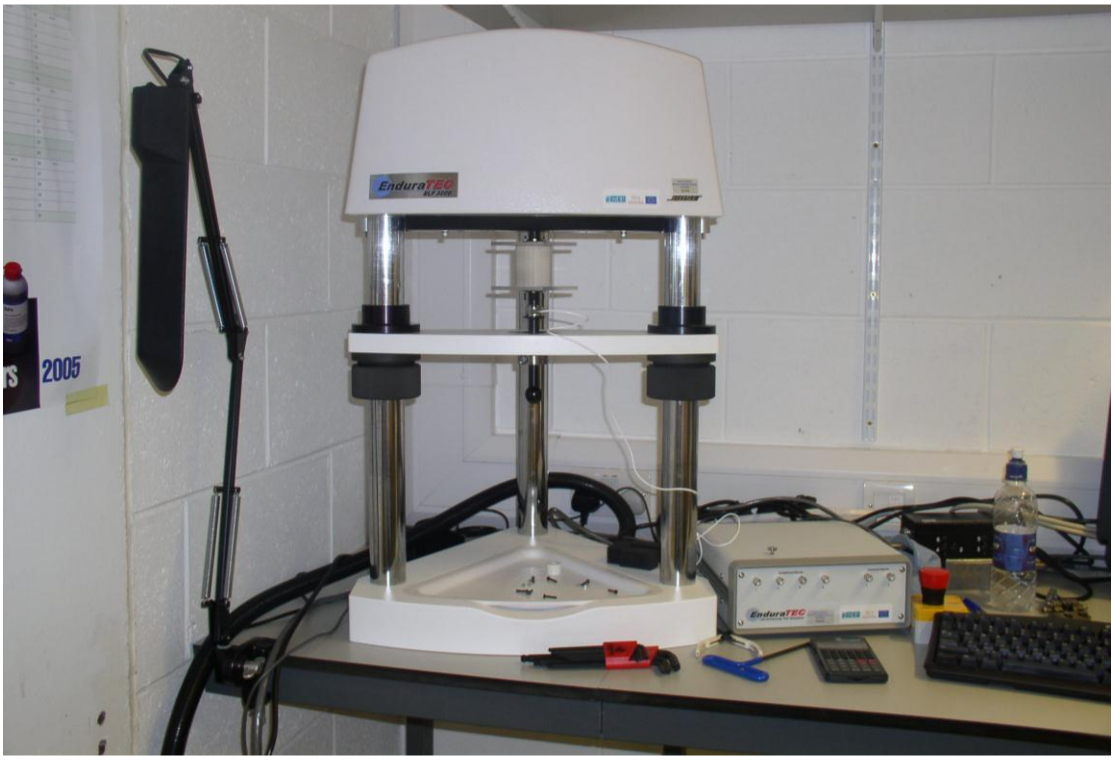

Figure 4.2. The Enduratec ® ELF® 3200 System.

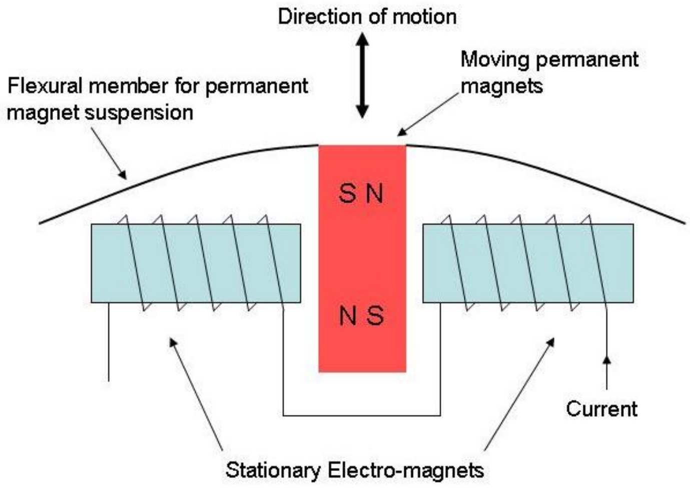

Figure 4.3. Operating mechanism of ELectroForce ® systems. Only one flexural member is shown, there are in fact two, one at either end of the magnet.

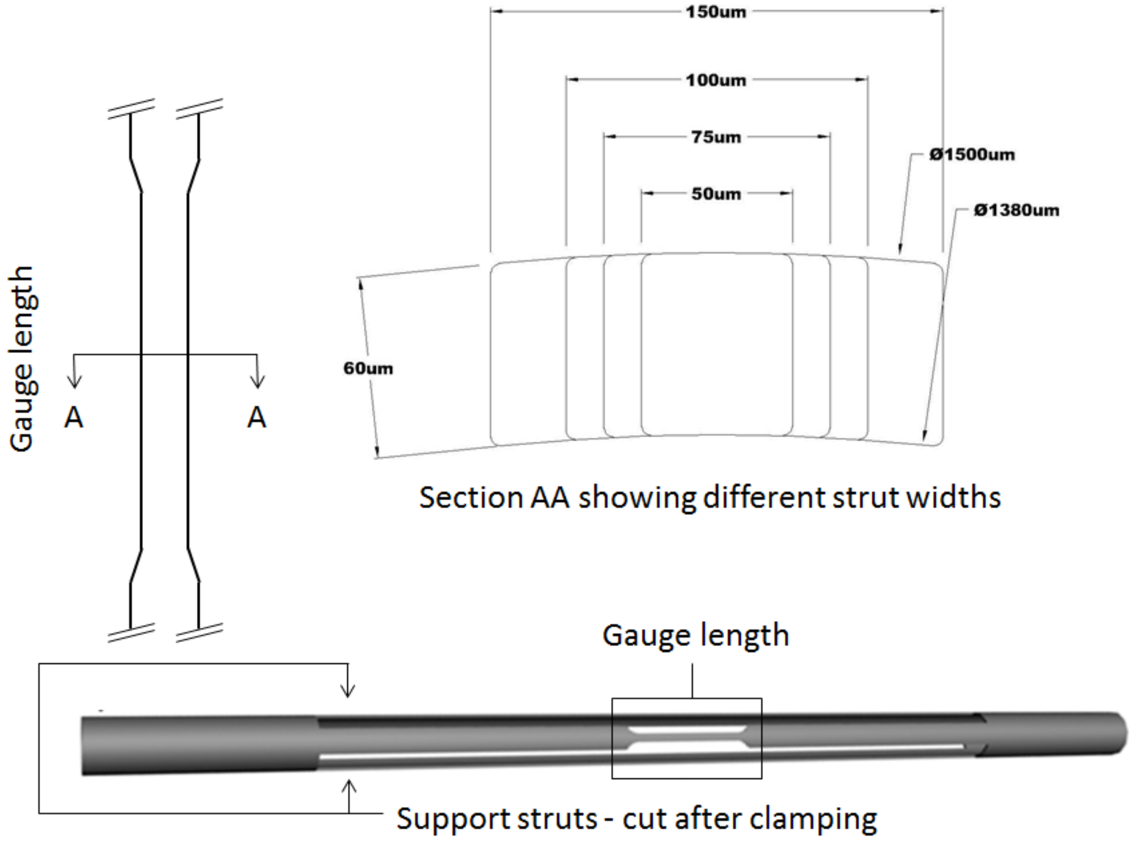

Figure 4.4. Cross section of test regions of the tube-based specimens – nominal dimensions.

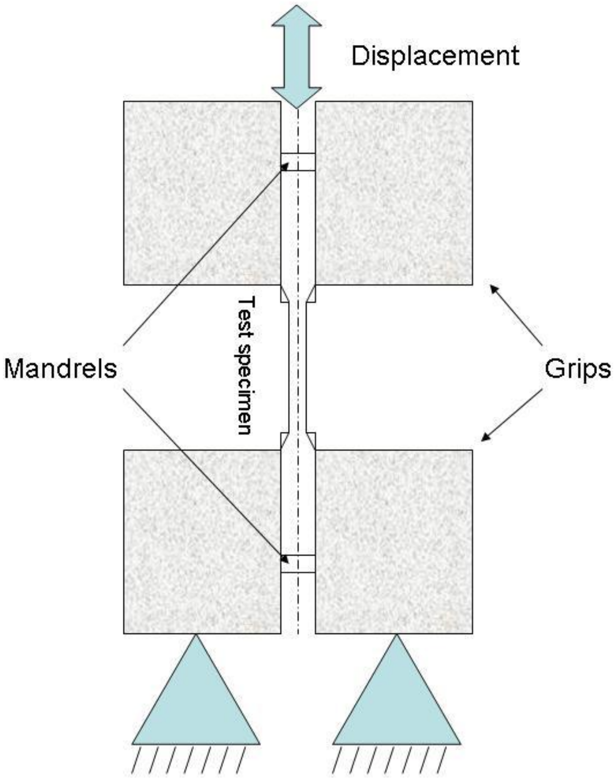

Figure 4.5. Fixturing of test specimens

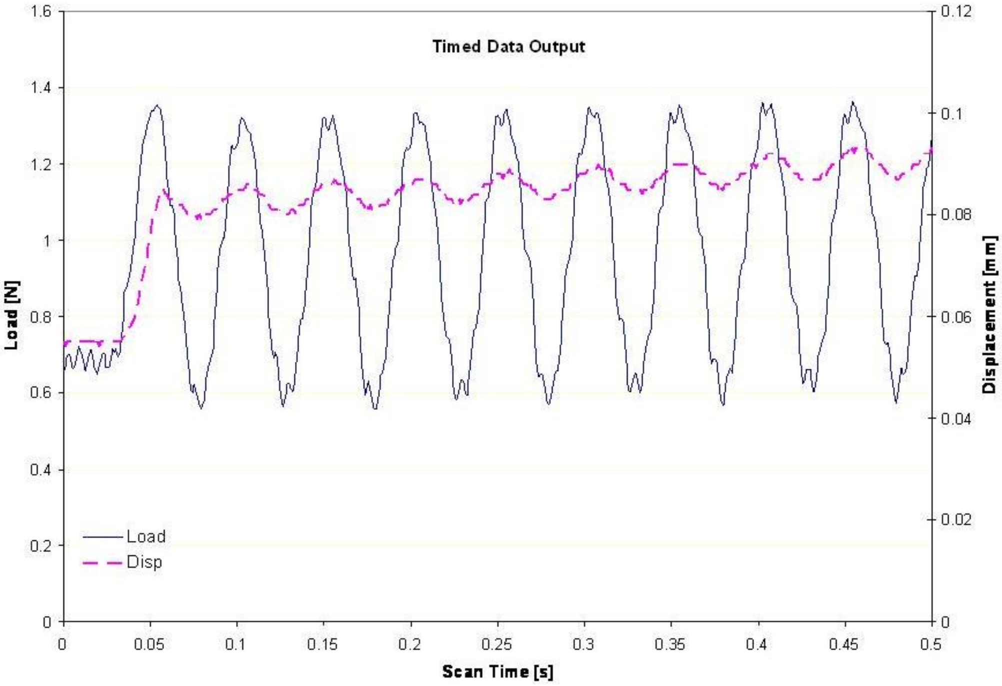

Figure 4.6. Load and displacement traces for timed data file (.tdf) output for the first ten cycles of a fatigue test. Sample width=50µm, frequency = 20Hz, R=0.5, target maximum load is 1.5N

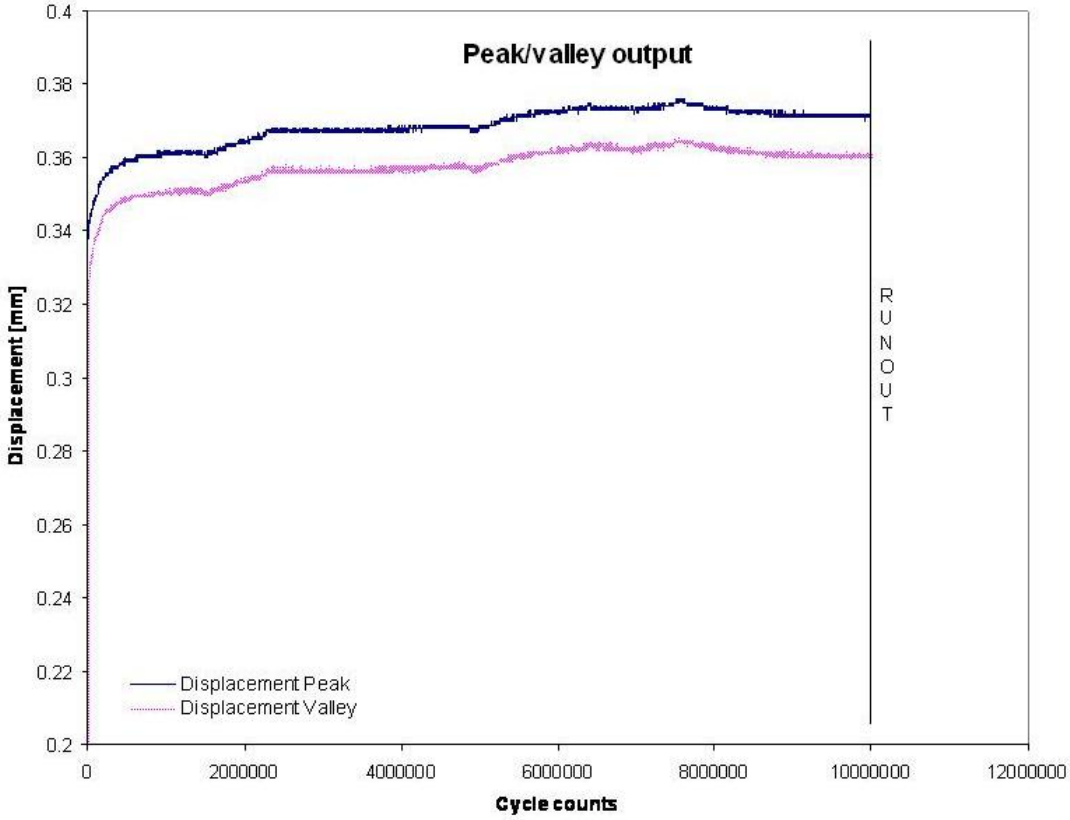

Figure 4.7. Peak and Valley displacement values for peak/valley file (.pvf) output for a runout fatigue test. Sample width=150µm, frequency =60Hz, R=0.5, maximum stress=525MPa

EXPERIMENTAL RESULTS

5.1. Introduction

Four different sizes of micro-scale 316L stainless steel test specimens were subjected to fatigue testing. The results of the fatigue tests are presented in this chapter. The test specimens themselves are designed to be of a form and size similar to the struts of a cardiovascular stent. As shown in figure 5.1, residual tensile stress is imparted to the test specimens through the application of an axial tensile load in excess of the yield point, $\sigma_{yield,}$ of the material and subsequent fatigue cycling at a positive mean stress. Figure 5.2 shows a selection of tensile test curves for the 50 μm and 150 μm specimens. The fatigue testing is carried out at stresses in excess of the yield point of these specimens.

This combination of specimen design and uniaxial loading approximately describes the deployment process of balloon expandable vascular stents. As the balloon is expanded, the increasing diameter opens the stent and forces plastic deformation to occur in the hinge points. The residual strains in stents are both tensile and compressive in nature; upon deployment, tensile stresses are induced on the inner surfaces of the plastic hinges, compressive stresses on the outer surfaces of the plastic hinges. Figure 5.3 illustrates the concept. The test specimens investigated here capture only residual tensile strain as the fatigue loading exceeds the yield point of the material.

It is assumed that regions which remain in compression for part or all of the fatigue cycle are not a fatigue concern. Specimens are then cycled in tension-tension (positive R-ratio of 0.5). A total life approach was adopted, and a Stress – Life (S-N) curve was generated for each of the four specimen sizes under conditions of load control. The aim is to determine if differences in tensile behaviour, ratchetting behaviour and fatigue behaviour combine to produce a size dependent fatigue limit. Under the prescribed test conditions, this size-effect will manifest itself as a difference in the number of cycles to failure for a given maximum stress or alternately, as a reduction in the endurance limit of the affected series.

5.2. Populating S-N curves

As suggested by Suresh [5.1], the endurance limit was determined to be the stress amplitude that a given sample size could support for 10^7 cycles. In this work, for samples which had not failed at this point, the tests were stopped and the samples were termed to have 'runout'. The S-N curves were populated by testing specimens at a range of stress amplitudes (determined by maintaining the same R-ratio and varying the maximum and minimum stresses).

5.3. Rationale behind testing

Fatigue testing was undertaken initially in order to generate stress-life data for each specimen series. The results of the fatigue tests are presented in figure 5.4 and figure 5.5. As testing progressed, it became clear that the S-N curves for each series was very flat (as shown in figures 5.4 and 5.5) without an even dispersion of failure points below the endurance limit. Failure occurred in the majority of cases at less than 10^6 cycles, with very few specimens failing between $2x10^6$ cycles and 10^7 cycles. This phenomenon is described by shallow fatigue curves, where a small variation in maximum stress changes drastically the probability of failure. Wiersma *et al*. [5.2] found similar behaviour when testing micro-scale 316L components and attributed it to a 'quasi-brittle' type of fracture. Cracks grow faster when they are not inhibited by grain boundaries. It was hypothesised by Wiersma *et al*. that if a dominant crack initiates and propagates in a large grain, then a significant portion of the cross-section will be compromised before a grain boundary is reached. Rapid failure will ensue. If the first grain is relatively small, a greater number of cycles will be required to grow the crack and behaviour will be similar to that of a macroscopic specimen. Figure 5.6 illustrates the concept.

5.4. Stress – Life (S-N) curve fitting

Engineering Sciences Data Unit (ESDU) curve fitting protocol 97204 and associated software [5.3] for the “Derivation of endurance curves from fatigue test data, including run-outs” was used to develop S-N curves for each series of test specimens. The programme derives a linear median S-N curve through a set of S-N data. The median curve corresponds to a fifty per cent probability of failure.

Figure 5.7 shows that in terms of stress amplitude, the 150 μm, 100 μm and 75 μm series have a similar endurance limit of approximately 150 MPa, while the 50 μm series experiences a clear, size-dependent 30 MPa reduction in endurance limit.

5.5. Examining early life of 50 μm and 150 μm specimens

It has been established that the 50 μm specimens exhibit a lower fatigue limit than the larger specimens. Comparing the behaviour of the 50 μm and 150 μm specimens should make apparent any further differences which exist.

As described in Chapter 4, timed data files (.tdf) were generated for a period of 200 seconds, beginning at time zero, for all test specimens. At a ramp-up frequency of 20Hz, this data allowed for construction of hysteresis loops for each of the specimens for 4000 fatigue cycles. Several 50 μm specimens and 150 μm specimens were tested at a maximum stress of 450MPa with an R-ratio of 0.5. Hysteresis loops for a selection of cycles from 0 – 4000 for eight of those tests are shown here. The specimens included in this study are listed in Table 5.1. Six specimens achieved runout at 10^7 cycles and two specimens failed at less than 10^6 cycles. The general trends in cyclic strain accumulation for the run-out samples are visible in the hysteresis loops presented in figures 5.8 and 5.9. A 50 μm sample (shown in figure 5.8) complies almost immediately with the required maximum stress of 450 MPa and the stress amplitude of 112 MPa, whereas the 150 μm specimens (figure 5.9) require a ramp up period of 100 cycles or so to achieve compliance. The 150 μm specimens require a higher force in order to achieve a particular stress. The Enduratec fatigue tester ramps up to this force value over the 100 cycles. For the 50 μm specimens the lower force value is achieved within a few cycles. The cyclic strain accumulation for one of the failed 50μm specimens as shown in figure 5.10 behaves similarly to the 50 μm runout specimen shown in figure 5.8. The cyclic strain accumulation for the other samples detailed in Table 5.1 is shown in Appendix C.

It is clear from figures 5.8-5.10 that there is a significant difference in the strain levels experienced by the various specimen sizes. Therefore, the specimen behaviour was investigated further; various life fractions of the test specimens and corresponding strains are presented in Table 5.2 with a graphical representation of the averaged values shown in figure 5.11. This allows for a comparison to be made between the levels of plastic strain accumulation over the lives of the fatigue test for the small and large test specimens. In the cases examined, 62 – 92 % of the total strain occurs at 100,000 cycles (1% of total cycles). There is a slight size related difference in the levels of plastic strain accumulation, with the 150 μm specimens achieving a slightly higher percentage of the total strain (total strain being the strain at test end or 10^7 cycles) up to about 2,500,000 cycles relative to the 50 μm specimens. After 2,500,000 cycles the difference is negligible. There is also a difference in the levels of strain after ramp up and at 4000 cycles, again indicating that the 150 μm specimens have achieved a higher percentage of the total strain. An explanation is offered here and illustrated in figure 5.12. For wider struts, the strain that accompanies fatigue loading is evenly distributed within the structure. Each grain experiences some strain and while the levels of strain will vary slightly from grain to grain, the overall effect is a uniform distribution of strain. As the strut width is reduced, strain is localised in more favourably orientated or ‘softer’ grains within the strut. The high strains in these grains may result in localised work hardening within these grains, resulting in reduced total strains of the specimen. The overall effect results from a non-uniform distribution of strain and a lower total strain.

It appears that in general, the rates of plastic strain accumulation are similar for all specimens examined, although there is more scatter associated with the 50 μm specimens. Where differences exist, they occur before 2,500,000 cycles. While the results only relate to a small number of specimens, they are generally representative of the cyclic behaviour of the specimens under the prescribed test conditions.

5.6. Observations

Studying the hysteresis loops in figures 5.8-5.10 and in Appendix C allows for the following observations to be made:

- For all test specimens, at 4000 cycles, the average level of strain is 52% and as high as 70% of the total strain. This confirms that the specimens undergo an initial high plastic deformation (representative of deployment of a medical device).
- After 100,000 cycles, the rate of cyclic strain accumulation is reduced as the specimens work harden

- At the intervals investigated here, there is no significant difference in the rate of strain accumulation for 50 µm and 150 µm test specimens.

There is no size related difference in the rate of plastic strain accumulation or ratchetting after 100,000 cycles, so it is assumed that both the mechanism and rate of plastic strain accumulation are similar for all specimens. Indeed the mechanisms of plastic strain accumulation are hypothesised to remain the same throughout the fatigue test, and it is the differences in the distribution of plastic strain within the test specimens that result in the variation in fatigue life. As specimen size is reduced, the mechanical behaviour becomes increasingly less predictable; this is reflected in the increased level of scatter in the results of mechanical tests performed on the specimens. The size effect is therefore deemed to be due primarily to differences that arise in the manner of strain accumulation in the initial stages of the fatigue test and not during subsequent fatigue cycling.

In conclusion, the size effect is not caused by differences in the rates of strain accumulation.

5.7. Strain accumulation data for specimens

5.7.1. Strain accumulation data for 50µm failed specimens

The strain accumulation data shown in figure 5.13 for failed samples shows an incremental increase in total strain due to ratchetting up to the point where overload occurs and the specimen breaks. This process of cyclic accumulation of plastic strain under conditions of asymmetrical loading is known as “ratchetting” [5.4, 5.5]. There is no abrupt compliance change in any of the samples that could be related to the opening or closing of a crack. In some cases, a compliance change occurs at 10,000 cycles; this is related to a programmed increase in frequency from 20 Hz to 60 Hz. There is better control of specimens at 20 Hz which is important during ramp up, as a load undershoot during the initial cycles may be sufficient to buckle the test specimen. When the specimen reached the required load, the test frequency was increased to 60 Hz. There is no evidence in the strain history to suggest that specimens would not complete the 10^7 cycles for these failed samples. The data indicates that the mechanisms of failure accelerated rapidly immediately prior before failure of the specimen.

In contrast to the failed samples, the runout samples shown in figure 5.14 do show some evidence of changes in compliance as distinct from an incremental increase in total strain. Bearing in mind that while the log plot makes the compliance change more apparent, it may still be related to possible crack formation processes.

5.7.2. Strain accumulation data for 150 μm failed specimens

A comparison of strain accumulation histories of failed 150 μm specimens shown in figure 5.15 to the runout specimens shown in figure 5.16 shows that there is nothing to suggest that failure is a likely outcome of the fatigue test. The strain accumulation data indicate that the failed and runout specimens behave in a similar manner macroscopically, up to the point where failure occurs. As with the runout 50 μm specimens, the runout 150 μm specimens exhibit changes in compliance during the course of the test which may be indicative of crack growth processes, yet no failure was observed.

5.7.3. 50 μm and 150 μm specimens

Notwithstanding the difference in strain magnitude (due to the higher stress experienced by the larger specimens), the strain accumulation histories for both 50 μm and 150 μm specimens are similar in many respects, with both specimens series sharing the following key attributes:

- if failure occurs, it is generally before 1,000,000 cycles
- plastic strain accumulation rates are similar
- the manner of plastic strain accumulation of failed specimens is similar to that of runout specimens

The question then arises as to whether any information on the failure mechanism/s can be gleaned from the strain accumulation/displacement history of the test specimens.

5.7.4. Case study of a 150 μm specimen

The hysteresis loops (up to 4000 cycles), strain accumulation data (to failure) and associated cyclic strain amplitude for a 150 μm specimen tested at a maximum stress of 600MPa (and which failed after 838,000 cycles) are plotted in figure 5.17 (a), (b) and (c). The ramp up period as described by the hysteresis loops shows nothing remarkable. Ramp up behaviour (figure 5.17(a)) is similar to other 150 μm specimens. Fatigue cycling between maximum and minimum stress shows the expected incremental increase in strain (ratchetting). Figure 5.17(b) shows that there is progressive elongation of the specimen up to the point of failure. The variation in cyclic strain amplitude is low and the strain amplitude remains stable throughout the test as shown figure 5.17(c). As the strain amplitude remains stable throughout the test, this suggests that no significant crack growth takes place until fracture. As the tests are load controlled, crack formation would be highlighted by either a change in the strain amplitude or a change in the strain accumulation profile. This can be taken to indicate that the majority of life is spent in crack initiation and that the crack propagation period is rapid and quickly results in failure of the test specimen. The behaviour of this sample represents the typical behaviour of the 150 μm specimens tested in this work. While the specimen was tested at a maximum stress of 600MPa, the strain values at various life fractions are comparable to those of other 150μm specimens tested at a lower maximum stress of 450MPa as shown in Table 5.3.

5.7.5. 75 μm and 100 μm specimens

The fatigue behaviour of 75 μm and 100 μm specimens was also investigated in this study. However, the focus was mainly on identifying differences in the behaviour of the 50 μm and 150 μm specimens. It was expected that the size-related differences in material behaviour would be most obvious when comparing the performance of the smallest and the largest specimens. With regard to the behaviour of the 75 μm and 100 μm specimens, it can be seen from figures 5.18 (a) and (b) and 5.19 (a) and (b) that the strain range for both failed and runout specimens is comparable to that of the 150 μm specimens (figures 5.15, 5.16). The strain accumulation profile is also comparable, with little or no indication that failure is a likely outcome for failed specimens while runout specimens, in common with runout 50 μm and 150 μm specimens, exhibit compliance changes during the course of the fatigue test as shown in figures 5.14 (runout 50 μm), 5.16 (runout 150 μm), 5.18(b) (runout 75 μm) and 5.19(b) (runout 100 μm). It was such similarities that provided the justification for the focus on the 50μm and 150μm specimens.

In summary, the following points can be made on the strain accumulation data for the various specimen sizes:

- if failure occurs, it is generally before 1,000,000 cycles
- strain accumulation rates are similar
- the manner of strain accumulation of failed specimens is similar to that of runout specimens
- 75 µm and 100 µm specimen behaviour is comparable to that of the 150 µm specimens
- the variation in cyclic strain amplitude is low and the strain amplitude remains stable throughout the test
- indications are that the majority of life is spent in crack initiation and that crack propagation period is rapid and quickly results in failure of the test specimen

5.8. Strain history analysis

The peak-valley or strain-cycle count data for runout specimens shows that in some cases the specimen compliance changes as the test progresses. It has been hypothesised that this change in compliance is due to fatigue crack growth. In order to determine if such cracks were present, the outer surfaces of the runout specimens were examined using a Scanning Electron Microscope (SEM – Hitachi S4700).

5.8.1. 50 µm specimen micrographic examination

The outer surfaces of the four 50µm runout specimens were examined in the SEM, with particular emphasis being placed on the identification of potential cracks or crack-like features. Several such features were observed on the 50 µm runout specimens. Figure 5.20 shows a possible fatigue crack which was observed on the outer surface of a 50µm specimen 09_50 while figure 5.21 shows a feature on runout specimen 11_50 which is similar to a large crack identified on failed specimen 06_50. Such a feature may contribute to a compliance change and ultimately to failure of the specimen.

Another possible crack also appears elsewhere on the surface of specimen 11_50 as shown in figure 5.22. The deep fissures on the surface of specimen 14_50 shown in figure 5.23 are features which occur as a result of slip within and between grains, and while they are not necessarily defined as cracks, they may be considered to act as sites of stress concentrations in the same way as cracks would. While some of the features observed on the 50 μm specimens may resemble cracks, it was not shown conclusively that they are cracks. Other large features, such as those shown in figures 5.21 and 5.23, occur as a result of high levels of plastic deformation and may be considered to act as cracks i.e. the formation and extension of such stress concentration features will result in a compliance change and ultimately failure of the specimen. The fragility of the specimens prevented additional mechanical testing after removal from the fatigue tester; the level of manipulation required to reinsert the specimen into the tester would almost certainly have damaged the specimen and invalidated the results of any further testing. The inability to reinsert specimens into the fatigue tester also eliminated the possibility of performing crack growth rate studies. Crack growth rates could not therefore be ascertained.

5.8.2. Observations

- SEM examination of the surfaces of the specimens reveals the existence of crack-like features (figures 5.20, 5.21, 5.22). It is possible that these features are fatigue cracks. However, it was not possible to demonstrate conclusively that these features were cracks. Also present on the surface are large, deformation-related flaws.

- Some of the features identified (figures 5.21(a) and 5.23), while not fully developed surface cracks, occur as a result of high levels of plastic deformation and can be considered to act as stress concentration sites.

5.8.3 150 μm specimen micrographic examination

The 150 μm runout specimens shown in figure 5.24 were examined in a manner identical to that of the 50 μm specimens. While there was ample evidence of plastic deformation, no crack-like features or plastic deformation induced flaws were observed on any of the specimens investigated in the SEM. It cannot therefore be concluded that the compliance changes observed during the fatigue tests come about as a result of fatigue crack growth. It must be remembered that while the 150 μm specimens differ in width to the 50 μm specimens, the strut thickness of 60 μm is the same for both. Therefore, a thickness related feature which contributes to compliance change in a 50 μm specimen is likely to have a similar effect in a 150 μm specimen. Figure 5.25 shows such a feature. Features of plastic deformation that are related to the thickness of the specimens are equally likely to affect the 75 μm, 100 μm and 150 μm specimens.

5.8.4. Interpretation of .pvf data vis-à-vis fracture mechanisms

As discussed, the strain – history data for failed specimens indicates that crack formation and ductile overload occurred rapidly. This is suggestive of an initiation dominated fatigue life, with a brief crack propagation phase:

$$N_f = N_i + N_p \qquad (6.1)$$

$$N_i \gg N_p$$

where N_f is the number of cycles to failure, N_i is the number of cycles required to initiate a crack and N_p is the number of cycles required to propagate the crack to failure or to the point of ductile overload.

5.9. Relationship between fatigue and tensile behaviour of test specimens

Fatigue testing is performed at stresses above the yield point of the material. Fatigue testing is performed at stresses greater than 300MPa, the yield stress of the annealed 316L test specimens is 200MPa. This raises the possibility that specimen failure occurs as a result of tensile failure mechanisms only with the possibility that fatigue failure mechanisms contribute little, or nothing to specimen failure. In order to investigate this thoroughly, tensile tests were performed on test specimens identical to those used for the fatigue tests. The results are shown in figure 5.26 for 50 μm and 5.27 for 150 μm specimens. As the strain in a fatigue test is dependent upon the instant of recording, two strain values are presented. *"test start"* refers to the strain value recorded upon the first instance of the required maximum load associated with a fatigue test, while "*load drop and runout"* refers to the strain value registered at failure of a specimen (determined at the instance when the load registered by the load cell drops significantly), or the strain value registered at runout of a specimen at 10,000,000 cycles, i.e. the terminal relevant strain value. The comparison of fatigue strain values taken at test start (defined above) and tensile strain values (figure 5.26(a)) shows that there is no clear correlation between the two data sets. This finding is reinforced in figure 5.26(b), where the terminal fatigue strain for the various specimens (at load drop or runout) cannot be directly related to the tensile failure strain. The variation in the fatigue behaviour of the 50 μm specimens is greater than that which occurs during tensile testing of the same specimens. The differences indicate that mechanisms other than static mechanisms of failure are influencing the fatigue behaviour of 50 μm specimens.

However, it is worth noting that the strain rate differed for the fatigue and the tensile testing. It is likely that the higher strain rate of the fatigue tests contributed to the higher initial strain values experienced by the test specimens (higher strain rate results in elevation of the yield point and a reduction in the failure strain. While this effect has not been quantified, it alone does not explain the differences in fatigue and tensile behaviour, particularly the apparent increase in failure strain that is experienced by certain test specimens.

The fatigue and tensile test results for the 150 μm specimens are in general accordance. While fatigue testing results in a higher rate of hardening initially (as shown in figure 5.27(a)), the strain values are pulled into the tensile envelop defined by the maximum and minimum stress strain curves with the accumulation of cyclic strain (figure 5.27(b)).

Relative to the tensile tests, the fatigue tests produce failure at lower strain values. The greater rate of strain hardening associated with the fatigue tests may be attributed to the rate dependence of the stainless steel. As the fatigue test progresses with a constant maximum stress and stress amplitude, the level of plastic strain within fatigue specimens increases due to the effect of ratchetting or ratchetting. Unlike the 50 μm fatigue specimens, the fatigue failure strain of the 150 μm specimens is less than the tensile failure strain of the same specimens. This suggests that mechanisms other than static mechanisms of failure are influencing the fatigue behaviour of 150 μm specimens.

In conclusion, a comparison of tensile data and fatigue data generated with identical test specimens suggests that mechanisms other than static mechanisms of failure influence the fatigue behaviour of 50 μm and 150 μm specimens.

5.10. Ductility exhaustion

Cumulative damage theories propose that failure of a metal will occur when a finite amount of plasticity has been induced in that metal. Miner's linear damage rule [5.6], the simplest and most generally applicable cumulative damage theory, proposes that the first observation of cracking designates the end point of the test. In the study carried out here, the strain value at failure/load drop or runout has been selected as the endpoint of the fatigue test; this is considerably different from Miner's method. No microscopic observation of specimen surfaces was undertaken during testing so cracks were not observed until test completion or specimen failure occurred. Subsequent micrographic analysis showed that cracks had formed on run out specimens and that certain failed specimens showed evidence of secondary cracking. However, there was no way of knowing when these cracks started to propagate using the methods in this work. It must be assumed that where runout occurs, the critical level of plasticity has not been achieved. Ductility exhaustion, "D" was calculated by taking the ratio of the fatigue strain at load drop and the tensile strain at failure. The data for 50 μm, 75 μm, 100 μm and 150 μm specimens are presented in figure 5.28. Individual specimen data are presented in figure 5.29(a)-(d). The D values of certain 50 μm specimens exceeds unity (figure 5.29(a)) indicating that the fatigue strain is greater than the tensile strain to failure. This suggests that deformation mechanisms associated with cyclic loading extend the total strain past that achieved during tensile loading of the specimens. Data for the 75 μm specimens suggests that the fatigue strain to failure is similar to the tensile strain to failure, while 100 μm and 150 μm data suggests that deformation mechanisms associated with cyclic loading serve to reduce the fatigue strain to a value lower than that achieved during tensile testing.

The selection of the fatigue strain at load drop or runout, as opposed to a value associated with the appearance of the first observable crack will undoubtedly result in higher fatigue strain values for the various specimens. However, taking this into account, there are sufficient differences between fatigue and tensile data and between the behaviour of the various specimens to indicate that (a) fatigue processes in addition to tensile deformation processes influence the final strain value associated with a specimen and (b) that the influence of such factors is not constant for the different specimens.

5.11. An initiation dominated fatigue life

Test data shown in figure 5.30 demonstrates that failure of specimens occurs within 1,000,000 cycles or does not occur within the lifetime of the fatigue test. Where failure occurred, it can be assumed that a fatigue crack initiated and propagated to a length where ductile overload of the remaining ligament occurred (as discussed in Section 5.8.3). Where failure did not occur, it is assumed that fatigue cracks are in the initiation phase and have not yet achieved a critical crack length. Figures 5.20-5.22 support the idea that the 50 μm specimens remain in the intitiation phase, with runout occuring at 10,000,000 cycles.

As no evidence of crack formation was visible on the surfaces of the 150 μm specimens, it is concluded that these larger specimens remain within the initiation phase of fatigue crack development for the duration of the 10,000,000 cycles. The presence of a pre-existing flaw or a sufficiently soft region(s) wherein strain localisation occurs reduced greatly the duration of the initiation phase of crack development. Up to the point of test stop, the entirety (150 μm, 100 μm, 75 μm) or the majority (50 μm) of life is spent in the initiation phase of a fatigue crack development.

5.12. Comparison of maximum stress and ultimate tensile stress (UTS)

If was found during tensile testing of these specimens that the ultimate tensile stress values varied as a function of size, with smaller specimens having lower UTS values than larger specimens [5.7]. If the maximum stress experienced by a test specimen is normalized by the UTS value for that specimen size, then this difference is taken into account, and its effect is neutralized. Such an analysis has been performed and is shown in figure 5.31(a) and (b). Figure 5.31(a) demonstrates that the maximum stress in some specimens is greater than the UTS. Examining figure 5.31(b) for samples tested at the same stress levels (450MPa) shows that normalizing with respect to UTS suggests that smaller specimens (50 μm, 75 μm) are tested at stresses closer to their UTS, i.e. a given common maximum stress is closer to the UTS value for the smaller specimens. At this maximum stress value, the 50 μm specimens have values closest to unity, followed by the 75 μm specimens, with the 150 μm specimens having the lowest ratio. No 100 μm specimens were tested at this maximum stress value. However, assuming a runout test outcome, an attributed maximum stress value of 450 MPa normalized by the UTS for 100 μm is included in figure 5.31(b). The data point is in keeping with the trend established by the other specimens.

As the ratio of maximum stress and UTS approaches unity, so the likelihood of failure increases. An examination of the normalized fatigue strain values associated with specimens tested at a maximum stress of 450 MPa is presented in figure 5.31(c). The data cannot be interpreted as clearly as the normalised stress plot shown in figure

5.31(b), but the general trend is maintained for the runout samples tested. The larger specimens show a lower ratio of fatigue strain to tensile failure strain, with little scatter in the data. The scatter of 50 μm and 75 μm data is considerable, and there is no apparent correlation between the level of ductility exhaustion and the number of cycles to failure. Such a variation in the results of the fatigue tests is due in large part to the reduced level of constraint experienced by grains within the smaller specimens. The scatter associated with lower width specimens has been a consistent feature of the data generated during this project.

In this section, a comparison was made for the specimen behaviour based upon a common maximum stress of 450MPa (figure 5.31(b)). It is perhaps more relevant to compare specimens based upon a common normalization factor. A normalized maximum stress of 450 MPa for 50 μm specimens produced a factor of 0.95, the maximum stress value required to produce the same factor for 150 μm specimens is 570 MPa. Therefore, several 150 μm specimens were tested at a maximum stress of 575 MPa and the normalized data is presented in figure 5.32(a). The data suggests that the size effect is related to the ultimate tensile stress of the test specimens rather than the failure stain (figure 5.32(b)). As the ratio of maximum stress and UTS approaches unity, so the likelihood of failure increases. For narrow width specimens, where the level of constraint has been compromised, proximity to UTS is a better indicator of likelihood of failure than ductility exhaustion methods.

5.13. Verification of the size effect

5.13.1. Effect of Area

The objective of this work was to investigate the possibility that the size effect is an artefact of the laser cutting process rather than a real material behaviour. Should there be a difference in the quality of the 50 μm strut from that of the 150 μm struts, i.e., the struts are not cut within the same tolerance for straightness, this will be manifested in a higher or lower stress than required. Should the stress be higher than required for the smaller samples, then the size effect may be null and void. On the other hand, should the stress be lower than required, then the size effect may be magnified.

During the experimental work, the load applied to a specimen was calculated by multiplying the cross-sectional-area (CSA) of the specimen by the desired maximum stress. The CSA of the specimen was calculated by multiplying the average of three width measurements by the average of three thickness measurements. The measurements were supplied by the specimen manufacturer, an example is provided in Table 5.4, and was taken at positions along the strut length as shown in figure 5.33. In order to take account of the variation in area along the strut, related width and thickness measurements were used to produce three different CSA readings. The actual stresses at three positions along the strut length were then recalculated using the nominal load value. From these three values, the maximum stress value and minimum stress value were selected and plotted for all samples in the 50 μm and 150 μm range as shown in figure 5.34. The nominal or target load (which was in all cases close to the average of the three values) was also included. The plot so generated allows for comparison of "runout values." It is obvious that there is no overlap between the 50 μm runout stresses and the 150 μm runout stresses, the latter being higher (in the order of 75-100 MPa) than the former. In conclusion, the size effect appears not to be an artefact of varying CSA. However, the question of the existence of the size effect is still not definitively answered. It is also necessary to investigate the combined effect of undersized area with the overload experienced by that specimen. In this scenario, the combined effect of reduced area and increased load may be sufficient to raise the stress level in 50 µm samples to that experienced by the 150 µm samples, thus nullifying the size-effect.

5.13.2. Machine Control

Here, the ability of the Enduratec fatigue tester to control within the specified load limits is investigated. It is necessary to quantify the load overshoot and undershoot for each specimen size. If control of the smaller specimens is poor, then the load overshoot alone may be sufficient to raise the maximum stress in a 50 µm specimen to the level experienced by a 150 µm sample. This may nullify the size-effect.

It was observed that the average maximum and minimum loads were very close to the target loads for both 50 µm and 150 µm specimens, with marginally better control of the 150 µm specimens i.e.:

- For 50 µm specimens the average maximum load was 99.75% of the maximum target load and the average minimum load was 99.68% of minimum target load.
- For 150 µm specimens, the average maximum load was 100.06% of the maximum target load and the average minimum load was 99.11% of the minimum target load.

5.13.2.1. Overshoot and undershoot of required loads

An average value was generated for highest recorded loads (overshoot) and lowest recorded loads (undershoot) experienced by the specimens during the fatigue test. As data points were logged every 500 cycles, it is not possible to state accurately the frequency with which these events took place. However, it must be noted that the overshoot and undershoot of the maximum and minimum loads was not a common occurrence, a statement borne out by the fact that the average of the recorded values for maximum and minimum loads were consistent with the nominal or target maximum and minimum load values.

The results are as follows for 50 μm specimens:

- average overshoots were 3.7% above the maximum required load
- average undershoots were 10.6% below the minimum required load

and for 150 μm specimens:

- average overshoots were 4% above the maximum required load
- average undershoots were 7.3% below the minimum required load

This gives an overshoot of approximately 4% of maximum load and an undershoot of approximately 10% of the minimum load in both cases. If it is assumed that a specimen was cyclically loaded at this higher stress level for its entire life, and is combined with the reduced areas discussed above, then a worst case scenario will be developed, wherein the stress experienced by the small samples will be magnified by the combined effects of reduced cross-sectional-area due to poor control of laser cutting process and increased load due to poor machine control. Figure 5.35 shows that when these factors are taken into consideration, the size-effect still holds true. There is no overlap of the maximum load and fail/no fail of 50 μm and 150 μm specimens. While the overshoot is in some cases sufficient to raise the stress level in a 50 μm sample to be equal to or greater than the stress level within a 150 μm sample, all 50 μm samples experiencing this level of loading failed. 50 μm samples which fail continue to do so at stress levels below the stress level at which 150 μm samples run out, even when the overshoot is included. Bear in mind that the overshoot does not occur on every single cycle (refer to average loads – very close to target), and that the 150 μm samples also experience a similar number of overshoots, so any amplifying effect present in 50 μm due to overshoot will also be present in 150 μm samples. In conclusion, the size effect is not an artefact of the level of control at different loads, but a real effect.

In summary, the fatigue testing carried out on 50, 75, 100 and 150 μm specimens showed that a size effect does indeed exist, reducing the fatigue limit of the 50 μm to below that of the wider specimens. It is worth noting that all the specimens were fabricated from tubing with a wall thickness of 60 μm. If specimen dimensions are considered not in terms of width or thickness, but in order of size then the fatigue results indicate that there is only a significant difference between 50 μm and 60 μm. Therefore, it is more appropriate to conclude that the experimental results presented in this work show a geometry effect in the fatigue behaviour based on the specimens' smallest dimension i.e. 50 μm for the 50 μm specimens and 60 μm for the 75, 100, 150 μm specimens.

References

[5.1] Suresh, S., (2004) Fatigue of Materials, *Cambridge University Press,* 2nd Edition, 221-224

[5.2] Wiersma, S. and Taylor, D., (2005) Fatigue of materials used in microscopic components. *Fatigue Fract. Engng Mater. Struct.*, **28**, 1153-1160

[5.3] Engineering Sciences Data Unit - ESDU 97024 "Derivation of endurance curves from fatigue test data, including run-outs" and associated software ESDUpac W9724v10

[5.4] Kang., G.Z., Li, Y.G., Zhang, J., Sun., Y.F. and Gao, Q., (2003) Uniaxial ratchetting and failure behaviours of two steels, *Theoretical and Applied Fracture Mechanics*, **43**, 199-209.

[5.5] Kang., G., (2007) Ratchetting: Recent progresses in phenomenon observation, constitutive modelling and application, *International Journal of Fatigue*, **30,** 8, 1448-1472

[5.6] Suresh, S., (2004) Fatigue of Materials, *Cambridge University Press*, 2nd Edition, 132-4

[5.7] Cuddy, H., (2005) Master of Engineering Thesis, National University of Ireland, Galway

Table 5.1. Hysteresis study on 50 µm and 150 µm specimens.

Sample number	**Width [µm]**	**Maximum Stress [MPa]**	**R-ratio**	**Test outcome**
CII_09_50	50	450	0.5	Runout
CII_11_50	50	450	0.5	Runout
CII_14_50	50	450	0.5	Runout
CII_12_50	50	450	0.5	Failure at 3.85E5
CII_15_50	50	450	0.5	Failure at 1.58E5
CII_23_150	150	450	0.5	Runout
CII_43_150	150	450	0.5	Runout
CII_45_150	150	450	0.5	Runout

Table 5.2. Test specimens and associated strain values at various life fractions. Bold print indicates failed specimens.

Specimen	**% strain at end ramp up**	**% strain at 4000 cycles**	**% strain at test end**	**Strain @ end ramp up as percentage of total strain**	**Strain @ 4000 cycles as percentage of total strain**	**Strain @ 100000 cycles as percentage of total strain**	**Strain @ 2500000 cycles as percentage of total strain**
CII_09_50	0.9	1.85	3.9%	23%	47%	62%	91%
CII_11_50	1.55	3.25	6%	26%	54%	88%	100%
CII_14_50	2.95	4.90	12%	25%	41%	87%	89%
CII_12_50	**2.3**	**4.40**	**9.35%**	**25%**	**47%**	92%	n/a
CII_23_150	3.65	5.60	8.55%	45%	70%	84%	98%
CII_43_150	2.45	3.70	9.5%	27%	41%	90%	93%
CII_45_150	1.95	3.30	5.2%	40%	66%	87%	98%

Table 5.3. Fraction of total strain at various life fractions.

150um series	**100,000 cycles**	**$2.5x10^6$ cycles**
23	0.83	0.98
43	0.85	0.90
45	0.87	0.98
21	0.84	0.89
26	0.85	0.87

Table 5.4. Example of Creganna supplied specimen measurements for 150µm samples showing corresponding width and thickness measurements.

		Width				Thickness			
1	width	0.135	0.133	0.133	thickness	0.036	0.035	0.034	out of spec
2	width	0.111	0.115	0.108	thickness	0.035	0.037	0.034	out of spec
3	width	0.113	0.117	0.113	thickness	0.029	0.034	0.031	out of spec
4	width	0.12	0.117	0.112	thickness	0.03	0.034	0.031	out of spec
5	width	0.133	0.131	0.127	thickness	0.035	0.036	0.032	out of spec
6	width	0.148	0.148	0.145	thickness	0.065	0.066	0.064	
7	width	0.149	0.153	0.144	thickness	0.063	0.065	0.069	
8	width	0.143	0.148	0.147	thickness	0.064	0.063	0.061	
9	width	0.147	0.148	0.147	thickness	0.065	0.063	0.064	
10	width	0.172	0.169	0.167	thickness	0.072	0.067	0.067	

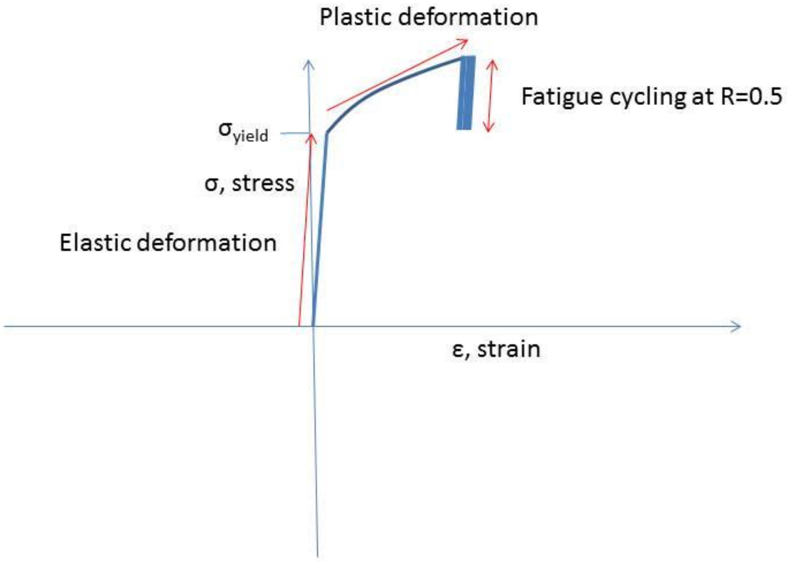

Figure 5.1. Residual tensile stress is imparted to the test specimens through the application of an axial tensile load in excess of the yield point of the material and subsequent fatigue cycling at a positive mean stress.

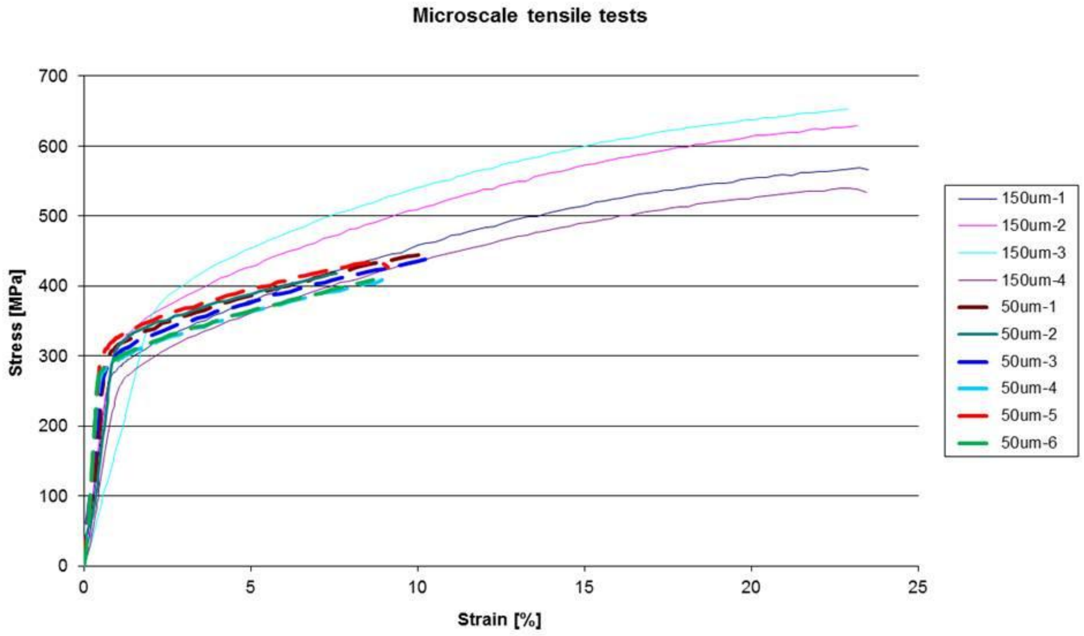

Figure 5.2. Tensile test curves for a selection of 50 µm and 150 µm specimens.

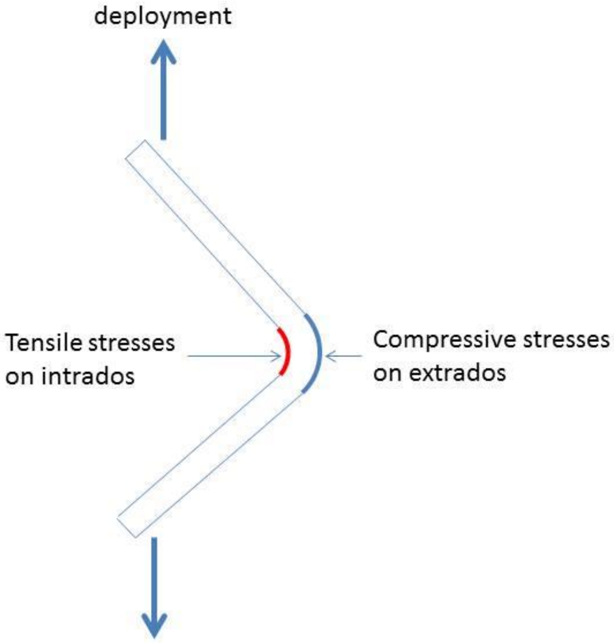

Figure 5.3. Schematic of plastic hinge showing tensile stress in inside or 'intrados' of hinge and compressive stresses on outside or 'extrados' of hinge.

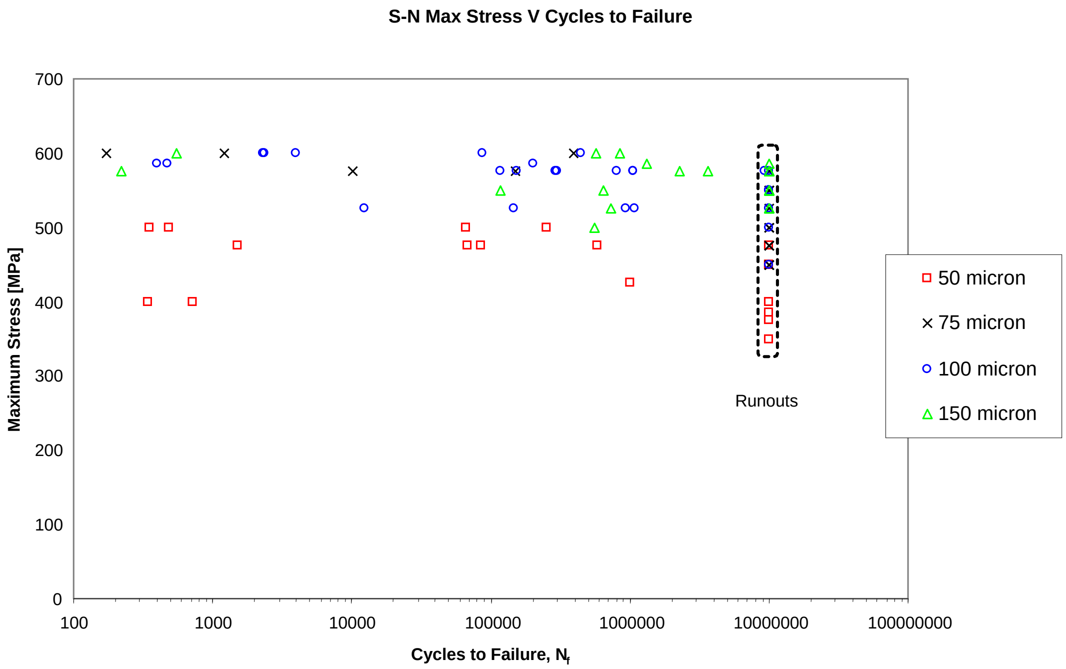

Figure 5.4. Results of fatigue tests on micro-scale 316L stainless steel specimens. Maximum stress on the abscissa.

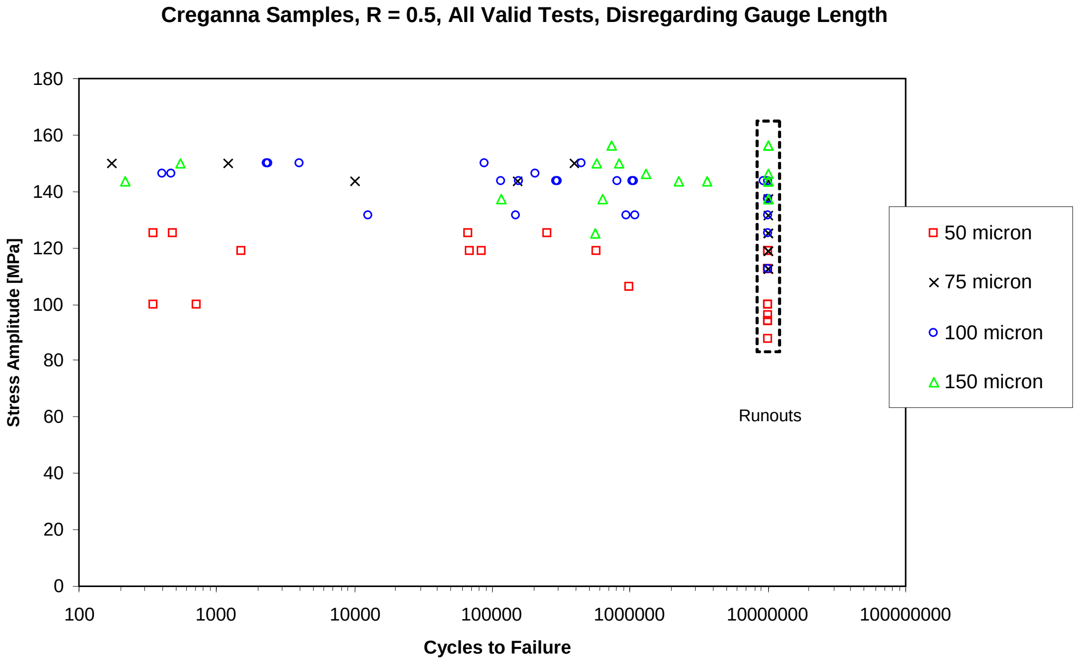

Figure 5.5. Results of fatigue tests on micro-scale stainless steel specimens. Stress amplitude on the abscissa.

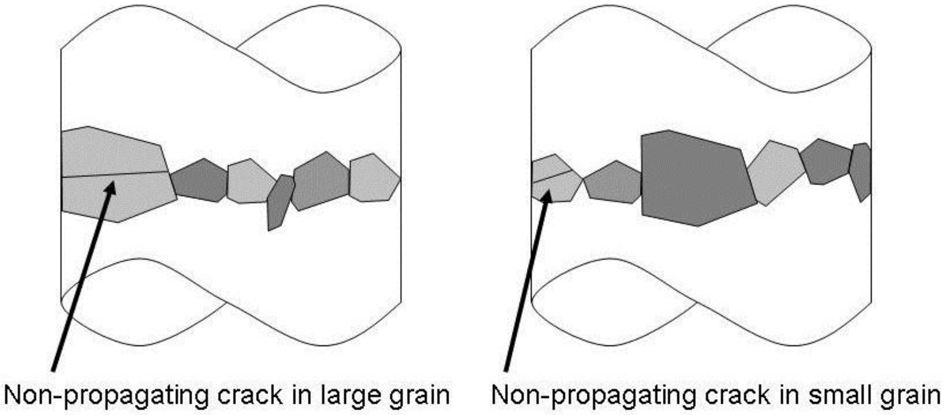

Figure 5.6. Quasi-brittle fatigue (after Wiersma et al. [5.2])

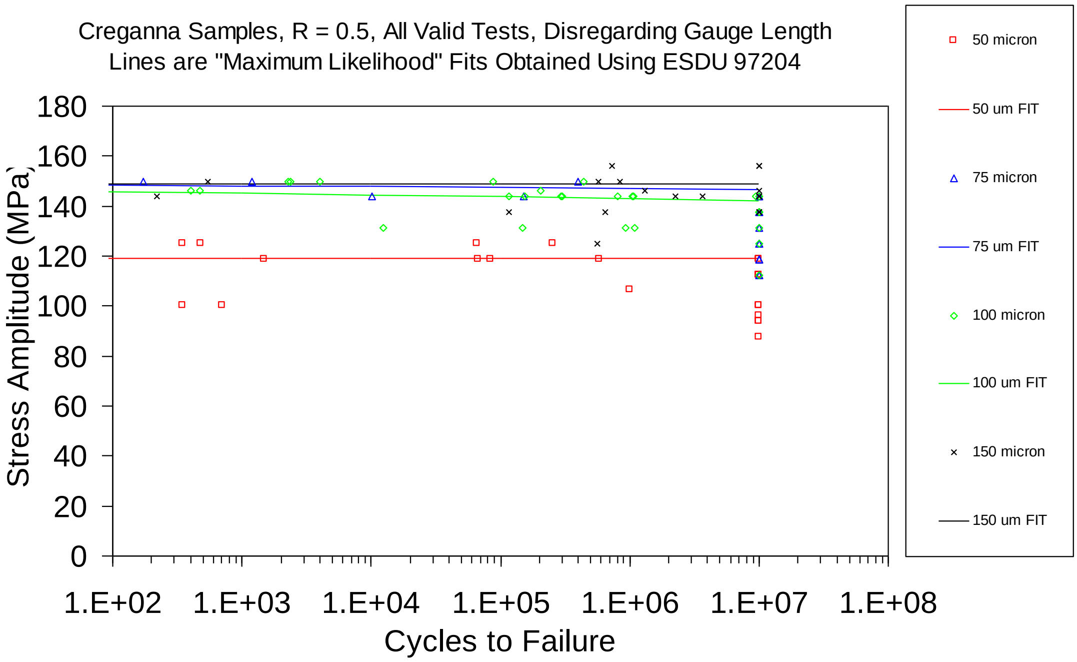

Figure 5.7. *S-N* curves for the different sample sizes generated by programme ESDU 9724.

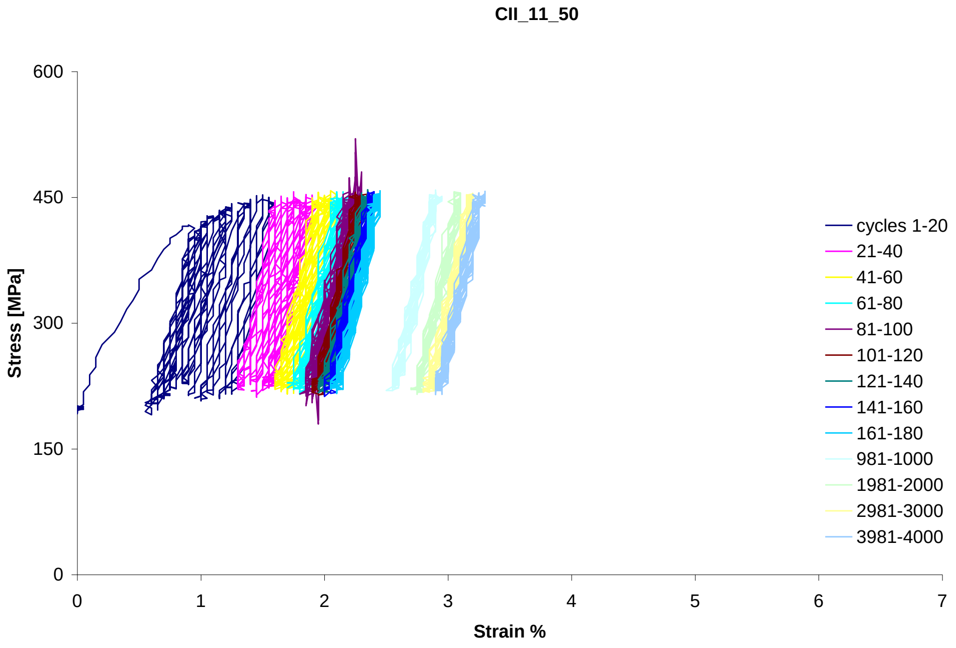

Figure 5.8. Hysteresis loop for a 50µm runout specimen, various cycles from 0 up to 4000. Each colour coded group contains 20 cycles.

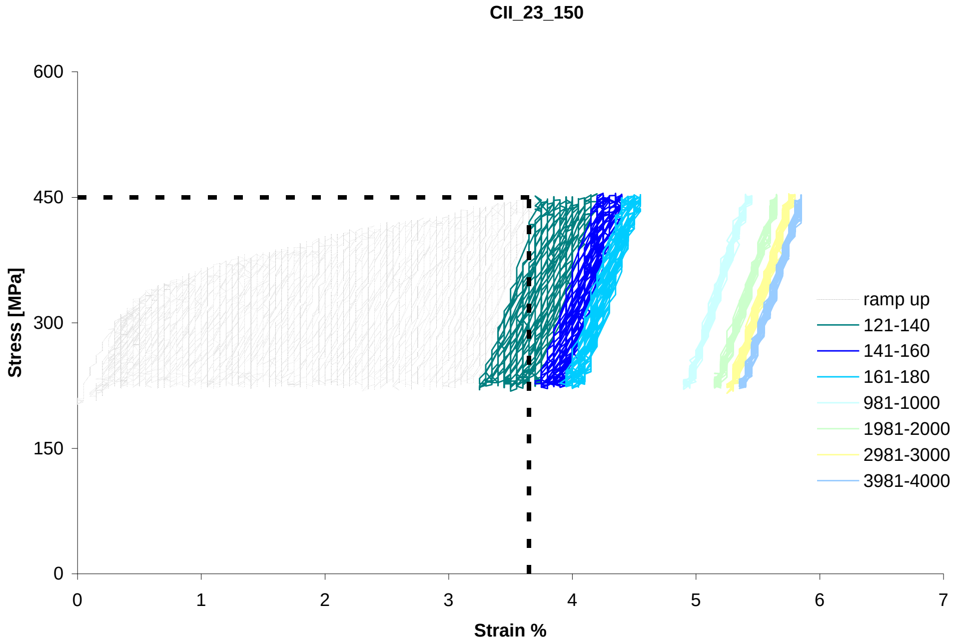

Figure 5.9. Hysteresis loop for a 150µm runout specimen, various cycles from 0 up to 4000. Each colour coded group contains 20 cycles. Ramp up period contained within dashed lined.

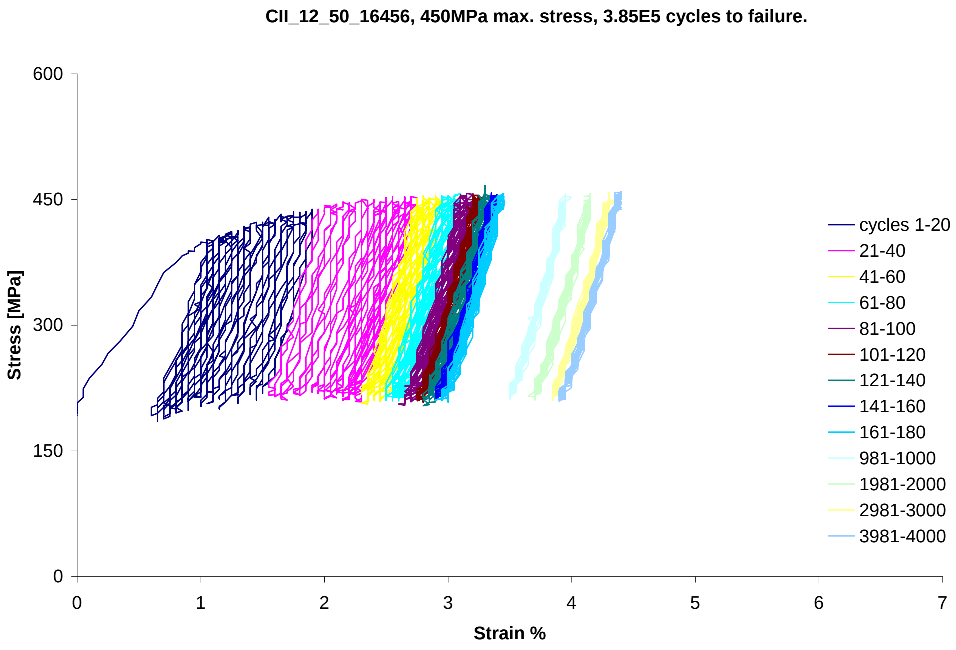

Figure 5.10. Hysteresis loop for a 50μm failed specimen, various cycles from 0 up to 4000. Each colour coded group contains 20 cycles (357,500 cycles to failure).

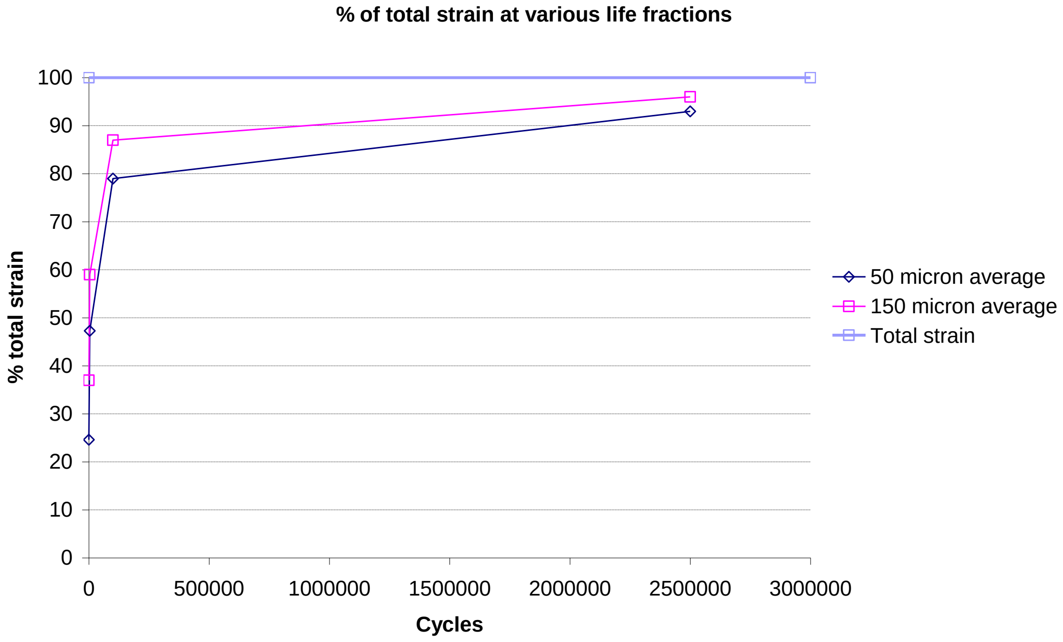

Figure 5.11. Graphical representation of strain values at various life fractions. Runout specimens only.

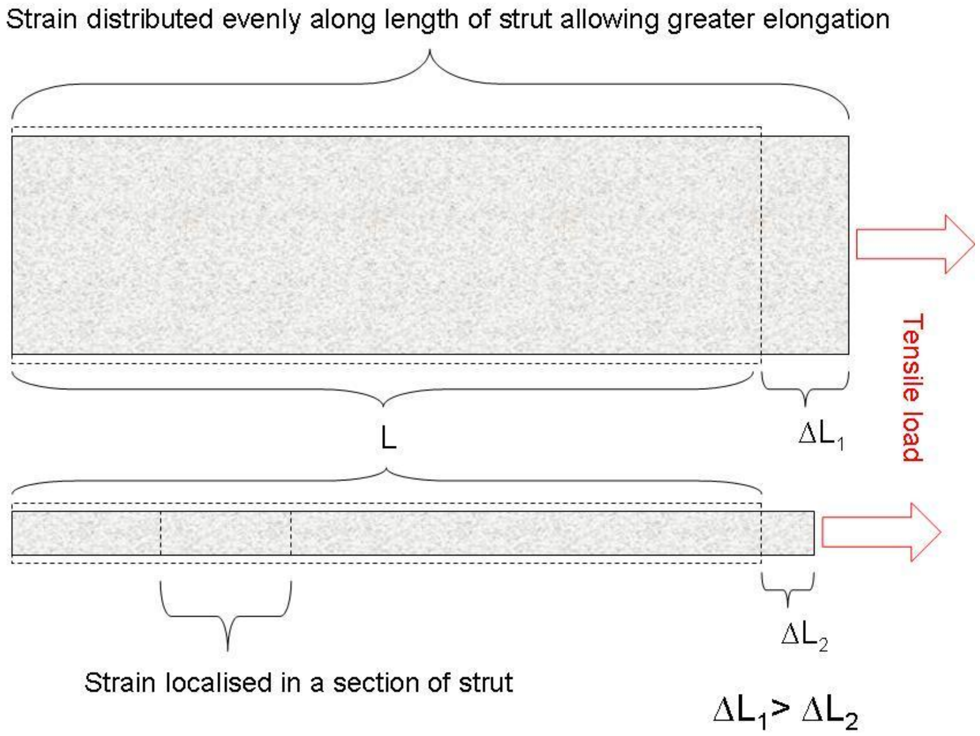

Figure 5.12. Large Vs small strut and a possible reason for differences in strain at different life fractions. Both strut have the same grain size, larger strut has higher grain size to specimen width ratio.

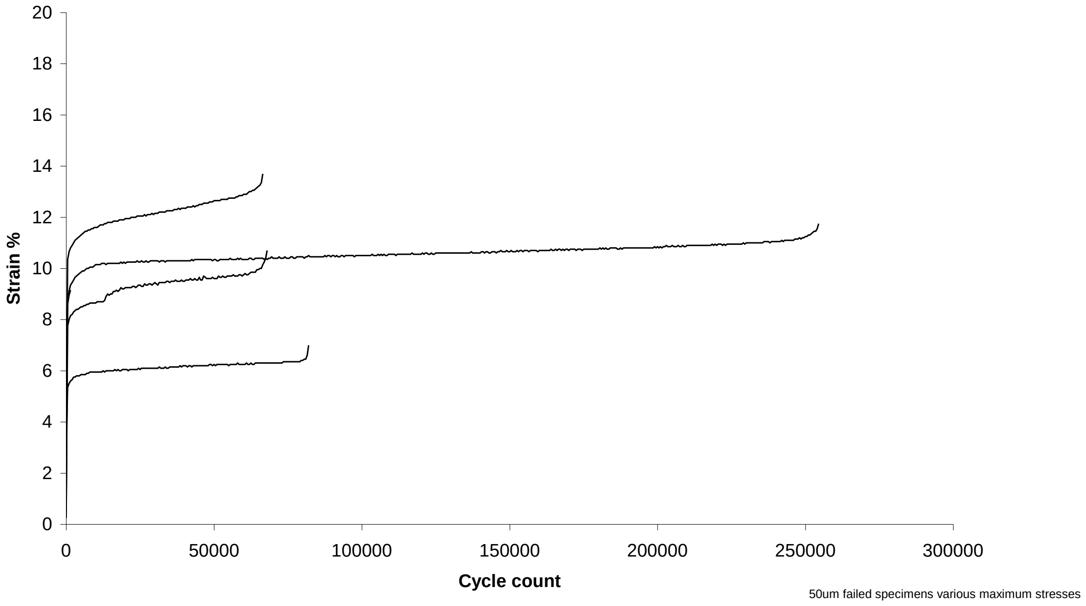

Figure 5.13. Strain accumulation data for failed 50µm specimens; various maximum

stresses. Abrupt changes in compliance are associated with a change in frequency of the applied load.

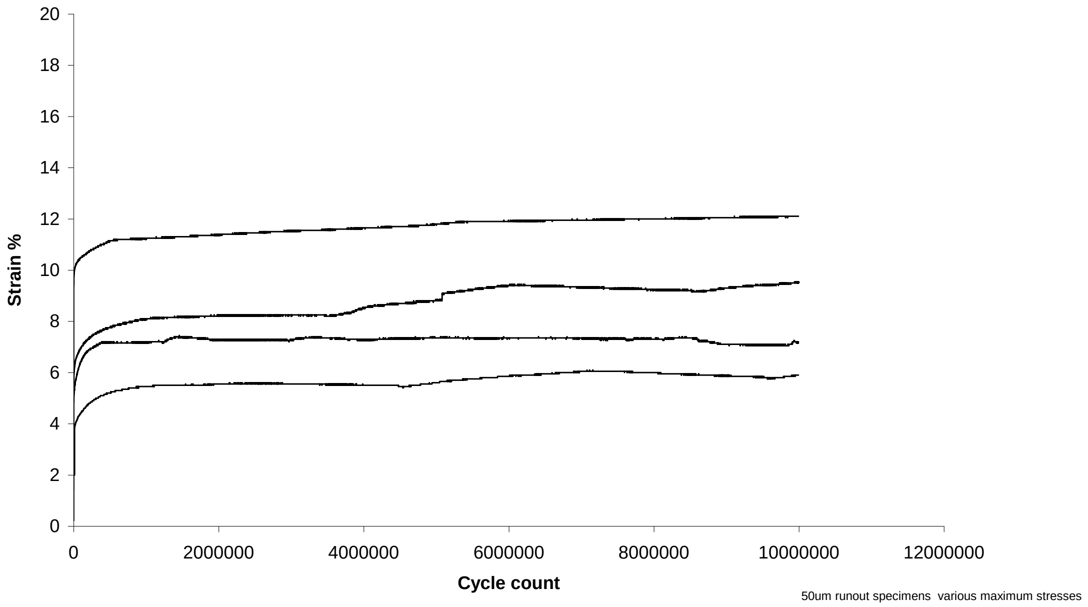

Figure 5.14. Strain accumulation data for runout 50 μm test specimens; various maximum stresses.

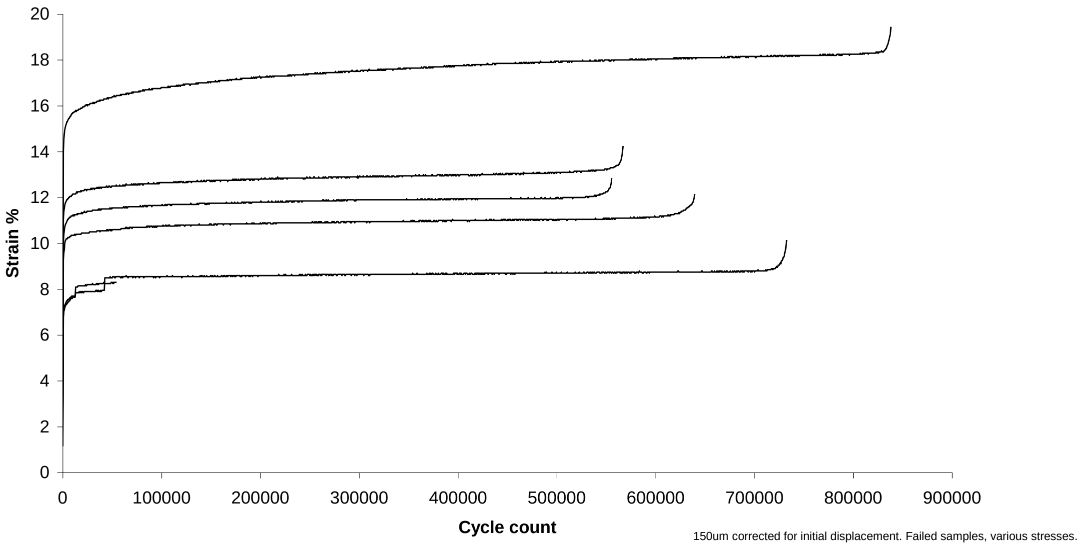

Figure 5.15. Strain accumulation data for failed 150 μm test specimens, various maximum stresses.

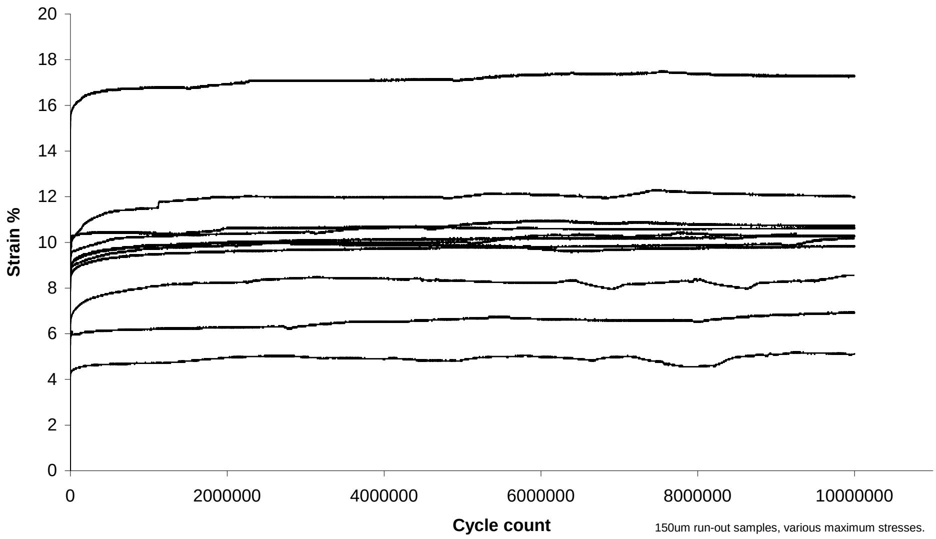

Figure 5.16. Strain accumulation data for runout 150 µm test specimens, various maximum stresses.

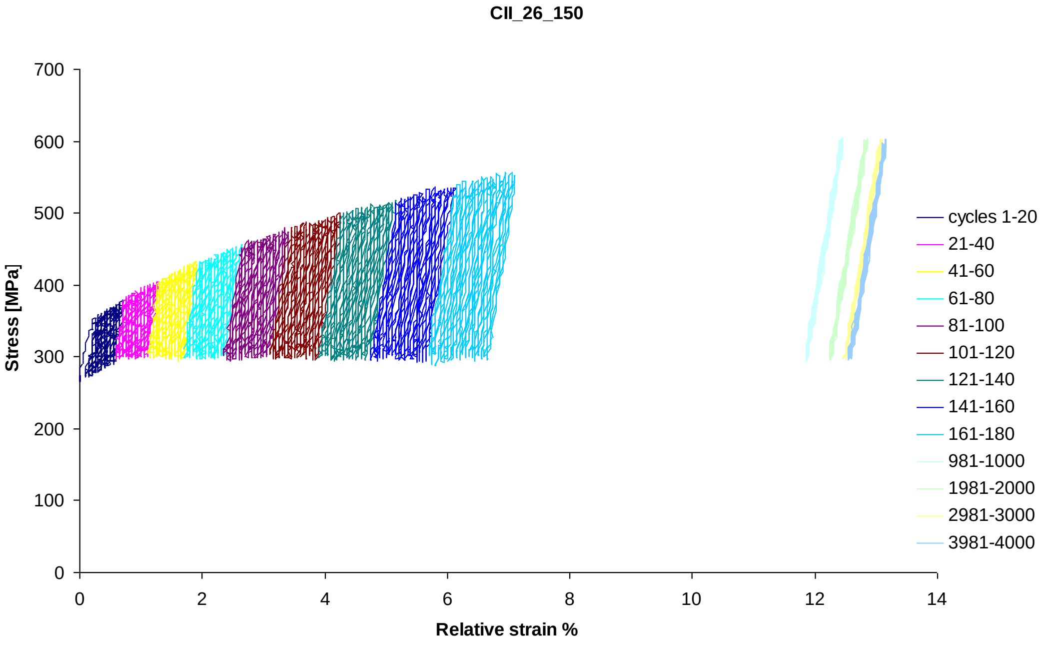

(a)

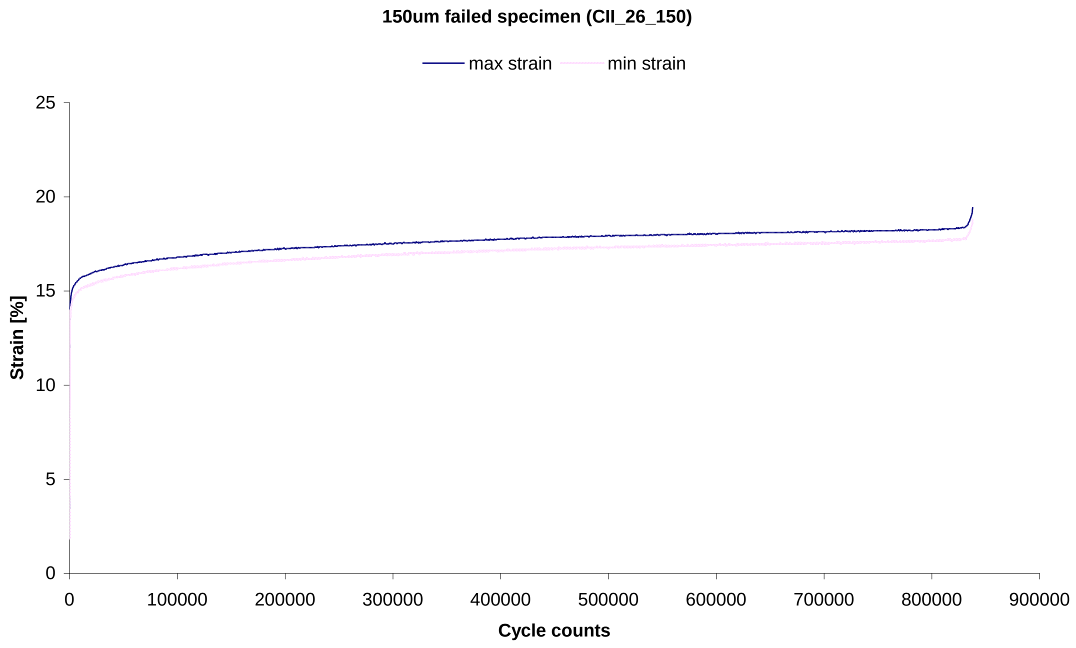

(b)

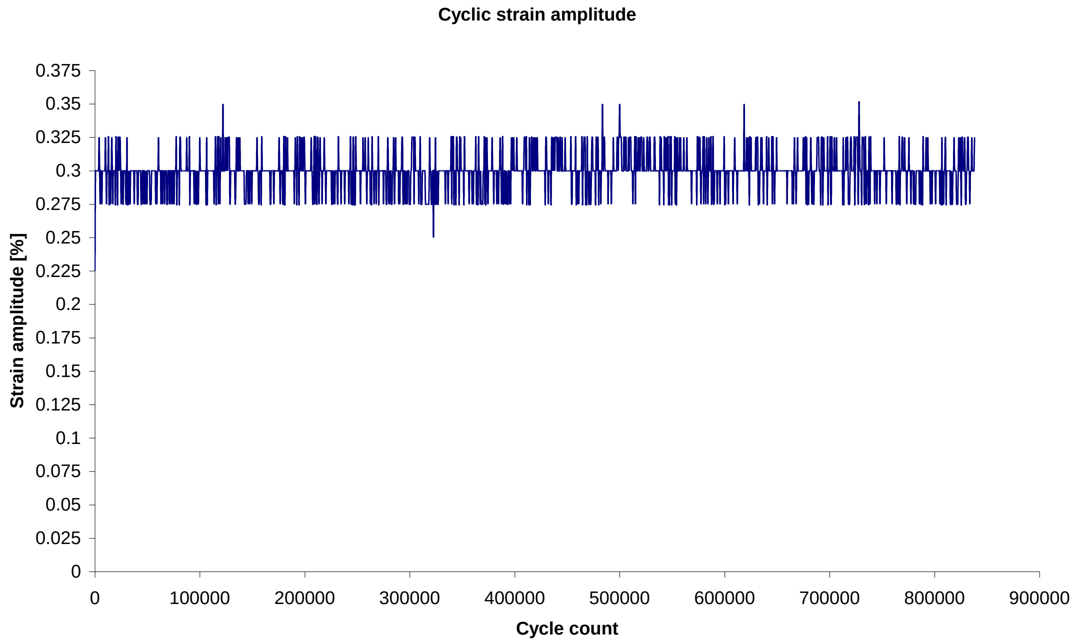

(c)

Figure 5.17. (a) Hysteresis loop for a 150μm failed specimen, various cycles from 0 to 4000. Each colour coded group contains 20 cycles (b) pvf (strain history) data for the same specimen (838,000 cycles to failure). (c) Strain amplitude.

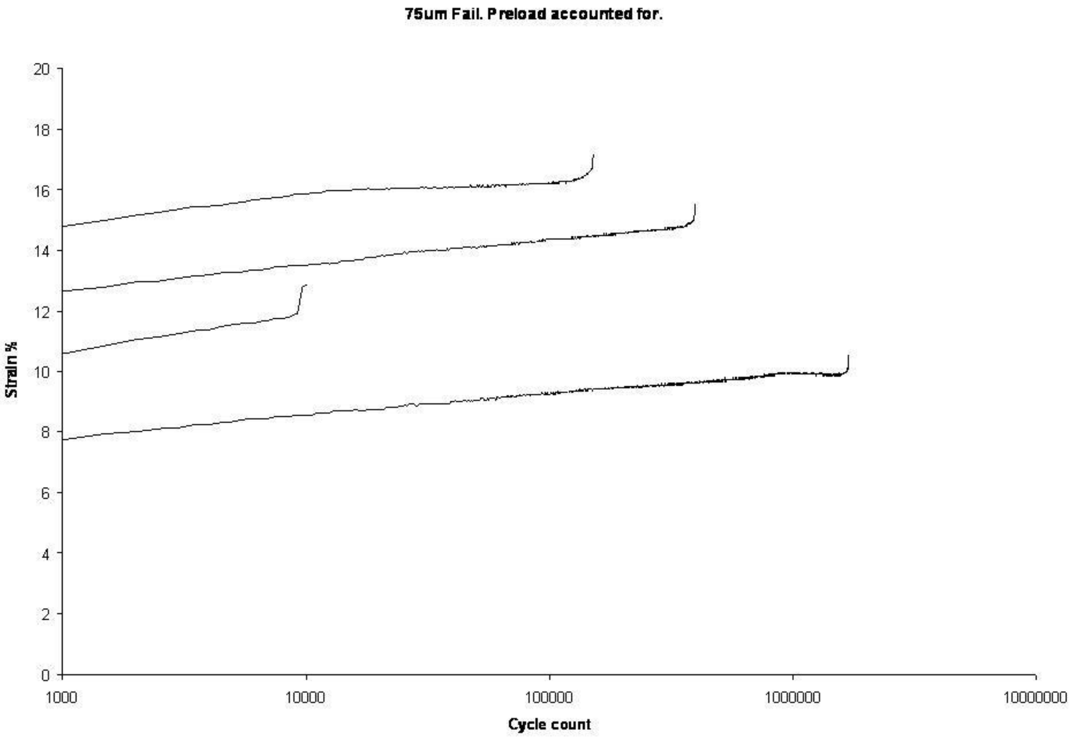

(a)

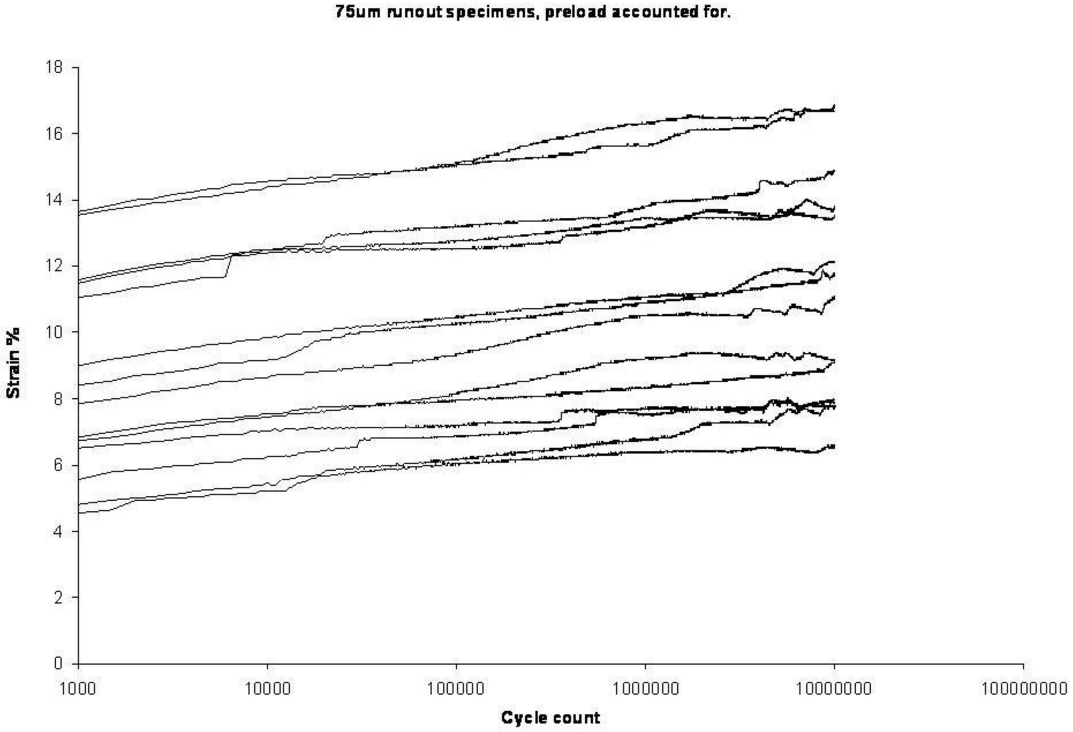

(b)

Figure 5.18. (a) .pvf data for failed 75 μm specimens, various maximum stresses (b) .pvf data for runout 75 μm specimens, various maximum stresses.

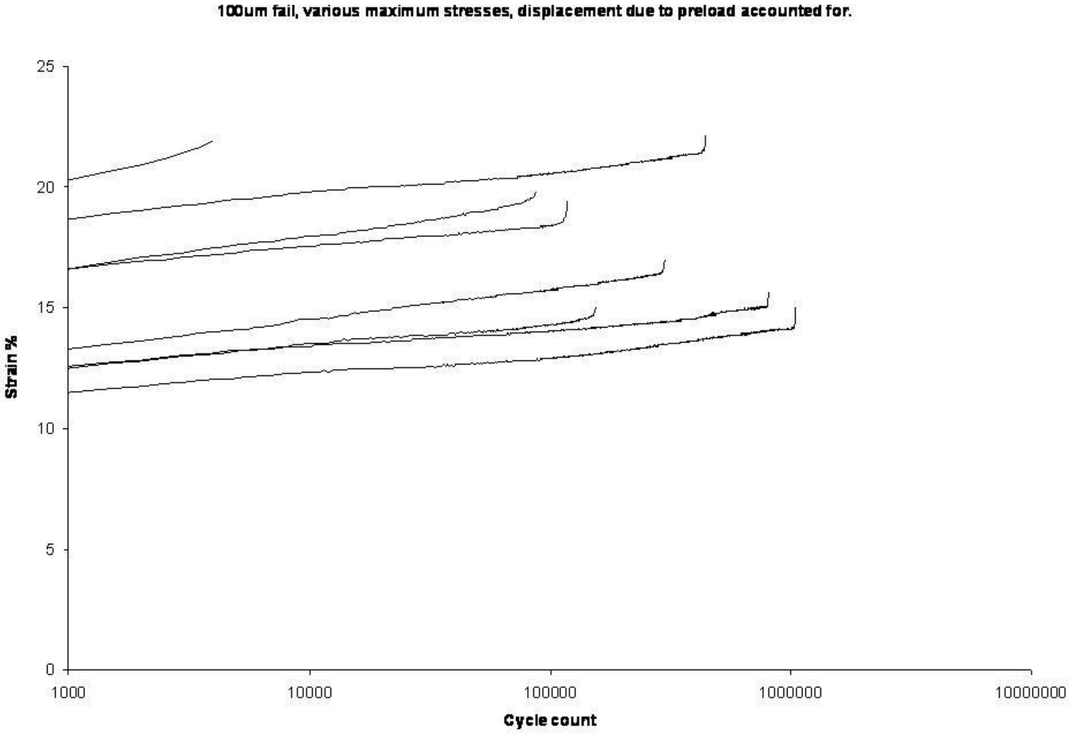

(a)

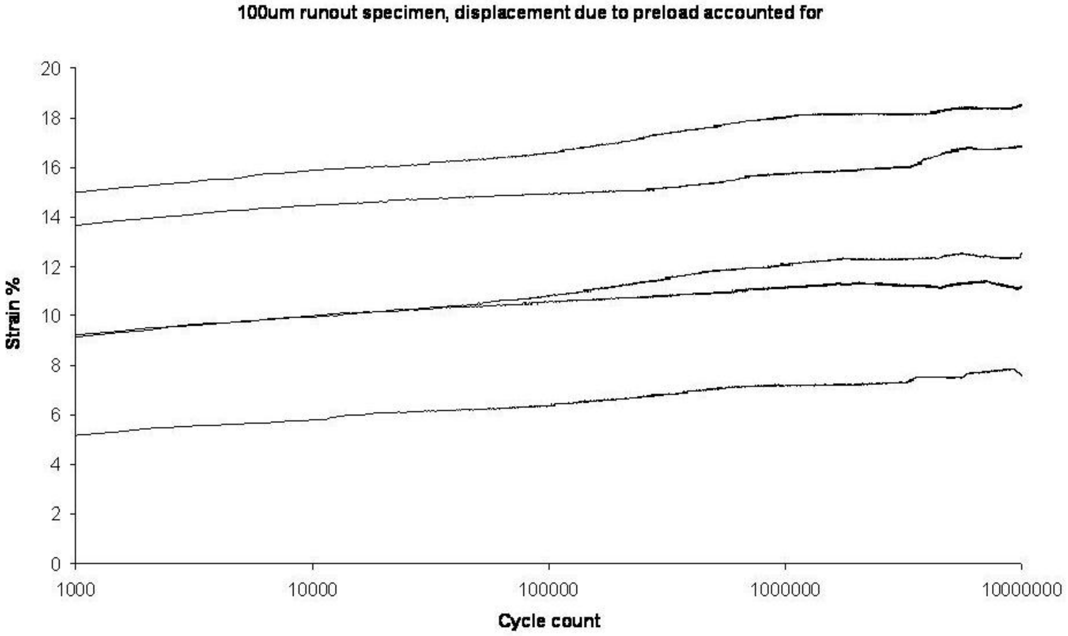

(b)

Figure 5.19. (a) .pvf data for failed 100 μm specimens, various maximum stresses (b) .pvf data for runout 100 μm specimens, various maximum stresses.

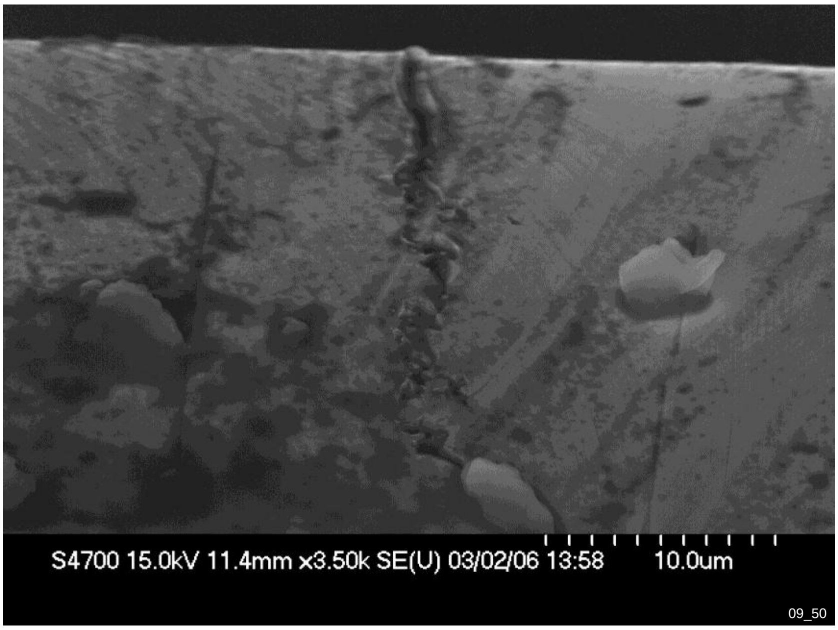

Figure 5.20. Possible fatigue crack observed on the surface of a 50μm runout specimen 09_50.

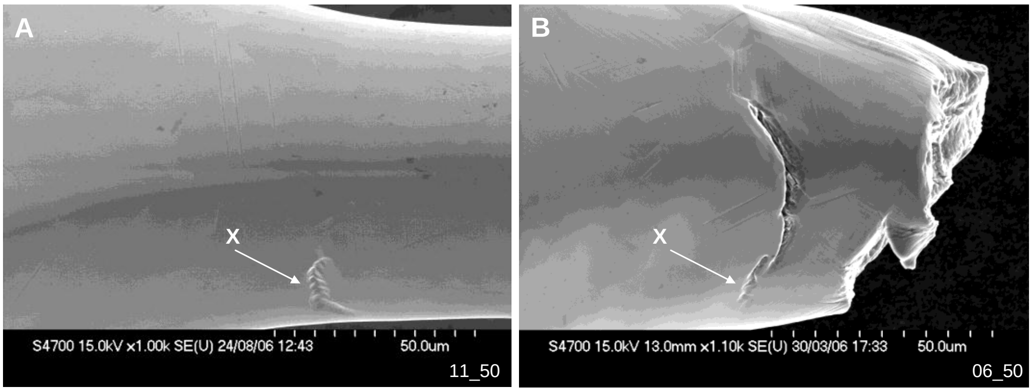

Figure 5.21. A feature (marked X on A) on a 50μm runout specimen which is similar to a large crack identified on a failed 50μm specimen (marked X on B).

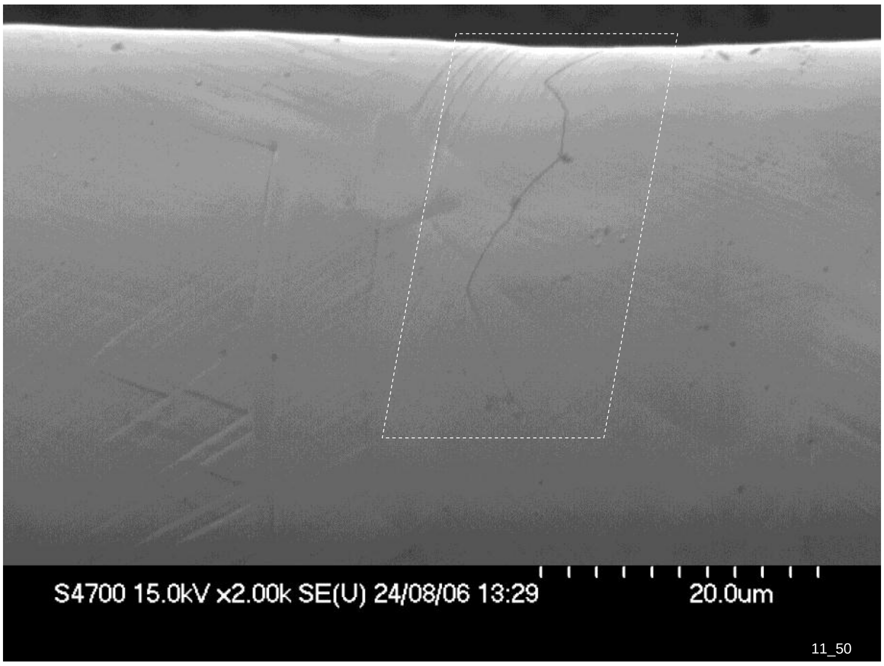

Figure 5.22. Possible crack observed on the surface of a 50μm runout specimen 11_50.

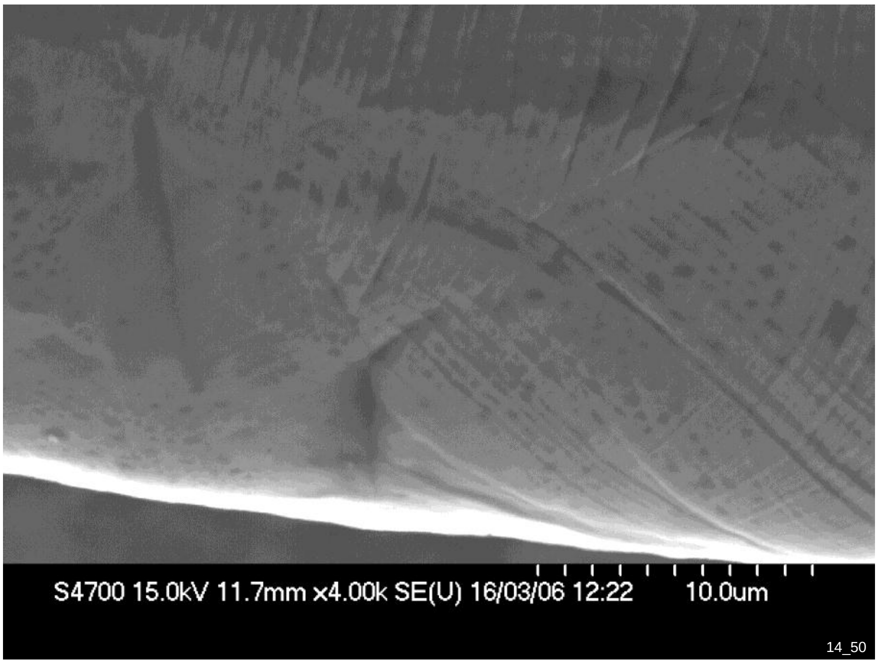

Figure 5.23. Deep fissures occurring on the surface of a runout 50μm specimen 14_50 as a result of plastic deformation.

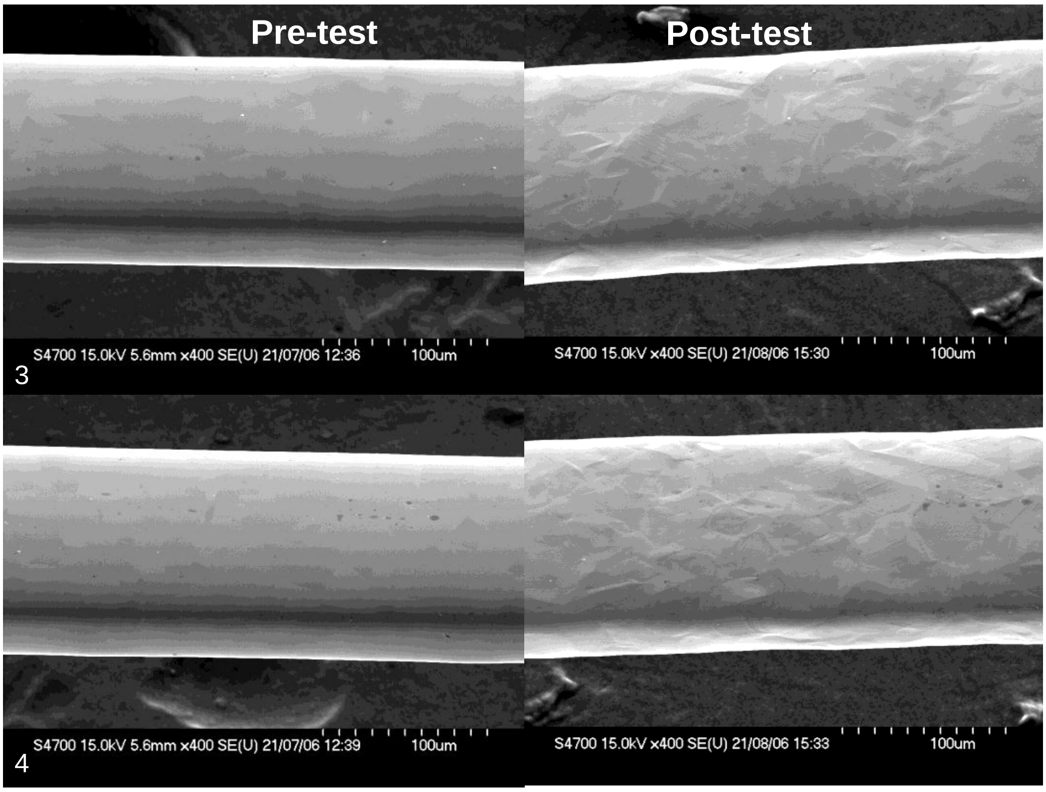

Figure 5.24. An example of the plastic deformation that results when a 150 μm specimen is fatigue tested at a maximum stress of 450 MPa for 10^7 cycles.

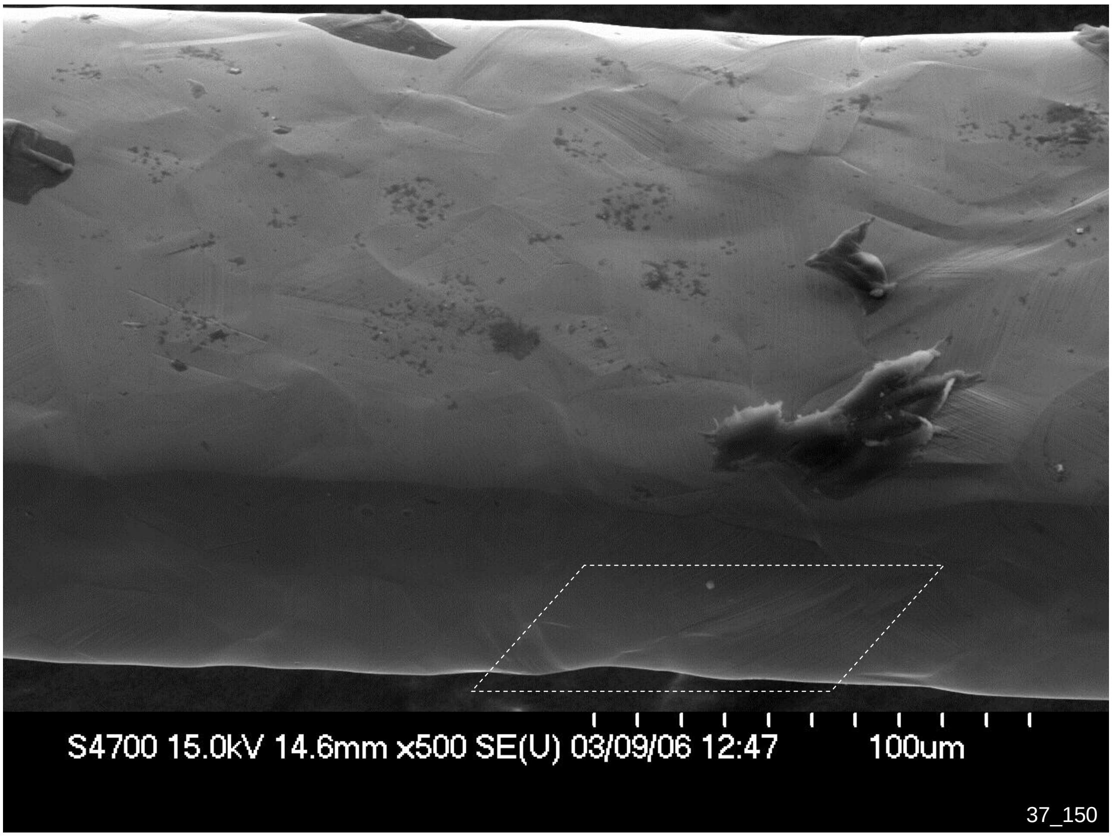

Figure 5.25. A thickness related deformation feature (highlighted) on a 150 μm specimen.

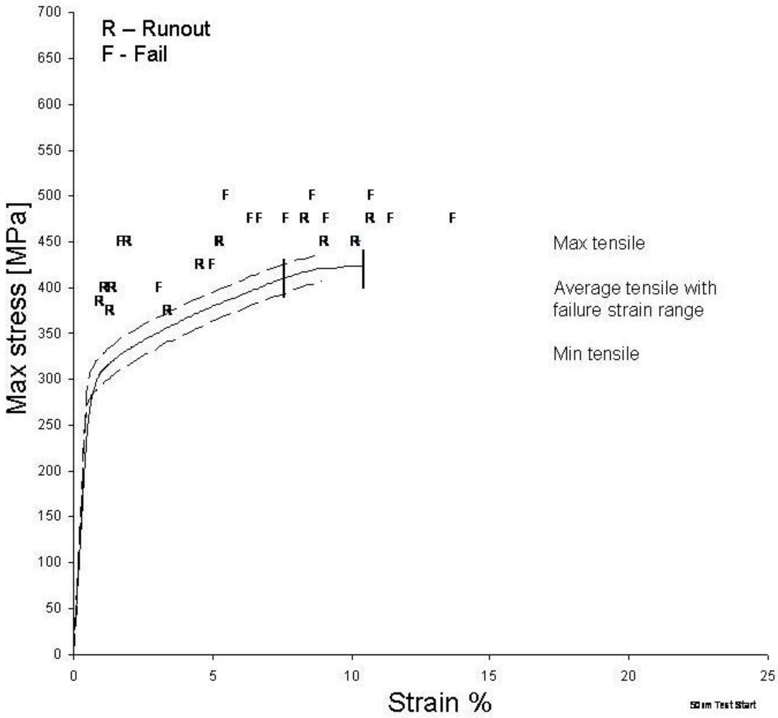

(a)

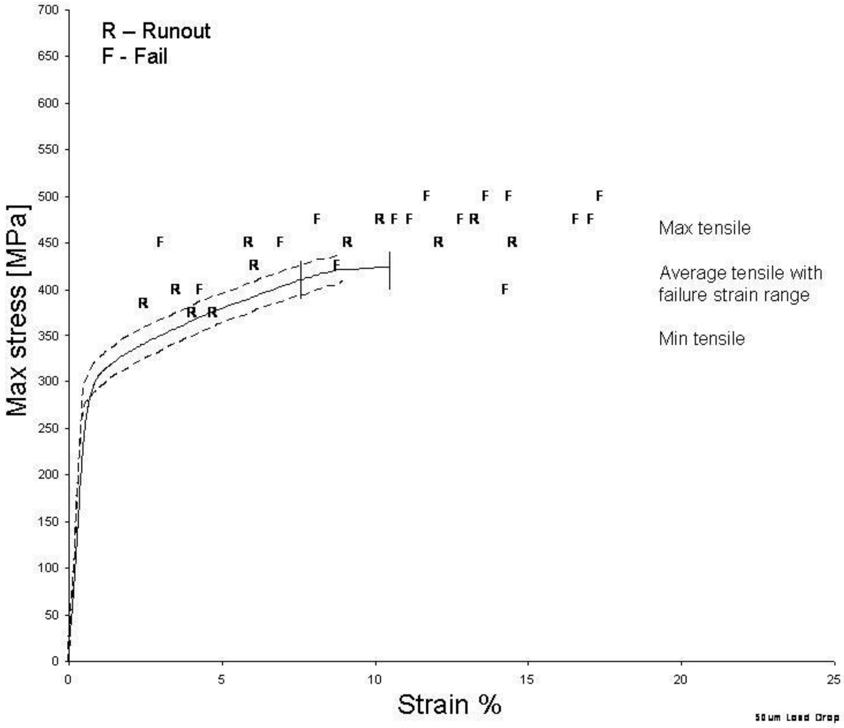

(b)

Figure 5.26 (a) “test start” fatigue strain and tensile strain comparison, 50 µm specimens and (b) “load drop and runout” fatigue strain and tensile strain comparison.

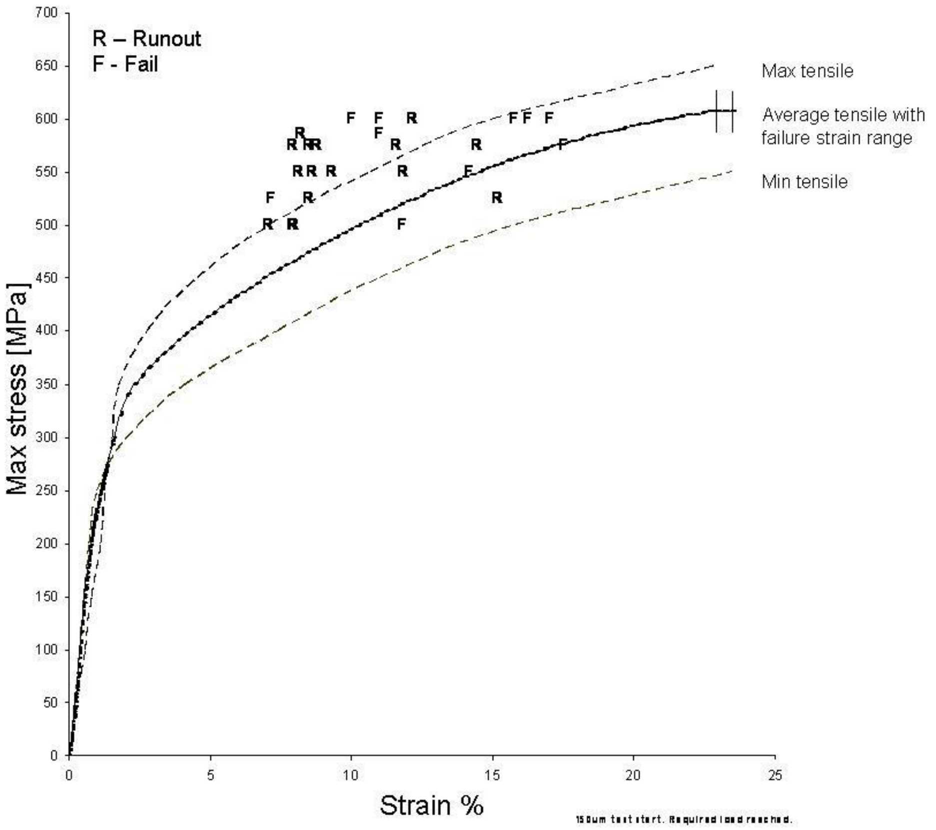
R – Runout
F - Fail
Max tensile
Average tensile with failure strain range
Min tensile
Max stress [MPa]
Strain %
0
50
100
150
200
250
300
350
400
450
500
550
600
650
700
0
5
10
15
20
25
150um test start. Required load reached.

(a)

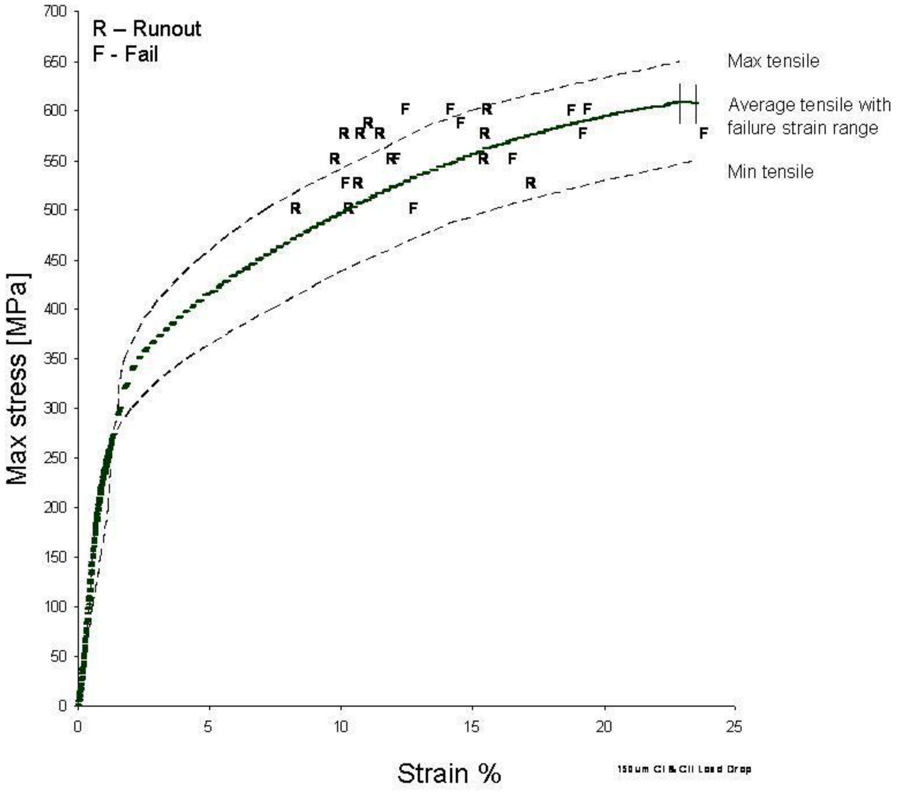
R – Runout
F - Fail
Max tensile
Average tensile with failure strain range
Min tensile
Max stress [MPa]
Strain %
0
50
100
150
200
250
300
350
400
450
500
550
600
650
700
0
5
10
15
20
25
150um CI & CII Load Drop

(b)

Figure 5.27 (a) “test start” fatigue strain and tensile strain comparison, 150 µm specimens and (b) “load drop and runout” fatigue strain and tensile strain comparison.

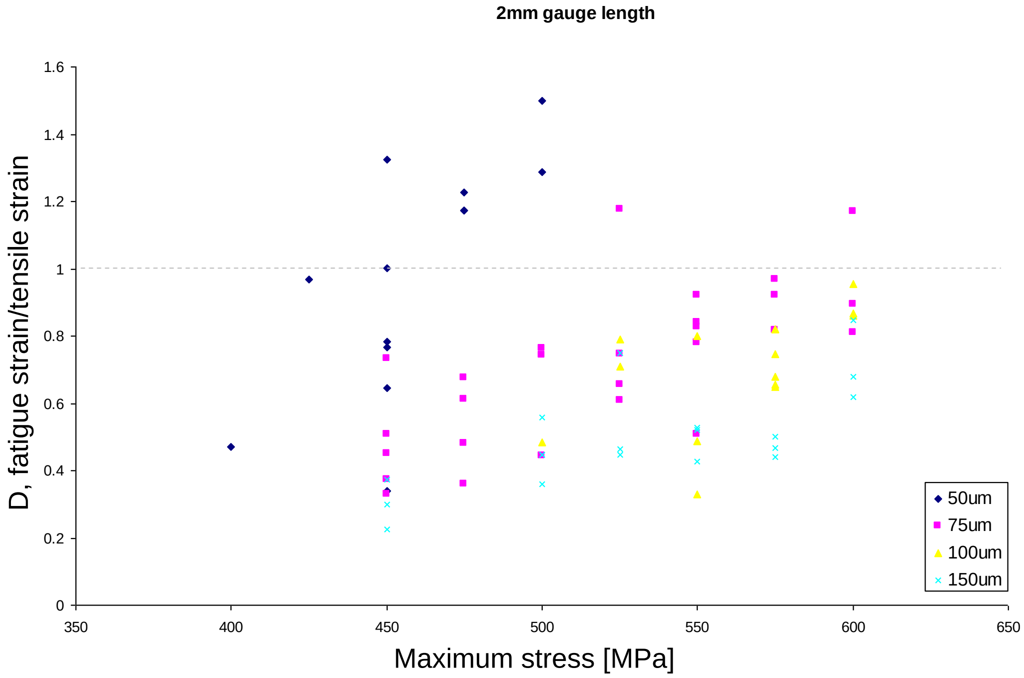

Figure 5.28. Ductility exhaustion study, all specimens. Dashed grey line indicates D=1, where fatigue strain = tensile strain.

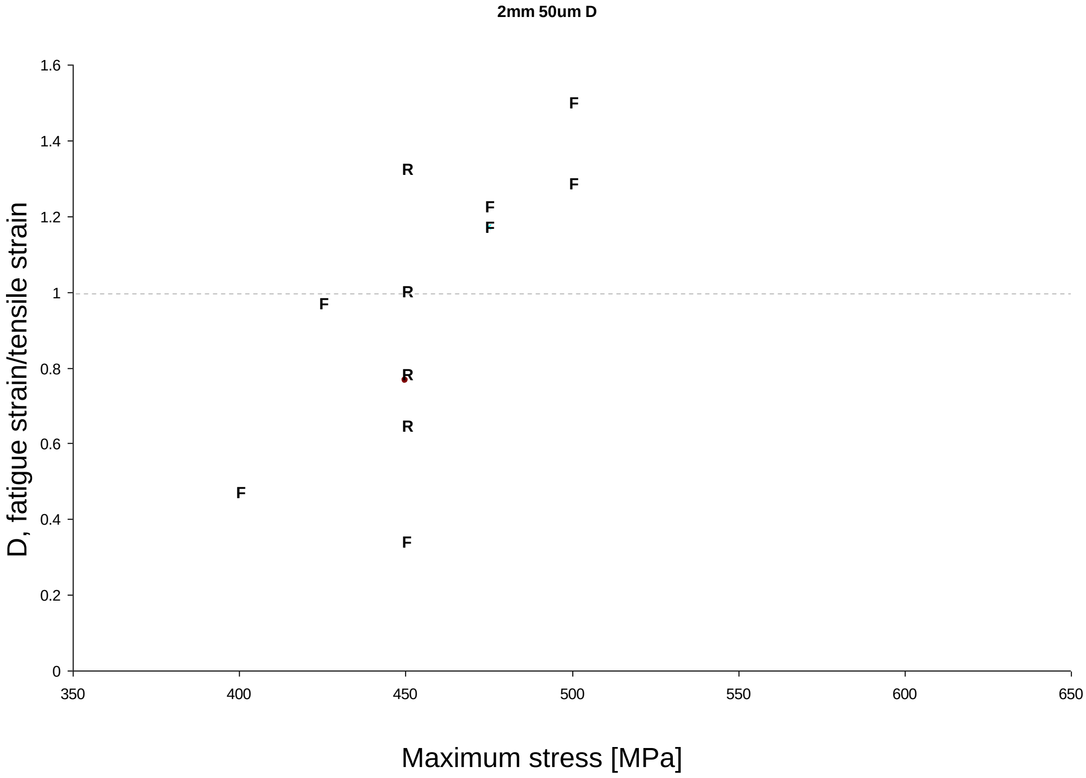

(a)

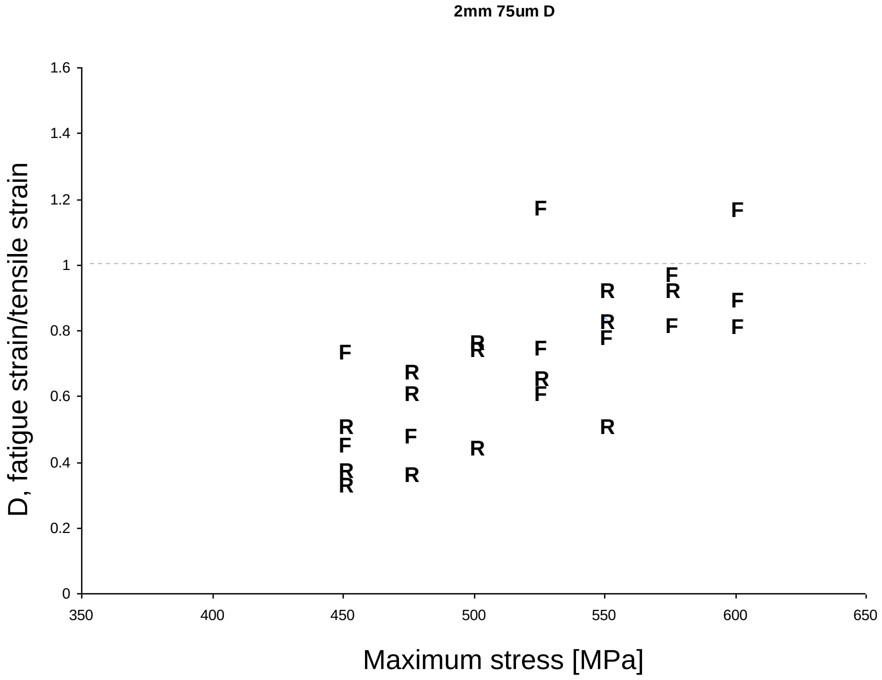
2mm 75um D
D, fatigue strain/tensile strain
Maximum stress [MPa]
0
0.2
0.4
0.6
0.8
1
1.2
1.4
1.6
350
400
450
500
550
600
650
F
R

(b)

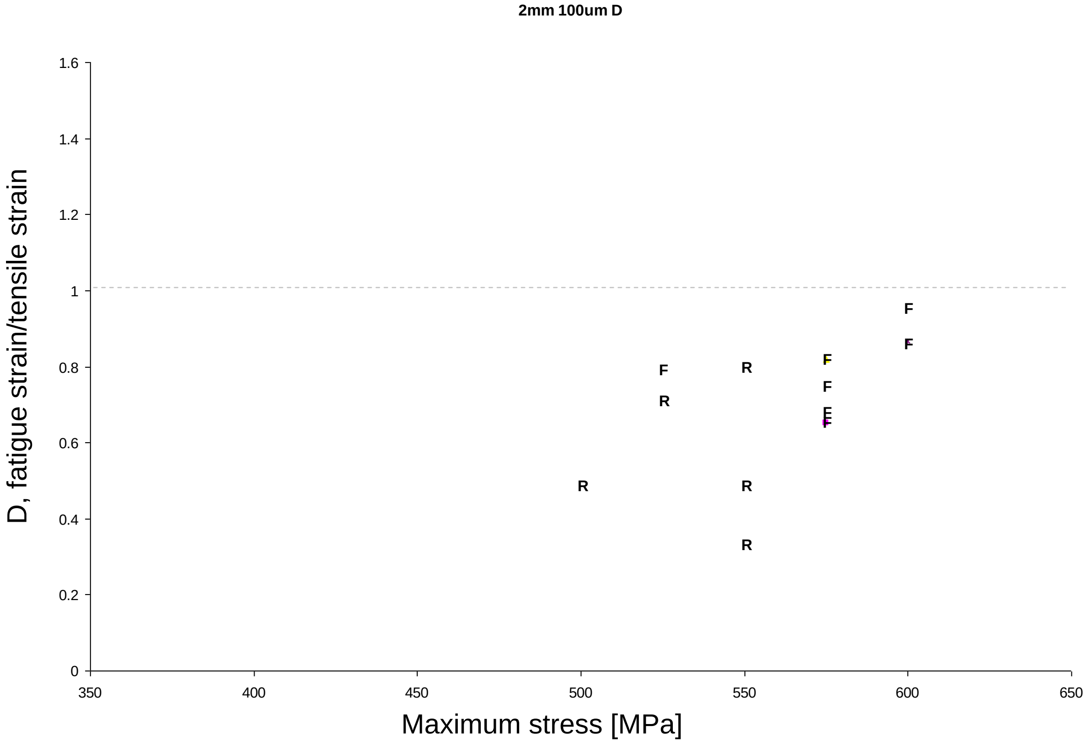
2mm 100um D
D, fatigue strain/tensile strain
Maximum stress [MPa]
0
0.2
0.4
0.6
0.8
1
1.2
1.4
1.6
350
400
450
500
550
600
650
F
R

(c)

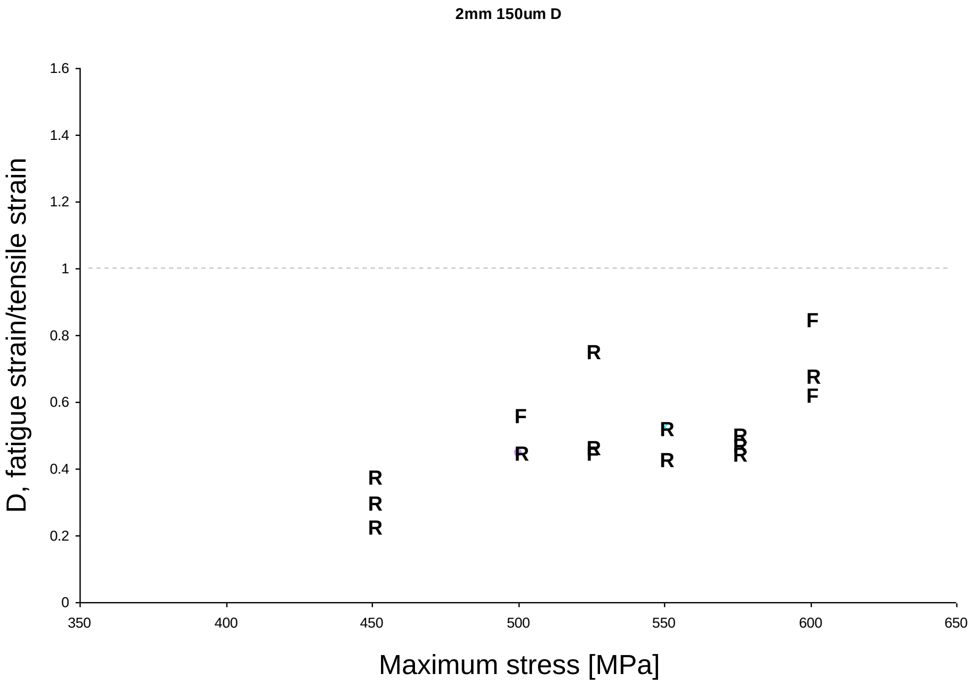

(d)

Figure 5.29. Ductility exhaustion study for (a) 50 µm, (b) 75 µm, (c) 100 µm and (d) 150 µm. Dashed grey line indicates D=1, where fatigue strain = tensile strain. R=runout, F=failure.

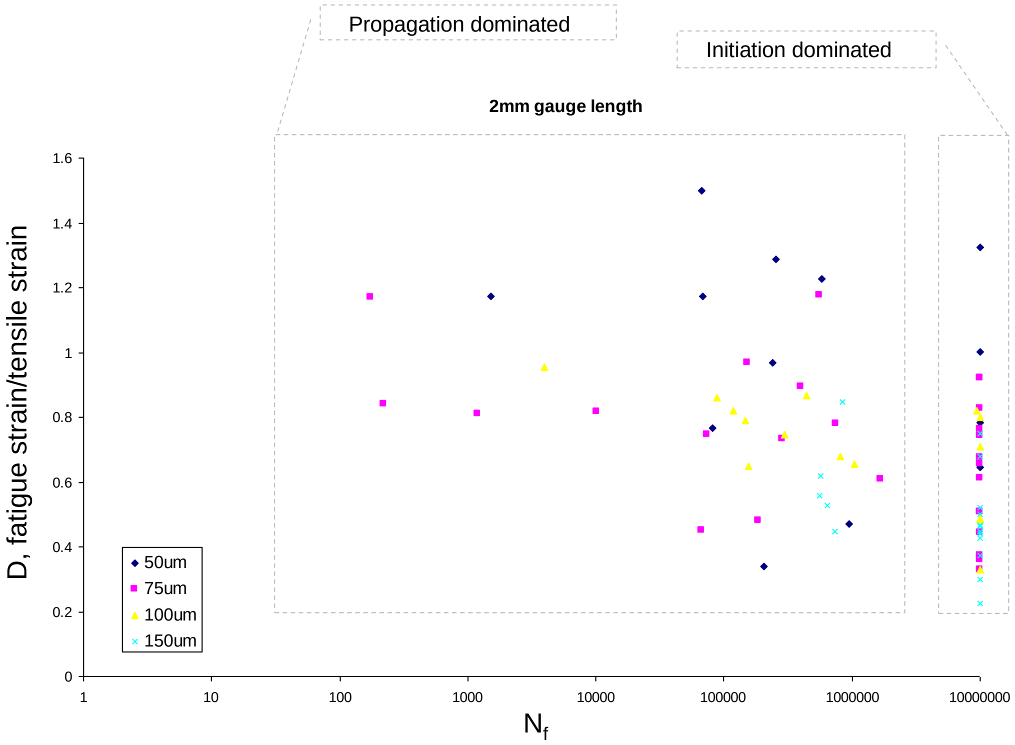

Figure 5.30. Simple classification of test specimens into propagation dominated and initiation dominated regimes.

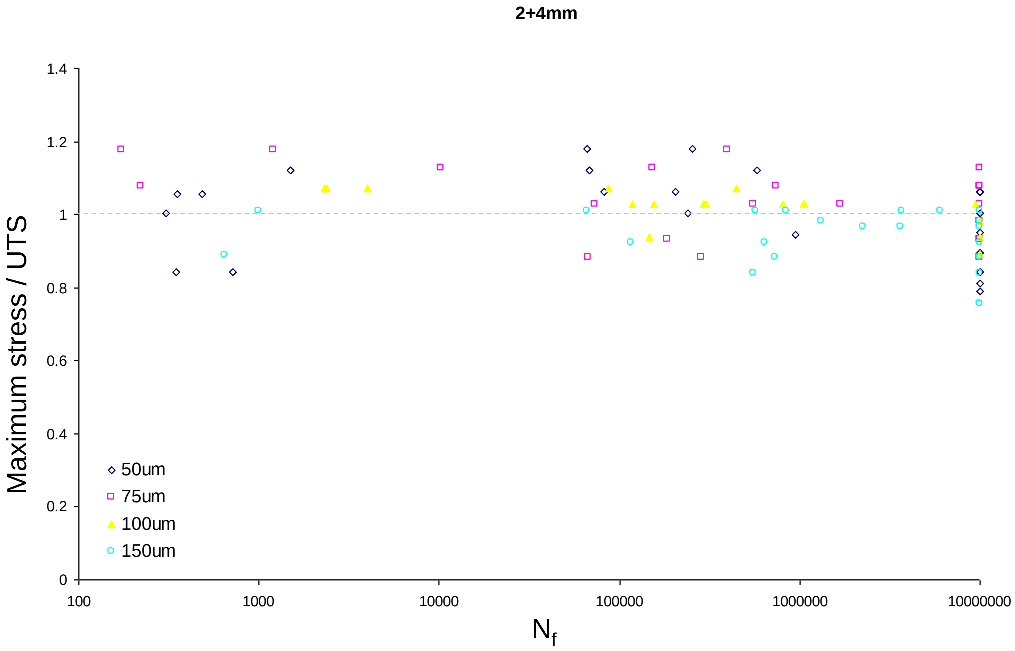

(a)

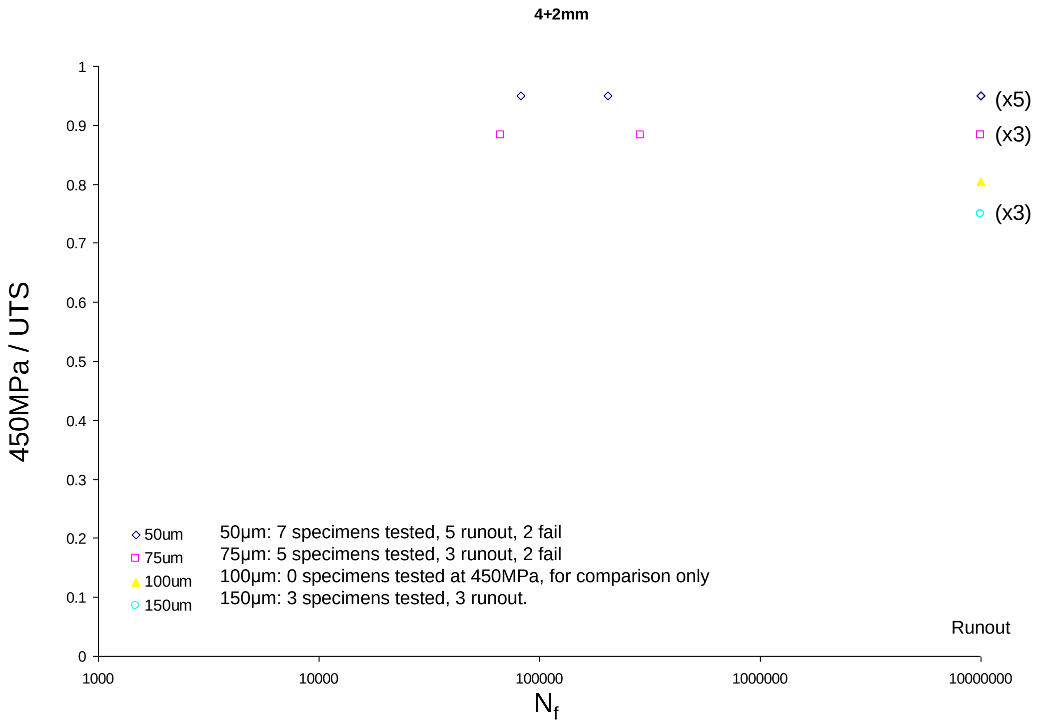
4+2mm
450MPa / UTS
1
0.9
0.8
0.7
0.6
0.5
0.4
0.3
0.2
0.1
0
(x5)
(x3)
(x3)
◇ 50um
□ 75um
▲ 100um
○ 150um
50µm: 7 specimens tested, 5 runout, 2 fail
75µm: 5 specimens tested, 3 runout, 2 fail
100µm: 0 specimens tested at 450MPa, for comparison only
150µm: 3 specimens tested, 3 runout.
Runout
1000
10000
100000
1000000
10000000
N_f

(b)

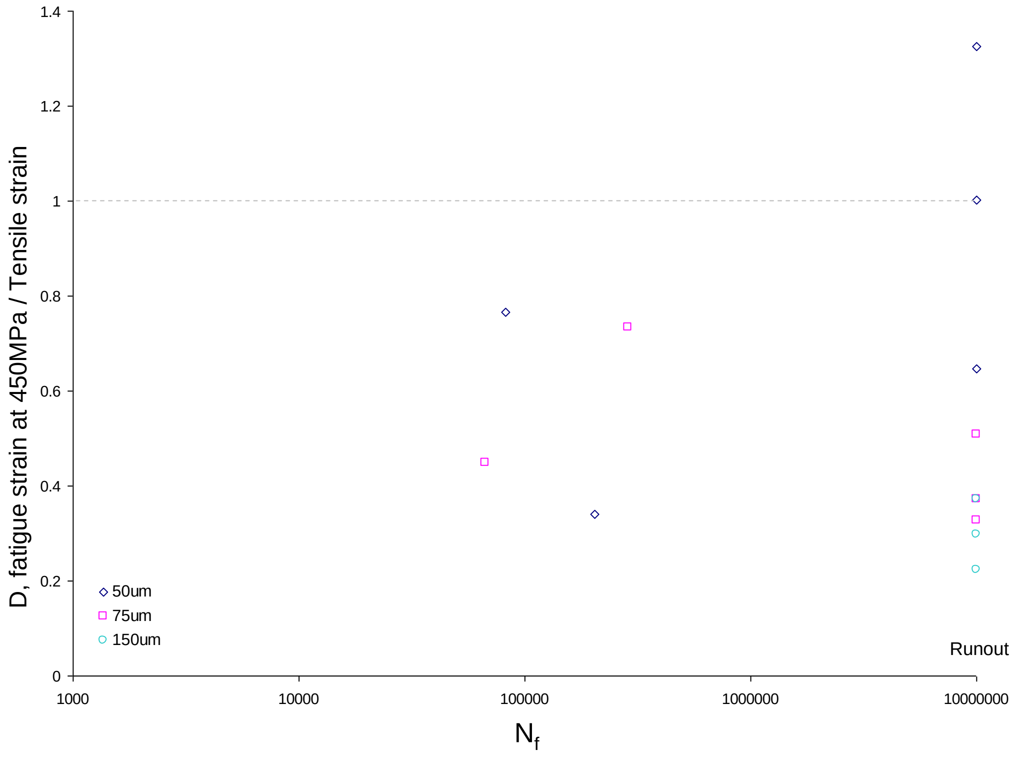
D, fatigue strain at 450MPa / Tensile strain
1.4
1.2
1
0.8
0.6
0.4
0.2
0
◇ 50um
□ 75um
○ 150um
Runout
1000
10000
100000
1000000
10000000
N_f

(c)

Figure 5.31. A comparison of maximum stress and ultimate tensile stress for (a) all specimens (b) specimens tested at a maximum stress of 450MPa, (c) corresponding ductility exhaustion plot for specimens tested at 450MPa.

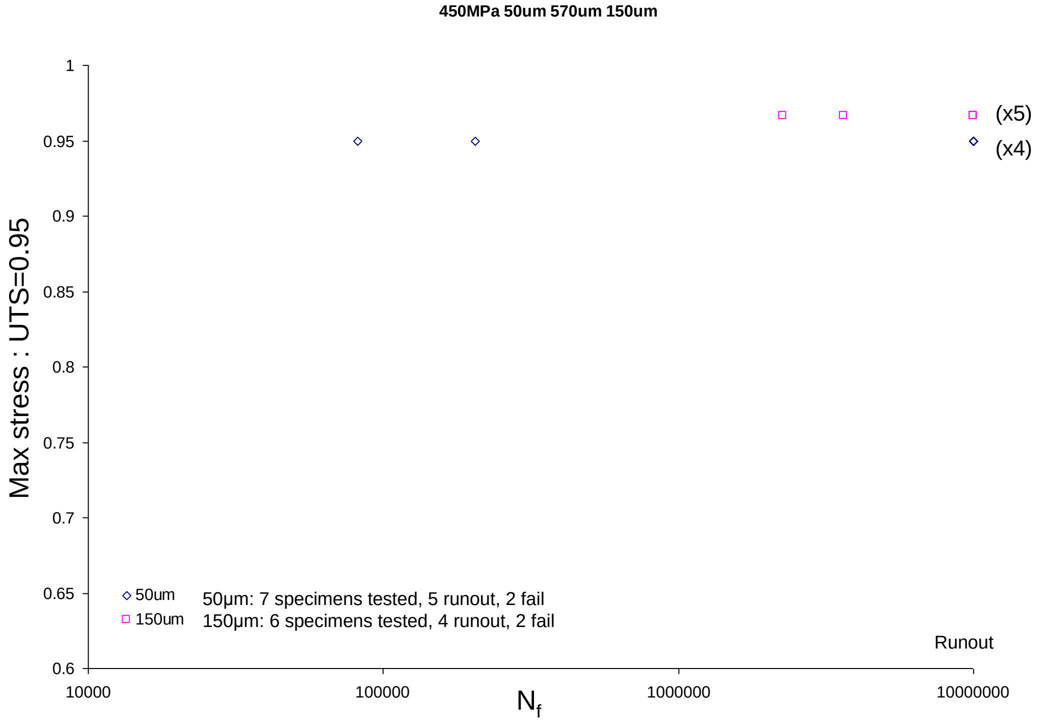

(a)

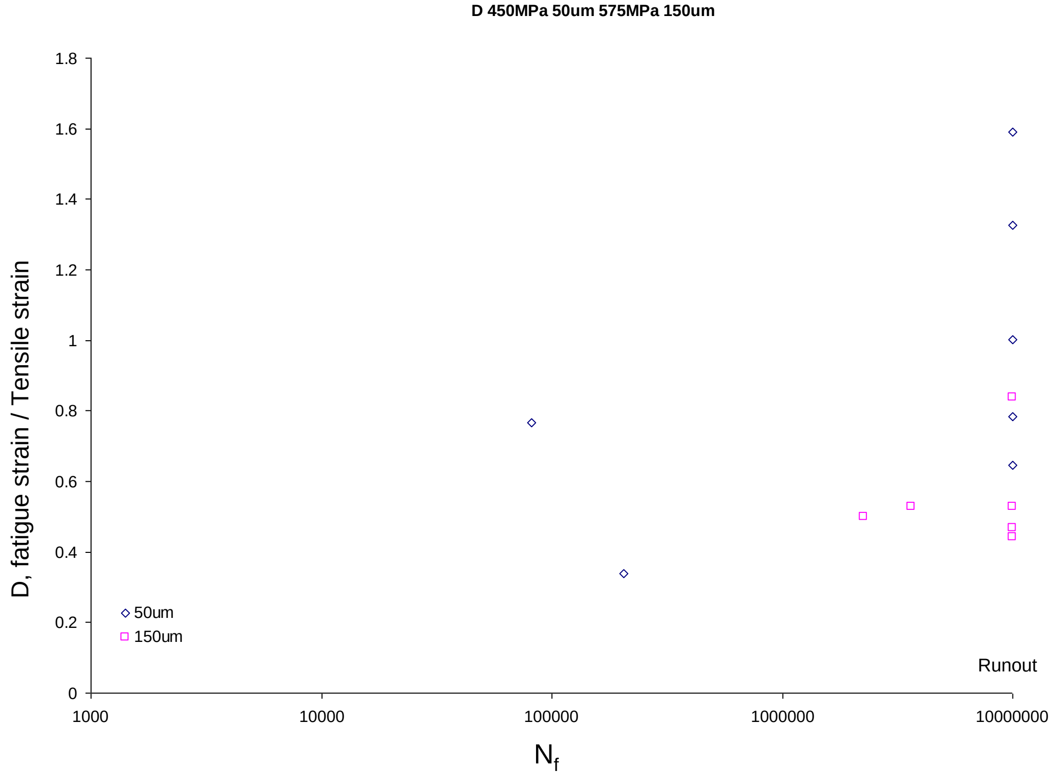

(b)

Figure 5.32(a) common normalization factor for 50 µm and 150 µm specimens, (b) associated strain values normalized with UTS.

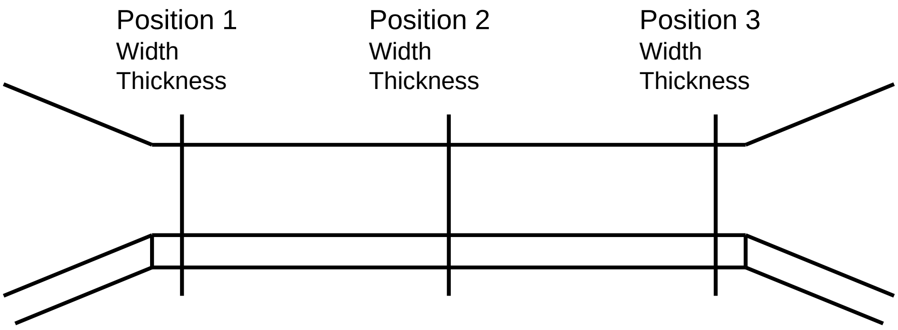

Figure 5.33. Location of width and thickness measurements as taken by specimen manufacturer. Position 1 is given by the first width and thickness measurement, position 2 by the second etc.

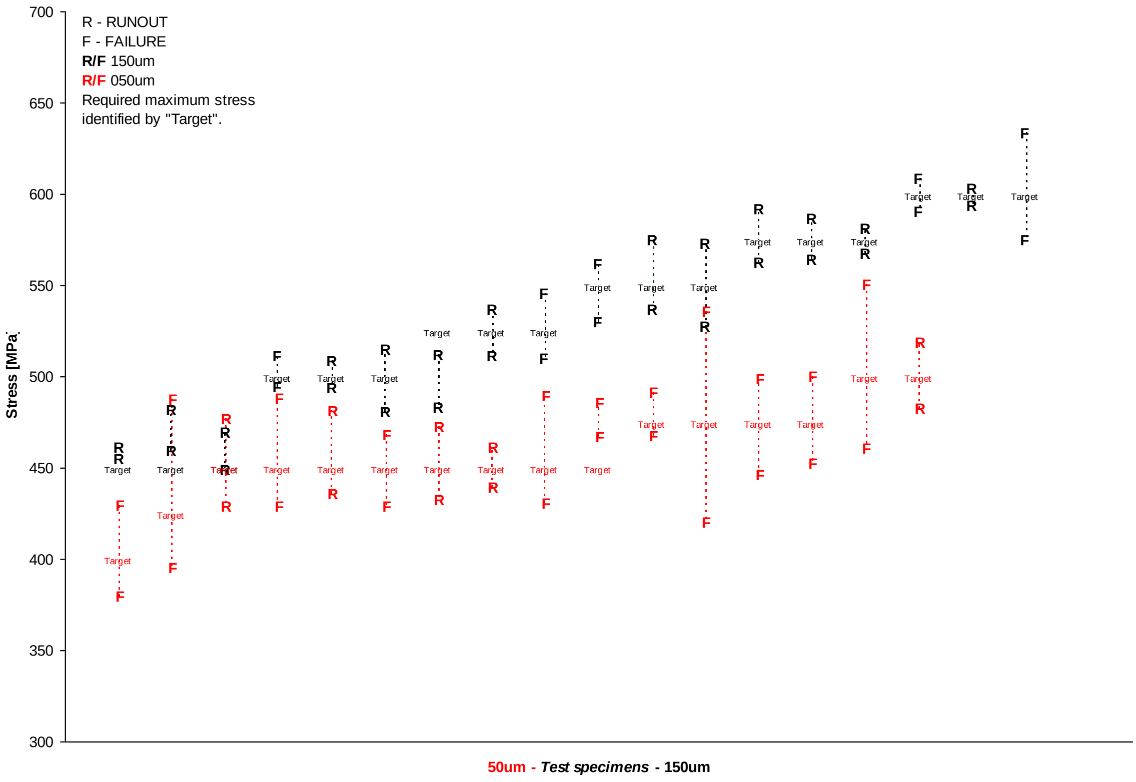

Figure 5.34. The effect of variation in CSA on maximum stress. 150 µm and 50 µm max/min stresses in sample at maximum load. Differences due to variations in CSA of specimens. CSA calculated at three points along gauge length and highest and lowest values selected.

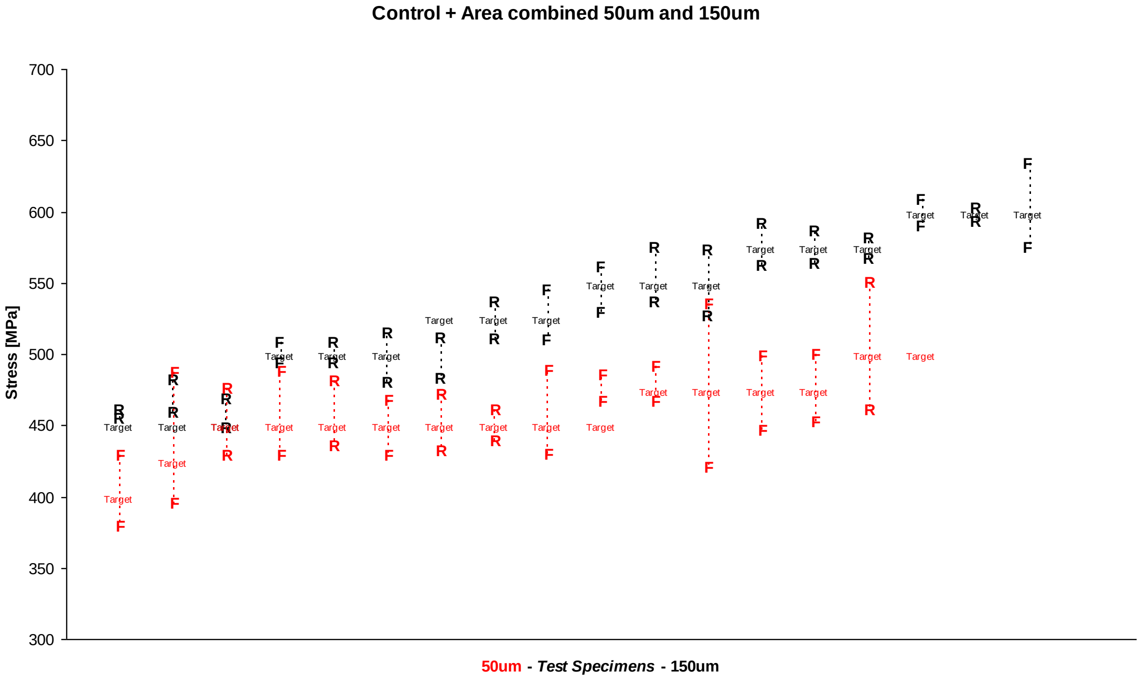

Figure 5.35. The combined effects of reduced area and increased load on the maximum stress within the test specimens.

SURFACE ANALYSIS AND FRACTOGRAPHY

6.1. Micrographic analysis of strain localization

Fatigue cracks normally initiate at the surface of a component. In an effort to determine the factors contributing to the size effect, the surfaces of various runout specimens were examined with the aid of a Scanning Electron Microscope. The micrographic examination focussed on attempting to identify differences in the distribution of plastic strain in the different specimen sizes. As the grain size to specimen width ratio is reduced, so too is the level of constraint experienced by individual grains within test specimens. In a process known as strain localization, softer regions, composed of more favourably orientated grains accumulate more plastic strain than less favourably orientated regions within the same specimen. The effects of strain localization will be evident on the surface of the test specimens, where grains experience the least constraint.

6.1.1. Micrographic surface examination of untested specimens

Test specimens have been laser cut from medical grade stainless steel tubing and subjected to medical grade electropolishing. Untested specimens have a smooth, unblemished surface finish, with a typical example shown in figure 6.1.

6.1.2. Comparison of pre and post-test specimens

A visual comparison in figure 6.2 (a) and (b) of the pre and post-test surfaces of a test specimen shows a clear difference in surface roughness. Individual grains become more apparent due to the process of plastic deformation which results in slip band formation and grain rotation as shown in figure 6.3. It is intended to use the phenomenon of slip band formation to identify differences in the mechanical behaviour of the various specimens. The more heavily deformed a grain, the more numerous and pronounced the slip bands.

6.1.3. Micrographic surface examination of runout 50 μm specimens

SEM studies of runout specimens were conducted. The entire length of a specimen was imaged, allowing visual assessment of the uniformity of strain accumulation along the length. Failed specimens were not imaged in this manner, as it has to be assumed that where failure occurs, the majority of plastic strain is concentrated in one region. It is the purpose of this study to determine if differences exist in the distribution of plastic strain within a specimen; it is therefore more informative to study the strain distribution in runout specimens. Figure 6.4(a) shows a plastically deformed region within the specimen, while figure 6.4(b) shows a relatively undeformed region within the same specimen. This example is typical of the form of strain distribution within post-test 50 μm specimens. Further examples are available in Appendix D.1. Such differences in the distribution of plastic deformation within the same specimen suggest that strain localization is occurring. The distribution of plastic strain within the 50 μm specimens has been observed to occur in this manner within the stress range of interest (300 – 500 MPa).

6.1.4. Micrographic surface examination of runout 75 μm specimens

The micrographic images of 75 μm specimens indicate that a more uniform distribution of plastic strain occurs. Figure 6.5(a) and (b) show two regions from the same test specimen. These two regions are representative of the nature of strain distribution within the specimen as a whole. A further example from the same specimen is provided in figure 6.6. Plastic strain appears to be distributed more uniformly than is the case for the 50 μm specimens. More images are included in Appendix D.1.

6.1.5. Micrographic surface examination of runout 150 μm specimens

The micrographic images of 150 μm specimens indicate that a more uniform distribution of plastic strain occurs. Figure 6.7(a) and (b) show two regions from the same test specimen. Again these regions are representative of the nature of strain distribution within the specimen as a whole. Further examples are provided in Appendix D.1. Plastic strain appears to be distributed more uniformly than is the case for the 50 μm specimens.

6.2. A quantitative measurement of strain localization

The micrographic study of the various specimens provides a subjective assessment of the level and distribution of plastic strain within those specimens. The SEM images suggest that there is a less uniform distribution of plastic strain within the 50 μm specimens, relative to the 75 μm and 150 μm specimens. In order to provide a quantitative measurement of the level of plastic strain within the specimens, a surface roughness (R_a) measurement technique was applied to runout specimens that were tested at the same maximum stress. Therefore, test parameters were the same for all samples included in this analysis.

6.2.1. Surface roughness measurement with white light interferometer

SEM imaging of the various specimens suggests that strain localisation is more likely to occur in the smaller 50 μm specimens. Quantitative measurements of R_a will allow conclusive statements to be drawn on whether this observed strain localization is an apparent or a real effect. Surface roughness values measurements were performed on a NewView 100 surface profiler. This scanning white-light interferometer relies on the principle of constructive and destructive interference of light waves to measure roughness values. It is a non-contact measurement technique, and has been found to compare well with tactile measurements of standard roughness gauges [6.1]. Importantly, the technique has been found to work well for sub micron scale features. It has also found an industrial application in the inspection of engine cylinder walls [6.2].

Scans were performed by the National Centre for Laser Applications (NCLA) at NUI Galway. The scanning technique involved selecting a scan area measuring 180 μm x 30 μm. This scan area must fit on all specimens and it must be the same size if results for the various specimens are to be comparable. All specimens were scanned at either end of the gauge length (not including the fillet radii) and in the middle of the gauge length providing three average roughness values per sample. An example of the scan data generated by the profiler is shown in below in figure 6.8(a). An SEM image of the same area is presented for comparison in figure 6.8(b). Note that the roughness values are given as average roughness (Ra (μm)) and RMS (μm). An untested specimen was also scanned in order to provide a reference roughness value.

6.3. Discussion

A baseline value for average roughness was established by measuring the surface roughness of an untested specimen. A clear difference, as shown in figure 6.9, both in terms of magnitude and range of R_a, exists between the tested and untested specimens.

The trends displayed in figure 6.9 indicate that plasticity development is more inhomogeneous in the 50 μm samples than in the 150 μm samples. While the minimum levels of surface roughness are similar, the maximum levels are quite different, those measured for the 50 µm sample being considerably higher than the maximum value recorded for the 150 µm sample. This suggests that plastic deformation is more evenly distributed throughout a 150 µm sample, whereas it is a less uniform process for the 50 µm sample. With reference to figure 6.8(b), it has been possible, in this instance, to match the interferometer image with an SEM image of the same area. The interferometer scans were taken in such a way so as to make this correlation easier. However, the matching is done by eye and success is not guaranteed. It is interesting to note that a visual comparison, based on SEM images, of the surface roughness of areas on a 150 µm sample does not indicate that there is a significant variation in the roughness values.

In other words, the distribution of roughness of a 150 µm sample appears to be more homogenous than it actually is, when estimated solely on the basis of SEM images. The SEM studies of the specimen surfaces suggested that a process of strain localisation was occurring in the smaller specimens; the measurement of surface roughness values has confirmed that strain localisation occurs in the 50 µm specimens and to a lesser extent in the 150 µm specimens

6.4 Fractography

Fatigue testing, by its nature, generates failed test specimens. Along with determining the number of cycles to failure for a given set of conditions, it is also informative to determine the mechanism by which the sample failed and as it has been demonstrated experimentally that a size effect exists in fatigue, to determine if this size effect finds its cause in a size-dependent fatigue mechanism. This may be done through micrographic examination of the fracture surfaces of the failed specimen in a process known as “fractography” [6.3]. In order to determine the mechanism(s) of failure of the test specimens, the fracture surfaces were examined using a Scanning Electron Microscope (SEM – Hitachi S4700, see Appendix D.2 for methodology).

6.4.1 Failure mechanisms

There are two possible outcomes of the fatigue tests: failure of the test specimen within the specified number of cycles, or runout of the specimen at ten million cycles. The failure mechanisms are varied, but all relate to the plastic deformation behaviour of the material. There are several mechanisms by which failure may occur. Figure 6.10 shows a typical fatigue fracture surface for the 316L stainless steel specimens. Though this is a 150 μm specimen, it is generally representative of all sizes tested. The fracture surface is divided up into a fatigue fracture region and a ductile fracture region. The fatigue region itself is composed of a cleavage-type fracture region (indicated). The ductile region may be identified by the presence of shear dimples.

Austenitic stainless steels such as 316L stainless steel do not typically exhibit classic fracture features such as striations and beach marks [6.4]. Figure 6.11 shows a typical 50 μm specimen fracture surface. No striations or beachmarks are discernable at this and higher magnifications. In the specimens tested here, prior plastic deformation creates slip bands and slip lines (Figure 6.5(b)). The tension-tension load state inhibits slip reversibility so the conditions exist for stage I crack propagation. Stage I [6.5, 6.6] crack propagation occurs principally by slip plane cracking where an extended, localized slip band develops during cyclic plastic straining and crack extension occurs within this slip band. The crack extends on the most favourably orientated plane as shown in Figure 6.12. It is hypothesised that once the crack moves beyond the original grain with its favourably orientated slip plane (region 1 in figure 6.12), the fracture morphology becomes much more disordered, as the crack jumps from slip plane to slip plane, following a discontinuous crack path (region 2 in figure 6.12) before ductile overload occurs (region 3). The difference between the discontinuous, zigzag cracking and slip plane cracking is marked. Figure 6.13 shows a higher magnification view of a facetted cleavage-type fracture surface while Figure 6.14 shows a planar cleavage-type fracture. As grains in polycrystalline metal will have many different orientations, this leads to the facetted, cleavage-type fracture surfaces, and, as mentioned, there are generally no striations. The tendency towards stage I crack propagation is strongly affected by anything that concentrates slip and by environments that affect slip reversibility.

The fracture surface features described in this section are common to all specimen sizes. No size dependent fatigue mechanism was identified. Fractographic analysis of failure surfaces shows areas of cleavage and facetted failure regions together with ductile failure region. Cleavage and facetted failure surfaces are formed more quickly and consequently are associated with more rapid crack growth. This suggests that the majority of life is spent in crack initiation, with a rapid crack propagation phase. Additional images are included in Appendix D.3.

6.4.2 Cracking due to inclusions

Previous work on stent material [6.7] related a reduction in the fatigue resistance of small diameter wires to the presence of cubic titanium nitride particles. These large particles (typically in the order of 5μm^3) are created during the melt process when titanium in the alloy reacts with nitrogen. Large cubic particles were observed on the surface of the 316L fatigue specimens as shown in Figure 6.14 and were confirmed to be titanium nitride (TiN) particles by energy dispersive x-ray microanalysis (EDX). Evidence from extensive fractography work showed no direct relationship between the presence of TiN particles and crack formation and specimen failure. Indeed, no cracks were observed to emanate from any observed TiN particles, even where the particles themselves had fractured as shown in Figure 6.15. The failure of specimens could not therefore be attributed to the presence of such particles. In conclusion, TiN particles were not responsible for specimen failure.

6.5 Failure process

It is proposed that the final shape of the failed specimens, as shown in Figure 6.17 is due to mechanism illustrated in Figure 6.18. Plastic straining concentrates slip and inhibits slip reversibility. A crack initiates and propagates along a favourably orientated slip band by the process of stage I crack propagation (Figure 6.18 (I)). The crack grows to a length sufficient to cause a change in compliance (II). As the specimen is no longer able to support the load to which it is being subjected, it begins to neck and as this necking occurs, a portion of the fatigue fracture surface is pulled upwards (III). The necked region becomes ever smaller in diameter (IV) until ductile failure finally occurs (V), leaving tell-tale elongated shear dimples behind. No size dependent fatigue mechanism was identified. The fractography suggests that specimens share a common fatigue mechanism, with the majority of life spent in crack initiation and a rapid crack propagation phase. Inclusions were not found to play any significant role in fatigue performance.

References

[6.1] Windecker, R., (1999) Optical Roughness Measurements using extended white-light interferometry, *Optical Engineering*, Vol.38, Part 6, pp 1081-1087

[6.2] Windecker, R., (2001) High resolution optical sensor for the inspection of engine cylinder walls, *International Journal for Light and Electron Optics*, **112**, 9, 407-412

[6.3] Engel, L., Klingele, H., (1981) An atlas of Metal Damage, Manson Publishing Ltd., London

[6.4] Suresh, S., (2004) Fatigue of Materials, *Cambridge University Press*, 2nd Edition, pg. 336
[6.5] ASM Handbook, Volume 19, Fatigue and Fracture
[6.6] Romeyn, A., (1993) Physics of Plastic Deformation and Fatigue, National Conference Publication, Institute of Engineers, Australia, 1993, Vol. 2, Part: 93, p. 457-462
[6.7] Bradley, D., Kay, L., (2004) Optimising fatigue resistance of medical wire, Medical device technology

<u>Figures</u>

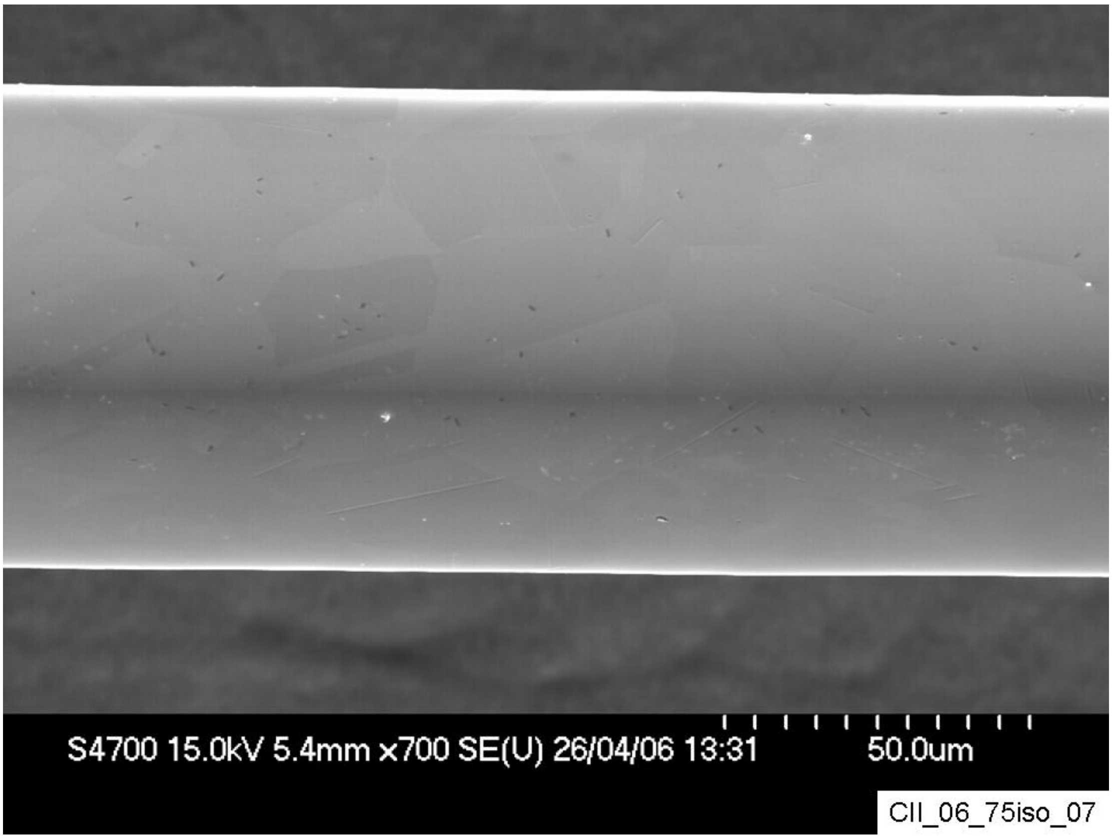

Figure 6.1. SEM image of a section of an untested 75μm specimen.

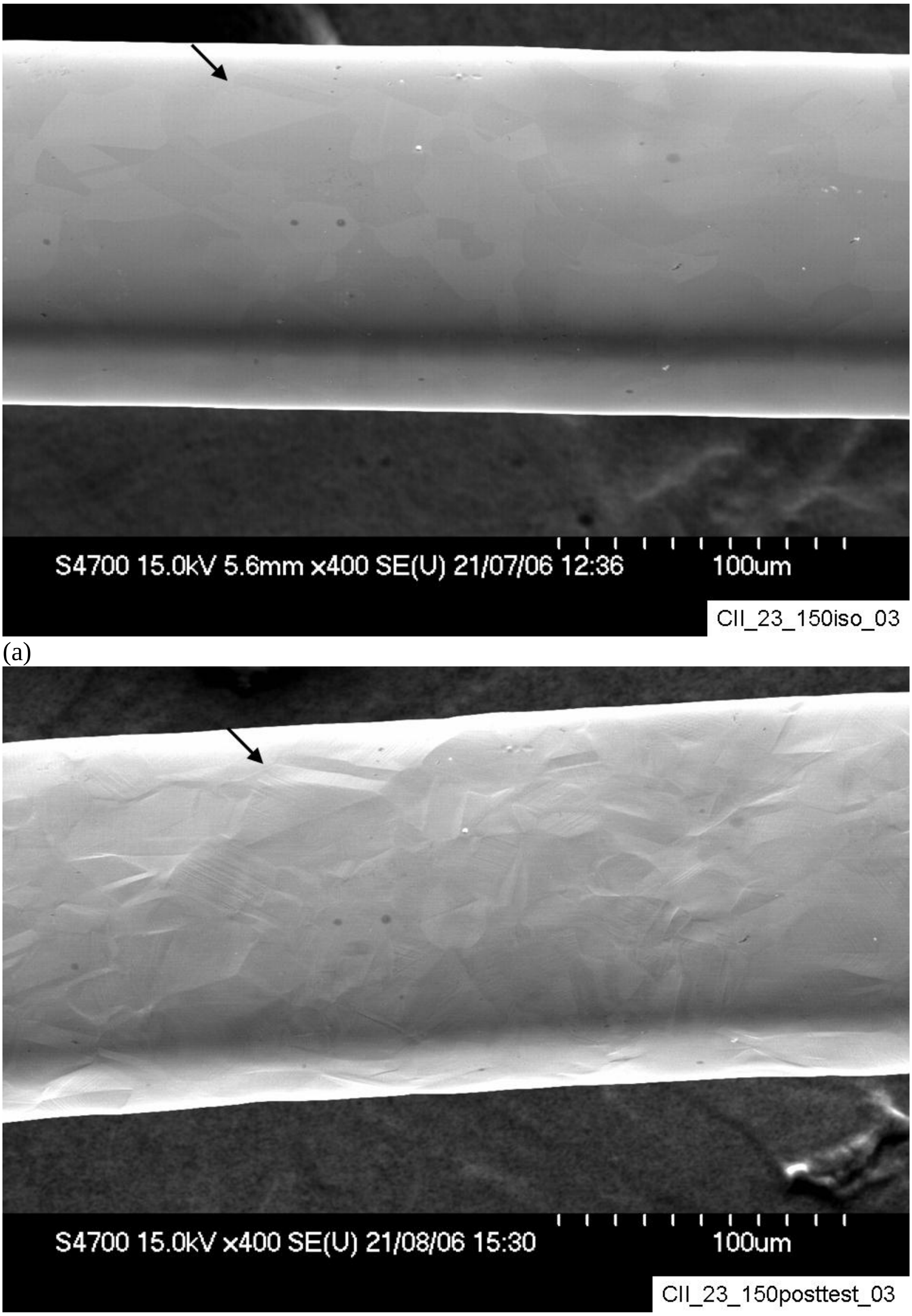

(a)

(b)

Figure 6.2. The effect of cyclic straining on a test specimen, (a) pre and (b) post-test SEM images of the same section in a 150μm specimen. Arrows identify reference grain.

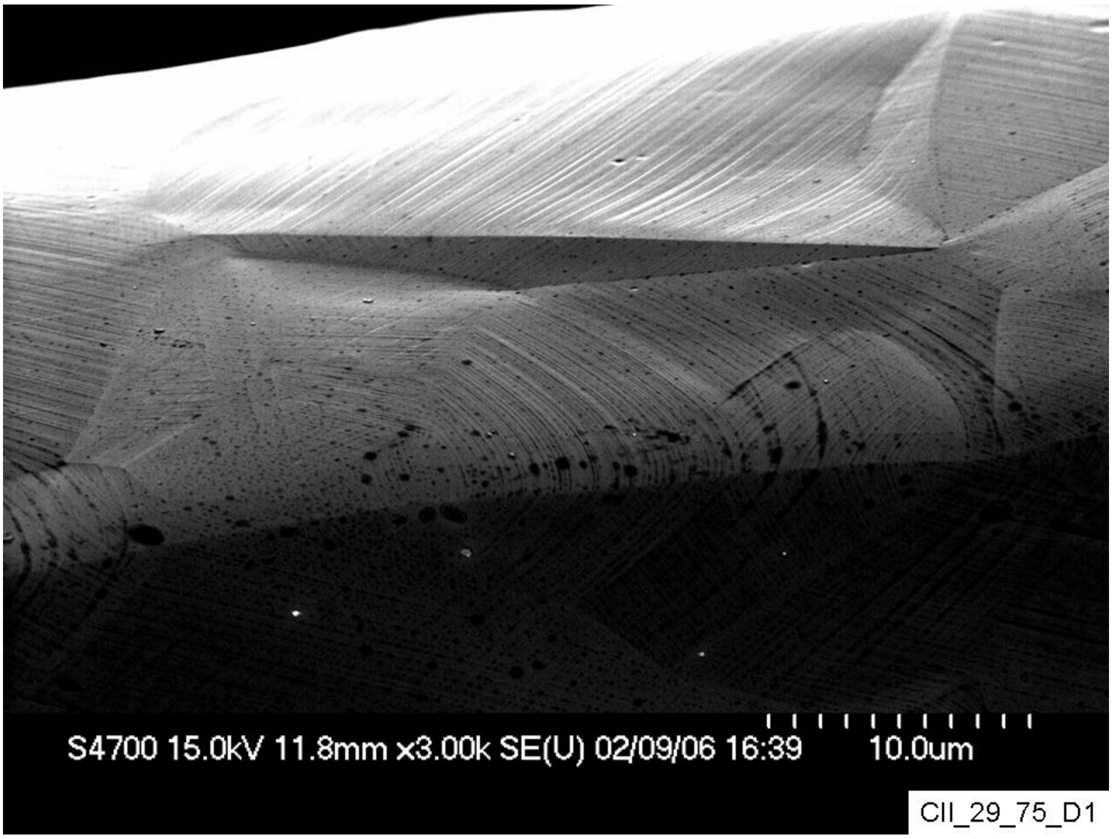

Figure 6.3. Plastic deformation within grains; slip band formation and grain rotation.

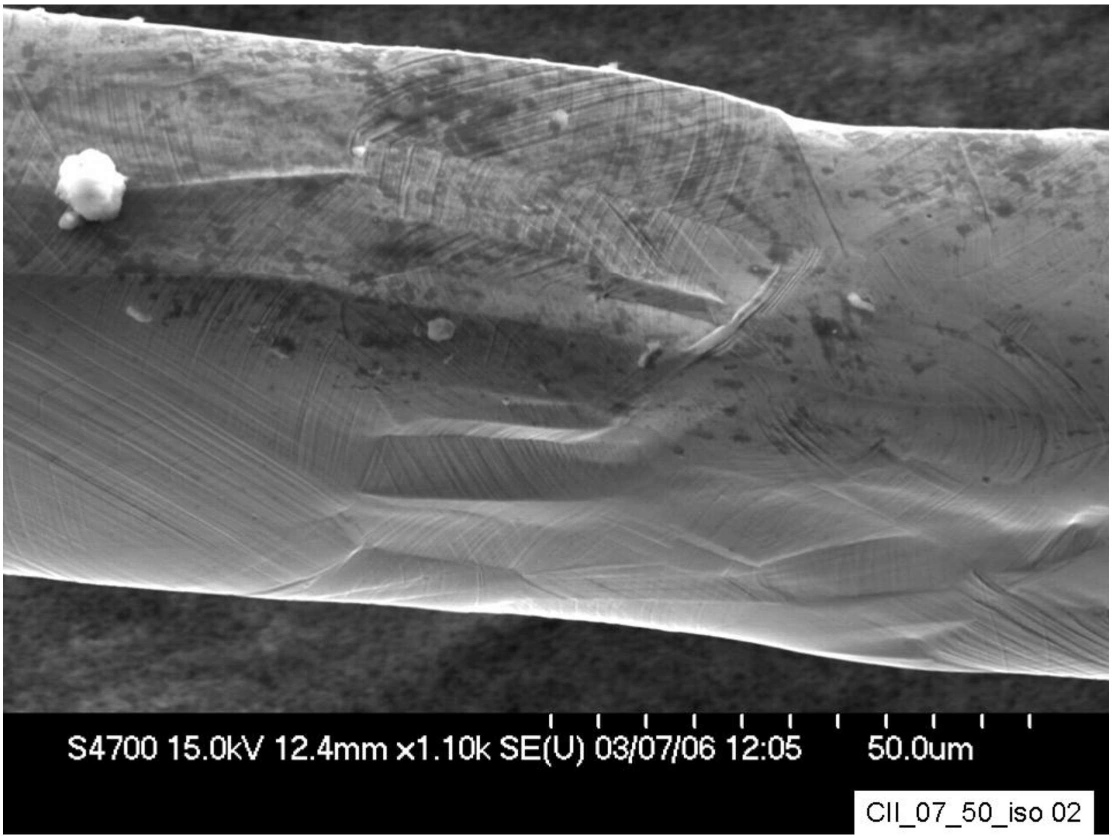

(a)

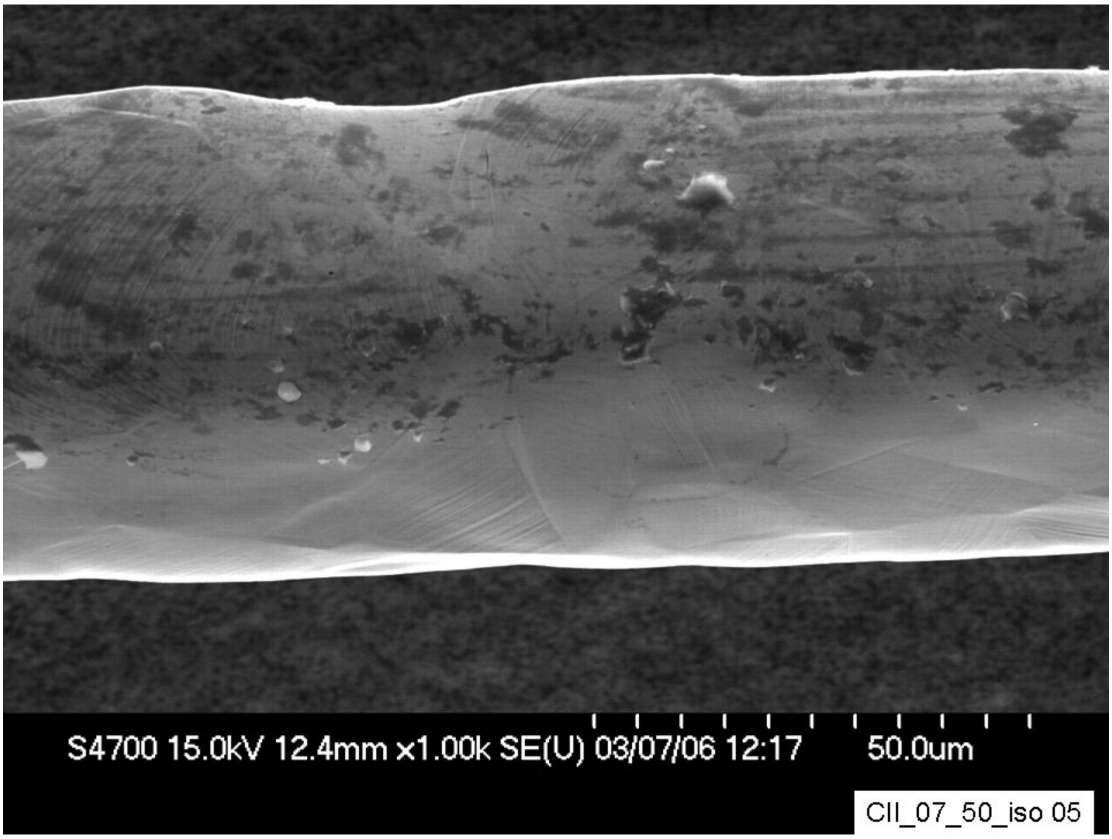

(b)

Figure 6.4. Plastic deformation within a 50μm specimen; (a) more heavily deformed region than (b), both from same specimen.

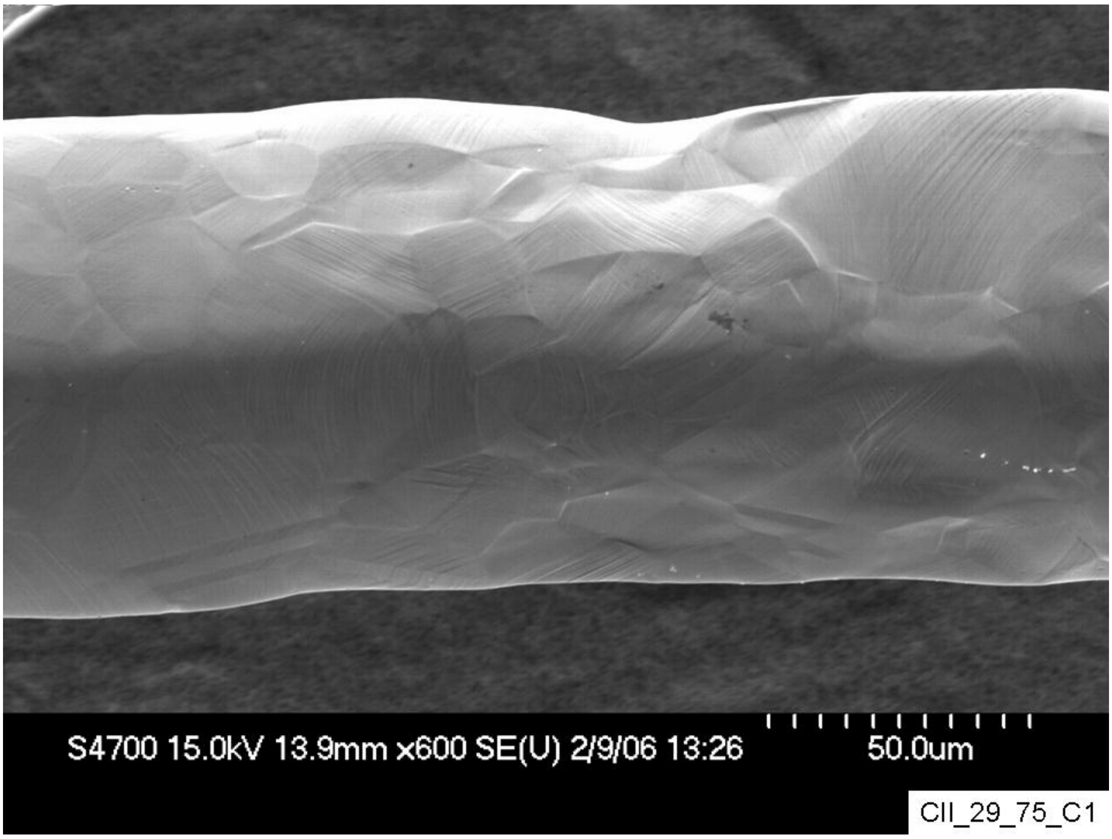

(a)

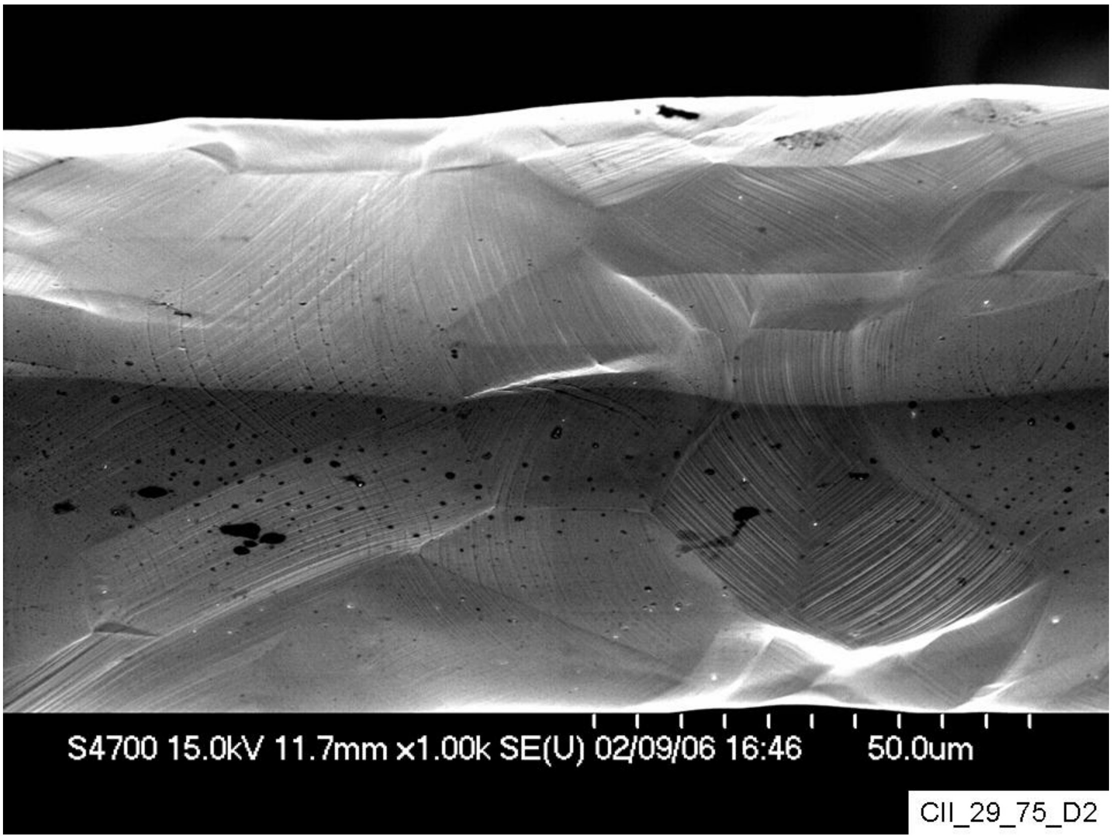

(b)

Figure 6.5. Plastic deformation within a 75 µm specimen; (a) heavily deformed region (b) comparably deformed region. Both images from same specimen.

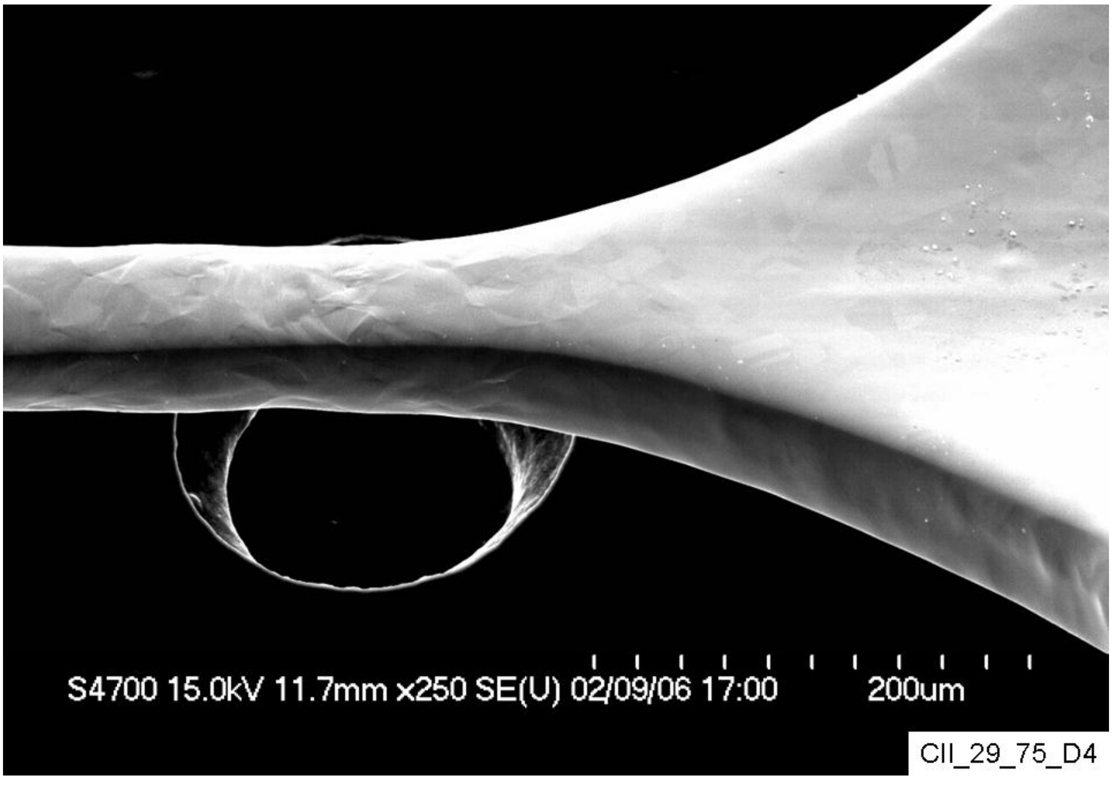

Figure 6.6. Strain distribution within a runout 75 µm specimen.

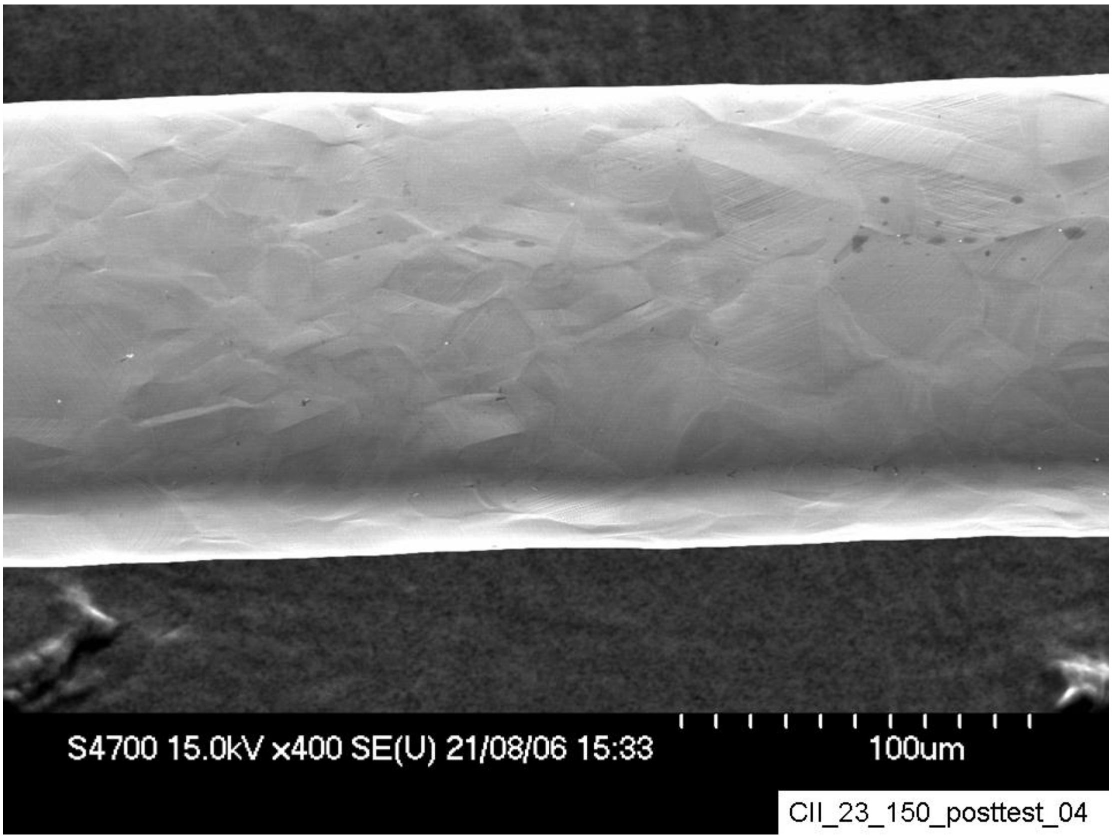

(a)

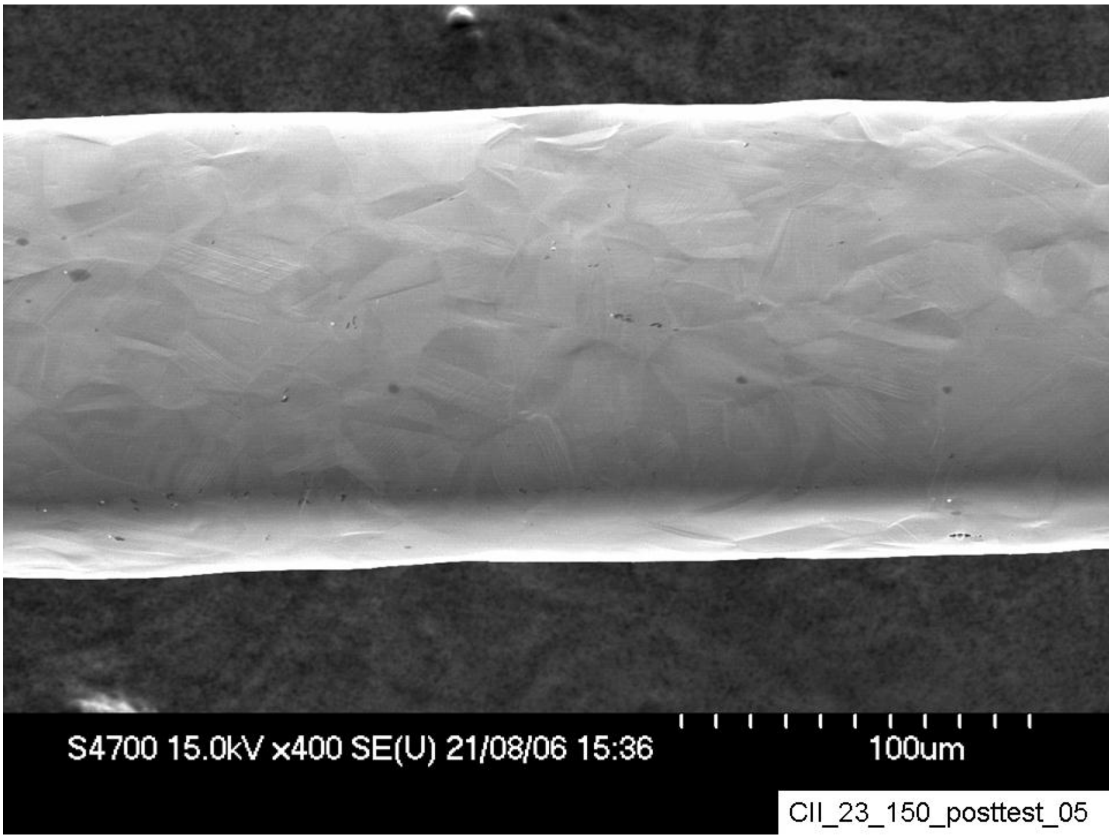

(b)

Figure 6.7. Plastic deformation within a runout 150 µm specimen; (a) heavily deformed region (b) comparably deformed region. Both images are from same specimen

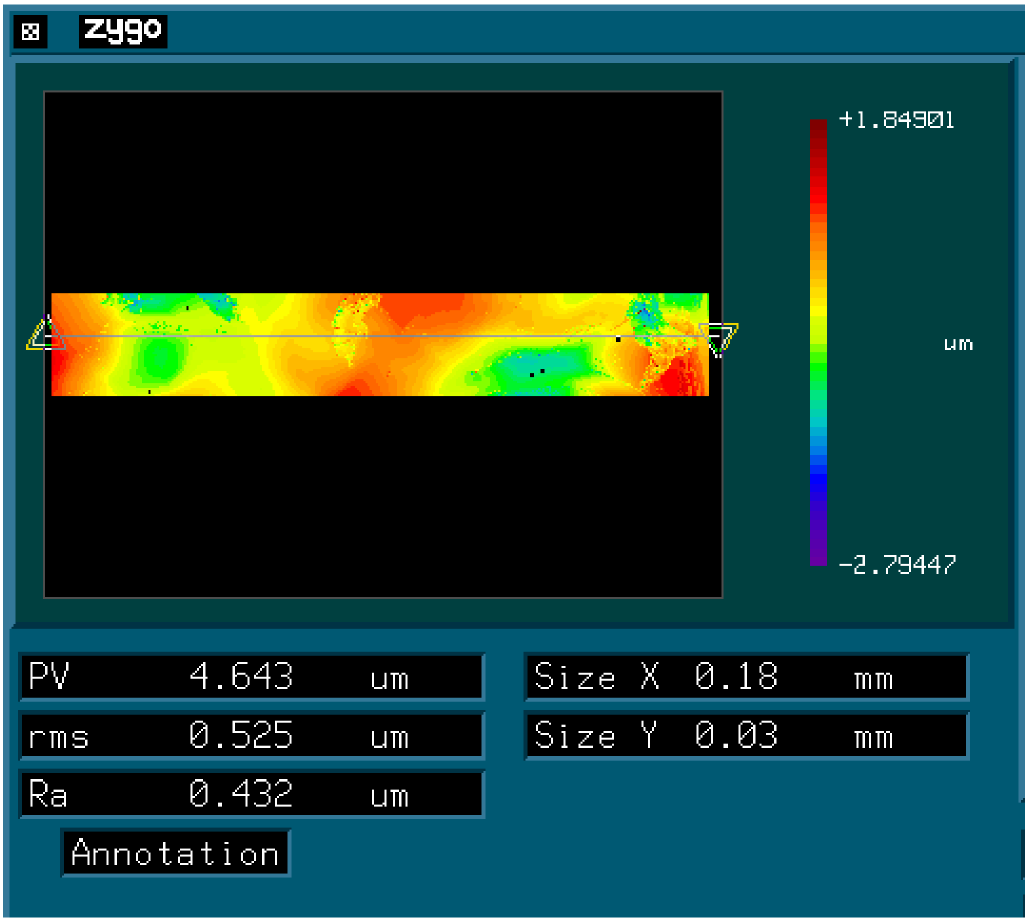

PV 4.643 um

rms 0.525 um

Ra 0.432 um

Size X 0.18 mm

Size Y 0.03 mm

(a)

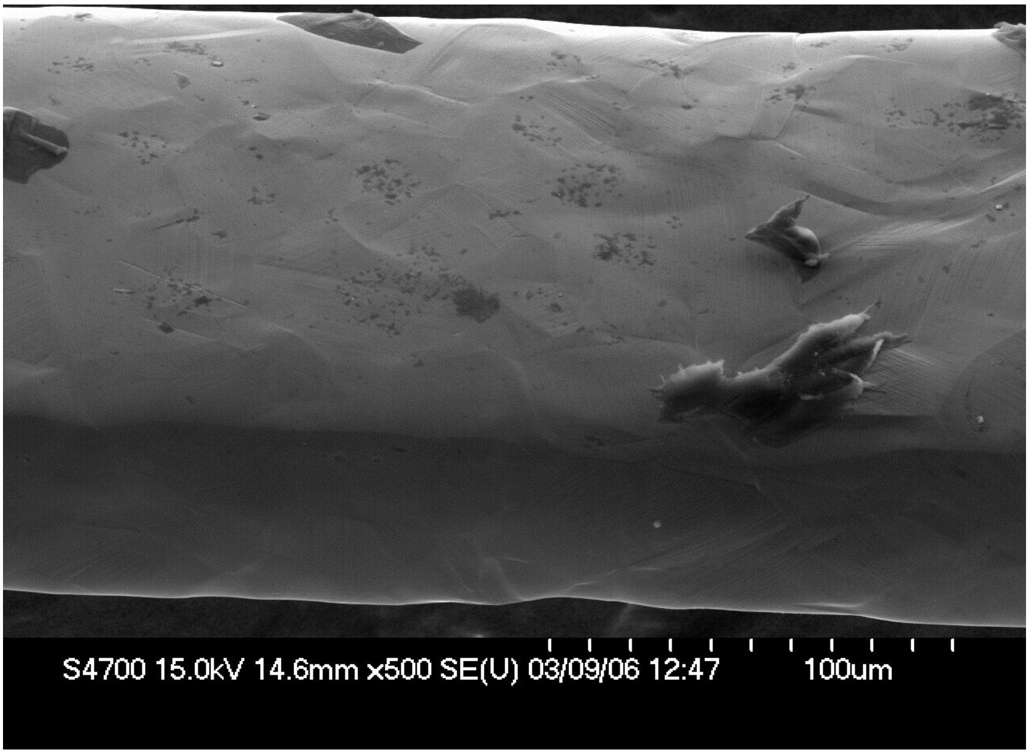

(b)
Figure 6.8(a) white light profiler scan data of region of specimen (b) micrograph of same area.

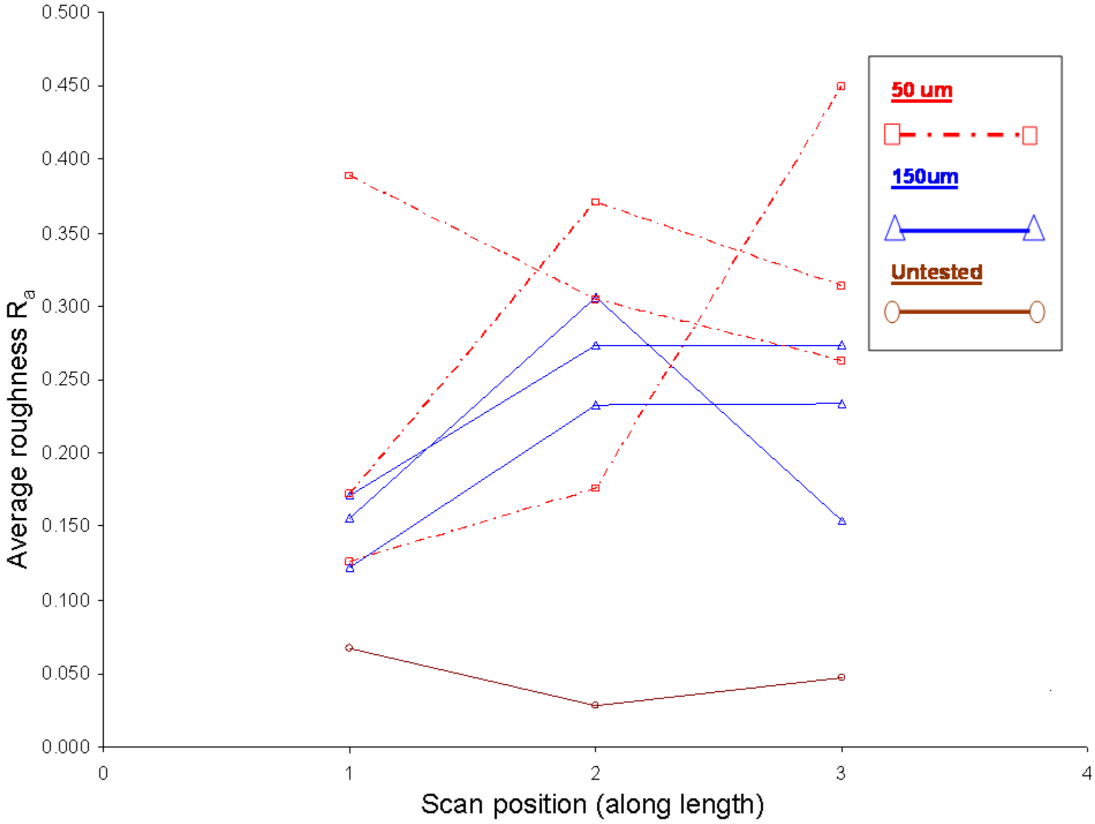

Figure 6.9. Surface roughness measurements taken at three positions along the gauge length of a selection of runout 50 μm and 150 μm specimens. Untested specimen included as a control.

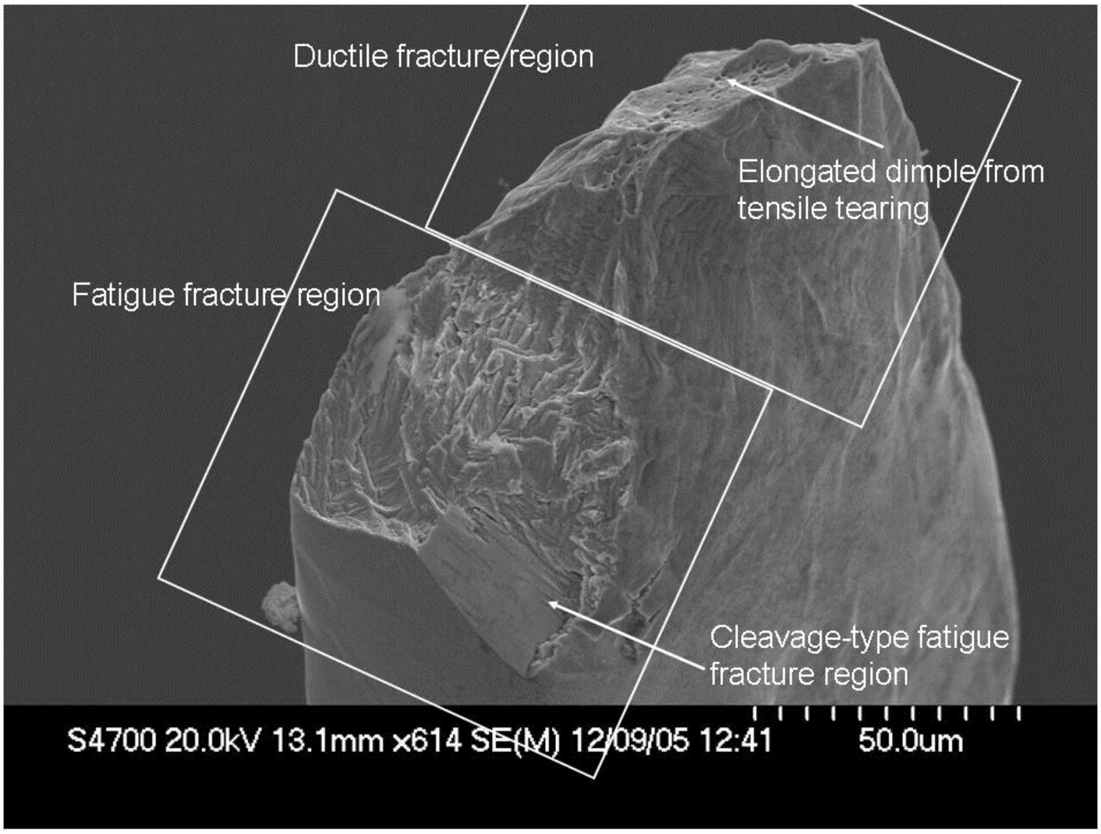

Figure 6.10. Typical fracture surface topology. Crystallographic and facetted failure profile indicates high level of strain hardening and consequent rapid crack growth. Highly localised ductility exhaustion/saturation. 150 μm specimen.

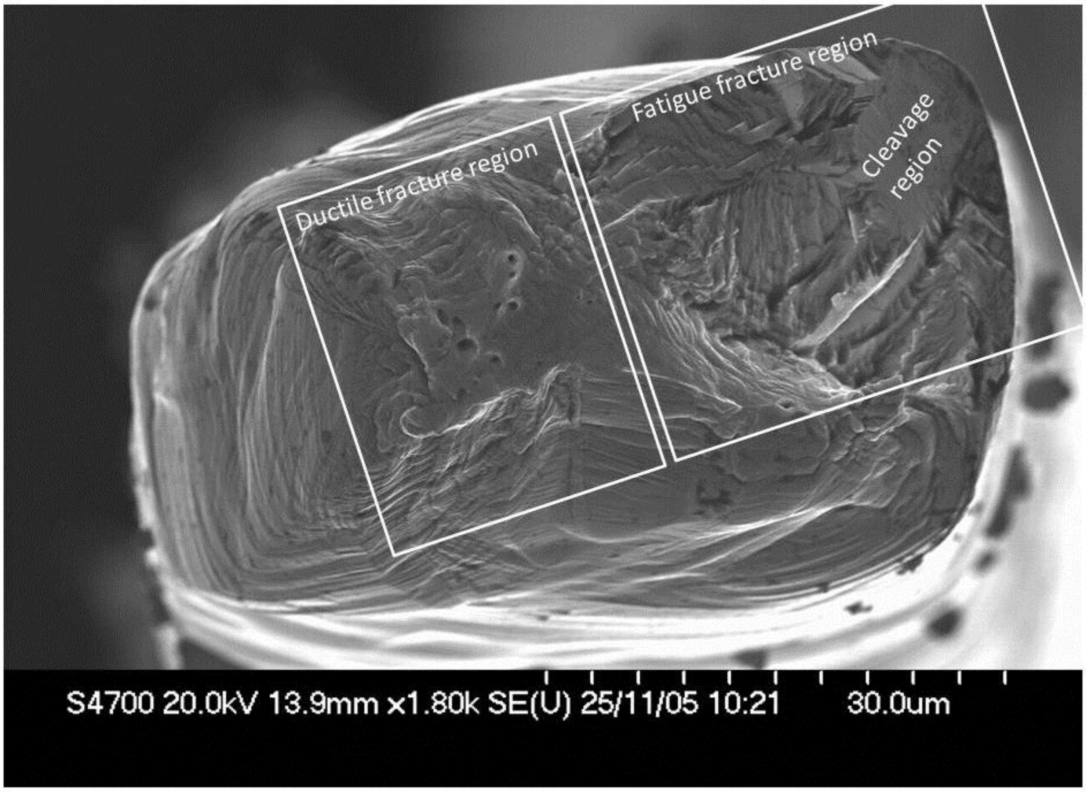

Figure 6.11. Typical fracture surface of 50 μm specimen. Notice the similarity to Figure 6.10.

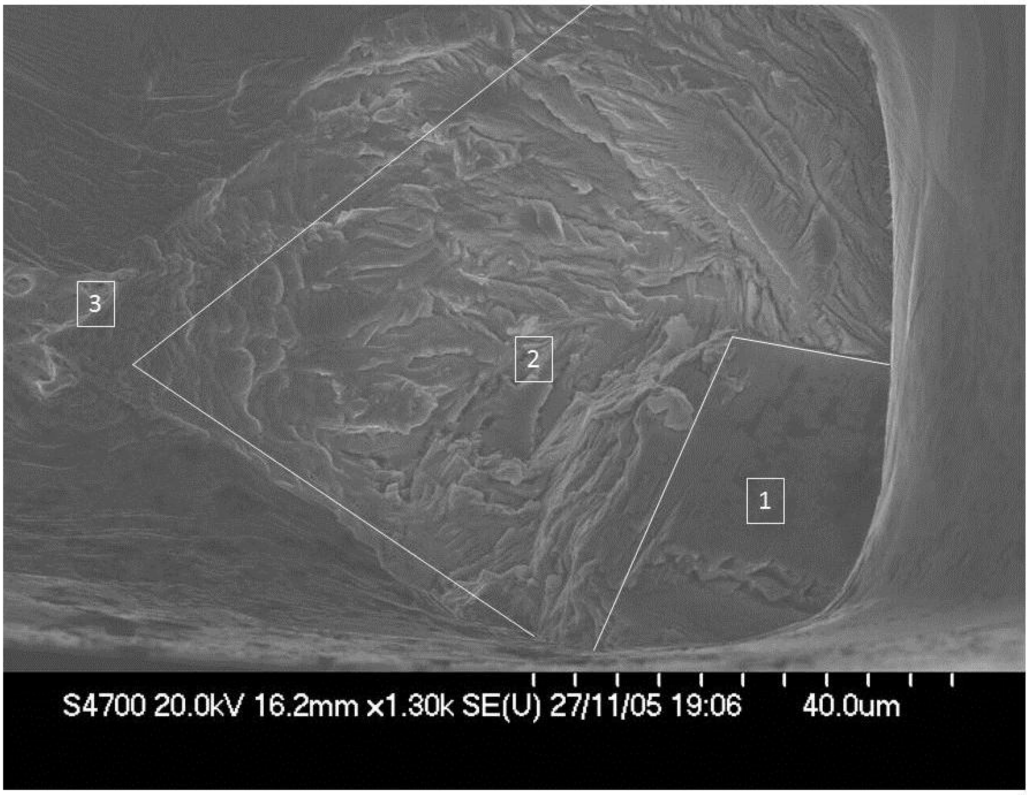

Figure 6.12. Cleavage-like fracture surface (1) with additional discontinuous crack morphology (2) formed as the crack jumped from slip plane to slip plane before ductile overload (3). 150 μm specimen.

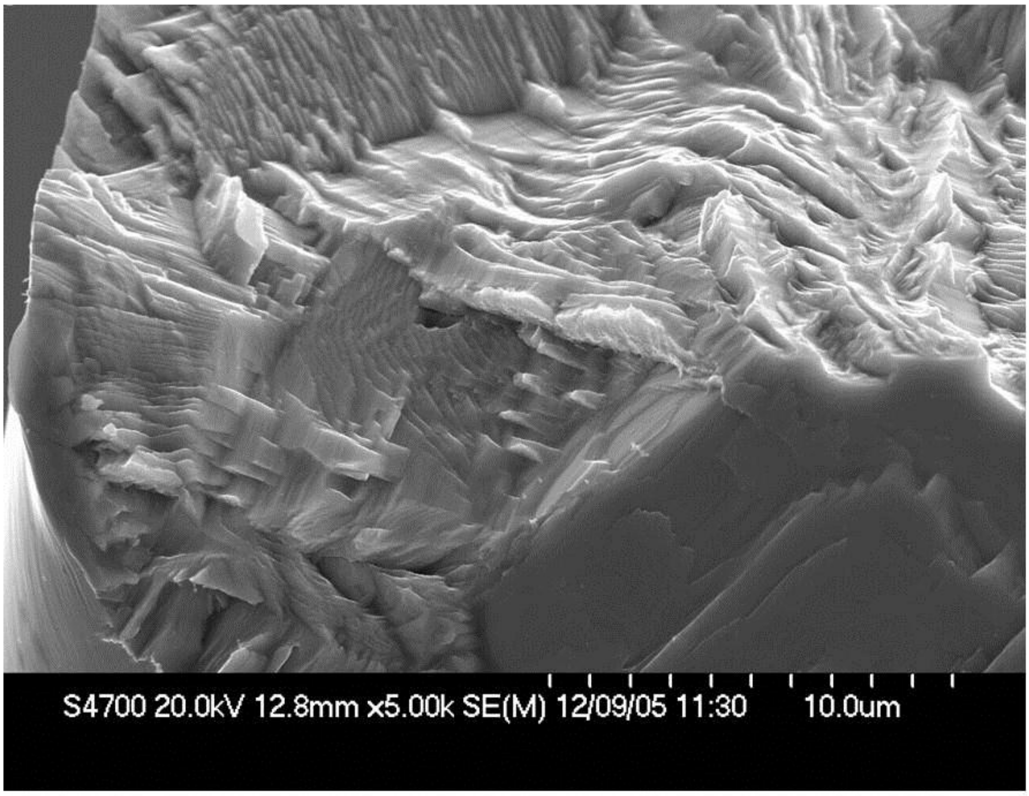

Figure 6.13. Higher magnification image of cleavage-like fracture surface with additional discontinuous crack morphology formed as the crack jumped from slip plane to slip plane. 150 μm specimen.

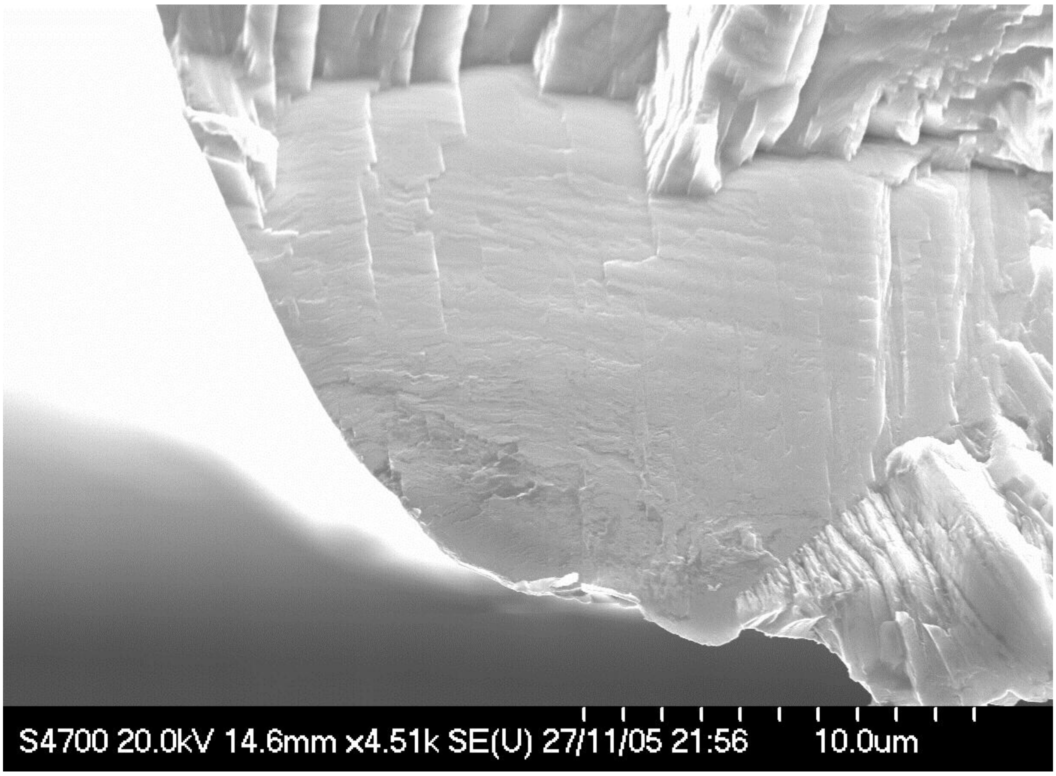

6.14. Slip plane cracking.

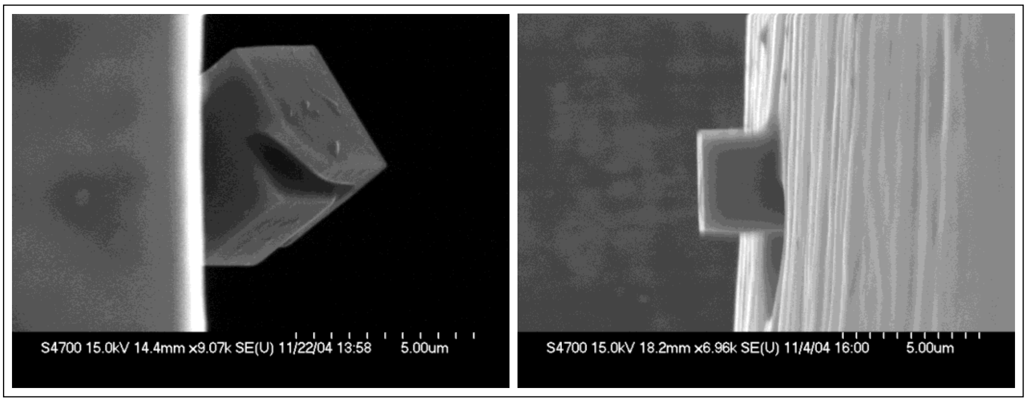

Figure 6.15 Titanium nitride (TiN) particles on the surface of 316L fatigue specimens.

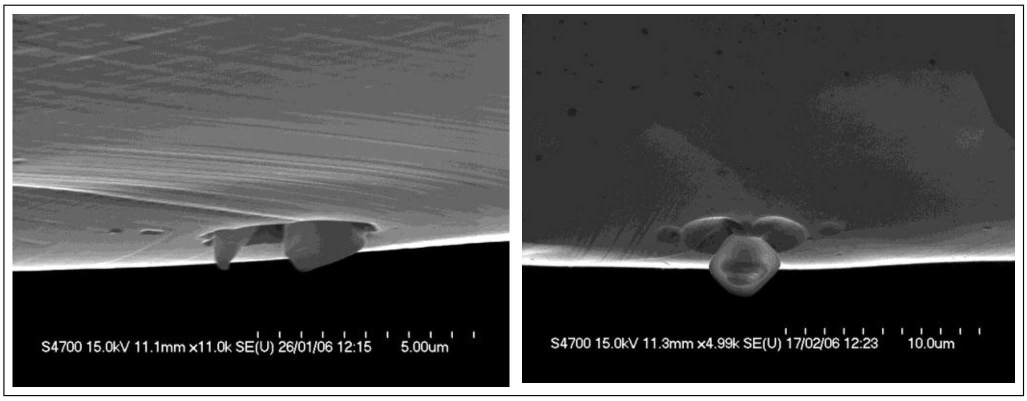

Figure 6.16 TiN particles in post-fatigue test specimens.

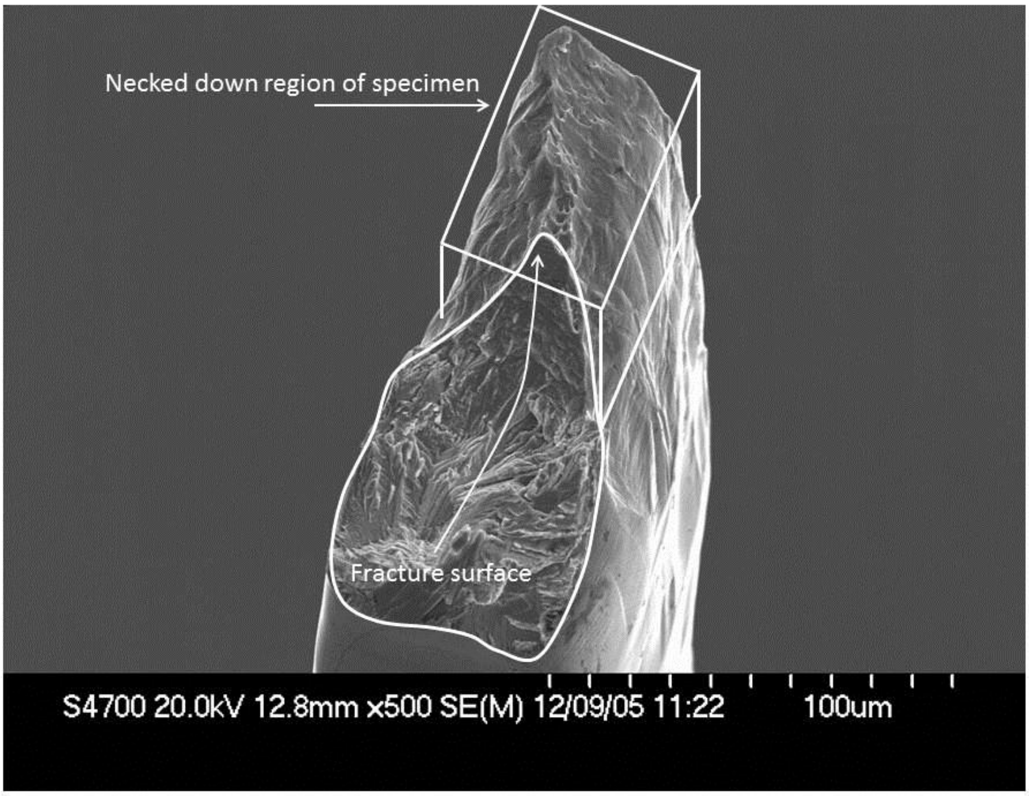

Figure 6.17. Necked down region of specimen with fatigue fracture surface reorientation.

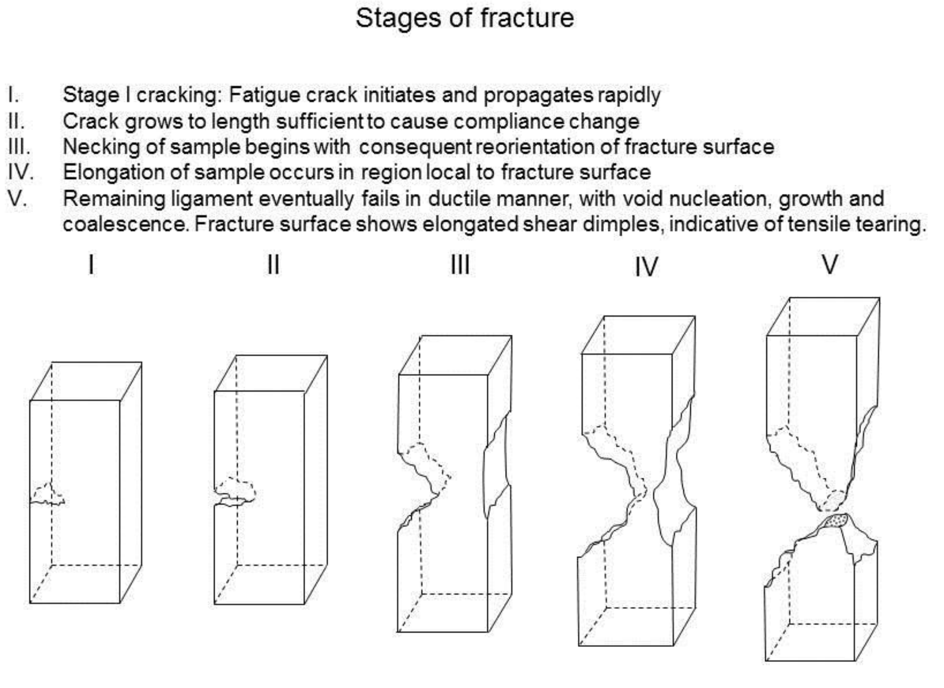

Stages of fracture

I. Stage I cracking: Fatigue crack initiates and propagates rapidly
II. Crack grows to length sufficient to cause compliance change
III. Necking of sample begins with consequent reorientation of fracture surface
IV. Elongation of sample occurs in region local to fracture surface
V. Remaining ligament eventually fails in ductile manner, with void nucleation, growth and coalescence. Fracture surface shows elongated shear dimples, indicative of tensile tearing.

Figure 6.18. Proposed mechanism of fracture surface creation.

COMPUTATIONAL METHODOLOGY FOR MICROSCALE SPECIMENS

7.1. Introduction

In the computational modelling work on cardiovascular stents, described in Chapter 3, the stent material (i.e. 316L stainless steel) the material was assumed to behave as a continuum. This approach assumes that bulk material properties apply to the structure, i.e. material behaviour is scale independent. However, it has been shown in previous studies [7.1, 7.2, 7.3] that this is not the case; as size is reduced, and the grain size to specimen width ratio drops below a critical value, mechanical size effects arise. For stainless steels this critical value ranges typically from 6 – 10 grains across the width [7.1, 7.2, 7.3, 7.4]. These size effects cause material behaviour to deviate significantly from bulk material behaviour. If such a deviation in behaviour is to be captured within computational models, it is necessary to represent in some way the crystalline structure of a metal and the anisotropic behaviour of individual grains within the models. The following chapter describes the development of such a modelling methodology.

7.2. Model design

The models were designed to approximately represent the microstructure of the experimental specimens. Figure 7.1 clearly shows the grains and grain boundaries in a polished and etched sample of 316L stainless steel. The strut is traversed by four grains giving a grain size to specimen width ratio of 4. These grains are approximately equiaxed and are represented in the models by an idealised, hexagonal grain geometry as shown in Figure 7.2. A series of 2D struts of length 500µm, combined with a hexagonal grain shape and varying aspect ratio were created. The aspect ratio was changed by increasing the strut width through the addition of more through-thickness grains (i.e. keeping the grain size constant). Widths of 14 µm, 19 µm, 28 µm and 75 µm were created, and further widths were modelled by applying symmetry boundary conditions to the 75 µm model to represent a 150 µm sample while still taking account of the Poisson’s ratio effect. The strut geometries were completed by adding half hexagons to the upper and lower surfaces. Table 7.1 lists the model specifications

The 2D finite element mesh was generated with pre-processing/finite element software MSC.Patran 2003. For additional accuracy a through-thickness component of constraint was afforded to the 2D structure by the use of 8-noded quadrilateral CPEG8R generalised plane strain elements. Completed input files were then processed and post-processed by ABAQUS ® V 6.5 on a 24 CPU super computer.

7.3. Modelling methodology

Ten models were created for each series of specimen sizes (the series 14 µm, 19 µm, 28 µm, 75 µm and symmetric boundary applied to the 75 µm model to represent a 150 µm sample) and each model was subjected to twenty loading cycles during the finite element simulations.

Each grain in a crystalline solid is anisotropic in its material behaviour due to the predefined directions and planes of preferred slip; different loading directions elicit different responses from the grain depending on the orientation of the grain with respect to the specimen loading direction. This behaviour has been described by the crystal plasticity constitutive model developed by Asaro *et al* [7.5]. In crystal plasticity theory, plastic slip is assumed to obey Schmidt’s law, where the rate of plastic shear strain, $\dot{\gamma}^{(\alpha)}$ in the direction of a particular slip system α, is assumed to depend on the Schmidt resolved shear stress for that slip system,

$$\dot{\gamma} = \dot{a}\,\mathrm{sgn}\left(\tau^{(a)}\right)\left|\frac{\tau^{(a)}}{g^{(\alpha)}}\right|^{n} \tag{7.1}$$

where $\dot{a}$ and n are a reference strain rate and rate sensitivity exponent, respectively, and $g^{(\alpha)}$ is the slip system strain hardness. As n tends to infinity the material reaches the rate-independent limit [7.6]

Plastic flow is calculated in terms of continuum plastic shear strains on the individual slip systems, which are then summed across all the available slip systems to give the total deformation. As there are many hundreds of grains in even the simplest of strut models, such an approach, while potentially very accurate, is not suited to fatigue modelling in polycrystalline solids due to the excessive computational requirements imposed by the method. In order to circumvent this issue, a method known as the “Microstructural – J2” method was developed [7.7].

7.3.1. Microstructural – J2 (M-J2) modelling method

The M-J2 modelling method seeks to combine the relevant elements of crystal plasticity (i.e. its ability to describe single grain behaviour) with the computational efficiency of continuum mechanics. This is achieved by assigning to each grain in the strut its own material property. That material property is derived from the mechanical behaviour of a single crystal and its dependence on its orientation with respect to the global loading direction. This was achieved through simulations of a calibrated crystal plasticity model of a single grain [7.7].

More specifically, the calibration is achieved by using the crystal plasticity method to generate stress-strain curves for all possible loading orientations of a single anisotropic grain subjected to a standard load. The curves so generated were then reviewed and where duplication occurred, one of the curves was removed. This approach resulted in a selection of 43 unique stress strain curves, representing the behaviour of each grain with respect to its orientation to the loading direction. These curves, with some modification, were then randomly assigned to the grains within the strut models developed in this work. While a significant element of accuracy is sacrificed with the M-J2 method, the general behaviour of a polycrystalline material can be described. More detail on the accuracy and limitations of this approach is described in [7.7]. As the grains behave in a pre-determined manner, influenced only by the level of constraint and applied load, solution times are much faster than for an equivalent model incorporating the crystal plasticity constitutive behaviour.

7.4. Hardening model

If a specimen is plastically deformed in one loading direction, unloaded to zero stress and then reloaded in the opposite direction, the yield stress on reloading is less than the original yield stress. This directionality of strain hardening is known as the Bauschinger effect [7.8, 7.9]. A hardening model capable of describing this effect is necessary to model the accumulation of plastic strain that accompanies cyclic loading (and leads ultimately to fatigue crack initiation and growth). An isotropic hardening constitutive model will not describe the Bauschinger Effect as the yield surface expands uniformly in all directions, thus the yield point always remain the same, regardless of direction of loading. Therefore, a simple linear kinematic hardening model was adopted as the hardening model. This constitutive model, though limited in its range of application, is sufficient to describe the accumulation of plastic strain in the initial stages of a fatigue test (cycles 1 – 20). In this model, the Bauschinger Effect is described by allowing the yield surface to translate in the direction of loading. An increment of plastic strain will occur if the maximum stress in the cycle is sufficient to raise the yield point for reverse loading above the minimum stress in the fatigue cycle as illustrated schematically in Figure 7.3(a). Plastic strain accumulation with the linear kinematic hardening model is therefore reliant upon concordant values of R ratio, maximum stress and yield point. Figure 7.3(b) shows that if these parameters are not in agreement, then plastic strain is not accumulated.

7.4.1. Hardening Curves

A series of curves with non-linear hardening properties was previously generated with a crystal plasticity model as described previously [7.5]. The linear kinematic hardening property data is required in the form of a bilinear curve, composed of elastic and plastic portions. These bilinear curves must be generated from the crystal plasticity data through the process of a best fit approximation. The 43 different linear hardening curves are displayed in Figure 7.4. The hardening model regulates the yield point and hardening rate for each grain, while the elastic component of the curve (which is isotropic in its behaviour) is identical for all grains. Essentially, the material behaviour of the grain is controlled by two slopes, one defining the elastic behaviour, and the second the inelastic behaviour. One of the limitations of the linear kinematic hardening method is that within the plastic regime, the material will continue to deform infinitely in a manner dictated by the slope of the plastic curve. This is unrealistic, and limits the range of application of the method to a small number of cycles beginning with a state of zero plasticity.

7.4.2. Limitations of modelling method

It must be stated that the objective of the finite element modelling component of this work was *not* to develop a realistic, quantitively predictive modelling capability.

Rather, the modelling work was undertaken in order to provide an insight into the mechanisms responsible for the experimentally observed size effect.

Simulations were only performed for 20 loading cycles, and while material property data was generated by a crystal plasticity model of face centre cubic 316L stainless steel, the data was not calibrated against the actual test specimens. No damage mechanisms, other than plasticity, were incorporated into the models, and consequently, no failure mechanisms were represented. The models were used to replicate qualitatively the experimentally observed trends, and to elucidate the mechanisms responsible for the size effect. Given the experimental loading profile, where an initially high strain amplitude is followed by potentially millions of applications of cycles of a lower strain amplitude, it was hypothesised that the microstructural conditions that lead ultimately to fatigue failure and hence to the size effect would be established very early on in the life of the fatigue test. During finite element simulation of a fatigue test, the maximum load is achieved on the first cycle. Differences in plastic strain levels within grains will be evident at the end of this cycle. A small number of additional cycles are required to establish if the rate of strain accumulation after the first cycle is greater for grains with initially higher strain levels.

7.5. Generating the models

A total of ten models were created for each strut width. Each model within the series delineated by strut width differed in the arrangement and distribution of grain orientations. In order to achieve the level of randomness required to make ten different struts within each series, a random number generating programme was used [7.10].

7.5.1. Boundary conditions for 14, 19, 28, 75 µm struts

A schematic representation of the boundary conditions applied to struts 14, 19, 28, and 75 µm are shown in Figure 7.5. Fatigue loading of the strut was simulated by constraining the left-hand boundary of the model in the horizontal (or 1) direction. Rigid body motion was prevented by constraining the node at the bottom left-hand corner (NSET=COR_LB) in both the horizontal (1) and the vertical (2) direction. The bottom right-hand corner node (COR_RB) was also constrained in the vertical direction. This was necessary to prevent buckling from occurring for the low width struts, high aspect ratio struts (e.g. an aspect of 35:1 exists in the case of the 14µm strut). Displacement of the right-hand boundary (NSET=RIGHT) of the strut was controlled by prescribing the following condition:

$$U_2^{RIGHT} = U_2^{COR\ RB} \tag{7.2}$$

7.5.2. Symmetry boundary conditions

Symmetry boundary conditions were applied to the 75 µm series of models in order to increase the width to an apparent width of 150 µm as shown in Figure 7.6. Displacement of the right-hand boundary of the strut was controlled by prescribing that the displacement in the horizontal (1 direction) of nodeset ‘RIGHT’ is equal to the displacement in the horizontal (1 direction) of nodeset ‘COR_RB’, i.e:

$$U_1^{RIGHT} = U_1^{COR\ RB} \tag{7.3}$$

While displacement of the top surface was prescribed by:

$$U_2^{TOP} = U_2^{COR\,LT} \tag{7.4}$$

7.6. Cyclic Loading

Sinusoidally varying cyclic loads were applied to the stainless steel specimens during experimental fatigue testing, as described in Chapter 4. This waveform was replicated in the simulations through the use of the *AMPLITUDE option [7.11] which allows variable loading patterns to be prescribed through the use of a Fourier series as follows:

$$F(X) = 0.55 + 0.45Sin(x) \tag{7.5}$$

Only the first term of the series is required in order to describe a sinusoid. This curve is shown in Figure 7.7 for an R ratio of 0.1, the mean occurring at a multiple of 0.55 times the applied load, the maximum at a multiple of 1.0 times the applied load and the minimum at 0.1 times the applied load.

7.6.1 Selection of R-ratio

For load controlled tests, the R-ratio is defined as the ratio of minimum stress to the maximum stress:

$$R = \frac{\sigma_{min}}{\sigma_{max}} \tag{7.6}$$

Where σ_{max} is the maximum stress in the fatigue cycle and σ_{min} is the minimum stress in the fatigue cycle. An R ratio of 0.1 was selected in order to ensure that conditions were created where progressive plastic strain accumulation on a per cycle basis could occur in a number of grains within the strut models. This was necessary, due to the limitations imposed by the Linear Kinematic Hardening model utilised in this work and described in Section 7.4.

7.6.2. Loading

A negative pressure load (tensile stress) of 450MPa is applied to element faces making up the right-hand boundary of the model as shown in Figure 7.8.

7.7. Output requests of the Finite Element Analyses

Four types of data are extracted from the models:

- Contour plots showing Equivalent Plastic Strain Accumulation (PEEQ[1], a field value)
- History plot of Equivalent Plastic Strain Accumulation for each integration point within each element
- The overall displacement of the structure is obtained from a history plot of U1 (displacement in the 1 or X direction) for node COR_RB (as shown in figures 7.5 and 7.6).
- The displacement, U2 (displacement in the 2 or Y direction) of nodes that make up the top and bottom surfaces of the structure. This is related to the surface roughness.

The output from the modelling work must be of a form that contributes to the understanding of the experimental behaviour, hence the selection of the above-mentioned data types. The models must be able to mimic the experimentally observed

---

[1] The acronym PEEQ and equivalent term Equivalent Plastic Strain will be used interchangeably

size-related phenomena. Conclusions regarding the cause of the primary size effect (i.e. endurance limit related size effect) can then be drawn.

7.7.1. Selection of Equivalent Plastic Strain (PEEQ) as a damage parameter

Contour plots of plastic strain (PEEQ) provide an excellent visual indication of the occurrence of strain localisation within the M-J2 models used in this work.

7.7.2. History plot of PEEQ accumulation

The history plot of PEEQ is an attempt to provide quantitative information on the effect of strain localisation within the different sizes of struts under investigation. A particular grain orientation is selected (one which will accumulate plastic strain on each cycle at the R ratio and maximum stress used, in the case presented here, CRY37), and the PEEQ accumulation history for each grain of that type within a strut is outputted. This operation is performed for all struts in a series, the series being 14 µm, 19 µm, 28 µm, 75 µm and 150 µm (75 µm with symmetry boundary conditions). The *average* PEEQ accumulation within grains of this orientation is then calculated for each series and comparisons can then be made between the series.

There are several advantages of this method:

- The same grain type/orientation is investigated for all struts, therefore a direct comparison between struts of different widths are possible.
- Grains are randomly distributed throughout the strut, looking at PEEQ accumulation within the grains will give a good indication as to the nature of the PEEQ accumulation format within the structure as a whole.

- Studying the maximum and minimum PEEQ values that occur within grains will give information on the singular, nodal maximum and minimum values. This can be related to strain localisation.

Each grain is composed of 18 eight-noded CPEG8R elements. These reduced integration elements have four integration points each as shown in Figure 7.9. The PEEQ history for a grain is calculated by averaging the PEEQ histories of all integration points (a total of 72 integration points) within the grain.

7.7.3. Total elongation of struts

This parameter can easily be examined with the finite element fatigue simulations of the various strut sizes. The total elongation of the strut will be represented by the displacement of node COR_RB (Figures 7.5, 7.6). The value of U1 is extracted for each strut at 20 cycles and the values are compared. These values are representative of the total plasticity in struts at the point where the analyses stopped. Different values of total elongation indicate that there are different levels of plastic strain within the struts. Greater total elongation indicates that there is a higher level of plastic strain within a strut. However, no information on the distribution of that plastic strain will be provided by this analysis.

7.8. Surface Roughness (R_a) value

Interferometry refers to the use of the principle of interference of light waves to study microscopic surface features (refer to section 6.2.1 for a more comprehensive description of the technique). Interferometric studies of the surfaces of runout (10^7 cycles completed without failure) experimental specimens revealed that strain localisation was occurring, and that this could be verified by measuring the variation in R_a values on a surface. The method for calculating R_a is described in Figure 5.10. As a result of the microstructural representation within the finite element models, a form of surface roughness occurs. The R_a values for these surfaces can be calculated and comparisons based on these calculations can be made between the surfaces of different width specimens. The methodology employed in extracting the R_a values is described here and in Figure 7.11.

The X and Y nodal coordinate values for top and bottom surface nodes for undeformed conditions at zero load and zero time, and deformed conditions at 450MPa, 20 cycles and R=0.1 were outputted for a selection of struts. "COOR1" refers to the X-coordinate values, while "COOR2" refers to the Y-coordinate values. There are therefore four data sets:

1. Undeformed COOR1 (undeformed X-coordinates)
2. Deformed COOR1 (deformed X-coordinates)
3. UndeformedCOOR2 (undeformed Y-coordinates)
4. Deformed COOR2 (deformed Y-coordinates)

The coordinate sets were imported into excel, and where necessary, use was made of the Excel sort function to arrange data in a manner that allowed the surface profile to be plotted correctly as shown in Figure 7.11.

7.8.1. Undeformed surface measurement

The nodal coordinates of the undeformed surfaces (Top and Bottom) are calculated from the strut of interest in its undeformed state. For a surface in this state, the Y-values remain constant and the X-values range from 0 – 0.5 mm.

7.8.2. Best fit line

This value represents the best fit line (a line in 2D, a plane in 3D) to the deformed surface. It is calculated as the average of the deformed Y-coordinates data column. The use of the average function to calculate the best fit line can be justified as there are over one thousand data points in this column.

7.8.3. Deformed surface measurement

The X and Y nodal coordinate values for top and bottom surface nodes in the deformed state at 450 MPa, 20 cycles and R=0.1 were outputted for a selection of struts. For a surface in this state, both X-values and Y-values will vary.

7.8.4. R_a - average roughness

The surface profile will rise above and fall below the average or best fit line; it is therefore necessary to calculate the absolute value of the deviation in the plane of the Y-axis of each point from this line. The R_a is then the arithmetic average deviation of points on the deformed surface from the best fit line and is calculated as follows:

$$R_a = (|Y_1| + |Y_2| + |Y_3| \dots\dots\dots\dots\dots.. + |Y_n|)/\mathrm{n} \tag{7.7}$$

where Y_x is the absolute value of each point and N is the total number of discrete points.

7.8.5. Categories No. 1 and No. 2

- No. 1: In an attempt to see if sampling length would influence the results, the strut was divided into 50um segments, i.e. 0-50 μm, 51-100 μm ….. etc. The best fit plane was then calculated for each 50um segment, as was the Ra value for each segment.

- No. 2: The best fit plane as calculated for the 500 μm length was used to calculate the Ra value for each 50 μm segment.

COOR2 AVERAGE refers to the best fit plane calculated from the entire COOR2 (Y value) column. R_a AVERAGE refers to the R_a value calculated using COOR2 AVERAGE.

References

[7.1] Wiersma, S., Taylor, D. (2005) Fatigue of materials used in microscopic components. *Fatigue Fract. Engng Mater. Struct.* **28**, 1153-1160
[7.2] Weiss, S., Meissner, A. and Fischer, A. (2009) Microstructural changes within similar coronary stents produced from two different austenitic steels. *Journal of the Mechanical Behaviour of Biomedical Materials* **2**, 210-216
[7.3] Murphy, B.P., Savage, P., McHugh, P.E., Quinn, D.F. (2003) The stress-strain behaviour of coronary stents struts is size dependent. *Annals Biomed. Engng* **31**, 686-691
[7.4] Connolley, T., McHugh, P.E., Bruzzi. M. (2005) A review of deformation and fatigue of metals at small size scales *Fatigue Fract Engng Mater Struct* **28**, 1119-1152
[7.5] Asaro, R.J., Needleman, A. (1985) Acta Metallurgica 33 (6) 923-953
[7.6] Harewood, F.J., McHugh, P.E. (2006) Comparison of the implicit and explicit finite element methods using crystal plasticity. *Comput Mater Sci* **39**, 481-494
[7.7] Ilie, D., (2010) PhD thesis, NUI Galway
[7.8] Dieter, G.E. (1976) Mechanical Metallurgy, 2nd Ed., McGraw-Hill
[7.9] Suresh, S. (2004) Fatigue of Materials, 2nd Ed.,Cambridge University Press
[7.10] A C-program for MT19937: Coded by Takuji Nishimura, considering the suggestions by Topher Cooper and Marc Rieffel in July-Aug. 1997. Copyright (C) 1997 Makoto Matsumoto and Takuji Nishimura.
[7.11] ABAQUS Analysis User's manual V6.5, ABAQUS Inc., Providence, RI, USA

Table 7.1. Model specifications.

Model Width [μm]	**Model Length [μm]**	**No. of grains**	**Grain size: specimen width ratio**
14	500	362	3
19	500	452	4
28	500	633	6
75	500	1555	12

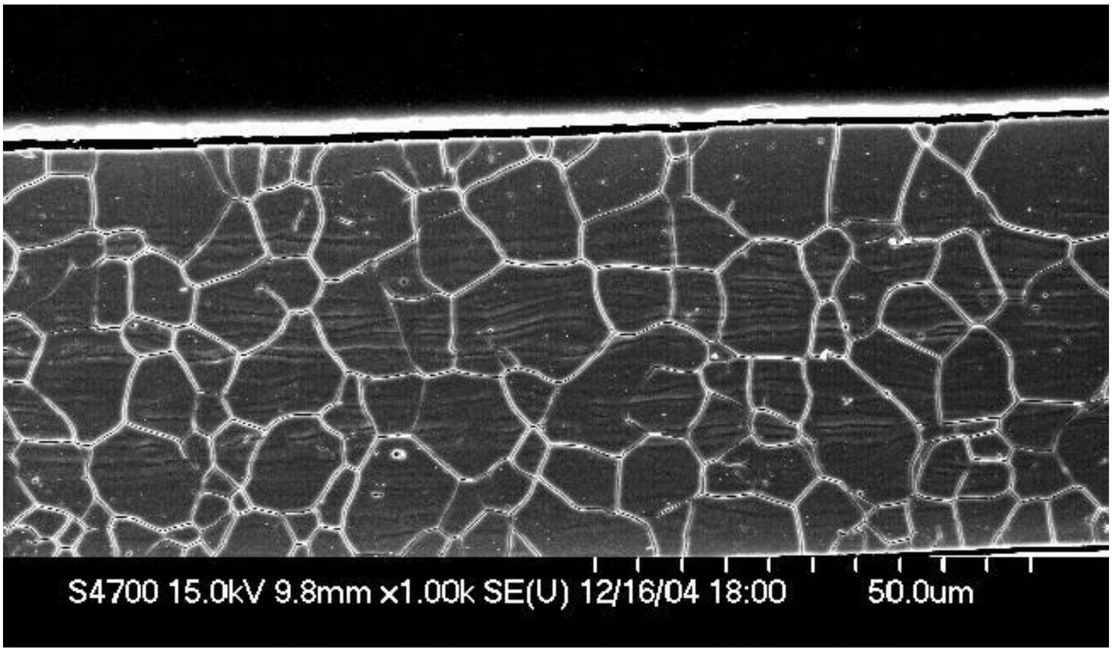

Figure 7.1. Micrograph of a polished and etched sample of 316L stainless steel with 10 μm grain size (courtesy Helen Cuddy, NCBES, NUI Galway).

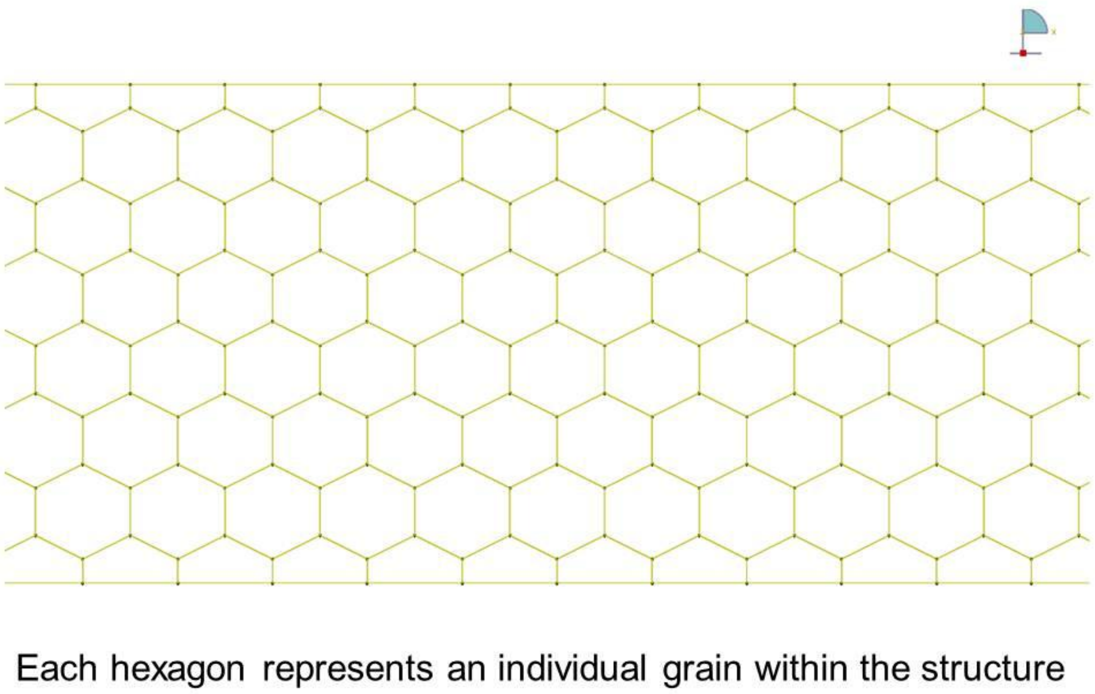

Figure 7.2. Section of strut showing both geometry of the model and the arrangement of the hexagonal grains.

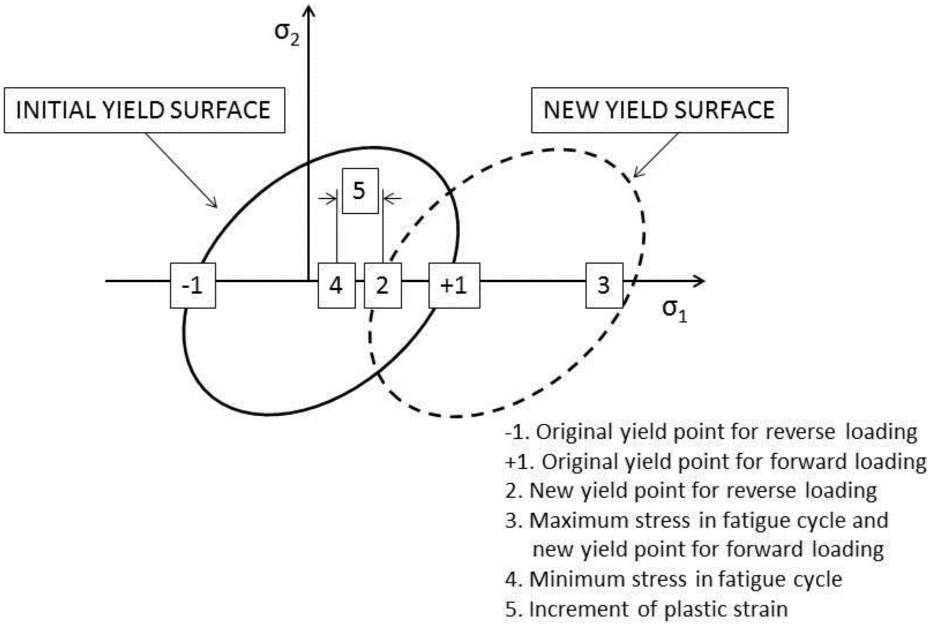

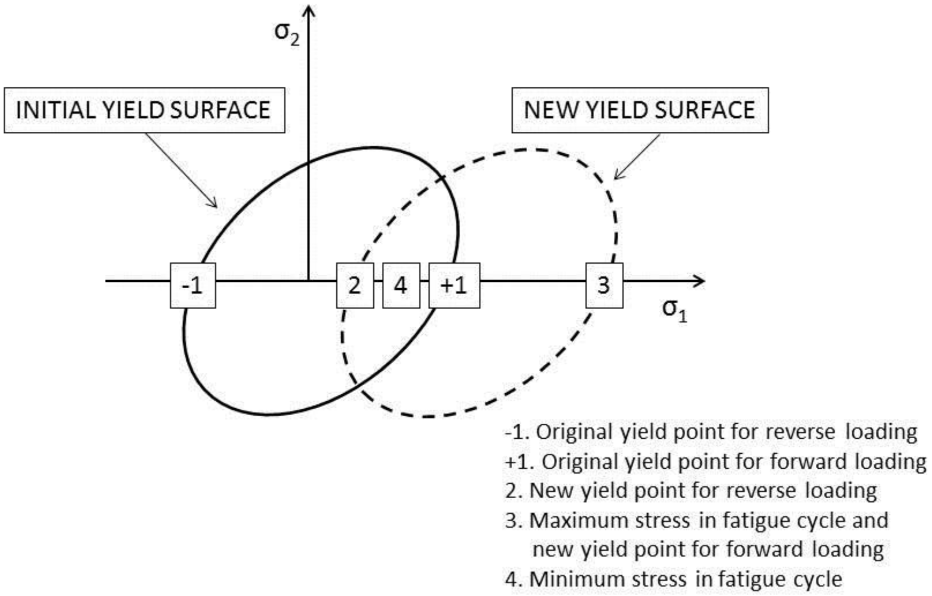

(b)

Figure 7.3(a) Progressive yielding will occur as the minimum stress in the fatigue cycle (4) is lower than the new yield point for reversed loading (2). An increment of plastic strain (5) will be accumulated on each cycle (b) Case of yield on first cycle only (non-progressive).

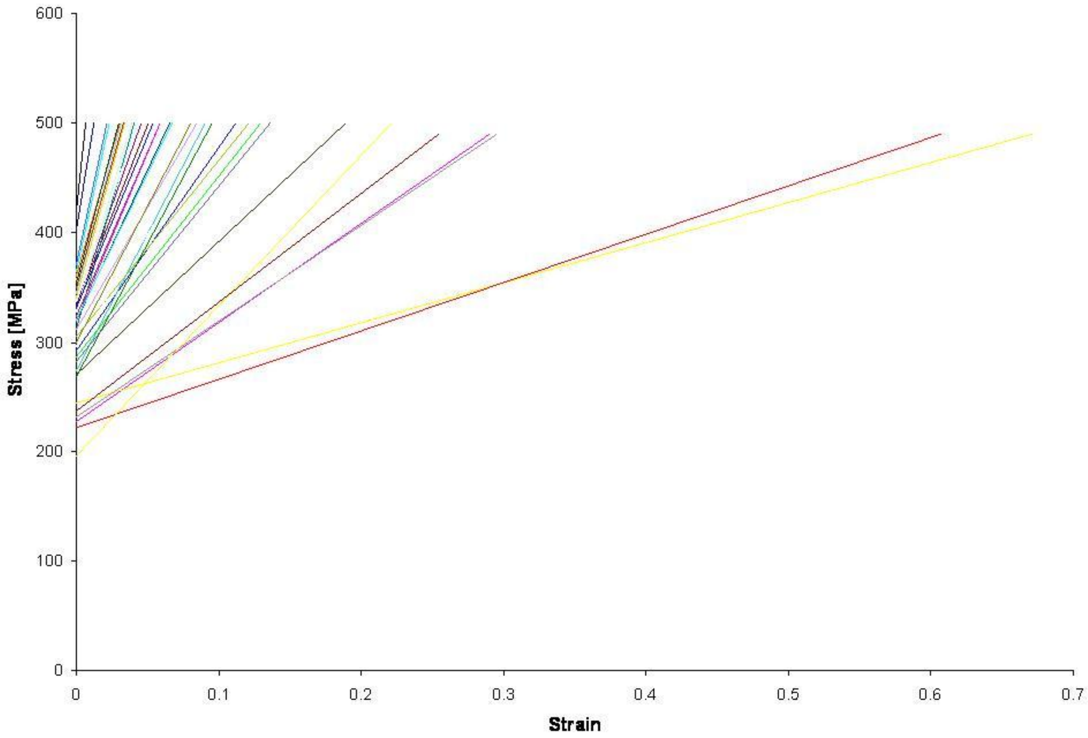

Figure 7.4. Hardening curves for 43 different crystal orientations.

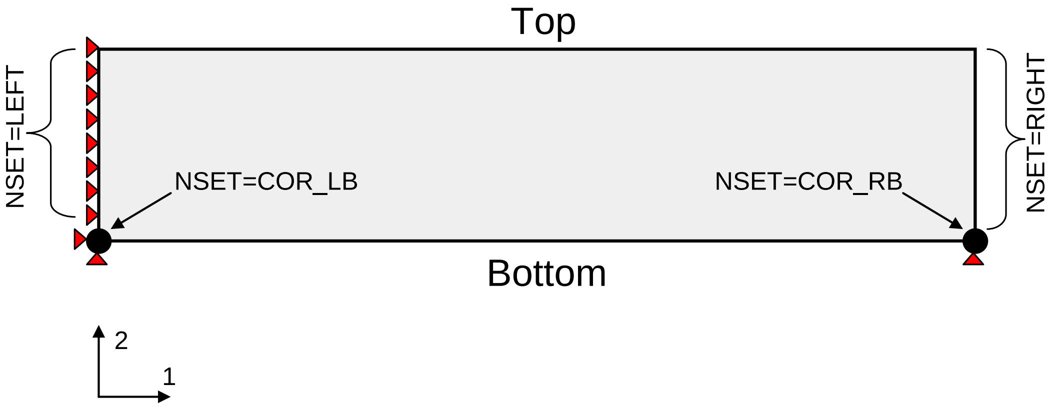

Figure 7.5. Schematic representation of boundary conditions for stand-alone struts. NSET is an ABAQUS abbreviation for “node set”.

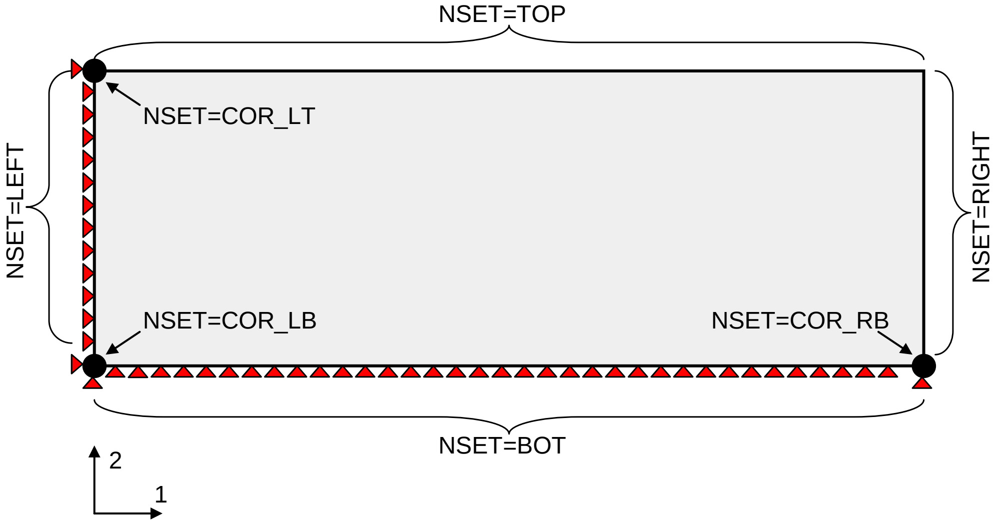

Figure 7.6. Schematic representation of symmetry boundary conditions as applied to 75 µm strut

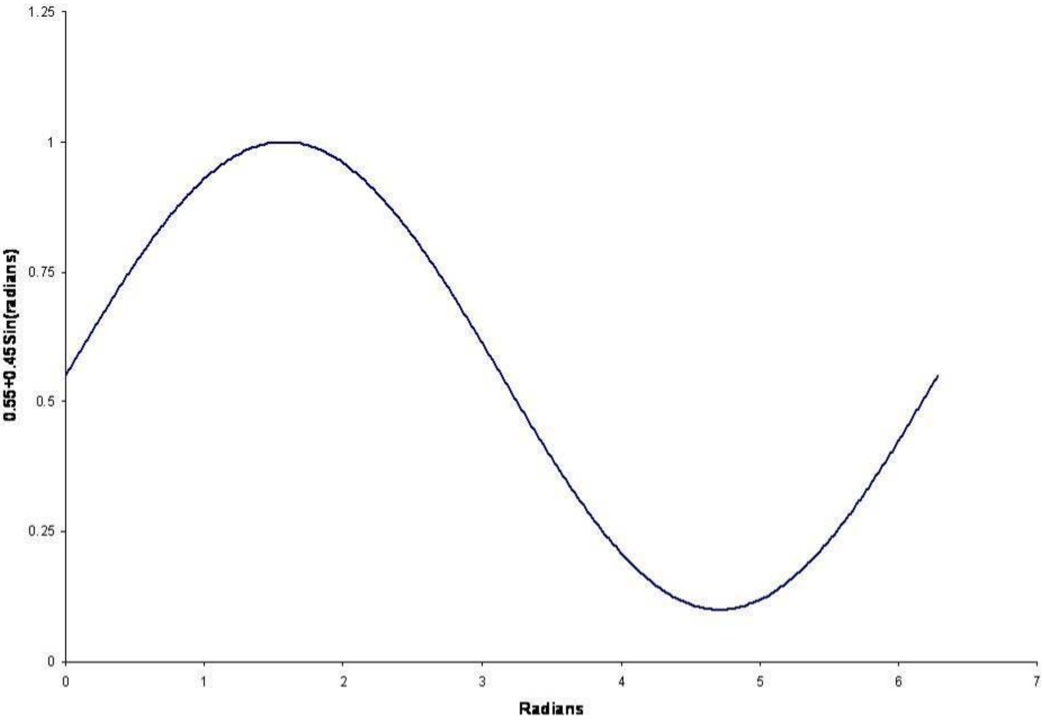

Figure 7.7. Sinusoid of the form used in the fatigue simulations.

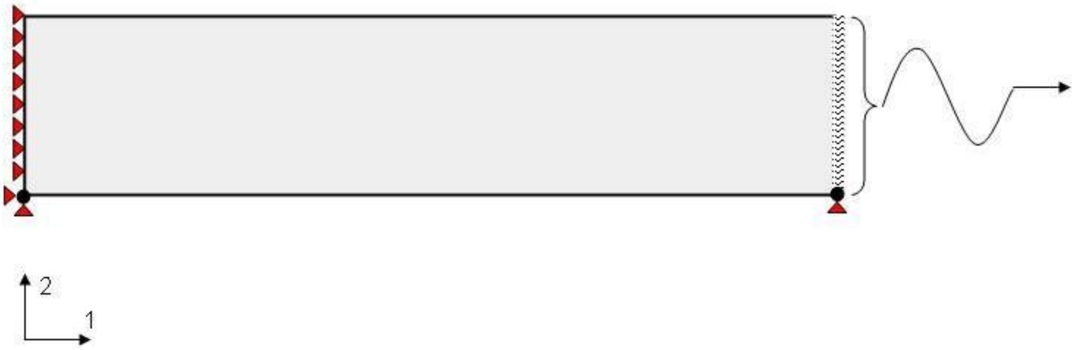

Figure 7.8. Distributed load on right-hand boundary of the model.

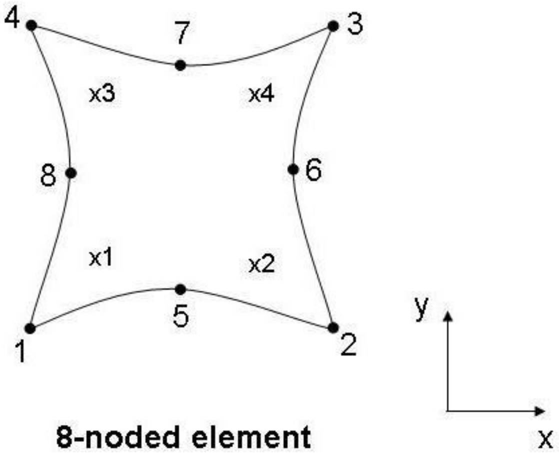

Figure 7.9. 8-noded element showing position of integration points, after ABAQUS Analysis User’s manual V6.5.

Surface roughness, R_a , is calculated as follows:

1. Measure the deviation from the centre-line (best fit line), i.e. Y_1, Y_2, etc.
2. Take the absolute value of each of these measurements
3. Calculate the average of the measurements

$$R_a = (|Y_1| + |Y_2| + |Y_3| \ldots\ldots\ldots\ldots\ldots\ldots + |Y_n|)/n$$

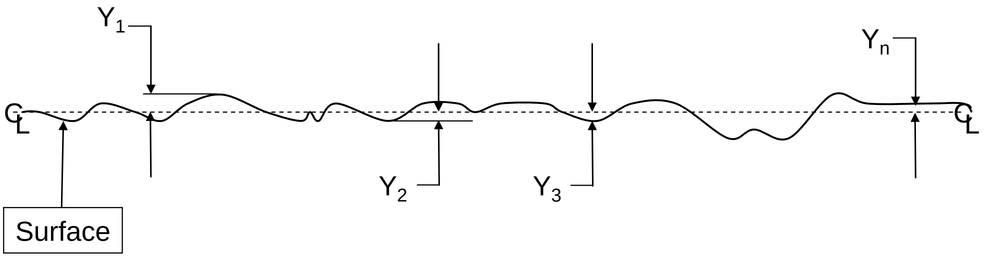

Figure 7.10. Calculation of surface roughness.

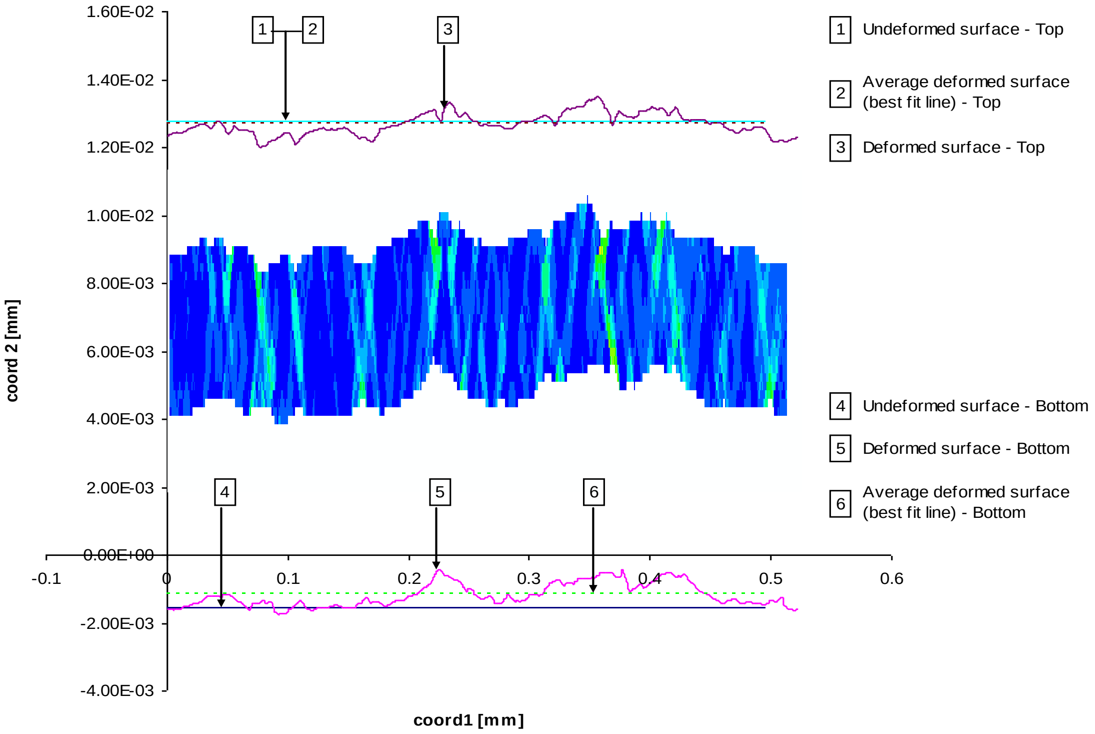

Figure 7.11. Surface roughness parameters. The plot features a foreshortened contour plot to show that strut surfaces are matched by those plotted by the method described here. In the case of the 14μm strut presented here, $\boxed{1}$ and $\boxed{2}$ are almost collinear.

COMPUTATIONAL MODELLING RESULTS FOR MICROSCALE SPECIMENS

8.1. Introduction

It has been shown in Chapter 5 that a size effect in fatigue exists for 50 μm specimens. This size effect reduces the fatigue limit of these microscale specimens to below that of 75, 100 and 150 μm specimens, recognising that the strut thicknesses are the same at 60 μm. The strain history data generated during fatigue testing show that a significant portion of plastic deformation occurs at the beginning of the test. Micrographic examination of the surfaces of post-test specimens indicates that strain localization occurs to a greater extent in 50 μm specimens than in the larger specimens. Surface roughness measurements confirm this. It is therefore necessary to further investigate this phenomenon of strain localization and to determine if it is matched by plastic strain localization within the grains. This is carried out with the aid of computational finite element models of the struts.

8.2. Contour plots of struts

A small number of cyclic loads at a common load ratio and maximum stress were applied to the various strut models. The idealized crystalline structure of the models describes the inhomogeneous nature of strain distribution. As an initial approach, a visual examination of the contour plots of the deformed struts allows for a simple, qualitative evaluation of the levels of strain localization.

8.2.1. 14 μm strut

An example of a 14 μm strut is shown in figure 8.1(a). A non-uniform distribution of plastic strain within the strut is evident after the 20 cycles of loading. More importantly, the contour plot shows that the strain distribution is localised. Two regions have been highlighted; Region 1 in figure 8.1(b) shows the region containing the node with minimum PEEQ value, while Region 2 in figure 8.1(c) shows the region containing the node with maximum PEEQ. These nodal values have been associated by observation with regions of high and low deformation. There is a considerable difference in the level of plastic strain accumulation between these two regions, even at 20 cycles, with Region 2 beginning to show the early stages of necking, while Region 1 (and other regions within the strut) is relatively undeformed. Should such strain localization occur during a real-life fatigue test, it is possible that a fatigue crack would initiate in and propagate through the region identified as Region 2. Figure 8.2 shows that the majority of plastic strain is accumulated on the first cycle of the fatigue simulation (as is the case during the fatigue experiments) with additional increments of plastic strain being contributed during each load application. In reality, such high levels of localised plastic deformation occurring early in the life of the specimen would undoubtedly have a detrimental effect on the fatigue life of the specimen.

As the strut is so narrow, with a grain size to specimen width ratio of 3, the occurrence of a through-thickness region of strain localization is clear. Indeed, there are so few grains though the thickness of this strut, and consequently the level of constraint is compromised to such a degree that the material behaviour of one or two grains could influence heavily the behaviour of the entire strut.

8.2.2. 19 μm strut

A 19 μm strut shown in figure 8.3(a) also exhibits the phenomenon of strain localization with bands of higher strained grains occurring at irregular intervals along the length of the strut. It was initially though that there was some significance attached to the fact that the high strain regions occur at orientations of ± 45º. However, grains (other than adjacent grains) are arranged with respect to each other at this angle, so should a region of localised plastic strain extend from one “layer” of grains into another “layer”, a band orientated at ± 45º will be created.

Again, two regions have been identified; Region 1 in figure 8.3(b) shows the node with the highest PEEQ value, and Region 2 in figure 8.3(c) shows the node with the lowest PEEQ value. As stated previously, these nodal values have been associated by observation with regions of high and low deformation. As the 19 μm struts have five grains through the thickness, the level of constraint afforded by the structure is slightly greater than that of the 14 μm struts.

8.2.3. 28 μm strut

The 28 μm strut has six through-thickness grains. As this number increases, the probability of finding a through-thickness band of softer orientation grains is reduced. Such bands are visible in 14 and 19 μm struts and serve as centres for intense strain localization. In this 28 μm strut, strain localization is evident, but the effects are not as pronounced as those for the 14 and 19 μm struts. However, the struts are narrow enough such that coalescence of two separate, softer bands of grains as shown in figure 8.4(c), leading to the creation of a single, through-thickness band. In the example shown here, the element with minimum equivalent plastic strain shown in figure 8.4(c) and the element with maximum plastic strain value in figure 8.4(d) both occur within the same grain indicating that regions of low and high plastic deformation occur immediately adjacent to one another. Such behaviour has been observed within the 14 and 19 μm series (with three cases in 14 μm series and two in the 19 μm series).

8.2.4. Comparison of 14 μm and 75 μm struts

Figure 8.5 has been arranged for the purposes of visual comparison and shows the contour plots of a selection of five 14 μm struts in figure 8.5(a) and five 75 μm struts in figure 8.5(b), each with the assignment of a random set of grain orientations, as described in Chapter 7. Differences in the distribution of plastic strain within the 14 μm and 75 μm struts are immediately obvious. Relatively speaking, there is a much more regular pattern of plastic strain distribution within the 75 μm samples. While there are regions of higher strain within these struts, the greater strut width and corresponding higher grain size to specimen width ratio (12 full grains through the thickness) prevents the formation of through-thickness bands of softer orientation grains simply by virtue of the fact that the probability of achieving such an arrangement decreases with increasing strut width. The additional constraint afforded by the increased number of grains will also stiffen the strut and reduce the influence of individual grains on the overall behaviour of the strut. For narrower samples the behaviour of one grain or two or more neighbouring grains can heavily influence the overall behaviour of the strut. For the wider samples, the strut influences more the behaviour of the grain, to the point where bulk material properties are achieved and further increases in strut width/grain size specimen width ratio have no effect of the strut behaviour.

8.3. History plot of PEEQ Accumulation

The generation of history plots of equivalent plastic strain (PEEQ) is an attempt to provide quantitative information on the effect of strain localization within the different sizes of struts under investigation. As there are many hundreds of grains within the struts, it is not practical to evaluate the plastic strain accumulation history for each grain. Instead a particular crystal orientation (labelled CRY37) is selected, one which will nominally accumulate plastic strain on each cycle at the R-ratio and maximum stress used, and the PEEQ accumulation history for each grain of this type within a strut is calculated by the ABAQUS © processing software. The information is outputted in the form of a PEEQ accumulation history plot for each integration point within an element as shown in figure 8.2(a). With each grain made up of 18 elements and with four integration points per element, there are a total of 72 curves per grain. The average of these curves is then taken to produce the PEEQ accumulation history for the CRY37 grain as shown in figure 8.2(b). This operation is performed for the selected CRY37 grain orientation in all struts (of which there are ten) in a series, each series being 14 µm, 19 µm, 28 µm, 75 µm, and 150 µm in width and having a random grain orientation / property assigned to it. (The 150 µm strut is represented by the 75 µm with symmetry boundary conditions).

The *average* PEEQ accumulation within grains of this orientation is then calculated for each series and comparisons can then be made between the series. There are several advantages to this method:

- Grains of the same crystal orientation are investigated for all struts; therefore direct comparison between struts of different widths is possible.
- Grains are randomly distributed throughout the strut; looking at PEEQ accumulation within the grains will provide a good indication as to the nature of the PEEQ accumulation format within the structure as a whole.
- This approach has been adopted as a convenient and time-efficient method of evaluating the internal mechanisms of strain accumulation.

8.3.1. Strain evolution in grain ‘CRY37’

There are 43 different crystal orientations identified for allocation to the grains represented within the computational models (struts) developed as 43 different material properties. Each grain within a strut can be assigned any one of these orientations / properties at random. There is no texture effect incorporated in the models. As described previously, in an effort to study the internal mechanisms of plastic strain accumulation that contribute to strain localization, one grain type (CRY37) was selected and the PEEQ accumulation history for every grain of this type within each strut was determined.

Crystal orientation CRY37 was chosen as it had the lowest yield point and 3rd lowest hardening rate, as detailed in Table 8.1. At an R-ratio of 0.1 and σ_{max} of 450 MPa, this crystal orientation will accumulate plastic strain on a per cycle basis within the limitations imposed by the linear kinematic hardening model. The averaged results presented in figure 8.6 were created by selecting the PEEQ accumulation history for all CRY37 grains within a strut and averaging those values to produce a single curve of CRY37 PEEQ accumulation for that strut. This was done for each of the ten computational model per strut width in the series and the curves so generated were in turn averaged to produce a single average curve of PEEQ accumulation within CRY37 orientation grains for the strut series. Figure 8.6 shows the evolution of plastic strain within each of the strut series. There are clear differences between the levels of PEEQ within the 14 μm and 19 μm struts, which are quantitatively similar, and the 28 μm, 75 μm and 150 μm struts. This demonstrates that grains which have been assigned a CRY37 crystal orientation will accumulate increased levels of equivalent plastic strain as the strut width decreases. R-ratio and maximum stress remain the same for all model series; therefore, the increase in plastic strain levels is associated only with decreasing strut width. The CRY37 grains are distributed at random throughout the struts; figure 8.7 shows that there is a significantly higher overall level of plastic strain within CRY37 orientation grains in the 14 μm struts when compared to the 19, 28, 75 and 150 μm struts. In fact, the minimum value of average plastic strain value calculated for a single 14 μm strut is greater than the maximum value of average plastic strain value calculated for a 150 μm strut. When the actual number of grains through the strut thickness (the ratio of grain size to specimen width) is taken into account, the plot shown in figure 8.8 is generated. Table 8.2 lists the calculated ratios. Here, the nature of the non-linear relationship between strut size and plastic strain accumulation is exposed. On average, the narrower struts have higher levels of plastic strain within the CRY37 orientation grains. The values that contribute to the calculation of this inter-strut arithmetic mean are also greater in range and in standard deviation within the narrower struts. Table 8.3 lists the calculated range and standard deviation values. Relative to the wider struts series, the 14 μm and 19 μm series have:

- Higher average PEEQ within CRY37 orientation grains
- Higher maximum PEEQ values
- Greater range of PEEQ values within CRY37 orientation grains and
- Greater standard deviation within those values

8.3.2. Intra-strut variation

As the CRY37 orientation grains are dispersed randomly throughout a strut, it is possible to relate the level of plastic strain accumulation within these grains to the general state of plastic strain accumulation within the strut. Greater range and scatter of plastic strain values within the grains of a strut indicates non-uniformity of mechanical behaviour within that strut. Conversely, lower range and scatter of granular plasticity indicates greater uniformity in mechanical behaviour. The greater the intra-strut variation in plastic strain values, the more non-uniform the distribution of plastic strain and the more pronounced the effect of strain localization. The variation in accumulated plastic strain within individual struts of width 14 μm and 150 μm is shown in figure 8.9, again based upon the plastic strain within CRY37 orientation grains at 20 cycles. The average of the plastic strains within all these grains in a strut, the maximum and minimum values of plastic strain within grains and the standard deviation within the granular plastic strains values are plotted. 14 μm and 150 μm struts were selected for comparison as the differences will be greatest between these two widths.

The occurrence of strain localization as suggested by the PEEQ contour plots of the various struts (figures 8.1, 8.2, 8.3) is confirmed by the data presented in figure 8.9. The plot shows considerable variation in the levels of plastic strain within individual 14 μm struts, while the 150 μm series behaves in a manner approaching that of a bulk material that can be assumed to behave homogenously. Relative to 150 μm struts, the individual 14um struts have:

- Higher levels of average PEEQ within CRY37 orientation grains
- Higher maximum PEEQ values
- Greater range of PEEQ values within CRY37 orientation grains and
- Greater standard deviation

The models generated in this work therefore indicate that the greater levels of scatter within the 14 μm series will likely result in scatter of experimental fatigue testing results and the higher levels of average PEEQ may well translate to shorter fatigue lives.

8.3.3. Maximum value of equivalent plastic strain within struts

Data presented to this point have focussed on equivalent plastic strain accumulation within a particular grain orientation, CRY37. In figure 8.10 , the plot shows the maximum PEEQ values within the struts presented independently of grain orientation. The maximum nodal PEEQ value was extracted from each strut in a series and is represented here as an average value per series with accompanying standard deviation. It is interesting to note that though the values have been selected independently of grain orientation and are based on a single value per strut, the trend as presented in figure 8.8 is maintained. The grain orientation associated with the maximum nodal PEEQ values in each of the struts of the series was then identified. The frequency of occurrence of these grain orientations within the 10 struts of each series is plotted in figure 8.12 It is clear that the maximum equivalent plastic strain (PEEQ) values occurs in grains other than CRY37 in a majority of cases. As the data sets that are used to generate the curves shown in figures 8.8 and 8.10 are somewhat different, (other than the fact that the PEEQ values of grain CRY37 are common to each data set), it is argued that the conditions which lead to the trend in figure 8.8 are the same as those that lead to the trend in figure 8.10. The conditions are those of reduced constraint due to reduction in specimen width and the consequent reduction in the number of grains through and within a sample.

8.3.4. Minimum value of equivalent plastic strain within struts

While not as pronounced (there is an order of magnitude in the difference between minimum and maximum PEEQ values), a trend also exists in the minimum PEEQ values observed within each strut series. When combined with the data presented in figure 8.10, this trend in the minimum PEEQ values supports the strain localization argument. The narrower struts (14 μm and 19 μm) have the greatest maximum PEEQ values and average maximum PEEQ values (figure 8.10) and the lowest minimum PEEQ values and average minimum PEEQ values as shown in figure 8.11.

For highly constrained/bulk materials, it is expected that there will be some repeatability in the grain orientation and plastic strain relationship, i.e. after a given number of cycles, the highest PEEQ value will occur in grains of the softest orientation (lowest hardening rate) while the lowest will occur in those of the hardest orientation. In low constraint struts, where softer regions exist wherein plastic strain is localised, the maximum PEEQ value will occur within the softest grain in that region. As these regions themselves occur because of preferentially orientated groups of grains, there will be a bias toward grains of softer orientation, as is the case for the 14 μm series shown in figure 8.12. The minimum PEEQ values occur within grains of harder orientation, as shown in figure 8.13. This is most certainly the case for the 150 μm struts, where the minimum PEEQ values occur in the grain of hardest orientation. This illustrates that the behaviour of specimens with greater grains size to specimen width ratios (and hence, higher levels of constraint) is more predictable. This is in accordance with observations relating to bulk material behaviour.

8.4. Macroscale deformation of struts.

A comparison of the total axial strain of the various struts is plotted in figure 8.14. In general, the trend is as expected; the narrower samples undergo greater elongation during the 20 cycle fatigue simulation. This is reflective of the higher levels of plastic strain that occur within the narrower struts. In the 14 μm example shown in figure 8.15(a), the effect of strain localization is evident. This sample has elongated to a greater extent than any other, and yet the strain is localised within no more than six regions, with one region in particular (highlighted) contributing significantly to the total level of deformation. The level of constraint is so low that the softest[1] band of grains has accumulated the majority of plastic strain, with very little strain distribution occurring throughout the specimen, even within the other soft bands. The average elongation of the 19 μm series is marginally greater than that of the 14 μm series (figure 8.14). It is proposed that the reason for this is due to the additional constraint afforded by the wider structure which allows for strain distribution to occur in more than one soft band of grains; more than one region of strain localization is activated to a significant degree and the total strain is greater as a result. As the strut width increases and the effect of softer regions are marginalised, the plastic strain is distributed in a more uniform manner as shown in figure 8.15(c)-(e).

8.4.1. Incremental Strain

Plots of both experimental data and modelling data are shown in figures 8.16 and 8.17 respectively. Figure 8.16 shows that majority of displacement associated with an experimental specimen occurs within the first cycle, during ramp-up to the required maximum load (the fatigue tests are load controlled). On the first cycle the displacement amplitude is at a maximum. Once the maximum load has been achieved, the displacement amplitude is reduced to a level consistent with that required by the R-ratio, and plastic strain is accumulated on a per-cycle basis at a much reduced rate. It has been shown in figure 8.14 that the gross elongation of the narrow specimens (14 μm and 19 μm) is greater than that of the wider specimens (28 μm, 75 μm, 150 μm). Figure 8.17 shows that independently of the first cycle, the increments of strain

---

[1] The term “soft” refers to grains of a favourable orientation for plastic deformation. A “soft region” is one made up of grain(s) which are orientated such that the critical resolved shear stress is reached earlier than in most grains.

accumulated during cyclic loading contribute to this behaviour as the narrow samples accumulate more plastic strain on a per-cycle basis than the wider samples. There is also a much greater range of strain values within the 14 μm and 19 μm series. The data for this analysis were generated by studying the displacement that occurs within the various models from cycles 0.25 to 19.25, as defined by figure 8.16.

Figure 8.18 clearly shows that differences exist in the magnitude of the incremental cyclic strains for different samples, where three struts, with respective displacements normalised to remove the effect of ramp-up, show small differences in displacement at 20 cycles. The differences apparent in figure 8.16 are not significant enough to account for the differences in gross material behaviour shown in figure 8.14. The modelling work has revealed that a material behaviour based size effect exists in the displacement of struts upon the initial cycle (cycles 0 to 0.25), where the gross displacement of the narrow samples is greater, and during subsequent cycles, where the magnitude of the increments of plastic strain induced by cyclic loading are greater in the narrow struts.

8.4.2. Strain localization after the first cycle

It has been shown for the models that there are higher levels of equivalent plastic strain within the narrower 14 μm and 19 μm struts after the first cycle. It has also been shown that the gross deformation of the struts at 20 cycles is greater in the case of the narrower struts; therefore, in addition to the greater level of plastic strain accumulated on the first cycle, the increments of plastic strain associated with each application of the cyclic load are also greater. In some cases, the potentially deleterious effect of strain localization on the first cycle is compounded by the fact that subsequent increments of plastic strain also occur within this region as shown in figure 8.19. This does not occur for all samples, but where it does, it will lead to a further reduction in fatigue life

While the linear kinematic hardening model is of limited applicability once an appreciable amount of plastic deformation has occurred (hardening continues at a constant rate, none of the complexities associated with saturation are captured), differences observed in the initial stages of the fatigue test will remain relevant to the real life situation. The 20 cycle limit serves primarily to amplify differences in behaviour that occur between 0 and 5 cycles.

8.5. Surface roughness effects

The studies described thus far demonstrate that the mechanical behaviour of the struts is size dependent. The internal mechanisms of strain accumulation have been investigated through analysis of contour plots of equivalent plastic strain (PEEQ) and studies of accumulation within a particular grain type. Interferometric examination of the surfaces of post-fatigue test experimental specimens have shown that the non-uniform distribution of plastic strain in narrow struts is matched by higher levels of and greater variation in, surface roughness along the specimen length. The results of the analysis of surface roughness of the finite element models, produced by the method described in Chapter 7, section 7.8 are presented in figure 8.20. The surface roughness, R_a, of a selection of struts from three different series, 14 μm, 28 μm and 75 μm is compared here. As each strut has two surfaces, the “top” and “bottom” surface, there are two R_a values per strut. The computationally determined roughness values clearly show a trend in keeping with that identified thus far, i.e. a size effect associated with the behaviour of narrower specimens. In this case, the surface roughness increases as the specimen width decreases. This is a non-exhaustive study, only a small number of struts have been selected at random. However, it is sufficiently detailed to show that the narrower specimens (14 µm) have a higher level of surface roughness than the larger specimens (75 µm).

It must be noted that the factors which contribute to the surface roughness of the finite element models are not the same as those that contribute to the roughness values of the experimental specimens. The R_a values of the experimental work are derived from topographic measurements and as such are due to topographic features such as slip bands, grain boundaries and rotated grains as shown in figure 8.21. The models do not have the capacity to describe energy dissipation through slip band formation or grain rotation, so a different mechanism is responsible for the surface roughness. The models may only absorb energy by distributing it within grains as plastic strain. The R_a value of the models is therefore directly related to the level of deformation within the grains and consequently, within the strut.

It was observed with the 75 µm series that the surface roughness of the “Bottom” surface was lower in all three cases than that of the “Top” surface. Therefore boundary conditions were reversed as shown in figure 8.22 (b) in order to investigate their influence on surface roughness. This reversal involved switching the arbitrarily assigned Top and Bottom surface constraints imposed on the corner nodes, as outlined in Chapter 7. A boundary condition dependence of R_a was observed (figure 8.20), but the trend as described is largely maintained.

8.6. Softer region study

There is much scatter in the results of the experimentally derived fatigue data for the 50 µm specimens, as discussed in Chapter 5. Though the finite element models do not directly represent the test specimens and do not incorporate a failure mechanism, they are capable of predicting a greater variation in behaviour of struts within the 14 µm and 19 µm series (figures 8.10, 8.11, 8.14, 8.16).

A comparison between two different 14µm struts is presented in figure 8.23. Figure 8.23(a) presents a strut wherein intense strain localization has occurred in the region identified as Region A. The severity and intensity of this effect is clearly illustrated in figure 8.23(b) where the equivalent plastic strain histories for grains identified in figure 8.23(a) are shown. It is of no surprise that the grains in the deformed region in figure 8.23(a) Region A (grains 58, 149, 240 and 330) have the highest PEEQ values and continue to accumulate PEEQ on a per cycle basis. However, it is interesting to note that grains which are immediate neighbours of these grains, for example GR329, have accumulated a fraction of the PEEQ in as many cycles, and in most cases, do not accumulate any plastic strain after the first cycle.

In comparison, figure 8.24(a) presents a 14 µm strut, which was subjected to the same global load, with two primary regions of strain localization, identified as Regions A and B. Neither Region A (shown in figure 8.24(b)) nor Region B (shown in figure 8.24(c)) have been deformed to the extent of Region A in figure 8.23(a), and plastic strain is accumulated after the first cycle in only one grain (figure 8.24(b) GR351). Both struts are of the same width and it is clear that their respective fatigue behaviour would differ. As the strut presented in figure 8.23 undergoes much higher localised equivalent plastic strain, it is more likely to experience static modes of tensile failure, with crack growth mechanisms interacting with void growth mechanisms.

8.7. Discussion

In the early stages of the modelling work, an attempt was made to initiate strain localization by seeding a strut with a grain of softer orientation. A grain was assigned a soft orientation and the PEEQ values were requested for all elements within that grain. The PEEQ accumulation history within that grain in a narrow specimen was then compared with that of a grain of identical orientation in a wider specimen. It was expected that such grains in narrow struts would have higher PEEQ values and PEEQ accumulation rates than in wider samples. This was not the case.

It became apparent from the contour plots that this seed did not necessarily accumulate the highest PEEQ value within the structure, nor were the grains where the highest PEEQ value occurred of the softest orientation. It was concluded that it is not the orientation of a single grain that is of importance, rather the orientation of a group of neighbouring grains that combine to create a soft region. In a situation of reduced constraint, when this soft region is loaded to a level sufficient to cause plastic deformation, localization of plastic strain will occur within that region.

An obvious observation is that all grain orientations occur many times within each strut making the above approach entirely redundant. As an evolution of the method, the equivalent plastic strain history of every grain of a particular type within a strut was calculated and an average value for that strut was determined. An average value for the entire series was then calculated. There are clear differences between struts of different widths, with narrower struts having higher levels of PEEQ than wider struts (as shown in figure 8.6). More specifically, the differences indicate that for a given stress, the magnitude of PEEQ within grains is dependent upon the size of the strut relative to the size of the grain (the specimen width: grain size ratio)

The contour plots of PEEQ values reveal a difference in PEEQ accumulation patterns between small and large struts with the smaller struts appearing to undergo a more localised form of PEEQ accumulation. The veracity of this observation was investigated by selecting grains of a particular orientation and by outputting the PEEQ accumulation history of these grains. As the grains are randomly distributed throughout a strut, studying their PEEQ accumulation history will establish if:

- there are differences in the general level of deformation within struts of different widths (inter-strut variation) and
- there are differences in the level of uniformity of equivalent plastic strain distribution within individual struts (intra-strut variation).

In this work, it was shown that there is a higher general level of strain within the 14 μm and 19 μm following cyclic loading, as given in figure 8.14. The total or gross elongation of the narrow struts is greater than that of the wider 28 μm, 75 μm and 150 μm struts.

It has also been shown that relative to the wider strut series, the 14 μm and 19 μm series struts, under conditions of cyclic loading, accumulate higher levels of average PEEQ within CRY37 orientation grains, have higher maximum PEEQ values, greater range of PEEQ values within CRY37 orientation grains and greater standard deviation within the values that contribute to the mean.

In addition to the above findings, it has been shown that under condition of cyclic loading, there is considerable variation in the mechanical behaviour of individual struts within the 14 μm series. On the other hand, 150 μm struts behave in a manner akin to that of a bulk material. Within the 14um series, there is considerable variation in the average accumulated PEEQ within CRY37 orientation grains, the maximum and minimum PEEQ values that occur within the struts and standard deviation of CRY37 values that contribute to the average value. Greater range and scatter of PEEQ values within grains indicates non-uniformity of plastic strain accumulation. Conversely, lower range and scatter indicates greater uniformity in PEEQ accumulation.

The narrower samples (14 μm and 19 μm) experience higher average levels of PEEQ within CRY37 orientation grains. The contour plots, combined with the irregular distribution of plastic strain within the CRY37 grains suggests strongly that strain localization is taking place. The finite element modelling approach has been used to elucidate the mechanisms that contribute to the size-dependent material behaviour in fatigue. The process of strain localization occurring as a result of cyclic loading, as identified initially by the contour plots of PEEQ, has been confirmed as being a size dependent effect, with higher plastic strain levels occurring in the narrow specimens.

It has also been shown that the narrower 14 μm and 19 μm struts have significantly higher maximum values of equivalent plastic strain than the wider 28 μm, 75 μm and 150 μm samples (as shown in figure 8.10). This trend, exhibited by the averaged value of the maximum equivalent plastic strain within each strut series is similar to that generated by the CRY37 study. In both cases, the trend has been attributed to conditions of reduced constraint due to a reduction in specimen width and the consequent reduction in the number of grains through and within a sample. The average maximum equivalent plastic strain value within the 28 μm, 75 μm and 150 μm struts is higher than the average equivalent plastic strain value calculated for the CRY37 grains within the narrow 14 μm and 19 μm. Therefore, it can be concluded that it is not the higher level of PEEQ within CRY37 grains alone (figure 8.8) that causes fatigue failure. However, it is a contributing factor.

The narrower 14 μm and 19 μm struts were also found to have significantly lower minimum values of equivalent plastic strain than the wider 28 μm, 75 μm and

150 μm struts (as shown in figure 8.11). In combination with the above result, the non-uniform nature of plastic strain accumulation within the narrow struts is again highlighted. Plots of both experimental data and modelling data (figures. 8.16 and 8.17) show that a significant portion of displacement is accumulated on the first cycle, during ramp-up to the required maximum load or stress. Figure 8.16 shows that independent of the first cycle, the increments of plastic strain accumulated during cyclic loading also contribute to this behaviour as the narrow samples accumulate more plastic strain on a per-cycle basis than the wider samples.

Interferometric examination of the surfaces of post-fatigue test experimental specimens have shown that the non-uniform distribution of plastic strain in narrow struts is matched by higher levels of, and greater variation in, surface roughness along the specimen length. The modelling work also exhibits similar behaviour, with the narrow struts developing higher levels of surface roughness. It is proposed that while the form of the surface roughness is different in both cases, the underlying mechanism, that of higher levels of non-uniformly distributed plasticity are common to both the models and the experimental specimens.

The mechanical behaviour of a narrow strut is entirely dependent upon the orientation and arrangement of its constituent grains. As the grains are randomly distributed within the strut, the strut will also display an element of randomness in its material behaviour. The narrower the strut, the greater the influence a softer region will have, and consequently, the more random its material behaviour. There does not exist a critical width below which the size effect is suddenly activated, it is more a sliding-scale type relationship, of the form shown in figure 8.10, with progressively narrower struts exhibiting greater variation in material behaviour. The purpose of the modelling work was not to develop a fatigue failure predictive capability but rather to elucidate the mechanisms involved in the experimentally observed size effect. The finite element modelling has demonstrated that a mechanical “size effect” has many different, but inter-related components. It is proposed that the various mechanisms, as identified here, also apply to the real life situation, and it is a combination of the mechanisms that lead to the experimentally observed size effect in 316L stainless steel struts. While the linear kinematic hardening description is limited in its applicability, it is sufficient to describe the evolution of plastic strain within the first few cycles. Such is the nature of a high cycle fatigue test that differences that become apparent at such an early stage will undoubtedly result in, or contribute significantly to, failure of the test specimen. As the specimen size is reduced, the mechanical size effect manifests itself in two ways:

1. A deviation of material performance, generally in the form of a reduction, from bulk material behaviour
2. Greater variation in the material behaviour of apparently identical specimens

8.8. Conclusions

A size effect has been found to exist which influences the behaviour of narrow struts (14 µm, 19 µm) in a manner which would lead to a reduction in the fatigue life of such specimens. Relative to the wider struts, the 14 µm and 19 µm struts have:

- higher average levels of PEEQ within CRY37 orientation grains (which has the lowest yield point) and greater standard deviation within the range of those PEEQ values. It is proposed that this is representative of the state of strain within the strut as a whole.

- greater intra-strut variation in CRY37 PEEQ values indicating non-uniform PEEQ distribution within grains of that orientation and by corollary, non-uniform PEEQ distribution within the struts as a whole
- higher maximum values of PEEQ within each strut
- lower minimum values of PEEQ within each strut
- greater gross deformation of struts with significant strain localization
- higher levels of surface roughness

It is surmised that it is a combination of these factors that lead to a reduction in fatigue life of narrow samples.

Table 8.1. Following page. Crystal orientations and associated rankings based upon yield point and hardening rate. For yield point the rank indicates order of grains in terms of yield point, i.e. position 1 is assigned to grain with the lowest yield point. For hardening slope, position 1 is assigned to the grain with the lowest hardening slope.

	Yield Point	
Type	**Yield Point**	**Rank**
CRY01	236.96	5
CRY02	227.30	3
CRY03	244.25	7
CRY04	363.94	39
CRY05	333.00	28
CRY06	333.38	29
CRY07	311.69	20
CRY08	291.50	15
CRY09	337.46	31
CRY10	337.46	30
CRY11	327.37	26
CRY12	268.64	8
CRY13	345.22	33
CRY14	349.18	35
CRY15	310.83	19
CRY16	356.75	37
CRY17	370.55	40
CRY18	273.76	12
CRY19	304.46	18
CRY20	340.22	32
CRY21	401.94	41
CRY22	359.46	38
CRY23	282.39	13
CRY24	231.55	4
CRY25	318.76	21
CRY26	268.64	9
CRY27	353.22	36
CRY28	270.42	11
CRY29	349.18	34
CRY30	322.78	25
CRY31	320.40	23
CRY32	417.60	43
CRY33	296.00	16
CRY34	221.96	2
CRY35	286.27	14
CRY36	330.85	27
CRY37	195.73	1
CRY38	319.33	22
CRY39	320.40	24
CRY40	236.96	6
CRY41	268.64	10
CRY42	401.94	42
CRY43	299.96	17

	Hardening slope	
Type	**Slope**	**Rank**
CRY01	9.95	6
CRY02	9.06	5
CRY03	3.66	1
CRY04	57.70	39
CRY05	36.51	27
CRY06	33.02	26
CRY07	45.89	32
CRY08	18.65	12
CRY09	37.93	28
CRY10	37.93	29
CRY11	44.56	31
CRY12	24.31	15
CRY13	48.62	37
CRY14	45.91	34
CRY15	22.27	14
CRY16	42.56	30
CRY17	60.35	40
CRY18	25.05	19
CRY19	16.15	10
CRY20	47.39	36
CRY21	79.19	41
CRY22	45.93	35
CRY23	16.03	9
CRY24	8.76	4
CRY25	27.52	22
CRY26	24.31	16
CRY27	49.76	38
CRY28	12.12	8
CRY29	45.91	33
CRY30	29.89	23
CRY31	26.77	20
CRY32	120.58	43
CRY33	20.53	13
CRY34	4.42	2
CRY35	16.48	11
CRY36	31.53	25
CRY37	6.09	3
CRY38	30.66	24
CRY39	26.77	21
CRY40	9.95	7
CRY41	24.31	17
CRY42	79.19	42
CRY43	24.84	18

Table 8.2. Strut geometries. 150 µm strut is achieved by using symmetry boundary conditions on the 75 µm series.

Model Width [µm]	**Model Length [µm]**	**No. of grains**	**Specimen width: Grain size**
14	500	362	3
19	500	452	4
28	500	633	6
75	500	1555	12
150	500	1555	24

Table 8.3. Tabular arrangement of equivalent plastic strain values used in Figure 8.8.

	014 µm	**019 µm**	**028 µm**	**075 µm**	**150 µm**
Maximum	0.152	0.131	0.103	0.093	0.082
Avg. + SD	0.142	0.129	0.095	0.088	0.078
Average	0.122	0.114	0.088	0.082	0.075
Avg. – SD	0.103	0.100	0.082	0.077	0.071
Minimum	0.091	0.087	0.081	0.074	0.069
Standard Deviation	0.020	0.015	0.006	0.006	0.004

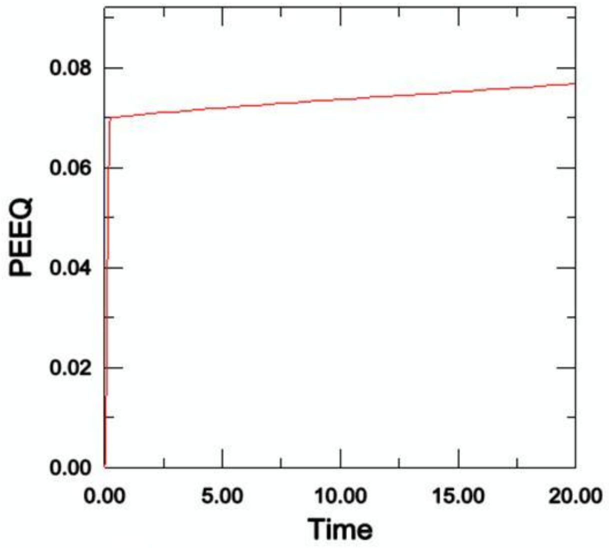

Figure 8.1. The majority of PEEQ accumulation occurs on the first cycle

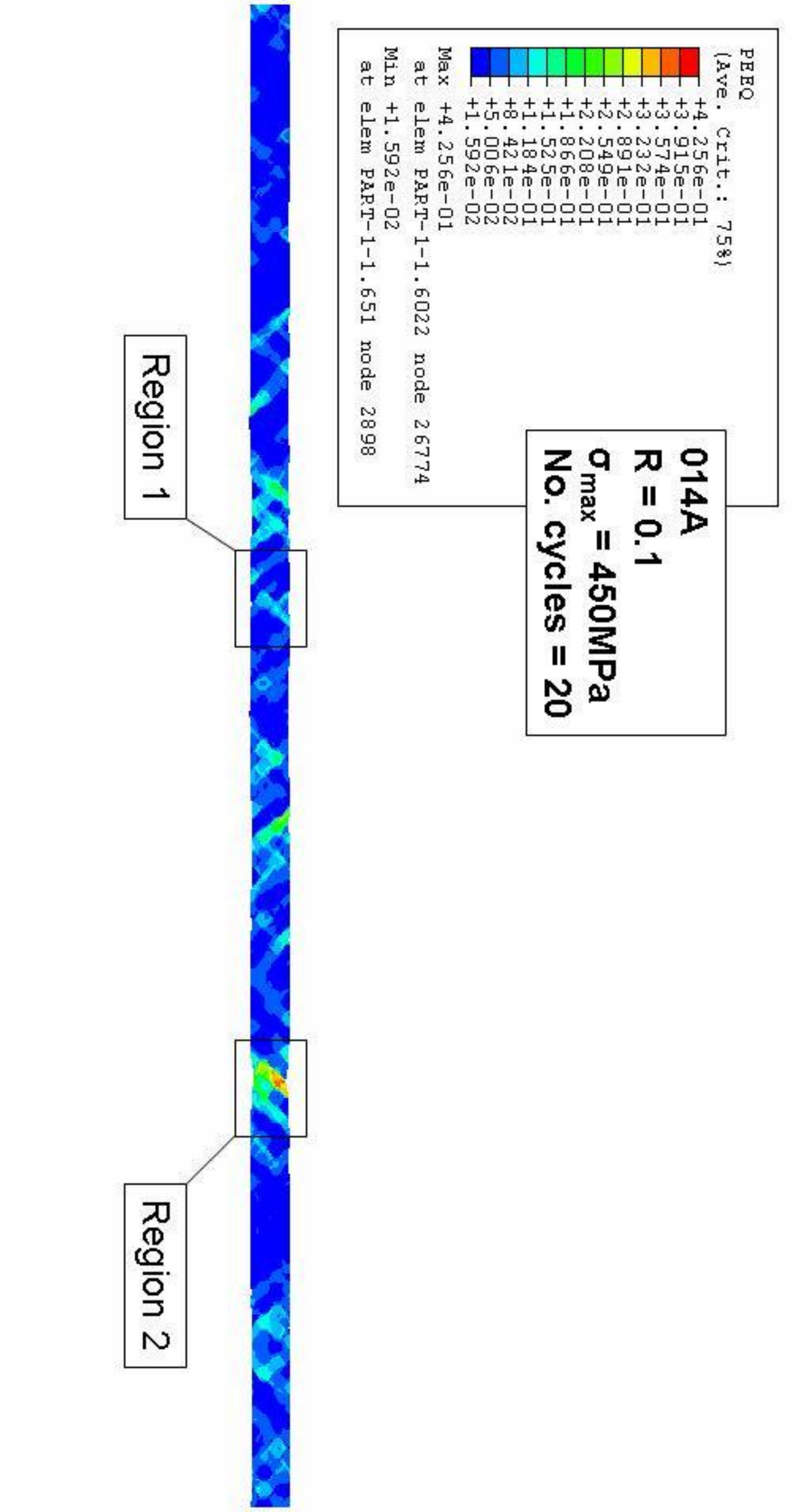
PEEQ
(Ave. Crit.: 75%)
+4.256e-01
+3.915e-01
+3.574e-01
+3.232e-01
+2.891e-01
+2.549e-01
+2.208e-01
+1.866e-01
+1.525e-01
+1.184e-01
+8.421e-02
+5.006e-02
+1.592e-02
Max +4.256e-01
at elem PART-1-1.6022 node 26774
Min +1.592e-02
at elem PART-1-1.651 node 2898
014A
R = 0.1
σmax = 450MPa
No. cycles = 20
Region 1
Region 2

(a)

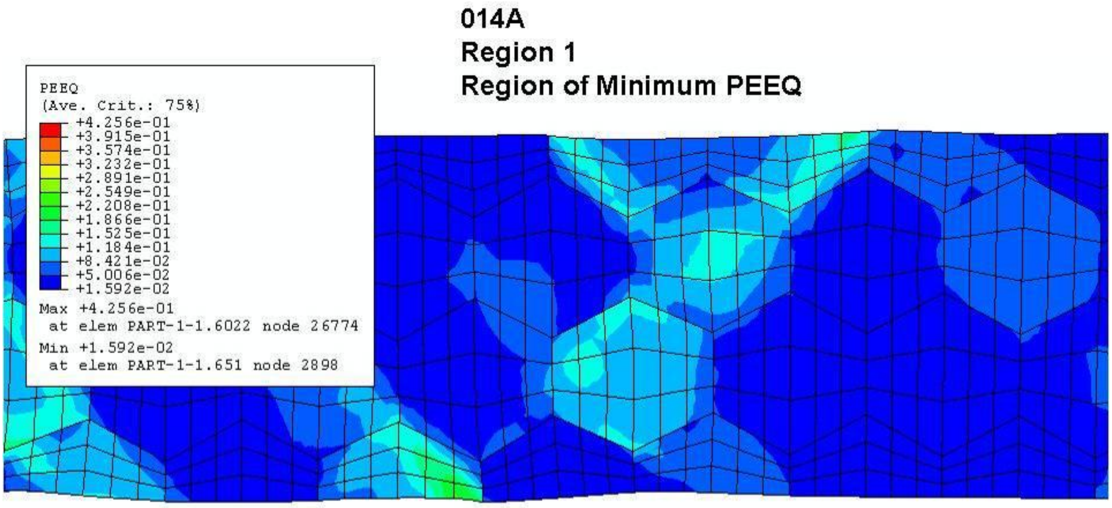

(b)

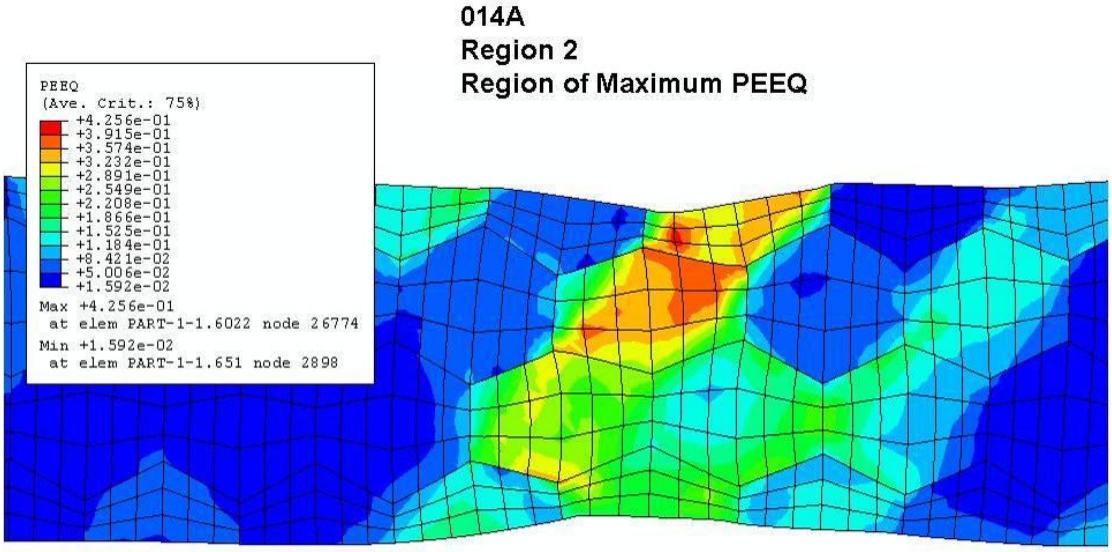

(c)

Figure 8.1 (a) Contour plot of a 14μm strut showing equivalent plastic strain accumulation within grains, (b) close up of region 1 identified in (a), (c) close up of region 2 identified in (a).

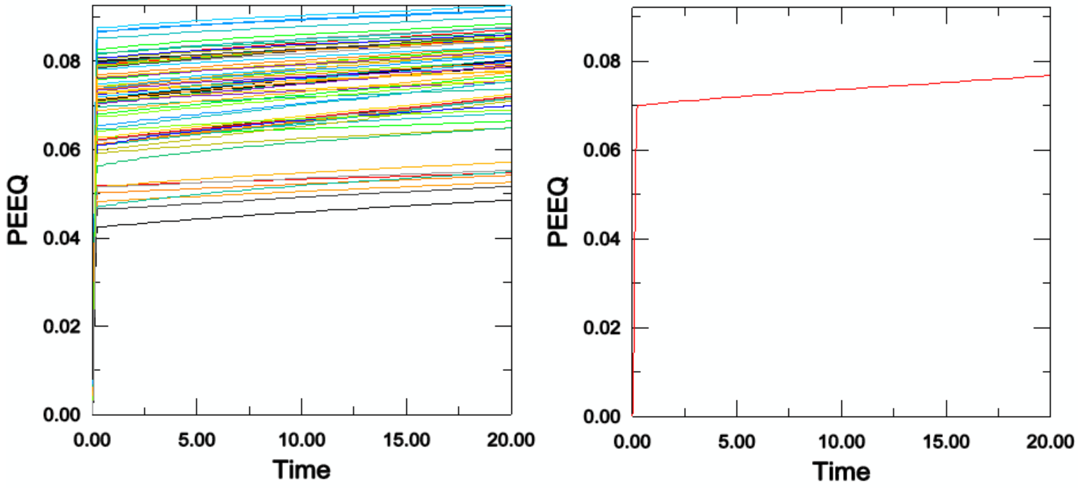

(a) (b)

Figure 8.2 (a) PEEQ accumulation history curves for each integration point within a grain (b) PEEQ accumulation history curve produced by averaging curves in (a).

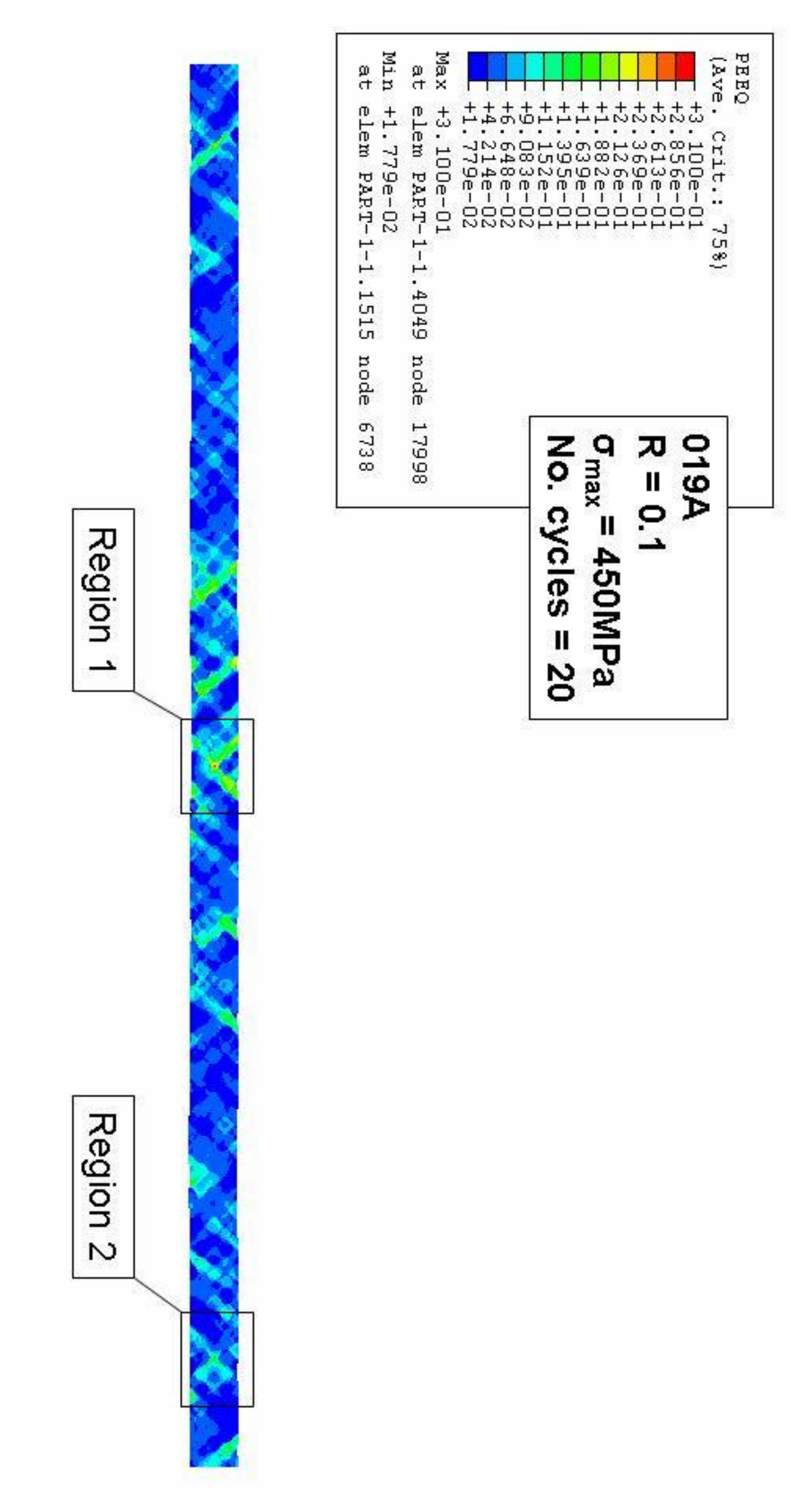
PEEQ
(Ave. Crit.: 75%)
+3.100e-01
+2.856e-01
+2.613e-01
+2.369e-01
+2.126e-01
+1.882e-01
+1.639e-01
+1.395e-01
+1.152e-01
+9.083e-02
+6.648e-02
+4.214e-02
+1.779e-02
Max +3.100e-01
at elem PART-1-1.4049 node 17998
Min +1.779e-02
at elem PART-1-1.1515 node 6738
019A
R = 0.1
σmax = 450MPa
No. cycles = 20
Region 1
Region 2

(a)

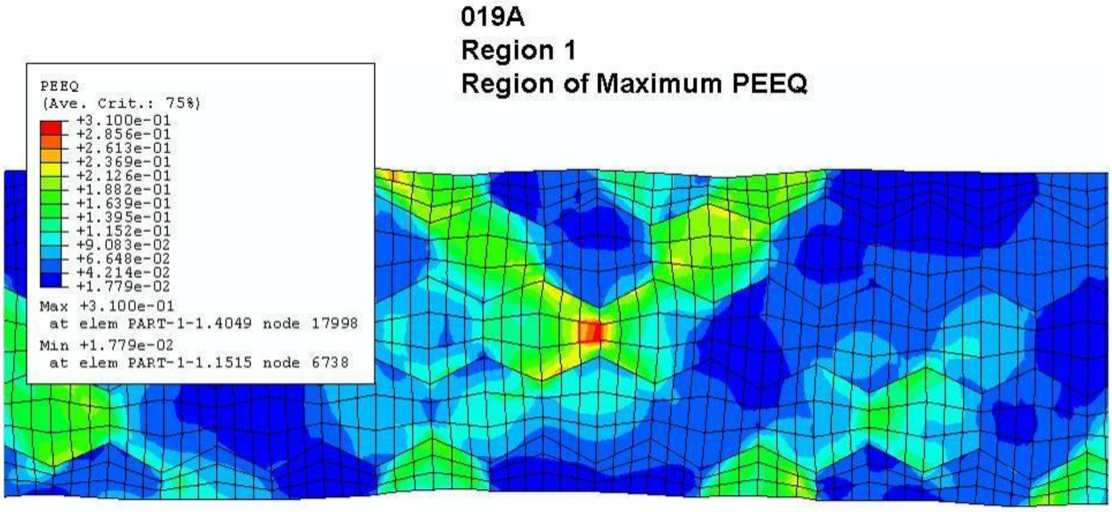

(b)

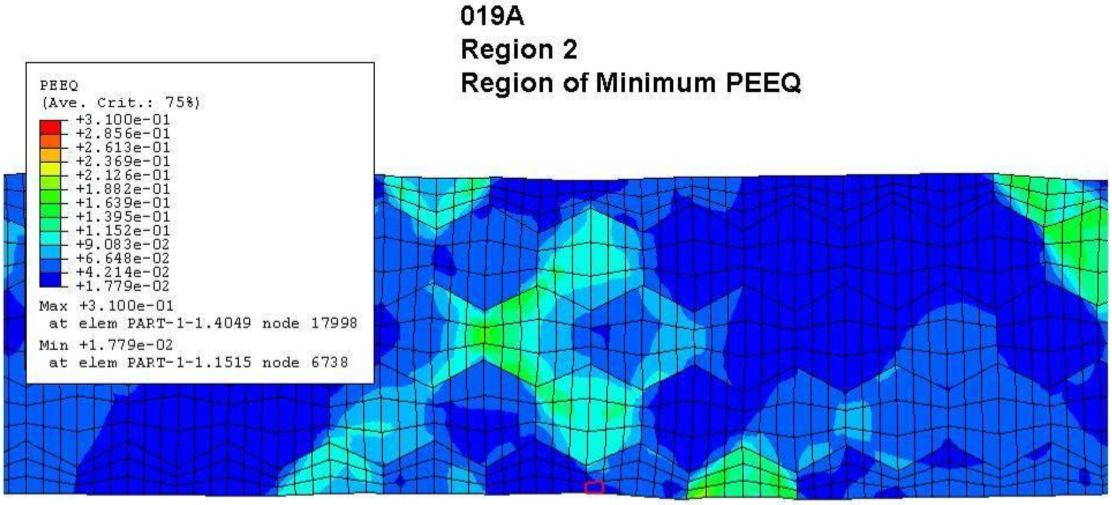

(c)

Figure 8.3. (a) Contour plot of 19µm strut showing equivalent plastic strain accumulation within grains, (b) close up of region 1 identified in (a), (c) close up of region 2 identified in (a).

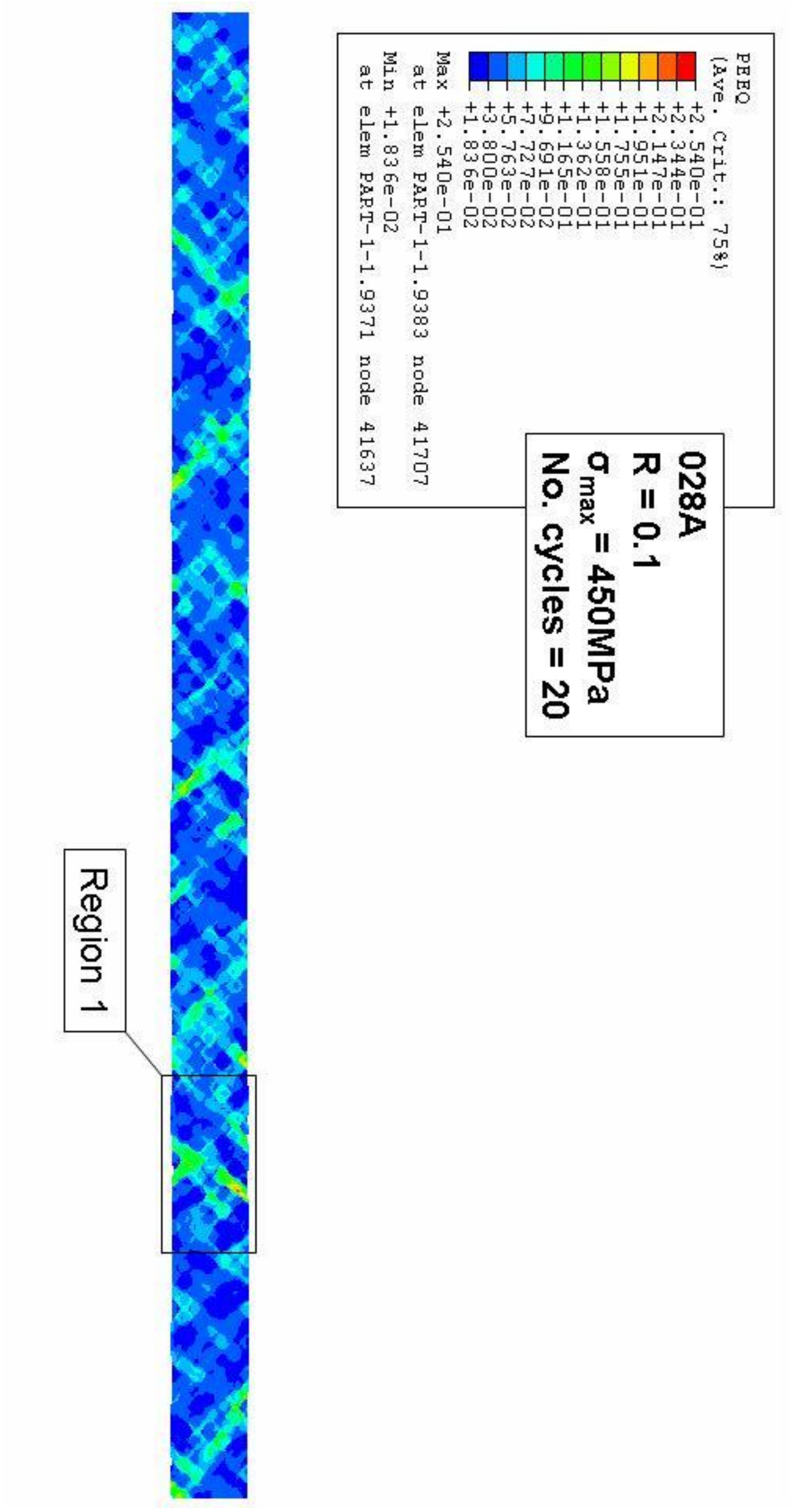
PEEQ
(Ave. Crit.: 75%)
+2.540e-01
+2.344e-01
+2.147e-01
+1.951e-01
+1.755e-01
+1.558e-01
+1.362e-01
+1.165e-01
+9.691e-02
+7.727e-02
+5.763e-02
+3.800e-02
+1.836e-02
Max +2.540e-01
at elem PART-1-1.9383 node 41707
Min +1.836e-02
at elem PART-1-1.9371 node 41637
028A
R = 0.1
σmax = 450MPa
No. cycles = 20
Region 1

(a)

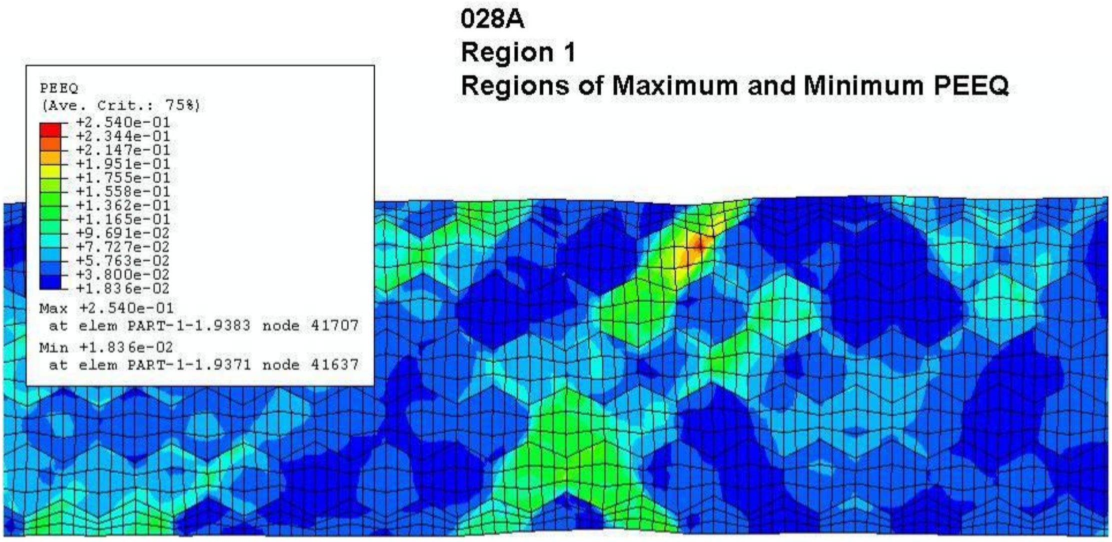
028A
Region 1
Regions of Maximum and Minimum PEEQ
PEEQ
(Ave. Crit.: 75%)
+2.540e-01
+2.344e-01
+2.147e-01
+1.951e-01
+1.755e-01
+1.558e-01
+1.362e-01
+1.165e-01
+9.691e-02
+7.727e-02
+5.763e-02
+3.800e-02
+1.836e-02
Max +2.540e-01
at elem PART-1-1.9383 node 41707
Min +1.836e-02
at elem PART-1-1.9371 node 41637

(b)

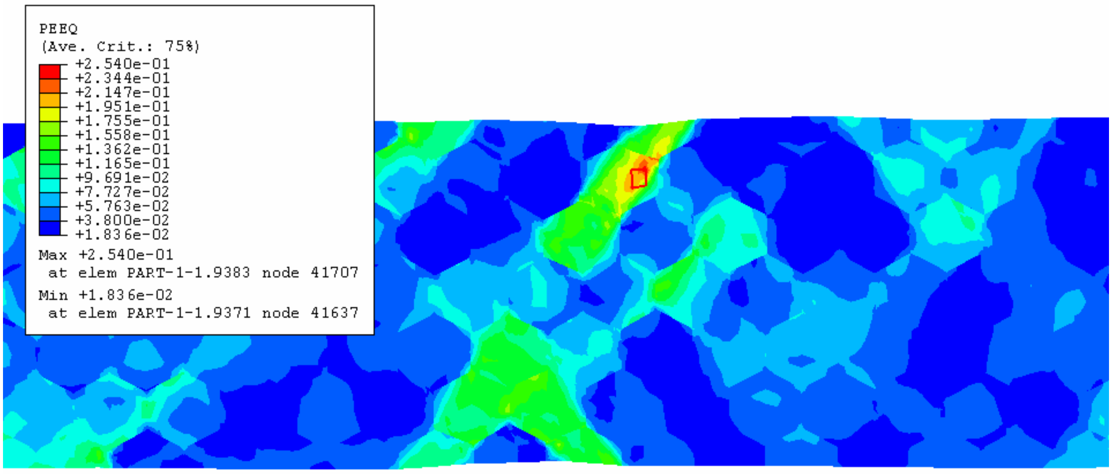
PEEQ
(Ave. Crit.: 75%)
+2.540e-01
+2.344e-01
+2.147e-01
+1.951e-01
+1.755e-01
+1.558e-01
+1.362e-01
+1.165e-01
+9.691e-02
+7.727e-02
+5.763e-02
+3.800e-02
+1.836e-02
Max +2.540e-01
at elem PART-1-1.9383 node 41707
Min +1.836e-02
at elem PART-1-1.9371 node 41637

(c)

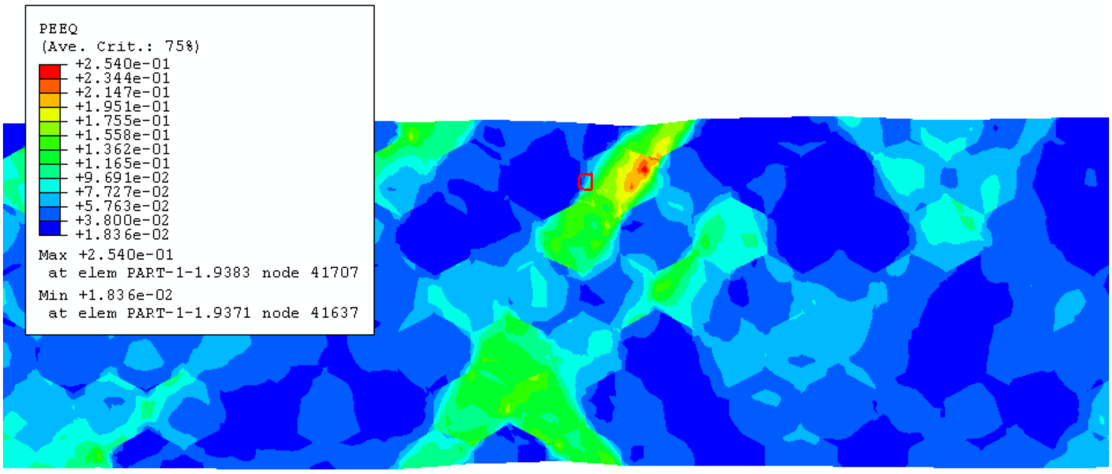

(d)

Figure 8.4 (a) Contour plot of 028µm strut showing equivalent plastic strain accumulation within grains, (b) close up of region 1 identified in with maximum and minimum strain occurring in the same region (a), (c) element with maximum PEEQ highlighted with red box, (d) element with minimum PEEQ highlighted with red box.

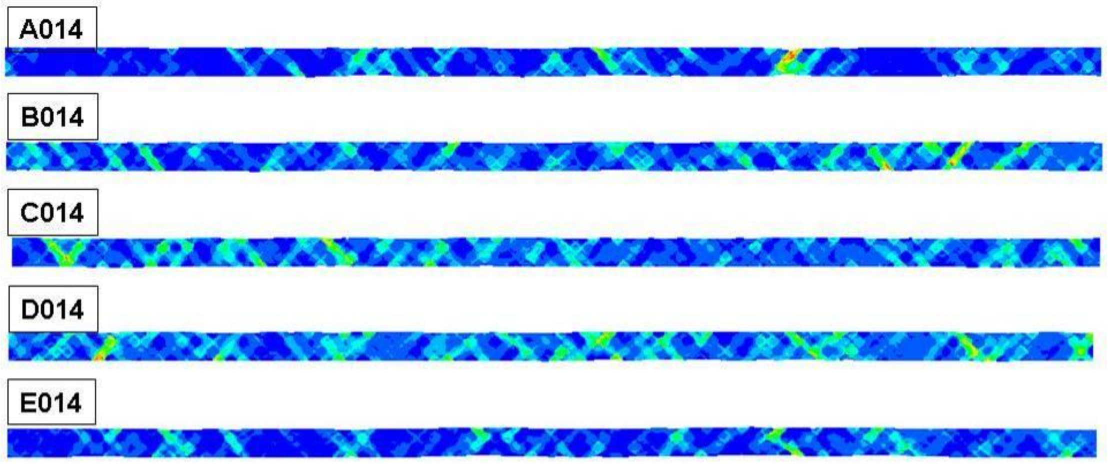

(a)

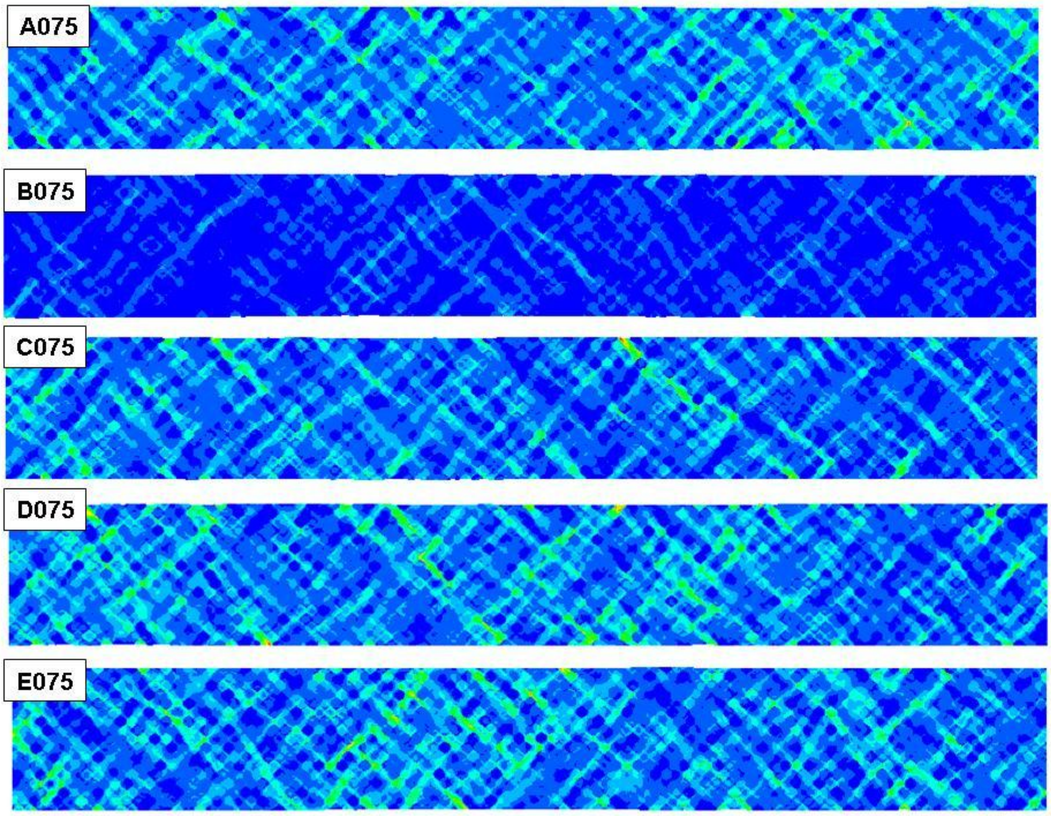

(b)

Figure 8.5. (a) Contour plots of PEEQ accumulation in five 14μm struts, (b) contour plot of PEEQ accumulation in five 75μm struts. For both cases the equivalent plastic strain contour plots are shown at 20 cycles with R=0.1 and σ_{max}=450 MPa. Notice the significant levels of strain localization that occur within the smaller struts.
Plots are not to the same scale.

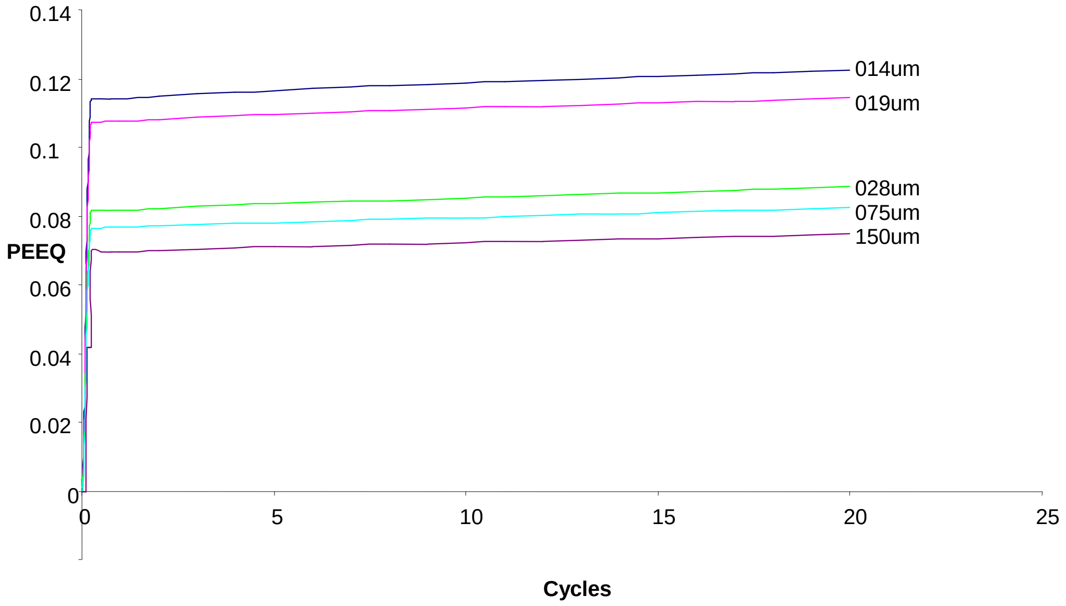

Figure 8.6. Average curves of equivalent plastic strain accumulation within CRY37 orientation grains

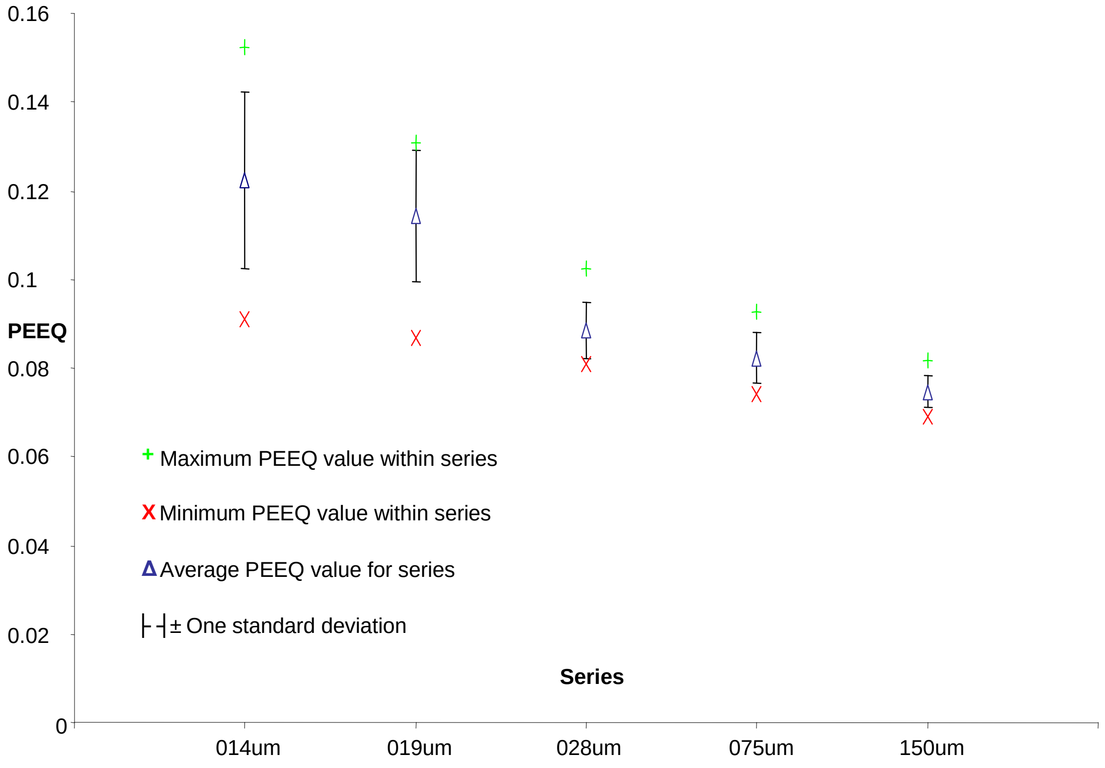

Figure 8.7. CRY37 PEEQ at 20 cycles. Plot shows Average, Maximum, Minimum and Standard Deviation[2].

---

[2] **Average** – the average PEEQ accumulation history over 20 cycles of all CRY37 orientation grains within a strut is calculated. This process is repeated for each of the ten struts that make up a series. The average of these ten values is in turn calculated and is plotted here for each of the five series (14um 19um, 28um, 75um, 150um).
Maximum and **minimum** establish the range of average CRY37 PEEQ values within a series.
Standard Deviation – calculated as the standard deviation of the ten struts within a series.

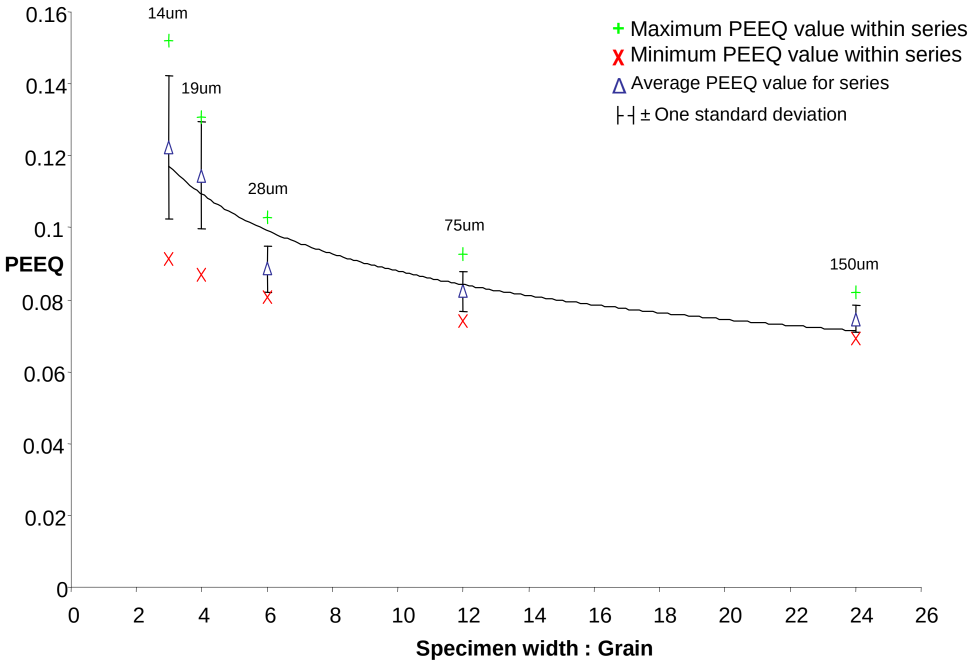

Figure 8.8. Average equivalent plastic strain (PEEQ) for strut series and associated specimen width to grain size ratio with trend line.

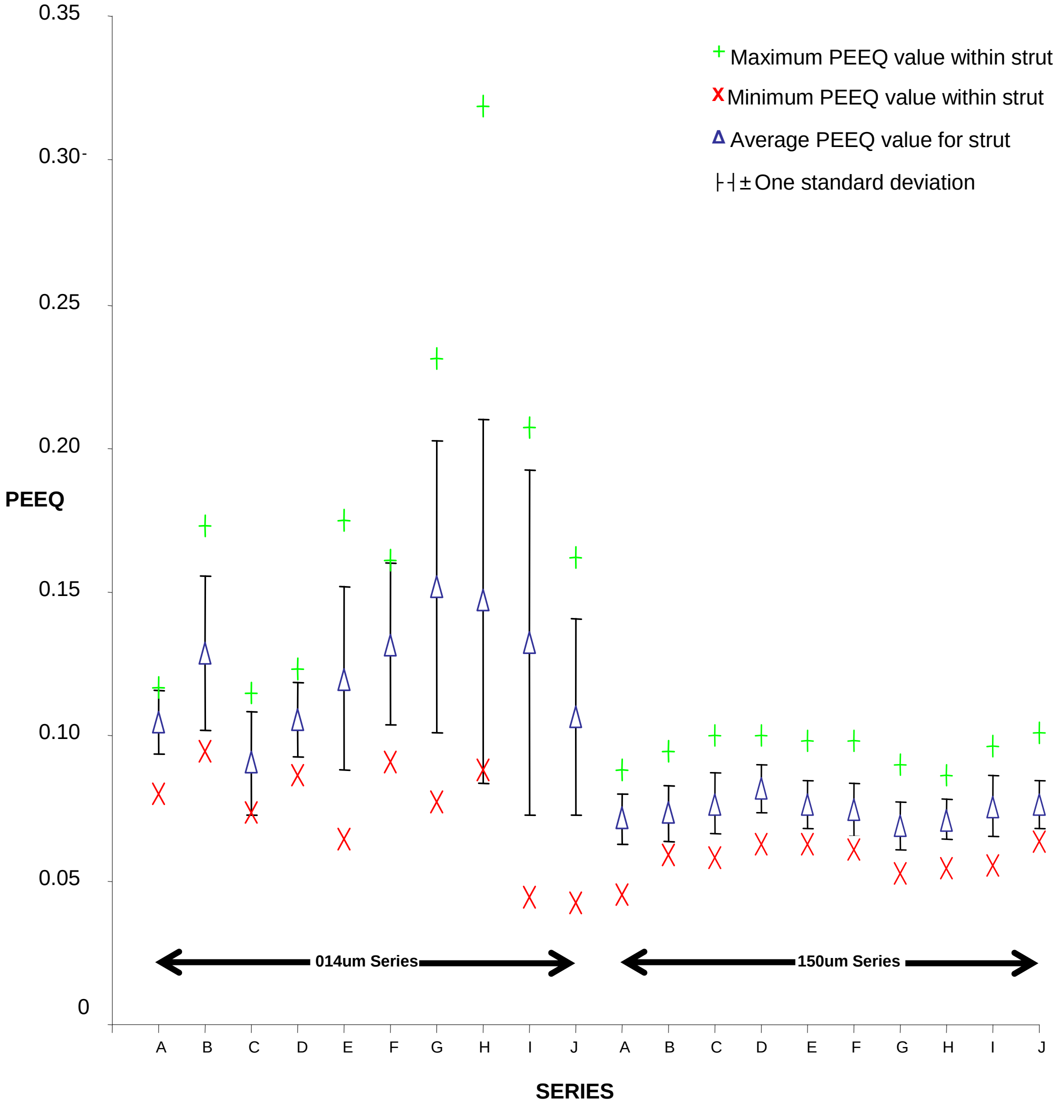

Figure 8.9. The intra-strut variation in equivalent plastic strain in the 14 μm and 150 μm series (plastic strain values are extracted from the CRY37 orientation grains). There are ten models per series, represented by the letters A-J.

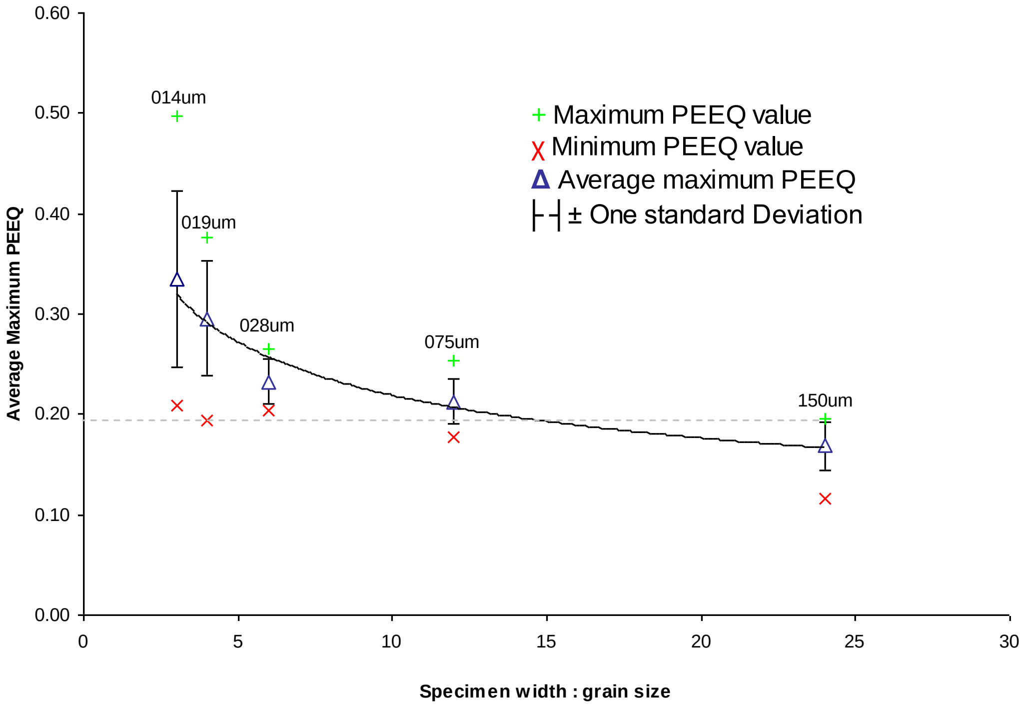

Figure 8.10. Average maximum equivalent plastic strain within struts, with standard deviation and range. Dashed line highlights the difference between 150 µm and 14 µm showing that the lowest value of plastic strain value in a 14 µm strut is greater than the highest value of plastic strain in a 150 µm strut

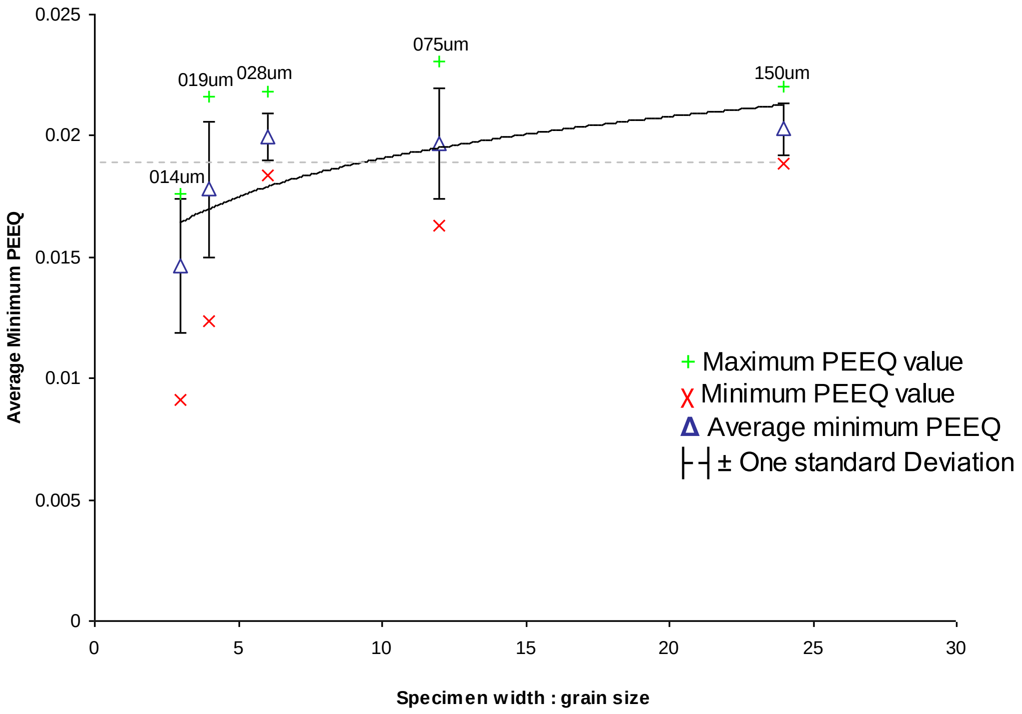

Figure 8.11. The average minimum equivalent plastic strain within struts, with standard deviation and range. Dashed line highlights the difference between 150 µm and 14 µm showing that the lowest value of plastic strain in a 150 µm strut is greater than the highest value of plastic strain value in a 14 µm strut

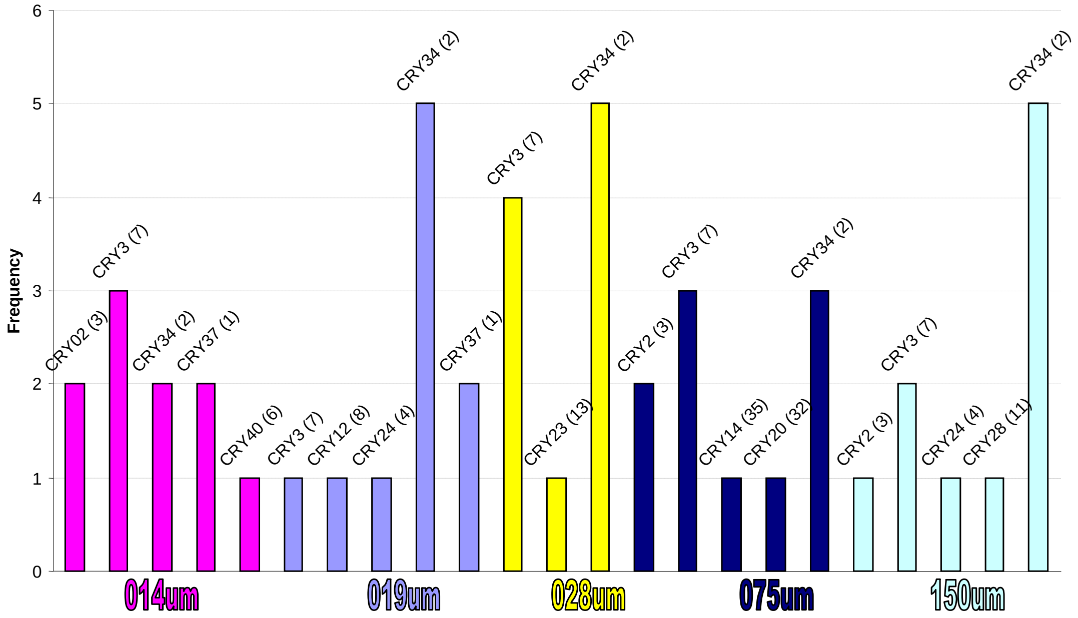

Figure 8.12. Crystal orientations associated with the maximum PEEQ values within each series. There are ten struts per series and the frequency with which a particular orientation is associated with the maximum PEEQ value is presented here. Figure in brackets after the CRY identification refers to the rank the yield point of that orientation assumes in a table where 1 is softest/lowest yield point and 43 is hardest/highest. Note the frequency with which CRY34 occurs (20 out of a total 50). It has the 2^{nd} lowest yield point and the lowest hardening rate.

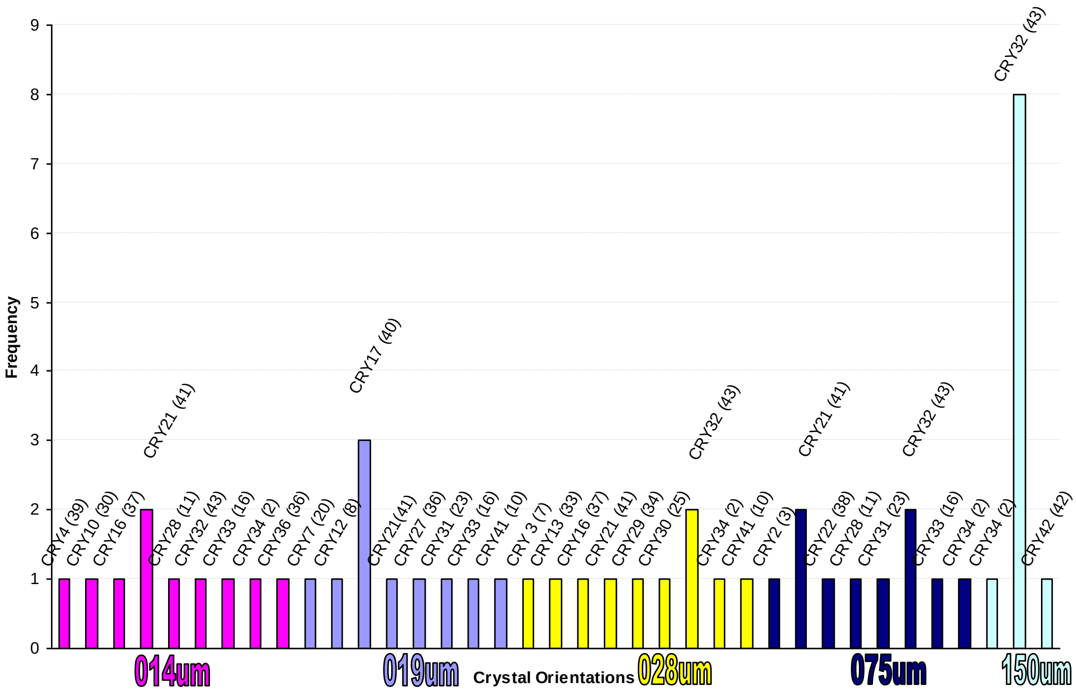

Figure 8.13. Crystal orientations associated with the minimum PEEQ values within each series. There are ten struts per series and the frequency with which a particular orientation is associated with the minimum PEEQ value is presented here Figure in brackets after the CRY identification refers to the rank the yield point of that CRY assumes in a table where 1 is softest/lowest yield point and 43 is hardest/highest.

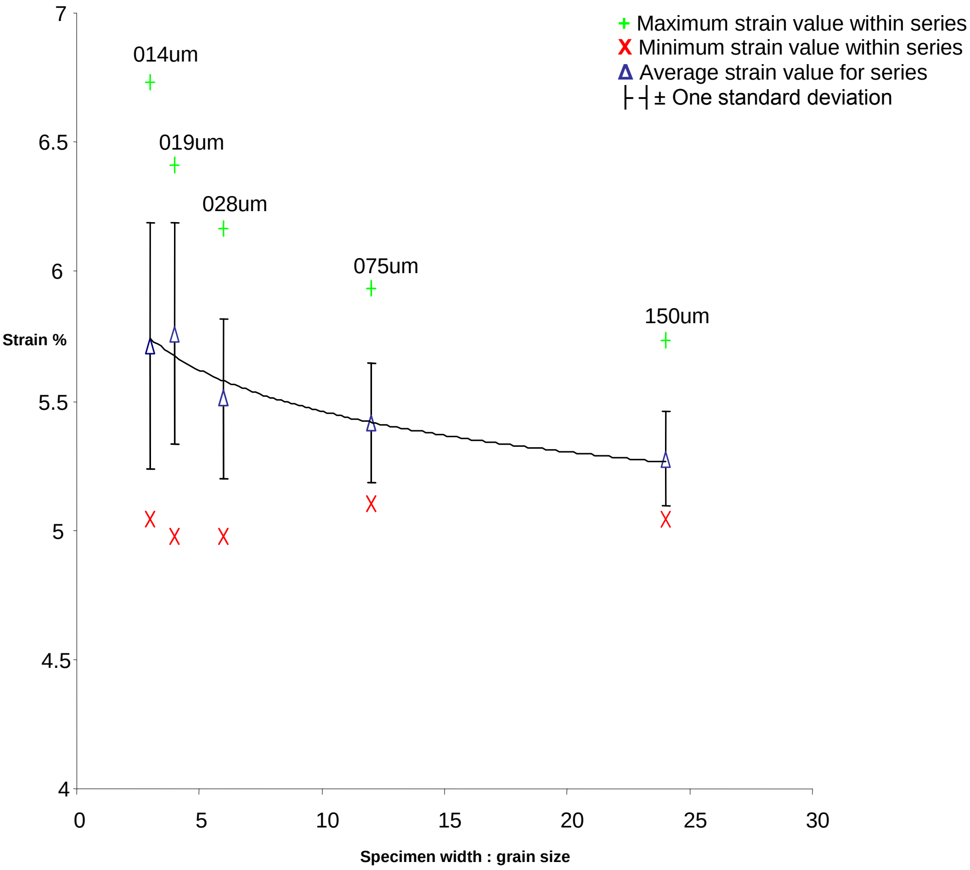

Figure 8.14. The average total % strain of each strut series, accumulated over cycles 0 to 20.

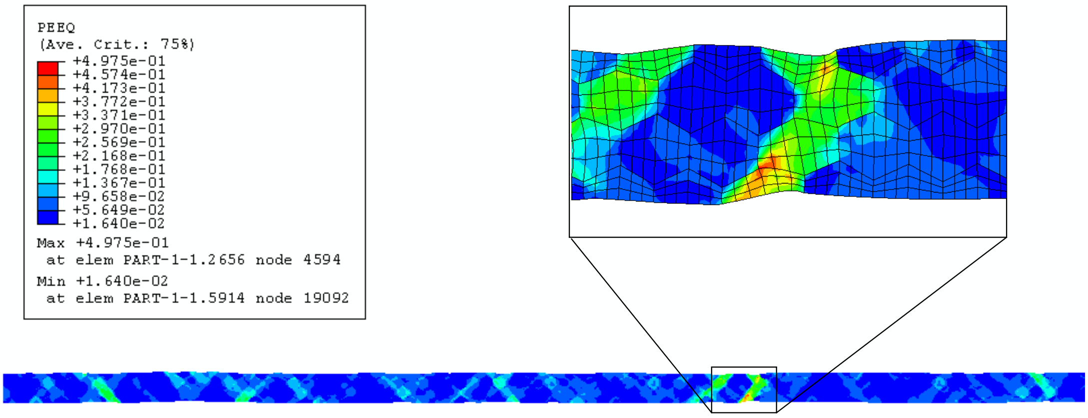

(a)

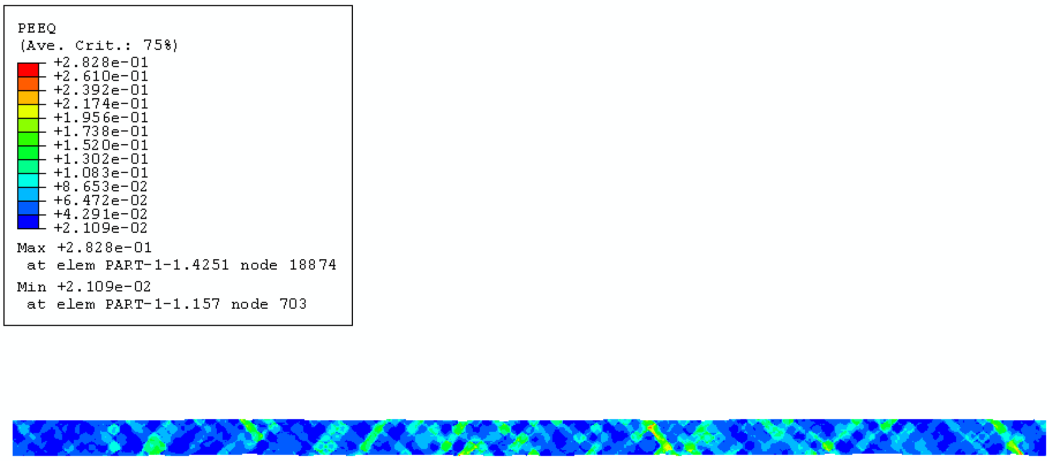
PEEQ
(Ave. Crit.: 75%)
+2.828e-01
+2.610e-01
+2.392e-01
+2.174e-01
+1.956e-01
+1.738e-01
+1.520e-01
+1.302e-01
+1.083e-01
+8.653e-02
+6.472e-02
+4.291e-02
+2.109e-02
Max +2.828e-01
at elem PART-1-1.4251 node 18874
Min +2.109e-02
at elem PART-1-1.157 node 703

(b)

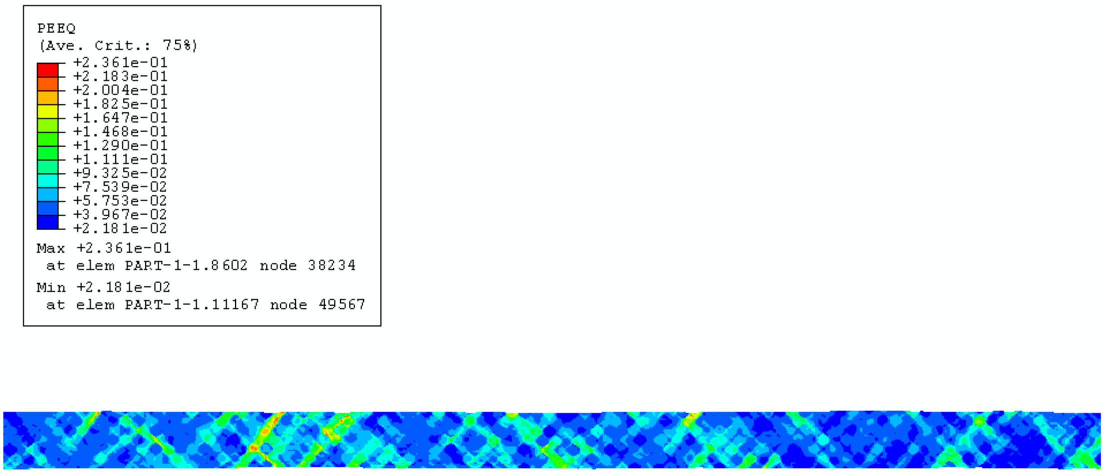
PEEQ
(Ave. Crit.: 75%)
+2.361e-01
+2.183e-01
+2.004e-01
+1.825e-01
+1.647e-01
+1.468e-01
+1.290e-01
+1.111e-01
+9.325e-02
+7.539e-02
+5.753e-02
+3.967e-02
+2.181e-02
Max +2.361e-01
at elem PART-1-1.8602 node 38234
Min +2.181e-02
at elem PART-1-1.11167 node 49567

(c)

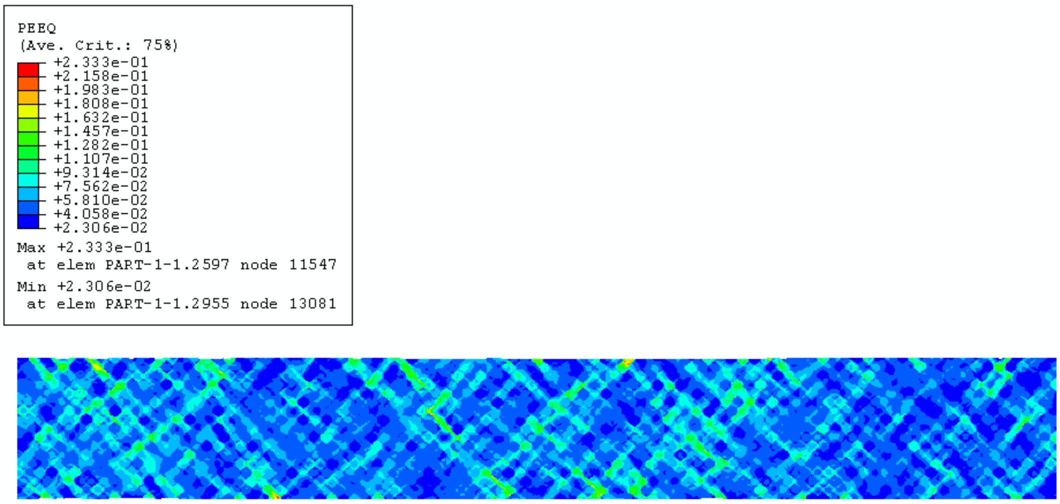

(d)

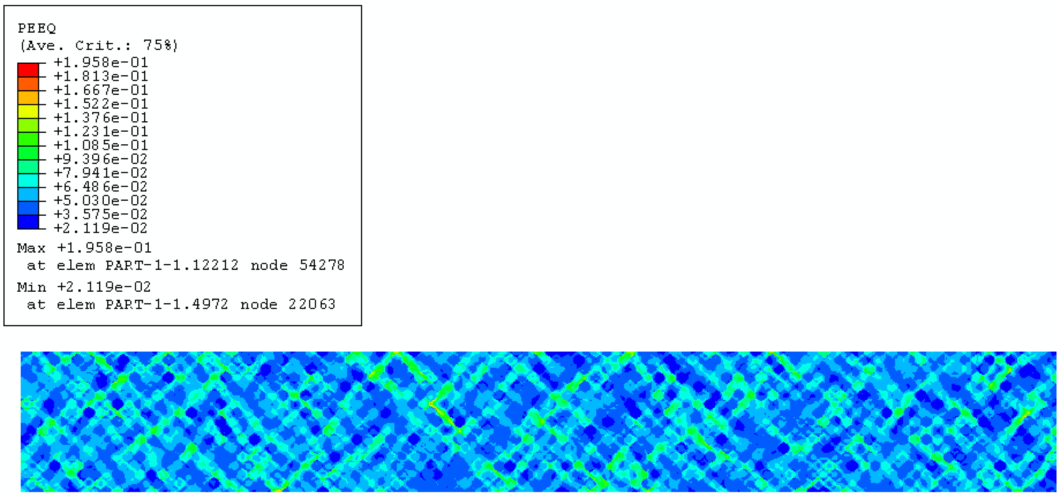

(e)

Figure 8.15. Contour plots of Equivalent Plastic Strain for struts with highest total strain values in each series. (a) 14$^{(H)}$ µm, (b) 19$^{(I)}$ µm, (c) 28$^{(C)}$ µm, (d) 75$^{(D)}$ µm and (e) 150$^{(D)}$ µm (superscript indicates model number) . The elongation values of these struts feature as the “maximum strain value within series” on the plot in figure 8.14.

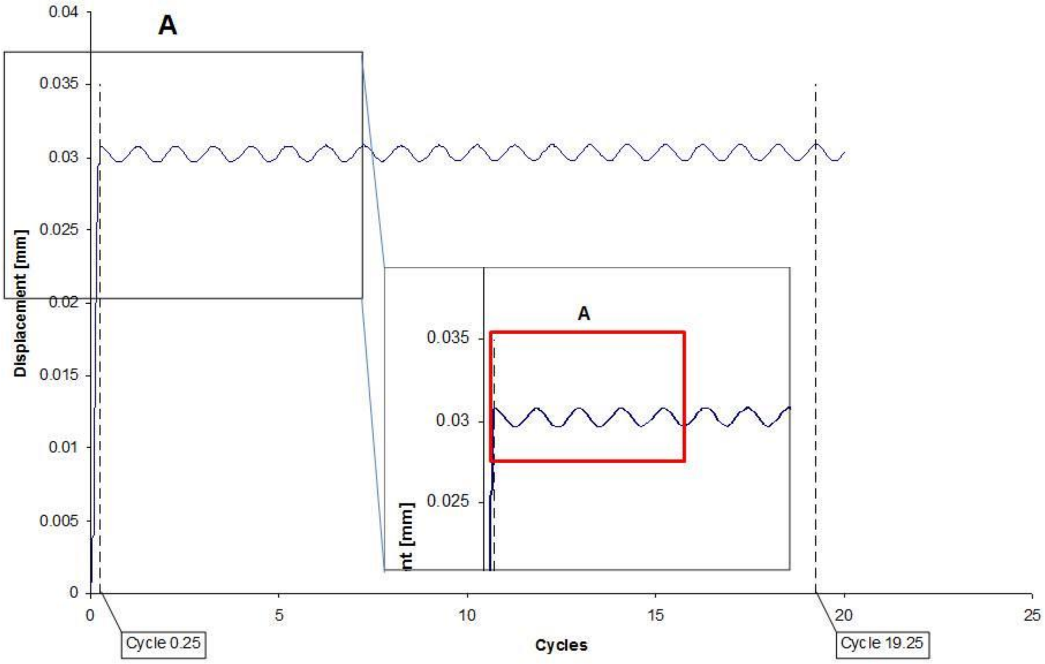

Figure 8.16. Specimen displacement as recorded by Enduratec ELF 3200. Majority of displacement occurs during ramp up (within a quarter of one cycle). This portion is indicated be the vertical dashed line. The region investigated in Figure 8.17 is contained within the red box.

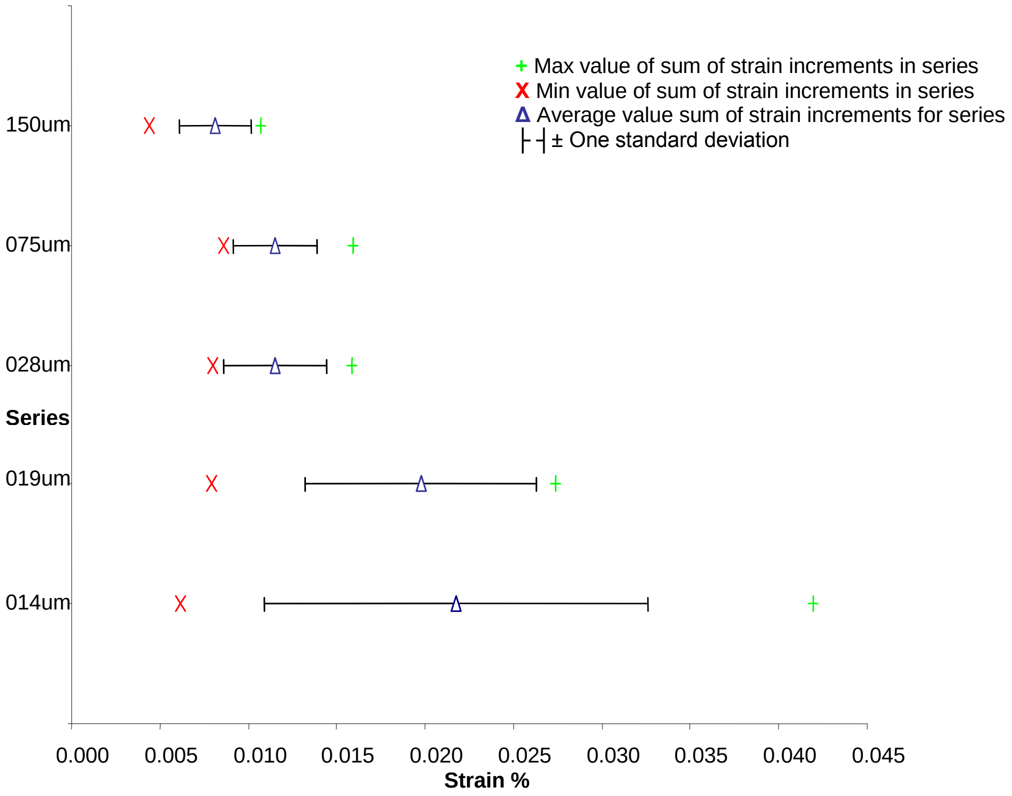

Figure 8.17. Total strain accumulated from cycles 0.25 to 19.25, (for clarity, omitting the strain accumulated from cycles 0 to 0.25 which is roughly equivalent to 19 times the incremental strain)The differences indicate that the magnitude of the per-cycle strain increment is dependent upon the strut width and consequently the level of constraint offered by the structure. The maximum values for each series refer to the individual sample within that series with the greatest accumulated strain between cycles 0.25 and 19.25. Minimum values are the converse of this.

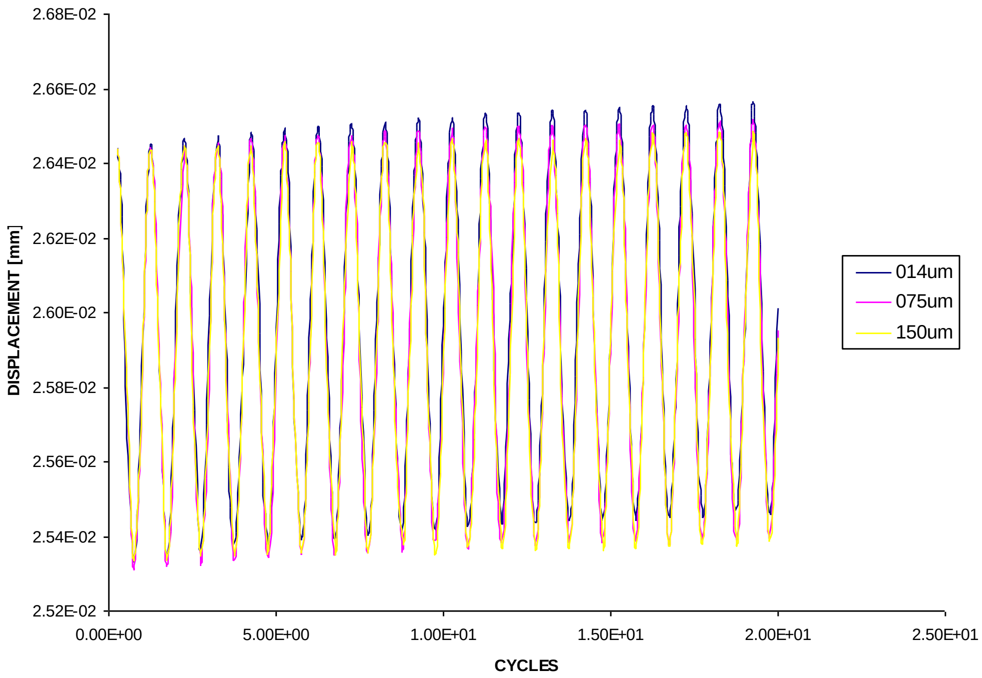

Figure 8.18. Normalised displacement of a 14 µm, 75 µm and 150 µm sample, showing the accumulated effect of differences in the magnitude of the respective cyclic strains.

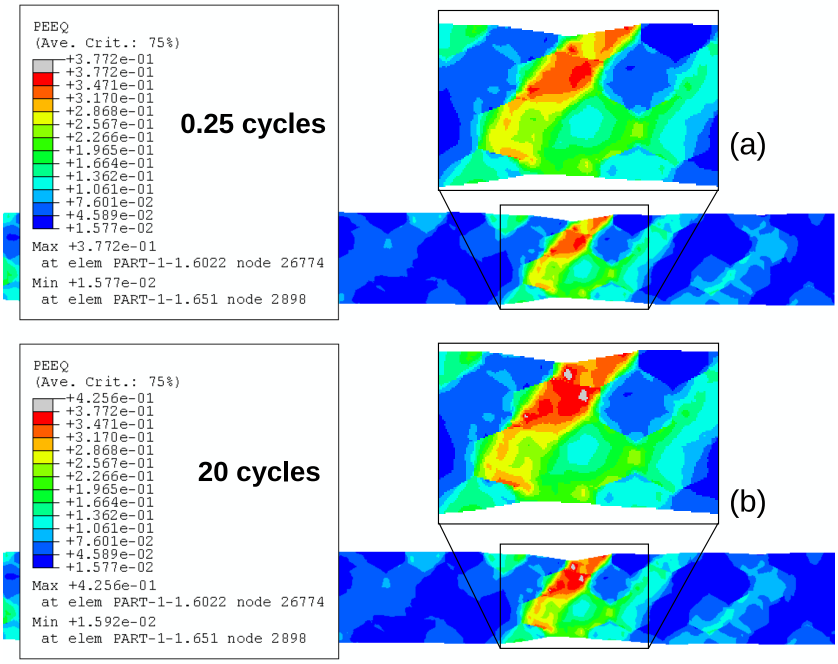

Figure 8.19. Plastic Strain localization within a 14 µm wide sample after: (a) first cycle, and (b) Cycle 20. Note the differences in PEEQ levels between (a) and (b).

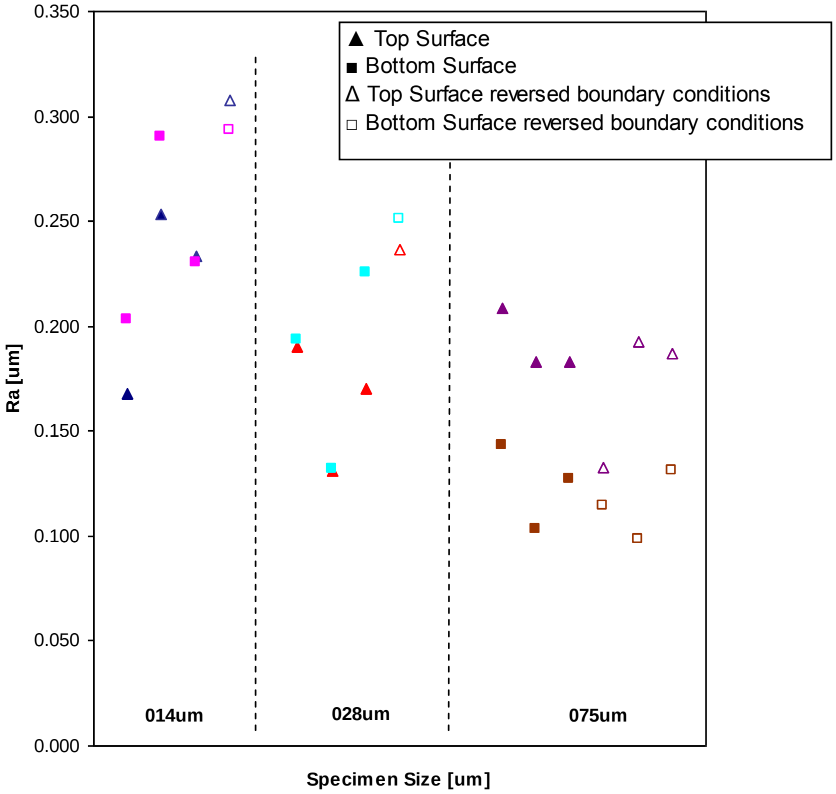

Figure 8.20. Note: in the undeformed state the models are perfectly flat and the surface roughness value is zero. Values are similar to those obtained for the interferometry

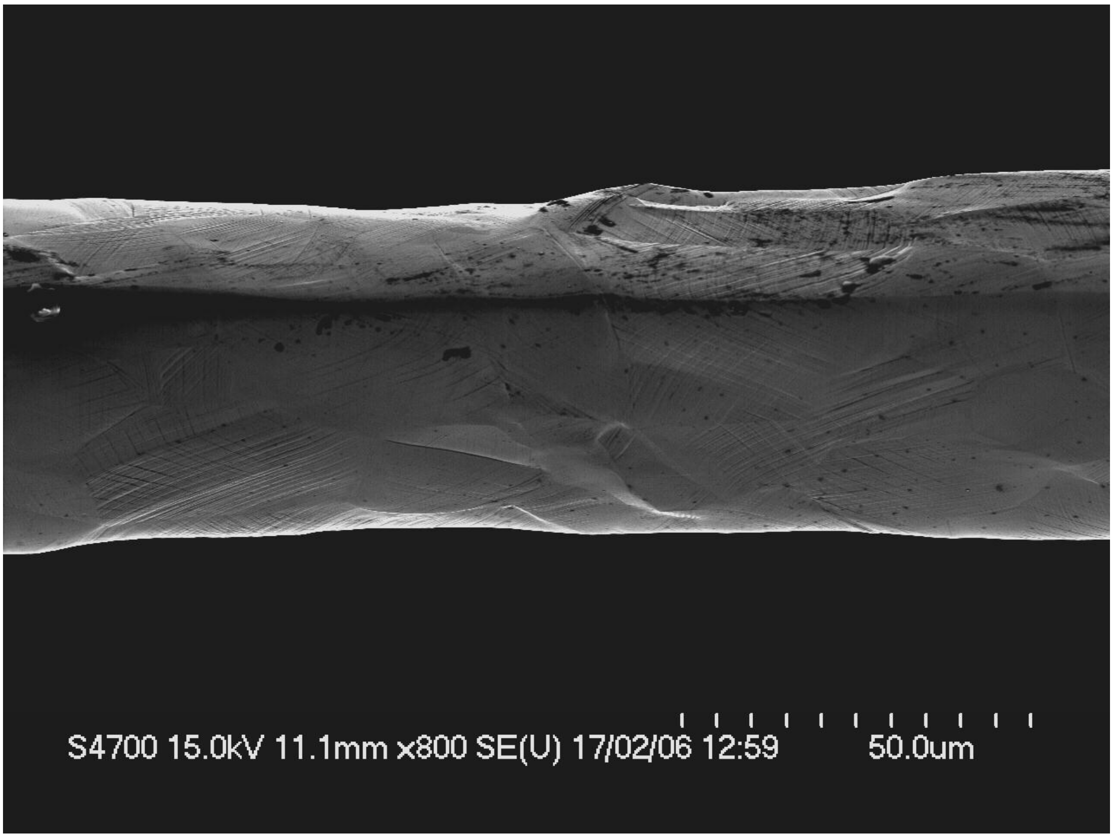

Figure 8.21. A 50 µm test specimens showing typical strain-related topographic features such as slip bands, grain boundaries and rotated grains.

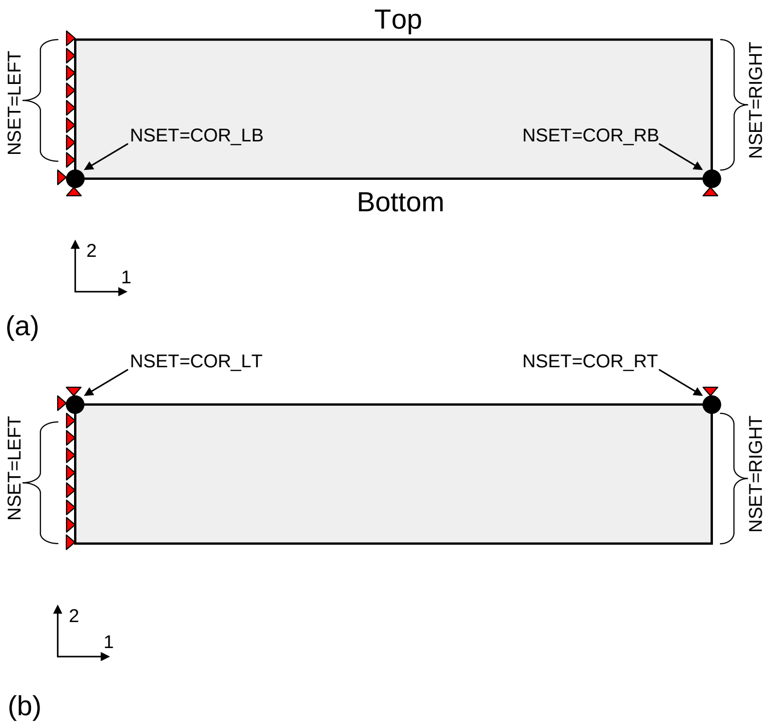

Figure 8.22. Schematic showing (a) normal and (b) "reversed" boundary conditions.

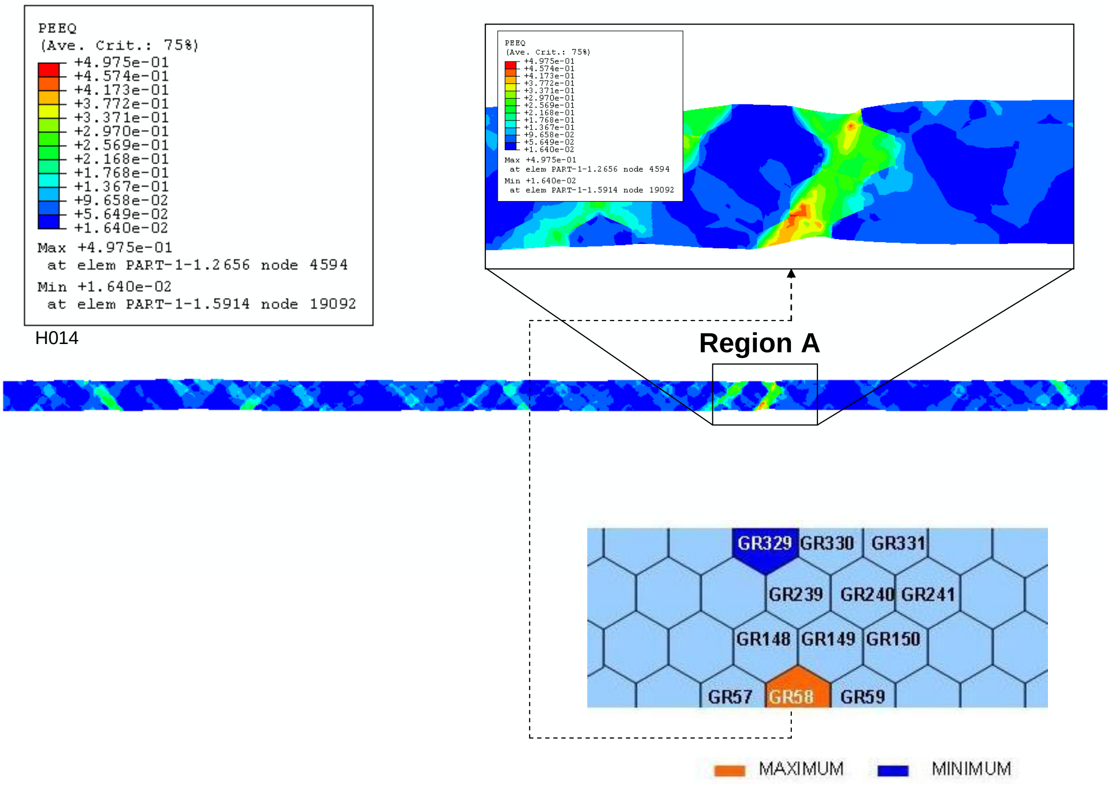

(a)

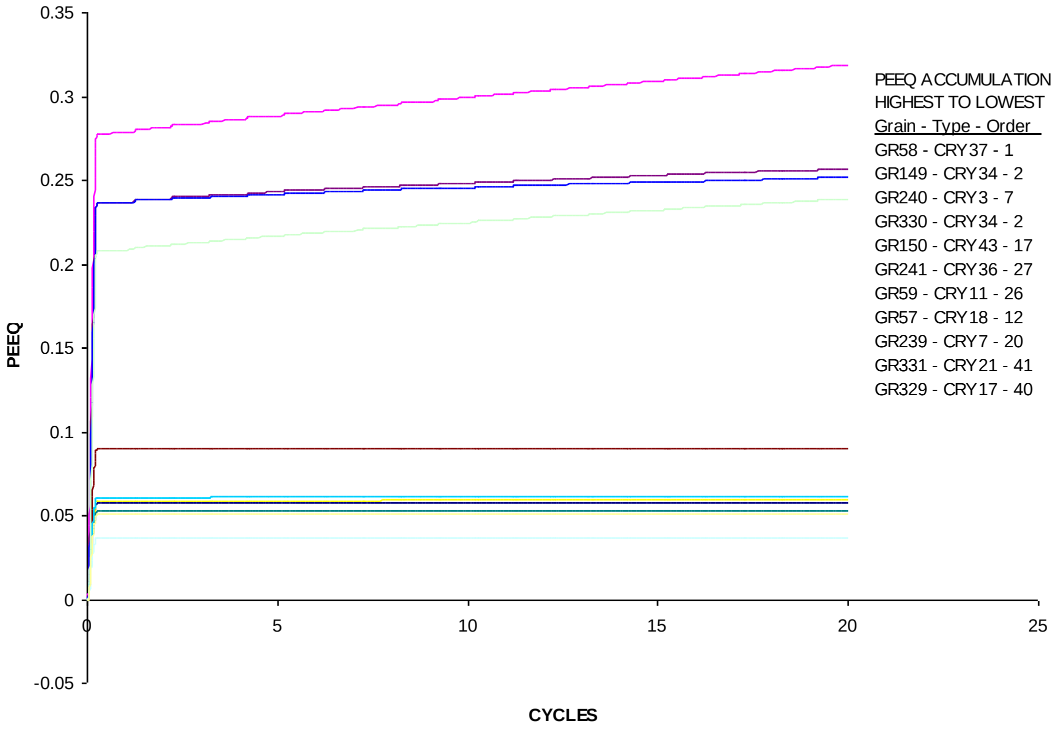

(b)

Figure 8.23. (a) Contour plot of 14 μm strut showing area of strain localization and corresponding grain numbers (b) PEEQ history plot of selected grains in Region A. Table to left of chart indicates order of grains.

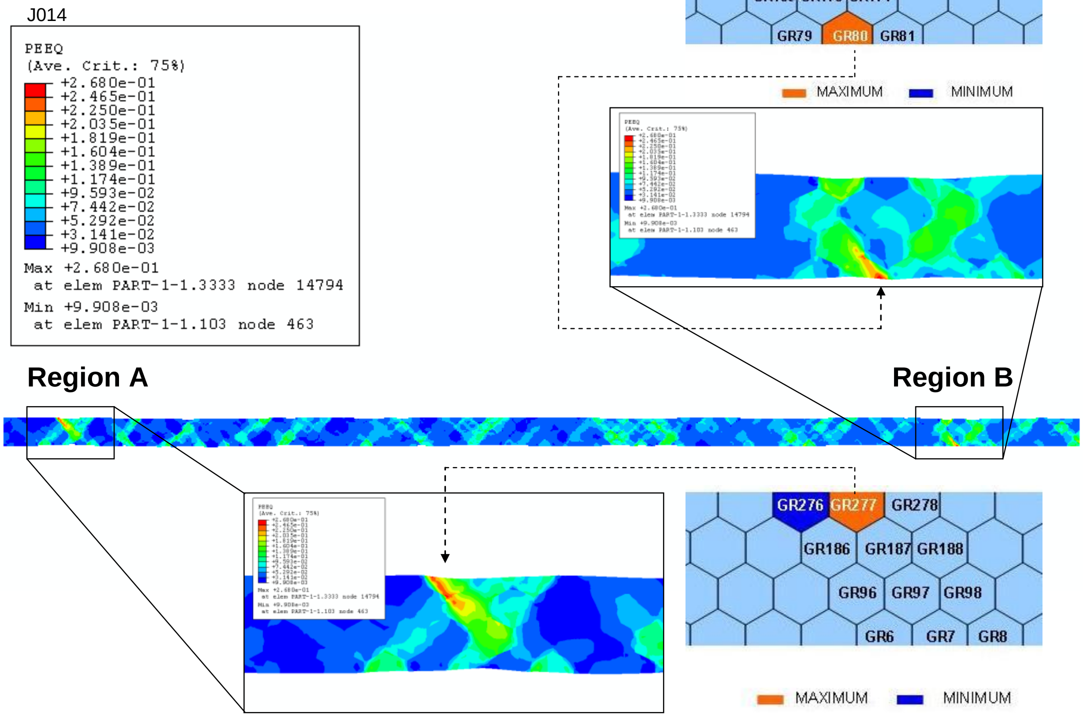
J014
PEEQ
(Ave. Crit.: 75%)
+2.680e-01
+2.465e-01
+2.250e-01
+2.035e-01
+1.819e-01
+1.604e-01
+1.389e-01
+1.174e-01
+9.593e-02
+7.442e-02
+5.292e-02
+3.141e-02
+9.908e-03
Max +2.680e-01
at elem PART-1-1.3333 node 14794
Min +9.908e-03
at elem PART-1-1.103 node 463
Region A
Region B
GR351
GR352
GR353
GR260
GR261
GR262
GR169
GR170
GR171
GR79
GR80
GR81
MAXIMUM
MINIMUM
GR276
GR277
GR278
GR186
GR187
GR188
GR96
GR97
GR98
GR6
GR7
GR8
MAXIMUM
MINIMUM

(a)

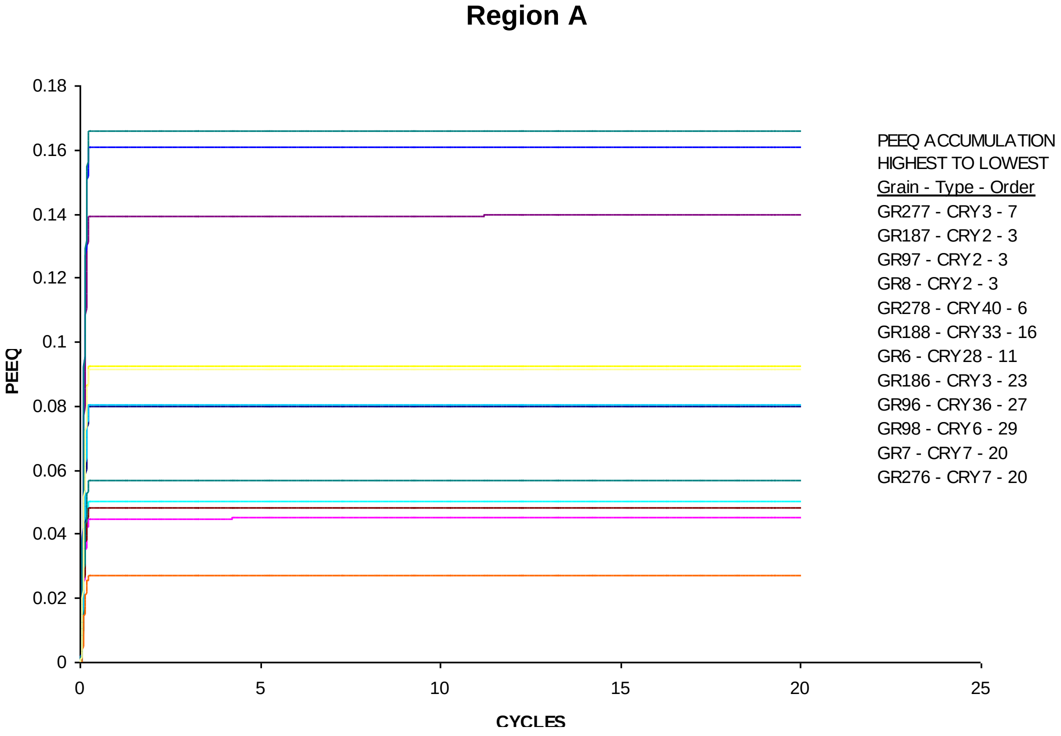
Region A
PEEQ
0.18
0.16
0.14
0.12
0.1
0.08
0.06
0.04
0.02
0
0
5
10
15
20
25
CYCLES
PEEQ ACCUMULATION
HIGHEST TO LOWEST
Grain - Type - Order
GR277 - CRY3 - 7
GR187 - CRY2 - 3
GR97 - CRY2 - 3
GR8 - CRY2 - 3
GR278 - CRY40 - 6
GR188 - CRY33 - 16
GR6 - CRY28 - 11
GR186 - CRY3 - 23
GR96 - CRY36 - 27
GR98 - CRY6 - 29
GR7 - CRY7 - 20
GR276 - CRY7 - 20

(b)

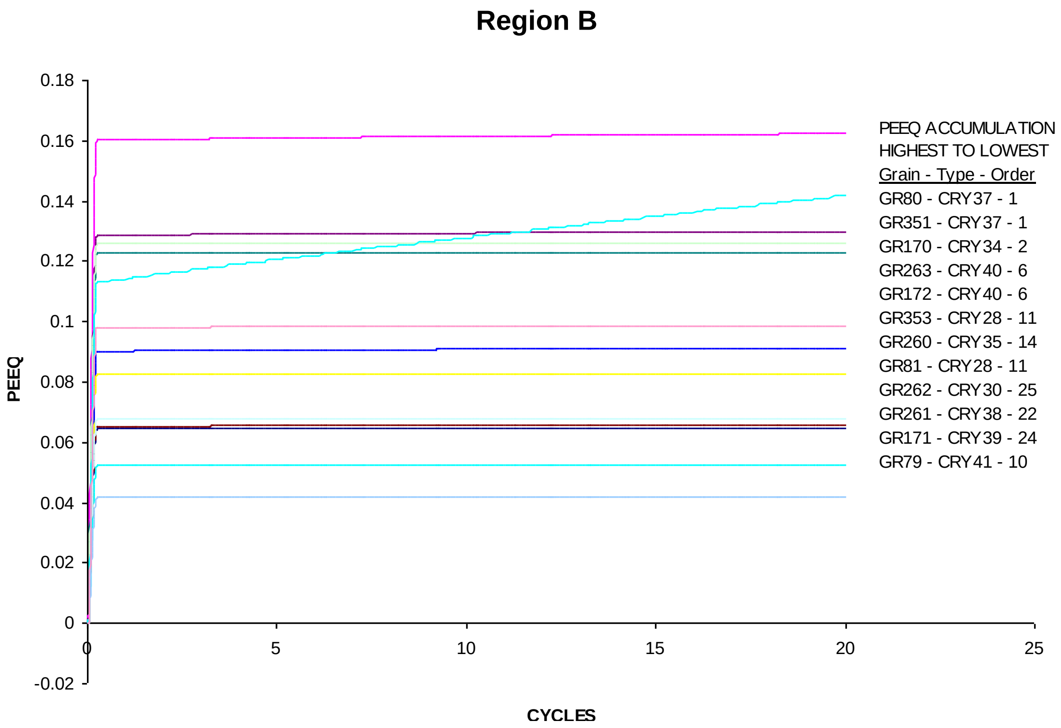

(c)

Figure 8.24. (a) Contour plot of 14 μm strut showing areas of strain localization and corresponding grain numbers (b) PEEQ history plot of selected grains in Region A and (c) PEEQ history plot of selected grains in Region B.

DISCUSSION

9.1. Introduction

The objective of this work was to establish if a mechanical size effect exists in the fatigue behaviour of microscale 316L stainless steel components. The fatigue testing carried out on 50, 75, 100 and 150 μm specimens showed that a size effect does indeed exist, reducing the fatigue limit of the 50 μm to below that of the wider specimens. It is worth noting that all the specimens were fabricated from tubing with a wall thickness of 60 μm, and the fatigue results indicate that there is only a significant difference in the results of the 50 μm data from the other samples. Therefore, it is more appropriate to conclude that the experimental results presented in this work show a size effect in the fatigue behaviour based on the specimens' smallest dimension (i.e. 50 μm for the 50 μm specimens and 60 μm for the 75, 100, 150 μm specimens). It is also worth noting that as the ratio of maximum stress and UTS approached unity, so the likelihood of failure increases. For narrow width specimens, where the level of constraint has been compromised, proximity to UTS is a better indicator of failure than ductility exhaustion methods.

Micrographic studies of the test specimen surfaces strongly suggested that the process of strain localization was most pronounced in 50 μm specimens; this observation was verified by comparing interferometric measurements of the surface roughness of 50 μm and 150 μm specimens. Fracture surfaces were also examined in order to determine the mechanism by which specimens failed and to investigate the possibility that the failure mechanism differed for the different size specimens. However, no conclusive difference in the fracture behaviours was observed. The process of strain localization with the application of cyclic loads and its relationship with a reduction in specimen thickness was investigated with the aid of finite element models. The 2D models described idealized polycrystalline structures of increasing thicknesses from 14 μm to 150 μm. This chapter aims to tie together all the various strands of the research into one cohesive section describing the size effect and its causes.

The research is targeted in general at the medical device industry and in particular at the vascular stent. There is a clinical drive to reduce the strut thickness of stents as lower thicknesses are associated with lower restenosis rates. Balloon expandable stents are deployed into coronary arteries where they are then subjected to hundreds of millions of fatigue cycles. Finite element modelling (detailed in Chapter 3) of a number of different vascular stents provided a range of target stress values for fatigue testing. It is known that the tensile properties of 316L are size dependent within the size range used in vascular stents. The question then arises as to whether the fatigue properties of the material in this size range are similarly affected.

9.2. Size effect in fatigue and its implications

Fatigue testing of the 316L specimens reveals that a size effect does exist. The size effect reduces the fatigue limit of the 50 μm specimens to below that of the 75, 100 and 150 μm specimens (where the smallest dimension for each is 60 μm). Figure 9.1 shows this effect when expressed in terms of strain amplitude. The “maximum likelihood” fits generated by the ESDU programme provide a median S-N curve through a set of S-N data. The median curve corresponds to a fifty percent probability of failure. For comparison, bulk material data for 316L stainless steel [9.1] are shown and using the Goodman relationship, the data is used to estimate the behaviour at a load ratio of 0.5. The median curve fit is again provided by ESDU programme 97204.

Bulk material fatigue behaviour differs significantly from that at the microscale. Microscale specimens support a lower stress amplitude and exhibit a much flatter S-N behaviour than macroscale components. Furthermore, within the range of microscale sizes investigated, the 50 μm specimens experience a further reduction in fatigue strength below that of the 75, 100 and 150 μm specimens. The implications of this size effect are clear. Reducing the strut thickness to below 60 μm compromises the fatigue strength of the material. Without taking this into consideration, devices such as small vascular stents may be designed non-conservatively and may fail in service under nominal loading conditions. This effect must be quantified through fatigue testing of components of a similar size, material and processing route.

9.3. Strain histories of test specimens

The strain accumulation data shown in figure 5.13 for failed 50 μm samples shows an incremental increase in total strain due to cyclic creep up to the point of failure. This process of cyclic accumulation of plastic strain under conditions of asymmetrical loading is known as “ratchetting” [5.4, 5.5]. There is no compliance change in any of the samples that could be related to the opening or closing of a crack and there is nothing in the strain history to suggest that specimens would not complete the 10^7 cycles. For 150 μm failed specimens (5.15), a comparison of strain accumulation history with that of runout (5.16) specimens does not reveal any element of behaviour that suggests that failure is a likely outcome of the fatigue test. The strain accumulation data indicate that the failed and runout specimens behave in a similar manner macroscopically, up to the point where failure occurs. As with the runout 50 μm specimens, the runout 150 μm specimens exhibit changes in compliance during the course of the test which may be indicative of crack growth processes. Crack-like feature were observed on the surface of some 50 μm specimens and it was speculated initially that these may in fact be cracks. However, it can be concluded that what has been observed are not critical fatigue cracks in propagation mode, but in initiation mode, i.e. they lack sufficient depth to be considered as cracks that will cause compliance change and lead to rapid failure.

In conclusion, the strain history data indicates that crack formation and ductile overload occurred rapidly and that the fatigue life of the test specimens at all sizes is initiation dominated.

9.4. Micrography and surface roughness

Micrographic examination of the outer surfaces of pre and post test specimens suggests that there is a less uniform distribution of plastic strain on the surface of the 50 μm specimens, relative to the 75 μm and 150 μm specimens. This observation was confirmed by measuring the surface roughness values with a white light interferometer. The maximum levels of surface roughness for the 50 μm specimens are higher, while the minimum levels are quite similar to those measured for the 150 μm specimens. This indicates that plastic deformation is more evenly distributed throughout a 150 μm sample, whereas it is a less uniform process for the 50 μm samples (figure 6.9).

9.5. Fractography and failure mechanisms

SEM studies of the fracture surfaces of many failed specimens failed to elucidate any size-related differences in failure mechanism. A typical fracture surface consists of a fatigue failure region and a ductile failure region as shown in figure 9.2. The cleavage type fracture regions of many specimens are suggestive of a high fatigue crack growth rate (near ΔK_{IC}). The ductile fracture surfaces, identified by the presence of shear dimples, sit atop a severely plastically deformed and necked down ligament. The crack growth and fracture process is described in figure 6.18. That fatigue crack growth is a rapid event is supported by the strain accumulation histories of the various specimens as described in section 9.2.

9.6. Finite element modelling and mechanisms of the size effect

Finite element models of a range of strut thicknesses were used to investigate the mechanism associated with strain localization. The struts are represented as an idealized crystalline structure; this structure describes in a simple manner the inhomogeneous nature of strain distribution. A small number of cyclic loads at a common load ratio and maximum stress were applied to the various strut models. A size effect was found to exist which influences the behaviour of thinner struts in a manner which in reality could lead to a reduction in the fatigue life of such specimens. The differences in behaviour are due to a reduction in constraint experienced by the thinner models. As illustrated by figure 9.3, as the grain size to specimen width ratio is reduced, the mechanical behaviour of individual grains assumes a greater role in determining the behaviour the entire strut. A wide strut contains sufficient numbers of grains of harder orientation to ensure that homogeneous material behaviour dominates over inhomogeneous behaviour. Reducing the strut width will reduce the level of constraint experienced by regions within the strut. Softer regions, such as those highlighted in red in figure 9.3, will be exposed as the grain size to specimen width ratio is reduced. Without the reinforcing effect of the harder grain network, strain distribution becomes increasingly inhomogeneous, with the consequent localisation of strain within softer bands of grains.

In summary, there occurs a higher general level of deformation within the thinner samples; there is a greater degree of strain localisation within thin samples, higher maximum and lower minimum values of plastic strain within thin samples, higher levels of total deformation, higher incremental strain accumulation values and higher levels of surface roughness. It is a combination of these factors that would in reality, likely lead to a reduction in fatigue life of thin samples as cracks will initiate earlier and propagate more quickly under load control cyclic loading. The low level of constraint also contributes to a great variation in the material behaviour of struts of the same width. In conclusion, under conditions of fatigue loading, the finite element models suggest that the material behaviour of thin struts differs from that of the wider struts in a manner which is likely to result in a decrease in the fatigue life of the thin specimens.

9.7. Size effect in fatigue of microscale 316L stainless steel specimens

Each strut is made up of many thousands of grains of random orientation and hence different material behaviour. There exists within each specimen or strut, collections of grains of ‘softer’ (i.e. more preferentially oriented) lattice orientation; this results in ‘softer’ regions within the specimen. As the specimen size is reduced and the grain size to specimen width ratio is lowered, so too is the level of constraint afforded by the structure that is the strut. When the structure experiences a stress in excess of the yield point of the material, the resultant plastic strain is accommodated within these regions more favourably orientated for slip. As the specimen size is reduced, this effect becomes more pronounced, with fewer regions being activated, until a stage is reached where the majority of strain is localised within one region. The larger, less compliant structure prevents any appreciable strain localisation and through the network of harder grains, forces the uniform distribution of plastic strain. The 50µm struts are less constrained and consequently more compliant when subjected to loads. On the other hand, plastic strain is more evenly distributed within the 150µm struts. Fatigue failure occurs by the following process as detailed below and shown in figure 9.4(a-h):

(a) Strain localization within grains favourably orientated for slip,

(b) The formation of persistent slip bands (PSBs) and

(c) Interaction of the PSBs with the free surface,

(d) Intrusion and extrusion formation,

(e, f) Fracture

9.7.1. Fail and runout specimens

For initially smooth, defect free microscale 316L specimens, the fatigue behaviour becomes more random as the specimen width is reduced in a form of reverse Weibull effect. Standard Weibull theory relates increasing specimen size to increasing probability of failure, the larger the component, the greater the possibility of finding a critical defect. At the microscale, as the specimens become thinner, the reinforcing effect offered by the presence of many grains across the thickness is reduced and plastic strain is localized within grains preferably orientated for slip. In a coupling of two mechanisms, the initial high strain amplitude serves to activate these softer regions in a tensile size effect, and the fatigue size effect ensures that the process of strain hardening process continues during fatigue cycling. Where saturation does not occur, the specimens can last for at least 10^7 cycles, even when tested at a mean stress and stress amplitude which has produced failure of similar specimens. The random nature of fatigue performance at the 50µm size can be explained by the ability of certain specimens to achieve a more even distribution of plastic strain. Strain localisation may still occur, but as the area hardens, strain is transferred to other, initially less favourably orientated regions. No sufficiently developed surface defect, capable of increasing the effects of strain localisation to the point where a crack develops, was observed to occur in the strain hardened regions within 10^7 cycles.

References

[9.1] Weldon, L.M., McHugh, P.E., Carroll, W., Costello, E. and O'Bradaigh, C., (2005), The influence of passivation and electropolishing on the performance of medical grade stainless steels in static and fatigue loading. *J Mater Sci Mater Med*, Feb; 16(2): 107-117

[9.2] Romeyn, A. (1993) Physics of Plastic Deformation and Fatigue. In: Australian Aeronautical Conference. 5th Australian Aeronautical Conference, no. 93/6, 457-462.

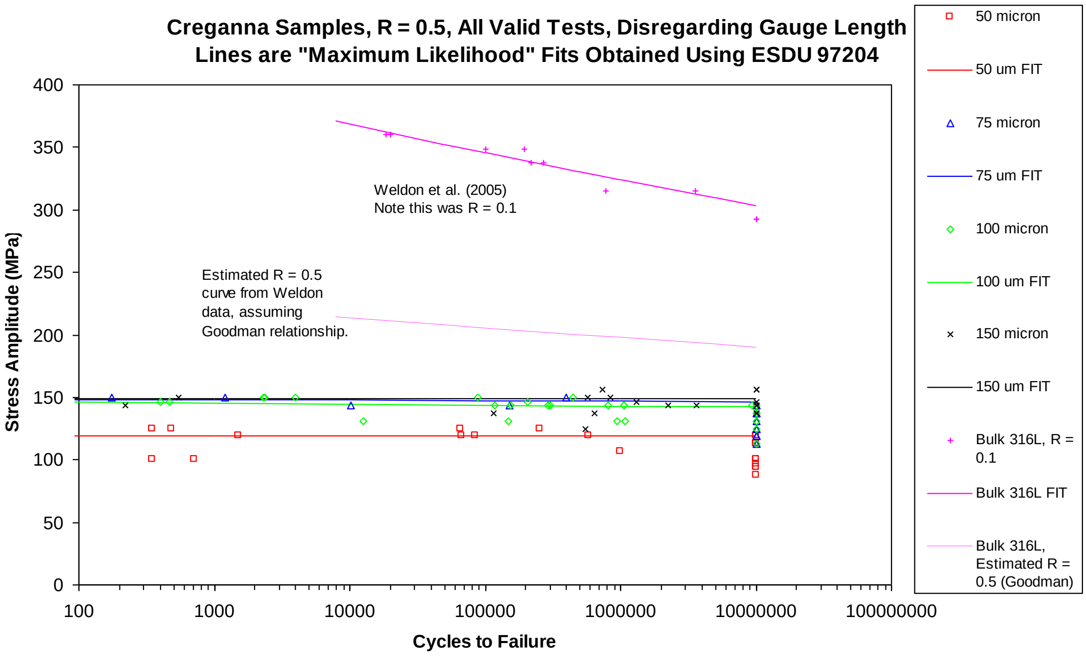

Figure 9.1. Micro vs macro 316L fatigue behaviour. Microscale specimens support a lower stress amplitude and exhibit a much flatter S-N behaviour than macroscale components.

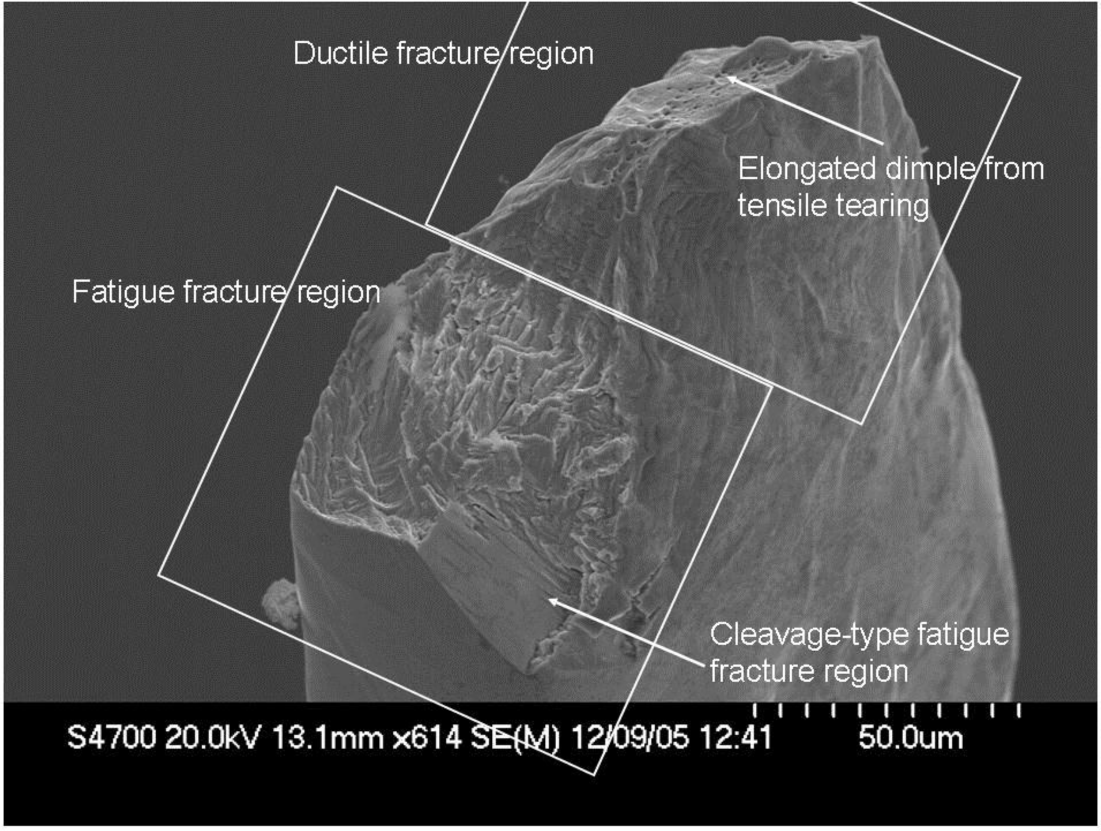

Figure 9.2. Typical fracture surface topology. Crystallographic and facetted failure profile indicates high level of strain hardening and consequent rapid crack growth. Highly localised ductility exhaustion/saturation.

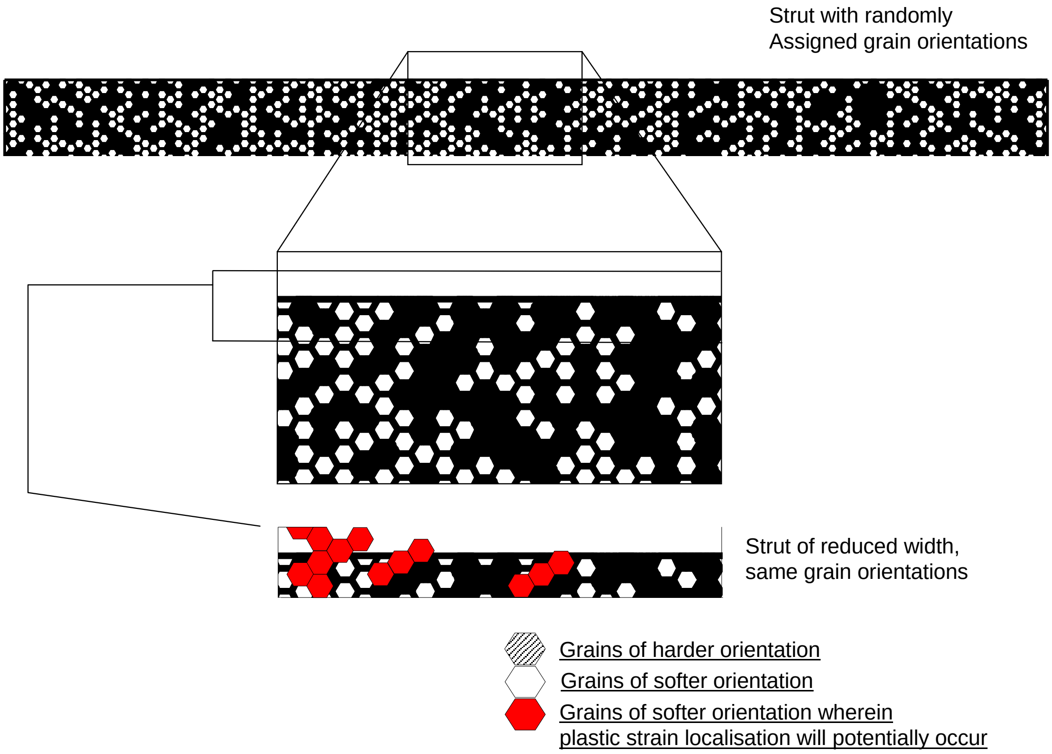

Figure 9.3. The effect of reducing strut width. High constraint ensures more uniform distribution of plastic strain in a wider strut. Reducing constraint "exposes" regions of softer orientation in a narrow strut. It is within these regions that strain localisation will occur.

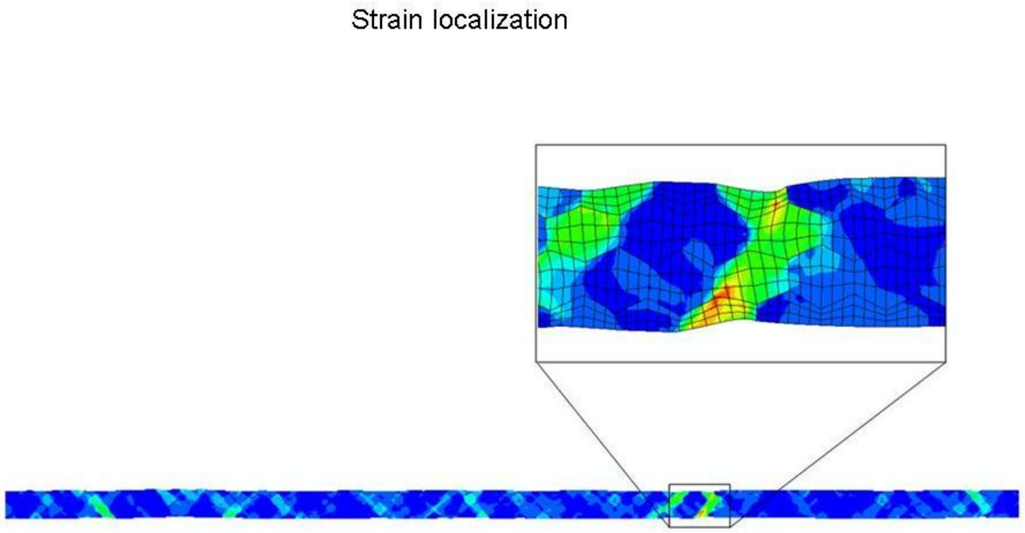

(a)

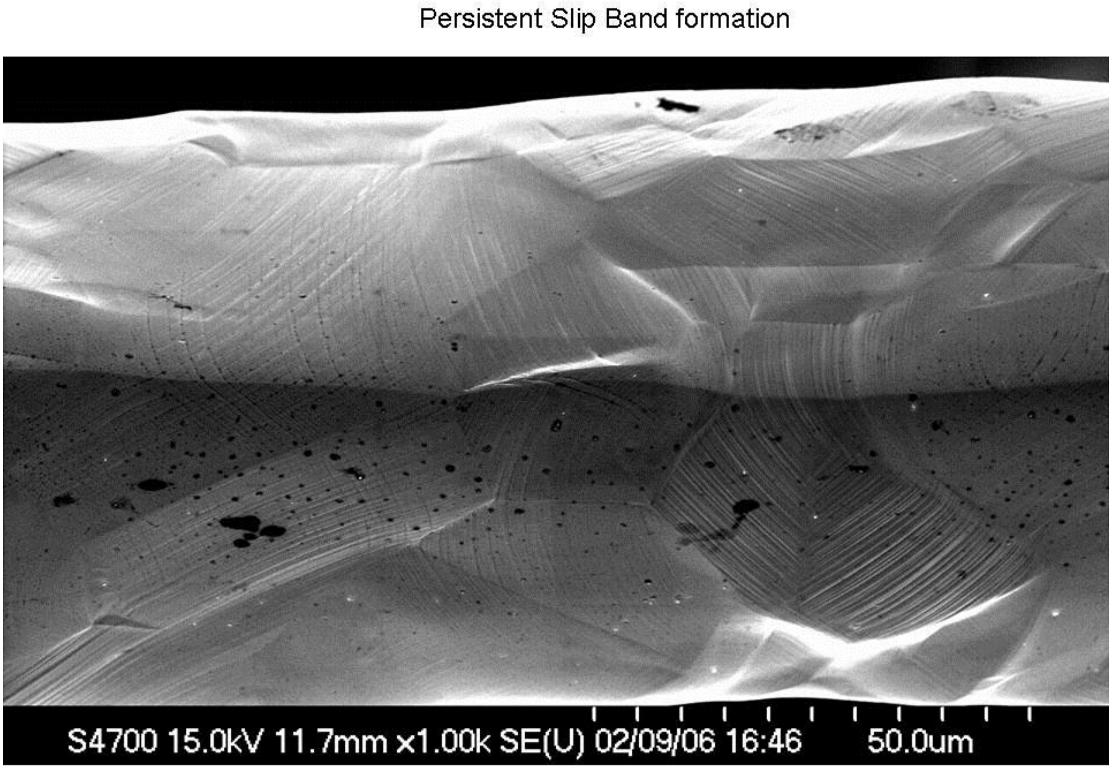
Persistent Slip Band formation

(b)

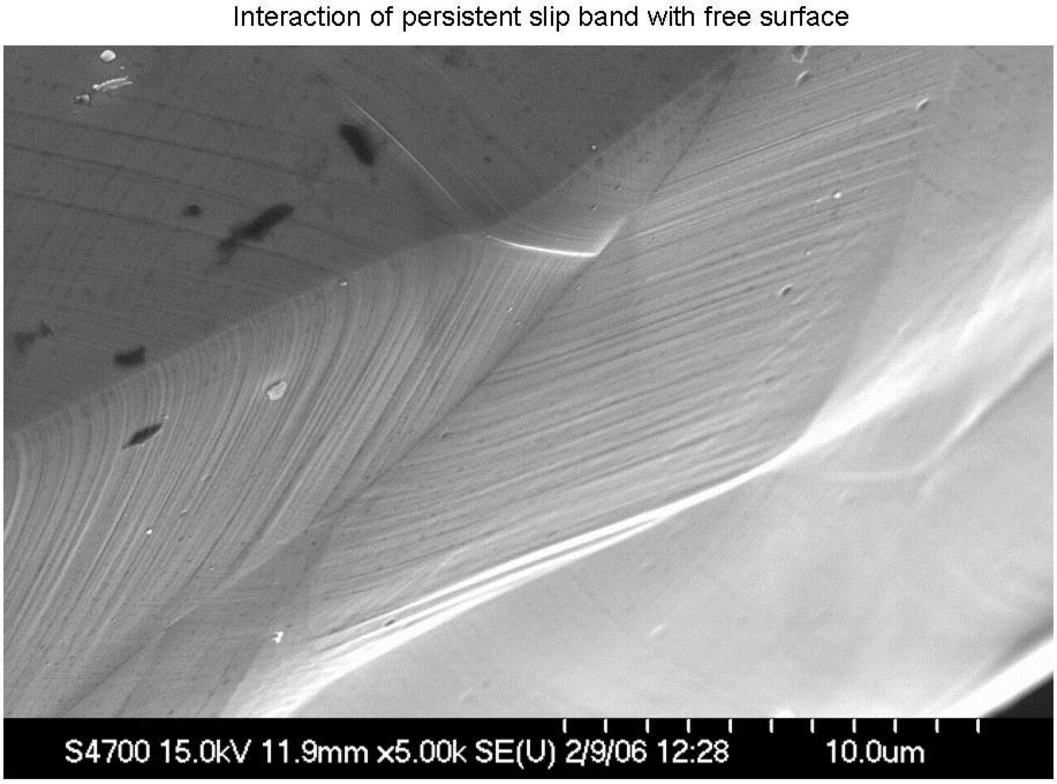
Interaction of persistent slip band with free surface

(c)

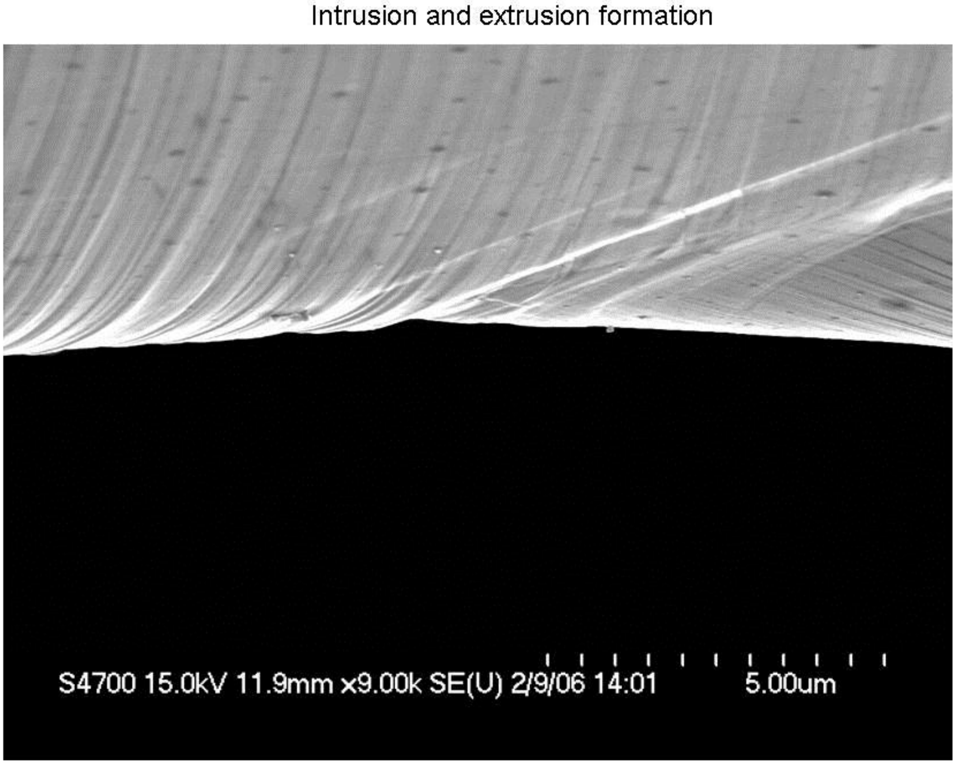
Intrusion and extrusion formation
S4700 15.0kV 11.9mm x9.00k SE(U) 2/9/06 14:01 5.00um

(d)

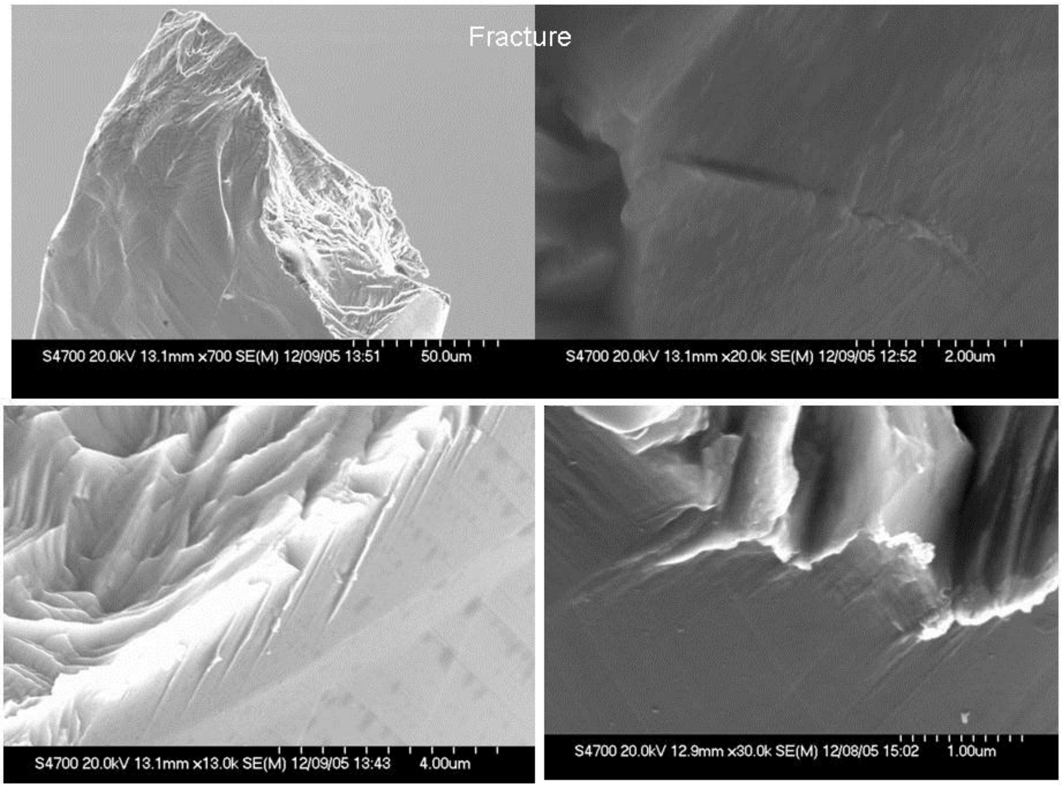
Fracture
S4700 20.0kV 13.1mm x700 SE(M) 12/09/05 13:51 50.0um
S4700 20.0kV 13.1mm x20.0k SE(M) 12/09/05 12:52 2.00um
S4700 20.0kV 13.1mm x13.0k SE(M) 12/09/05 13:43 4.00um
S4700 20.0kV 12.9mm x30.0k SE(M) 12/08/05 15:02 1.00um

(e)

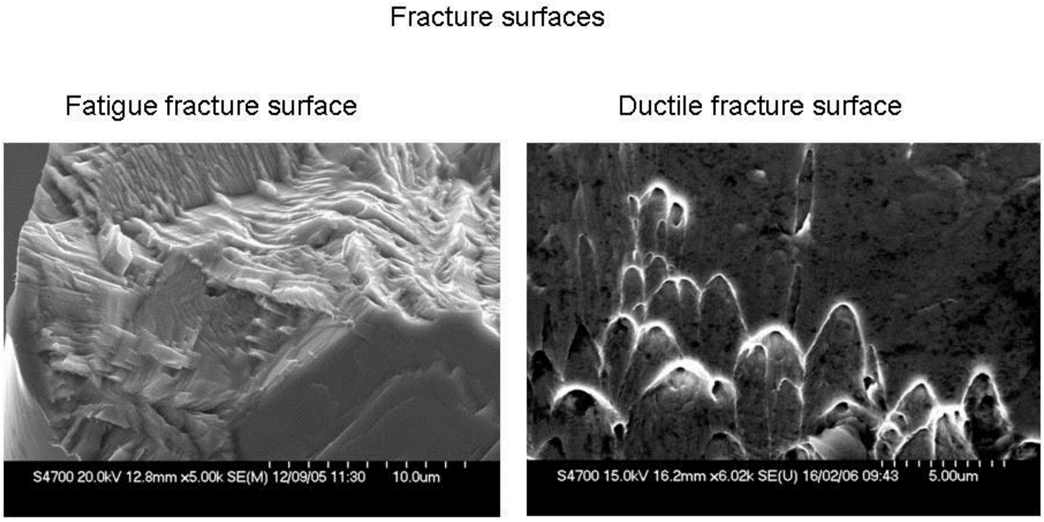

(f)

Figure 9.4. (a) Strain localization within grains favourably orientated for slip (b) The formation of persistent slip bands (PSBs) and (c) Interaction of the PSBs with the free surface (d) Intrusion and extrusion formation, (e) fracture (f) fracture surface features

CONCLUSIONS

10.1. Conclusions

The following conclusion are made with respect to the experimental testing, surface analysis and micromechanical modelling that were conducted in this work:

- Fatigue testing of the microscale 316L specimens reveals that a size effect does exist. The size effect reduces the fatigue limit of the 50 µm specimens to below that of the 75, 100 and 150 µm specimens (all of which have 60 µm as their smallest dimension.
- The strain history data indicate that crack formation and ductile overload occurred rapidly and that the fatigue life of the test specimens at all sizes is initiation dominated.
- There is a less uniform distribution of plastic strain on the surface of the 50 µm specimens, relative to the 75, 100 and 150 µm specimens.
- There is no obvious size-related difference in the failure mechanism.
- Cleavage-type fracture regions suggest that failure is initiation dominated and fatigue crack growth is a rapid event.
- Finite element modelling reproduced a size effect and exposed the underlying mechanism as one due to a reduction in constraint experienced by the thinner models.
- Under conditions of fatigue loading, the finite element models suggest that the material behaviour of thin struts differs from that of the wider struts in a manner which is likely to result in a decrease in the fatigue life of the thin specimens.

10.2. Future Work

The research in this thesis focussed on 316L stainless steel. While this remains a popular material selection for implantable medical devices, other materials such as the superelastic nickel-titanium alloy, Nitinol and the nickel-cobalt-chromium-molybdenum alloy, MP35N are now in widespread use in this field. Further work should investigate the existence of a fatigue-related size effect in such materials.

With regards to the experimental work performed in this work, the test specimens used were a modified form of the traditional hourglass fatigue specimen design. This design of the testing sample allowed for the fatigue behaviour of the specimens to be investigated under load control conditions. However, for research that focuses on the medical devices such as cardiovascular stents, a more relevant design that incorporates bending loading should be considered. Such as design may be that of a section of a stent frame, known as a “zig” or “diamond” [10.1]. The use of such a representative design should be considered for future experimental work.

In terms of the surface analysis performed in this work, the SEM examination and the surface roughness measurements demonstrated that strain localization was taking place, additional information on the grain orientation, rotation and reorientation can be acquired using techniques such as Electron Back Scattered Diffraction (EBSD) measurement [10.2] and Orientation Imaging Microscopy [10.3]. Such information would provide additional detail on the processes of plastic deformation in microscale components.

In conclusion, the present research focussed on exposing a fatigue-related size effect at the microscale and in describing the underlying mechanism. Based on the information provided in this thesis, additional work could be carried out to develop a predictive capability, either in the form of an empirical size-dependent fatigue failure relationship, or as a finite element model that describes explicitly the process of strain localization and its consequences as described in this thesis.

References

[10.1] Pelton, A.R., Schroeder, V., Mitchell, M.R., Gong, Xiao-Yan, Barney, M. and Robertson, S.W., (2008) Fatigue and durability of Nitinol stents, *Journal of the Mechanical Behaviour of Biomedical Materials I*, 153-164

[10.2] You, X., Connolley, T., McHugh, P.E., Cuddy, H. and Motz, C., (2006) A combined experimental and computational study of deformation in grains of biomedical grade 316LVM stainless steel, *Acta Materialia*, 54, 4825-4840

[10.3] Peralta, P., Dickerson, R,. Dellan, N., Komandur, K. and Jameel, M.A., (2005) Effects of Local Grain orientation on Fatigue Crack Growth in Multicrystalline fcc Metallic Materials, *J. Eng, Mater. Technol.* **127**, 1, 23-33

APPENDIX A

A.1. 316LVM material data sheets

Bar
Sandvik
Bioline 316LVM

Current Issue at: 15/01/2008 14:18:39. Cancels all previous editions

General description

Sandvik Bioline 316LVM is a Molybdenum alloyed vacuum remelted stainless steel for the production of both temporary and permanent implants.

Chemical composition (nominal) %

Sandvik Bioline	C max	Si	Mn	P max	S max	Cr	Ni	Mo	Cu max	N max
316LVM	0.025	0.6	1.7	0.025	0.003	17.5	14	2.8	0.10	0.10

Standards

Sandvik Grade: Bioline 316LVM
ASTM: F138-03
UNS: S31673
ISO: 5832-1
W Nr.: 1.4441
DIN: X 2 CrNiMo 18 15 3

Product standard
ASTM F138-03
DIN ISO 5832-1 Comp D, 2000
ISO 5832-1, Comp D, 1997.
BS 7252-1, Comp D, 1997.

Mechanical properties

Condition	Proof strength		Tensile strength		Elongation	Hardness
	$R_{p0,2}$ MPa min	ksi min	R_m MPa min	ksi min	A,% typical values	Brinell typical
Annealed	190	28	490	71	45	160
Medium tensile	700	101	900	131	15	285
High tensile	800	116	1100	160	12	300

Physical properties

Sandvik Bioline 316LVM		
Density (20 °C)	8.0 g/cm^3	0.29 lb/in^3
Modulus of elasticity, x10^3 (20°)	200 MPa	29.0ksi
Specific heat capacity (20°C)	485 J/(kg °C)	0.11Btu/(lb°F)
Thermal conductivity (20°)	14W /(m°C)	8 Btu/(lb°F)
Thermal expansion, x10^{-6} (30-100°)	16.5 per °C	9.5 per °F

Corrosion resistance

Bioline 316LVM has a very good resistance in physiological environments to:
- general and integranular corrosion due to high purity and low ferrite content.
- pitting and crevice corrosion due to the high molybdenum content

Bioline 316LVM is capable of passing the Moneypenny Strauss corrosion test where the test piece is heated to 650°C for 30 minutes and air cooled prior to test.

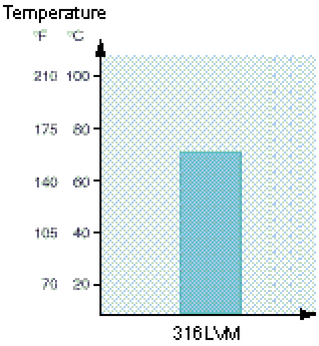

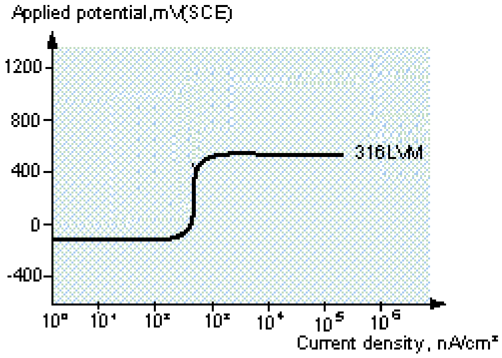

APPENDIX B

Experimental protocol for tube specimens

B.1. Enduratec Set-Up

1. Turn locals ON (select High)
2. Verify that Stop/Hold has been set to zero
3. Zero Load 1 and Displacement transducer (also high resolution transducer if attached).
4. Calculate Pmax and Pmin using spreadsheet.
5. Enter values in Direct Control in Waveform
6. Change file directories and file names to match those of specimen.
7. Zero cycle count value.

Important: During machine set-up, if movement of the base plate (plate on which bottom grip is mounted) is required, make sure you tighten the collars that lock the plate in place when adjustments have been completed.

B.1.2. Specimen preparation

1. Insert a pin (ø1.35mm) into the each end of the test specimen such that the pin protrudes through to the support struts. The pin acts as a mandrel and prevents the tube being crushed when the grips are tightened.
2. Using pliers, squeeze the tube (specimen) end around pin. Do this so that the major axis of the now slightly oblong tube will be parallel to the grip faces when inserted into the grips.
3. Repeat for other end of the test specimen.

4. Careful manipulation of the specimen is required as it is easily damaged. Perform this operation over the worktop. If the tube is dropped it will not have far to fall. Allowing the tube to fall to the floor will certainly render it useless.
5. Align the Enduratec grips using a flat plate. Figure A.1.1 shows the alignment plate position and procedure. The grips are not actually placed directly above each other, and are designed to "self align," but using the alignment plate will make this easier. Place the plate in the bottom set of grips and tighten the grip faces. Now align the top grip using the plate. When inserting the specimen, keep one side of the both grips in the same position (and move the opposing side only. Place the specimen in the grips. Having made sure that the specimen is centred within the grips (front, side, top and bottom), use the allen keys to tighten grip faces, tightening each grip alternately and making sure the specimen does not buckle during the process.
6. Use a bench lamp to assist in specimen alignment.

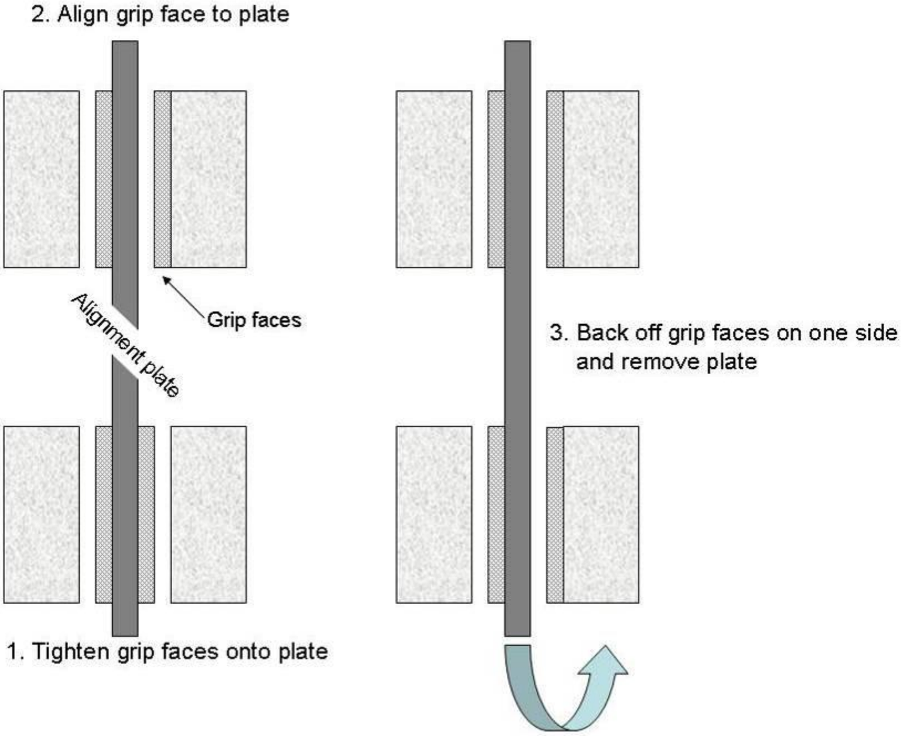

Figure B.1.1. Use of the alignment plate to align grip faces.

B.1.3. Further Enduratec Set-Up

1. Record Disp, Load 1 and Axial Cmd with the specimen in place.
2. Using Manual Voltage control method (toolbar designated by slide rule
3. symbol), adjust Axial Command Voltage until Load 1 is just less than Pmin in fatigue cycle. This will prevent buckling of the specimen during ramp up.
4. Return to Waveform in Wintest ® software to generate the waveform. Required entries are listed below:

Direct Levels V	*enter starting voltage*
Indirect Levels N	*enter maximum and minimum loads*
Frequency	*enter frequency of test in H*
Cycles	*enter number of cycles in test, determines runout*

   Adjust Direct Control Voltage so that it is equal to the voltage registering on the Axial Command Window, again in order to prevent buckling of the specimen during ramp up. The lower value of Direct Control voltage can be read off the meter in the main UI. A good value for the upper value of the Direct Control Voltage is (lower value + 0.03V), this seems to work for all samples.

5. With Axial Compensation on (0.005%), hit run and Zero Start.
6. Test started; observe at intervals during day to see whether specimen has failed.
7. Record the following values manually:

   Prior to insertion of specimen, zero displacement transducer and load cell.

   Insert sample, tighten grips and record Disp, Load and Axial Cmd values

   Cut support struts and record Disp, Load and Axial Cmd values

   Apply preload and record Disp, Load and Axial Cmd values.

This information will be needed to determine displacement of sample due to application of preload (for an explanation of how to do this see Appendix II). Unfortunately, this method does not permit resolution of straightening of sample from elongation of sample.

B.1.4. Actions during test

The frequency was set initially at 20Hz and increased to 60 Hz after 10,000 cycles had elapsed. This was done in order to achieve better control during the ramp-up phase of the test as the Enduratec controls better at 20Hz than at 60Hz. Once the specimen has elongated and stabilised somewhat, then the frequency is increased to 60Hz.

The R ratio was also increased from 0.1 to 0.5, as it was discovered that at an R ratio of 0.1, samples were damaged on ramp-up. This was because an R ratio of 0.1 ensures a very low minimum stress and consequently a low minimum load. In attempting to achieve the low minimum load, the machine would undershoot and buckle the sample. Increasing the R ratio to 0.5 increased the minimum load and solved the problem.

The frequency in increased by using the frequency tool bar and ramping the frequency up to 300% of initial value (20Hz x 3 = 60Hz). Fine tuning of the ramp up % was achieved by freezing the trace with a 0.2second time interval on the X-axis and counting the number of cycles. There should be 12 complete cycles in a 0.2 second interval at 60Hz.

B.1.5. Specimen Handling Post Failure

1. Remove both parts of specimen from grips, cut off struts and attach to cardboard. Return to plastic tube for future use.
2. For runout sample, remove load using Manual Voltage Control. It has been found to beneficial to leave a small preload on the runout sample, ~0.2N seems to be sufficient. This prevents the sample from buckling due to load removal and also when it is being cut top and bottom.
3. Using a good set of snips, cut the sample about 4mm above the top of the gauge length and at the same distance below the gauge length.
4. Handle the sample carefully as it is very delicate. Attach the sample to a piece of stiff cardboard and hold it in place with some masking tape. Return it to the tube from whence it came.

B.1.6. Data Transfer

1. On completion of test, use export option to export data to designated files, both .pvf (peak valley files) and .tdf (timed data files). Select .csv file extension in the file type options window.
2. Prior to exporting data, change the file extension manually to .csv, otherwise the data files may be overwritten e.g. CregII_01_50.pvf modified to CregII_01_50.pvf.csv for export and exported as a .csv file.

B.1.7. Determining the displacement of the sample due to the application of a preload

Displacement actuator meter Zeroed

Load Cell meter Zeroed

Data recorded:

1. Sample inserted, grips tightened

Record, Disp, Load1, and Axial Cmd*

2. Support struts cut

Record, Disp, Load1, and Axial Cmd

3. Preload Applied

Record, Disp, Load1, and Axial Cmd

Correction is then = |(Displacement at time 0 with preload applied) – (displacement after struts cut, before preload applied)|

The “Corrected” value of displacement is then:

System recorded value[1] – (Displacement at test start, preload applied) + (Displacement due to preload)

Example (refer to Figure B.1.2)

Sample: CregII_06_150

Support struts cut: Displacement= -0.041mm (logbook)

Preload applied: Displacement= -0.024mm (.tdf file and logbook)

Displacement due to preload = |(-0.041) – (-0.024)| = 0.017mm

Displacement at time 0 with preload applied (Displacement at preload) = -0.024

Displacement due to application of preload = 0.017

25 seconds into test a displacement of 0.118 mm is recorded (.pvf file). The corrected displacement is then: 0.118 – (-0.024) + 0.017 = 0.159mm (figure A1). Alternatively just add (0.118 and 0.041).

---

[1] System recorded Value is generally the displacement value at test end

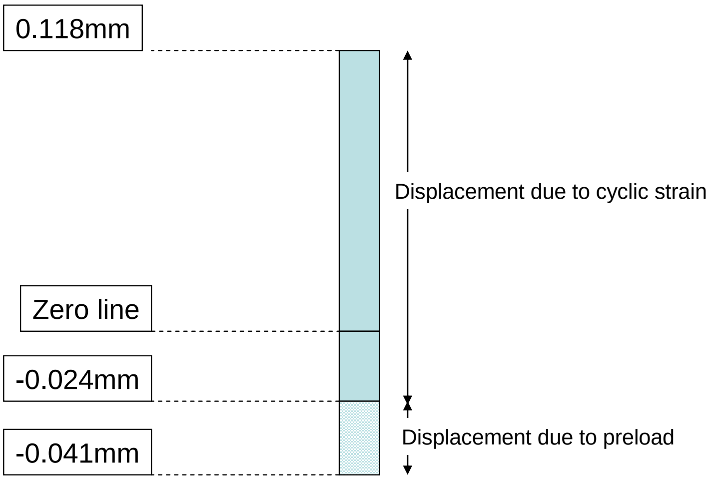

Displacement due to preload = |(-0.041) – (-0.021)| = 0.017mm
Displacement due to cyclic strain = 0.188 – (-0.024) = 0.142
Total displacement = 0.142 + 0.017 = 0.159

Figure B.1.2 . Schematic showing displacement correction for strut.

Drawbacks: This method does not account for any straightening (non elastic or plastic deformation) of the strut. Therefore, it is possible that a fraction of the "correction factor" is due to straightening of the strut. This will introduce a small error.

APPENDIX C

C.1. Hysteresis loops

Table C.1. Hysteresis loops for 50µm and 150µm specimens.

Sample number	Width [µm]	Maximum Stress [MPa]	R-ratio	Test outcome
CII_11_50	50	450	0.5	Runout
CII_14_50	50	450	0.5	Runout
CII_43_150	150	450	0.5	Runout
CII_45_150	150	450	0.5	Runout

Table C.2. Strain at various life fractions

Specimen	% strain at end ramp up	% strain at 4000 cycles	% strain at test end	Strain @ end ramp up as percentage of total strain	Strain @ 4000 cycles as percentage of total strain
CII_09_50	0.9	1.85	3.9%	23%	47%
CII_11_50	1.55	3.25	6%	26%	54%
CII_14_50	2.95	4.90	12%	25%	41%
CII_12_50	**2.3**	**4.40**	**9.35%**	**25%**	**47%**
CII_23_150	3.65	5.60	8%	45%	70%
CII_43_150	2.45	3.70	9%	27%	41%
CII_45_150	1.95	3.30	5%	40%	66%

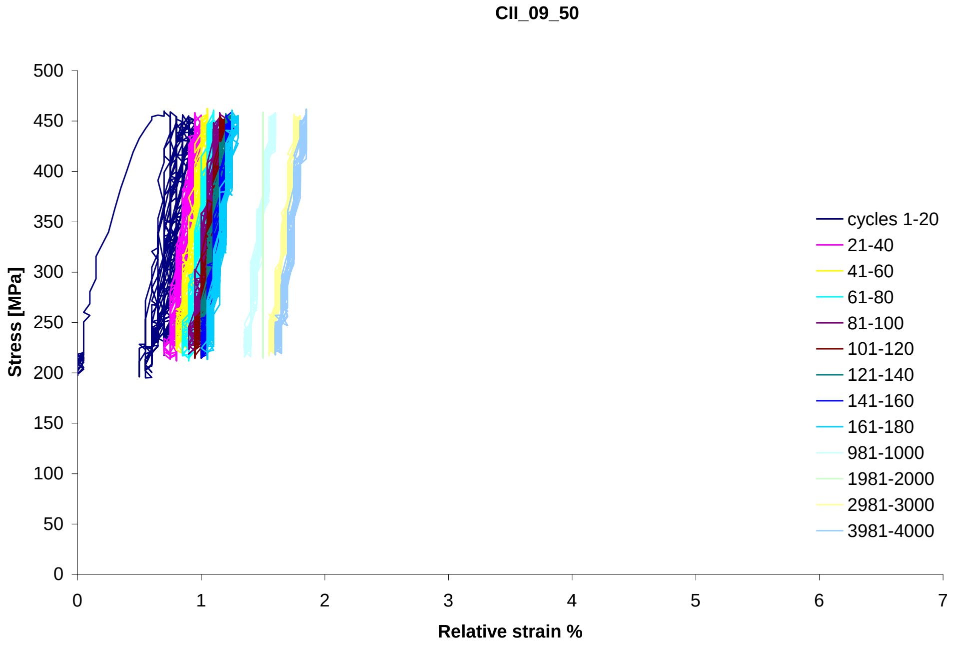

Figure C.1. Hysteresis loop for a 50µm runout specimen, various cycles from 0 up to 4000. Each colour coded group contains 20 cycles.

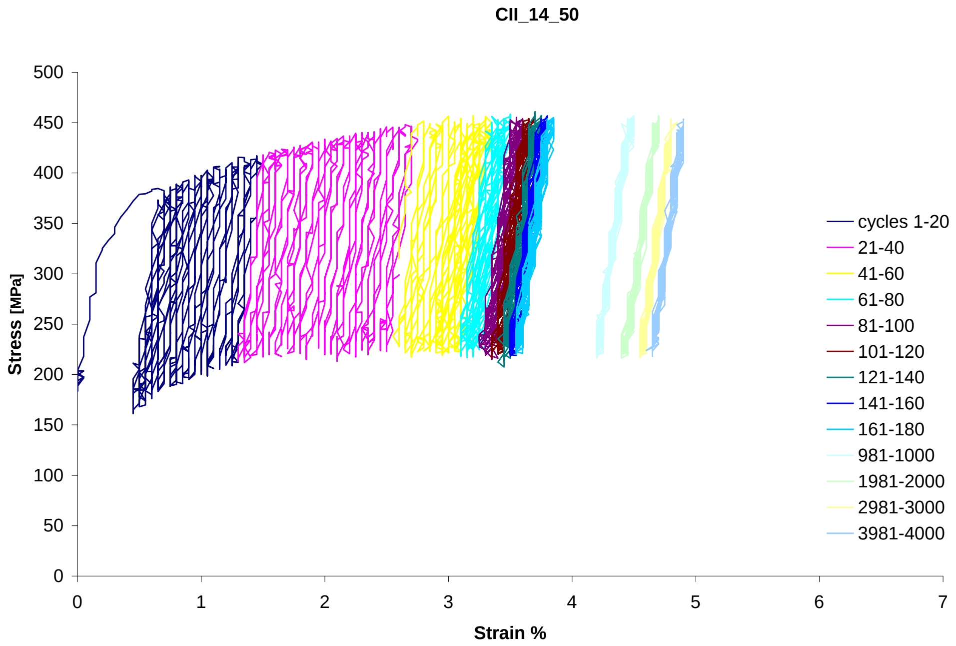

Figure C.2. Hysteresis loop for a 50µm runout specimen, various cycles from 0 up to 4000. Each colour coded group contains 20 cycles.

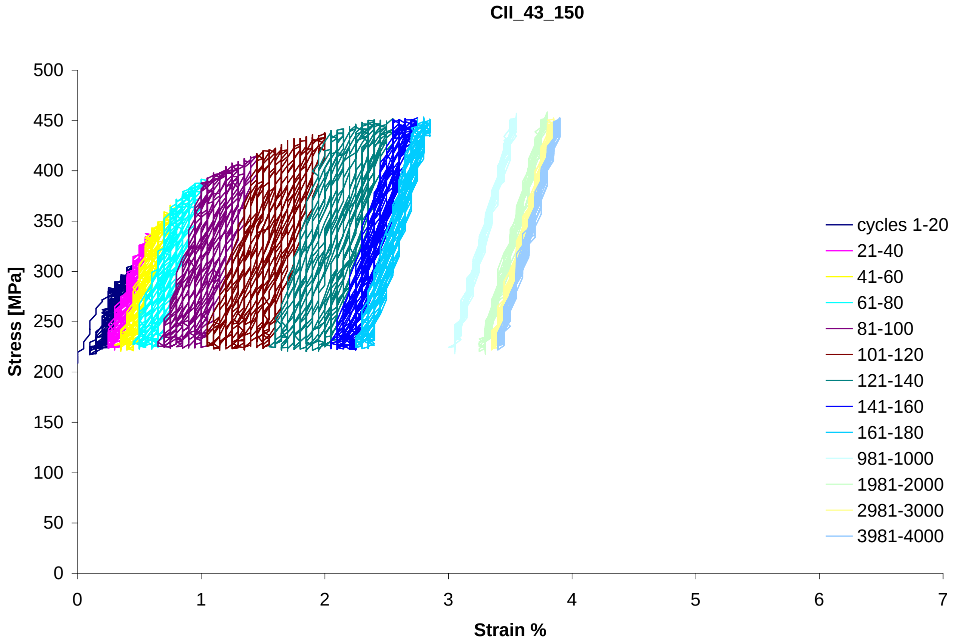

Figure C.3. Hysteresis loop for a 150µm runout specimen, various cycles from 0 up to 4000. Each colour coded group contains 20 cycles.

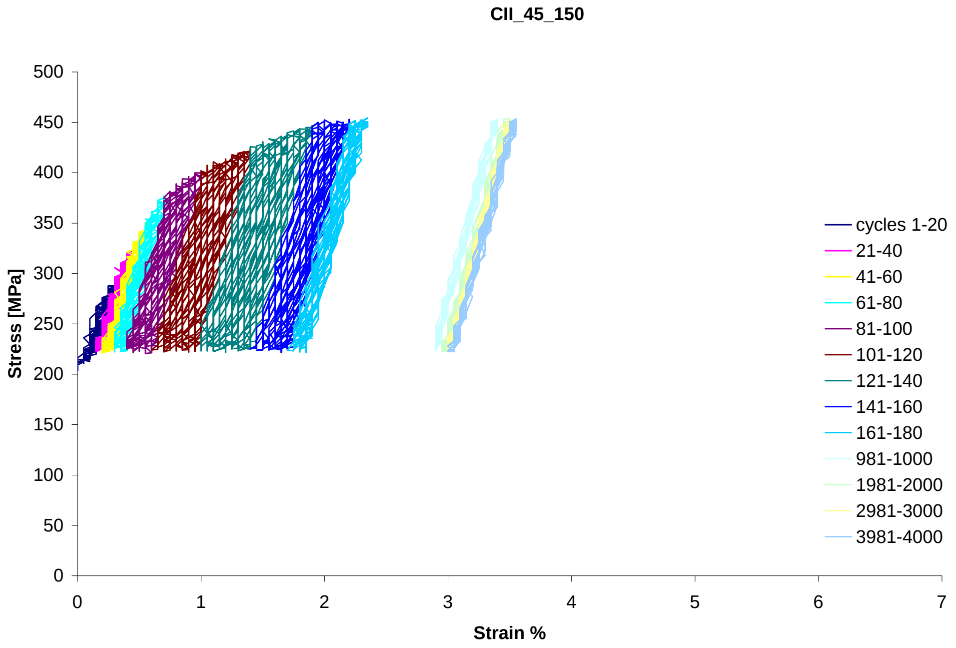

Figure C.4. Hysteresis loop for a 150μm runout specimen, various cycles from 0 up to 4000. Each colour coded group contains 20 cycles.

Appendix D

D.1. 50um specimens

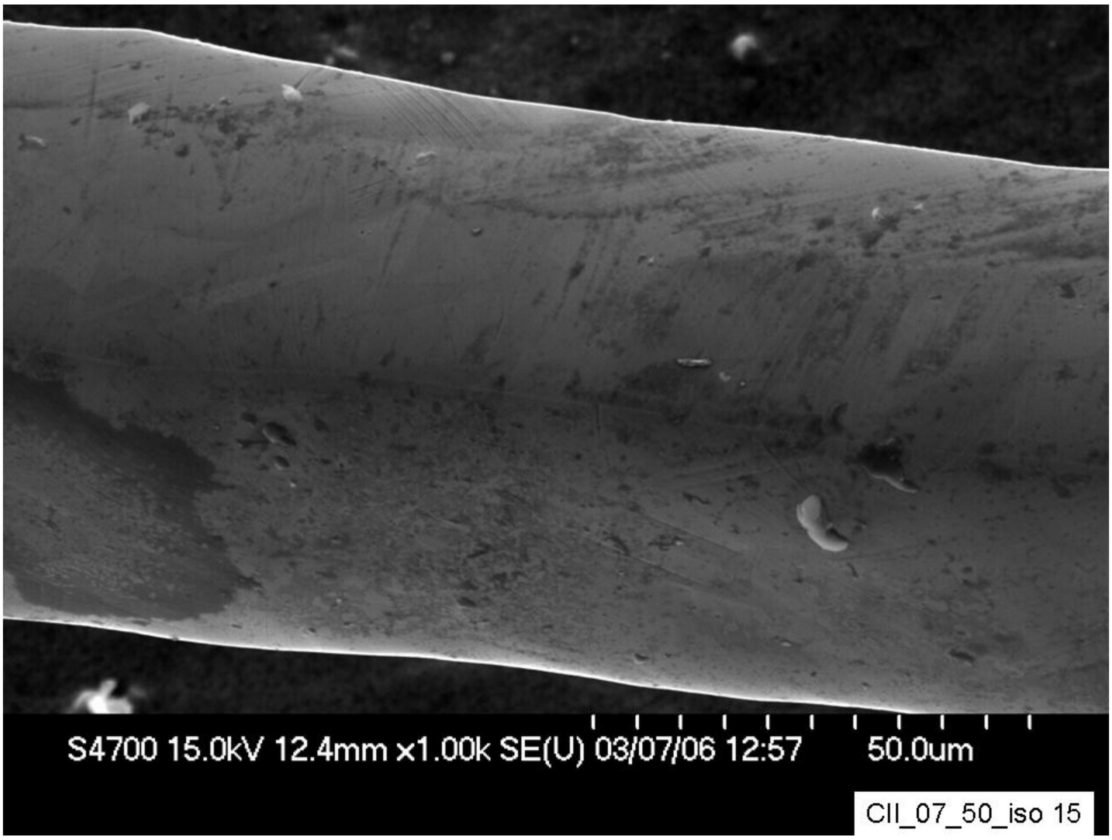

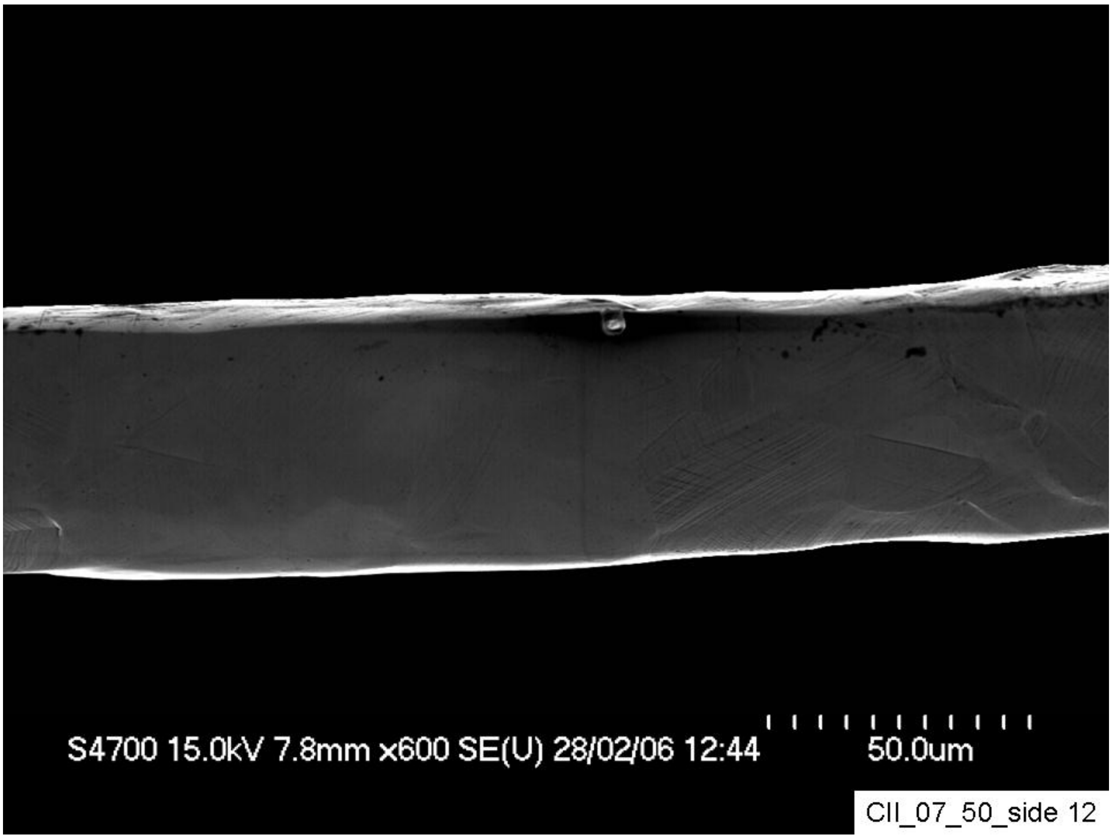

(a)

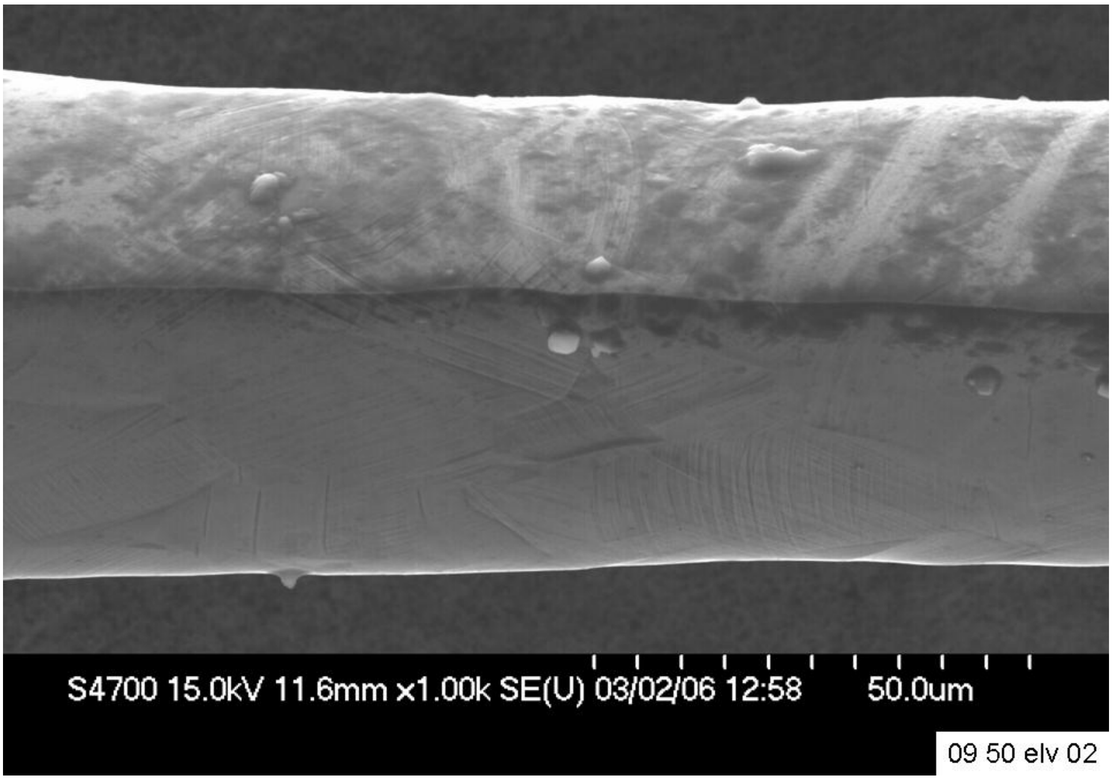
S4700 15.0kV 11.6mm x1.00k SE(U) 03/02/06 12:58
50.0um
09 50 elv 02

(b)

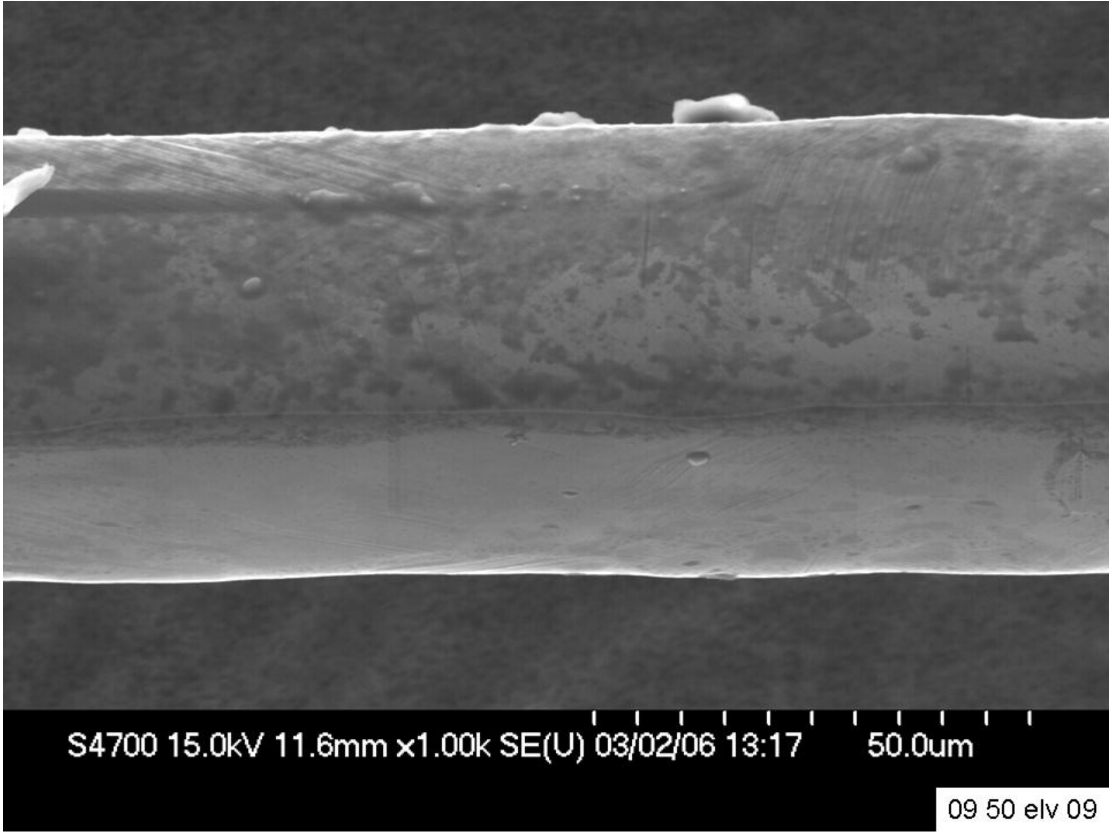
S4700 15.0kV 11.6mm x1.00k SE(U) 03/02/06 13:17
50.0um
09 50 elv 09

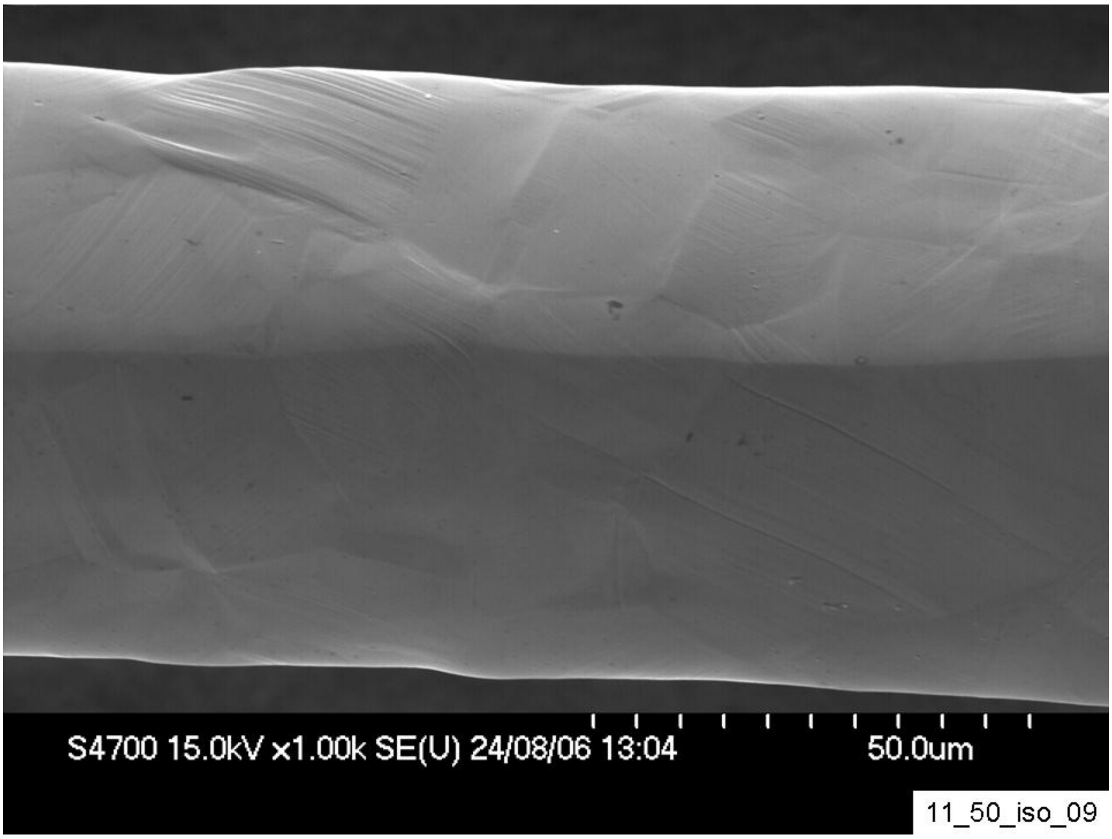
S4700 15.0kV ×1.00k SE(U) 24/08/06 13:04
50.0um
11_50_iso_09

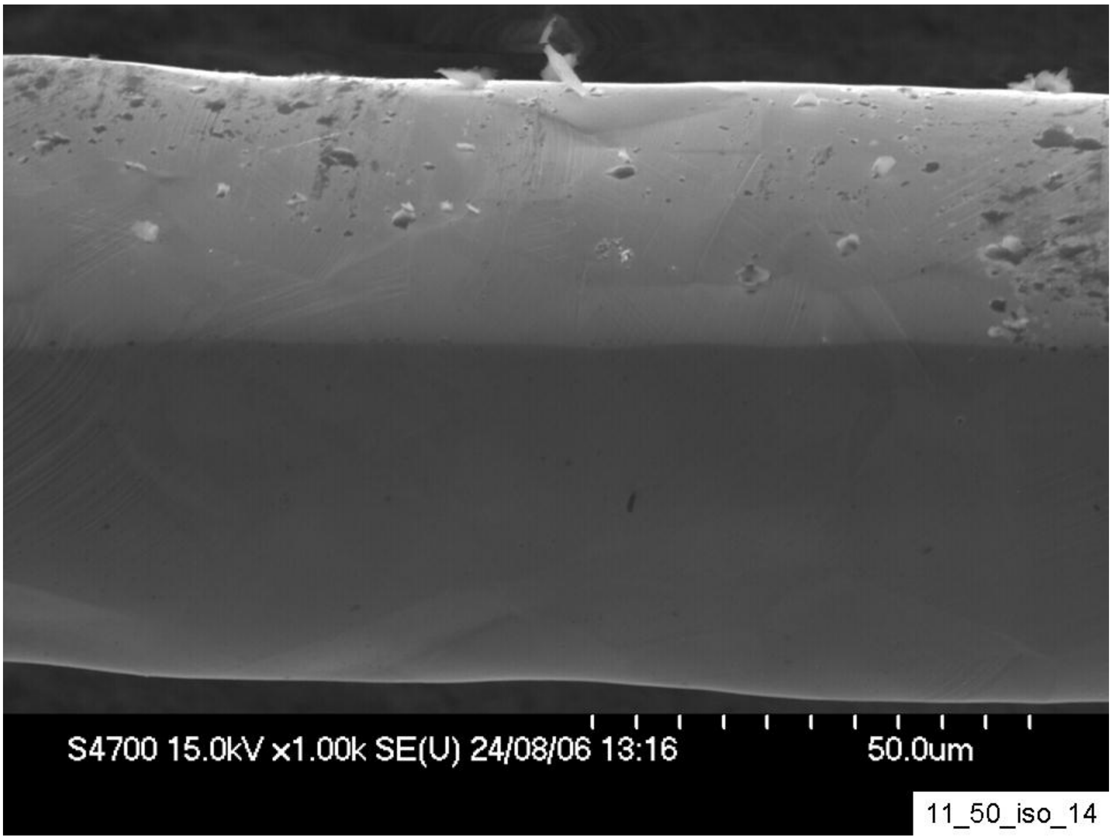
S4700 15.0kV ×1.00k SE(U) 24/08/06 13:16
50.0um
11_50_iso_14

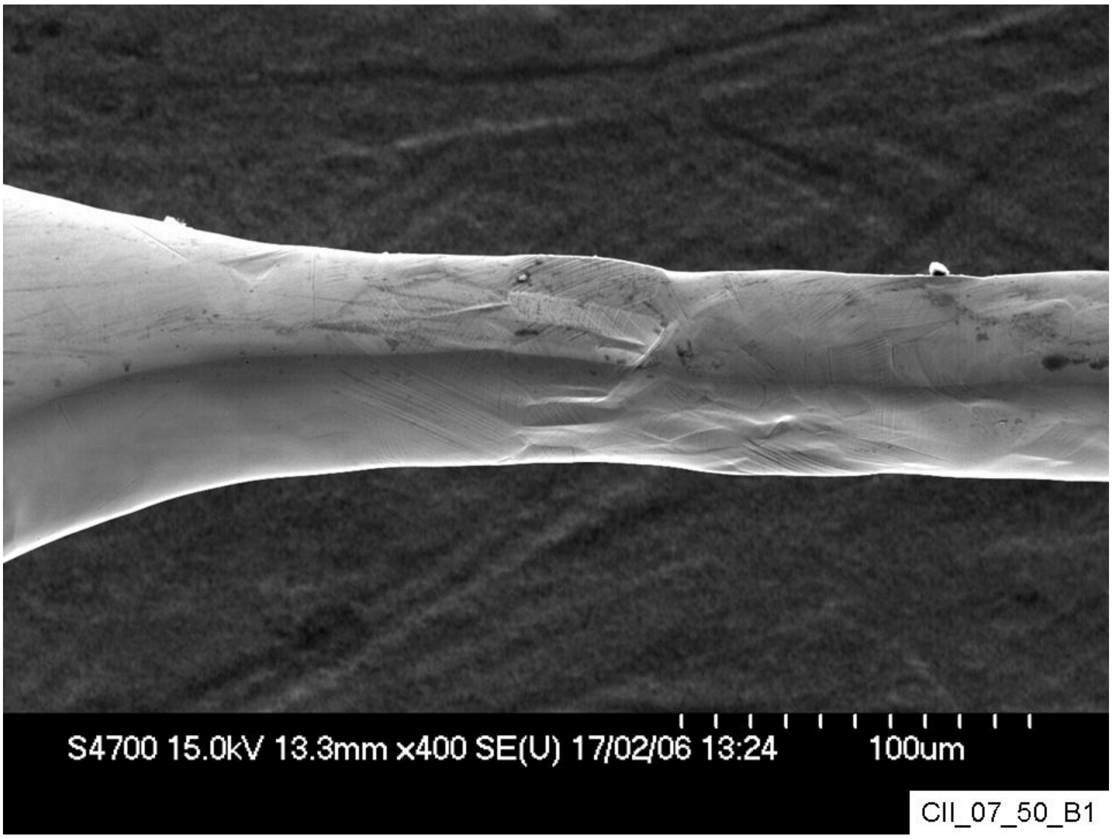

D.1.2. 75um specimens

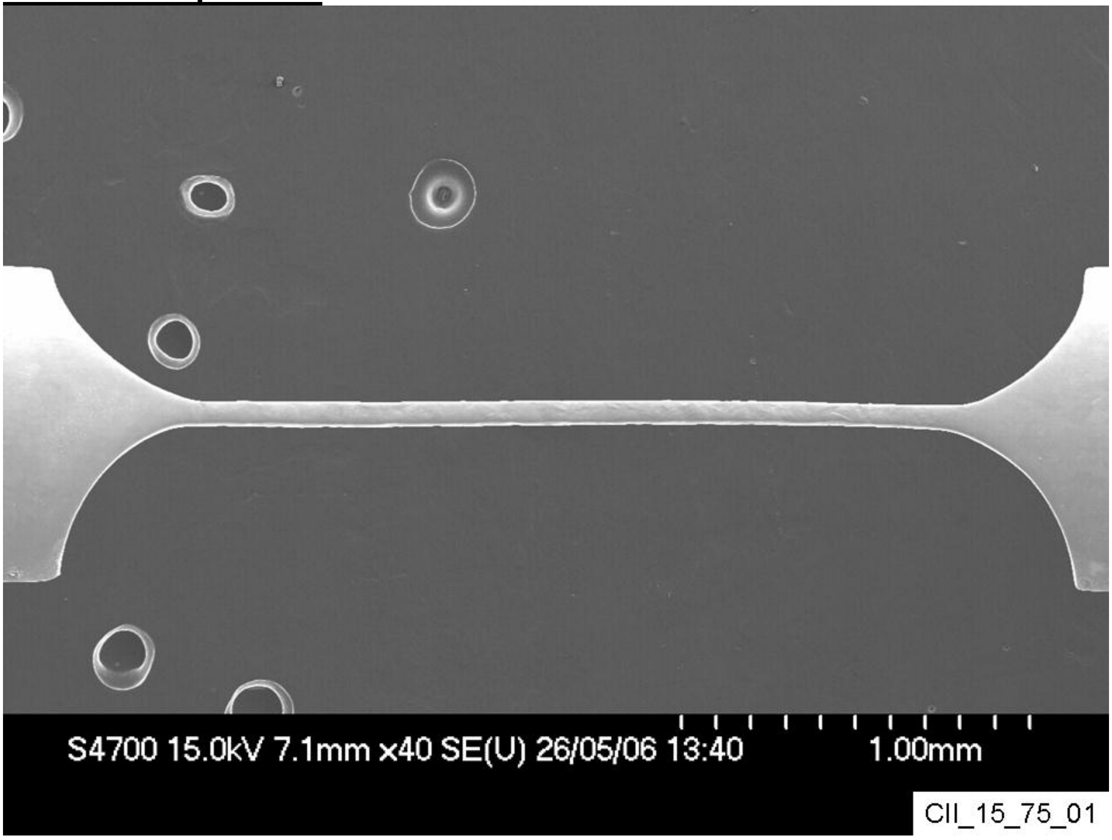

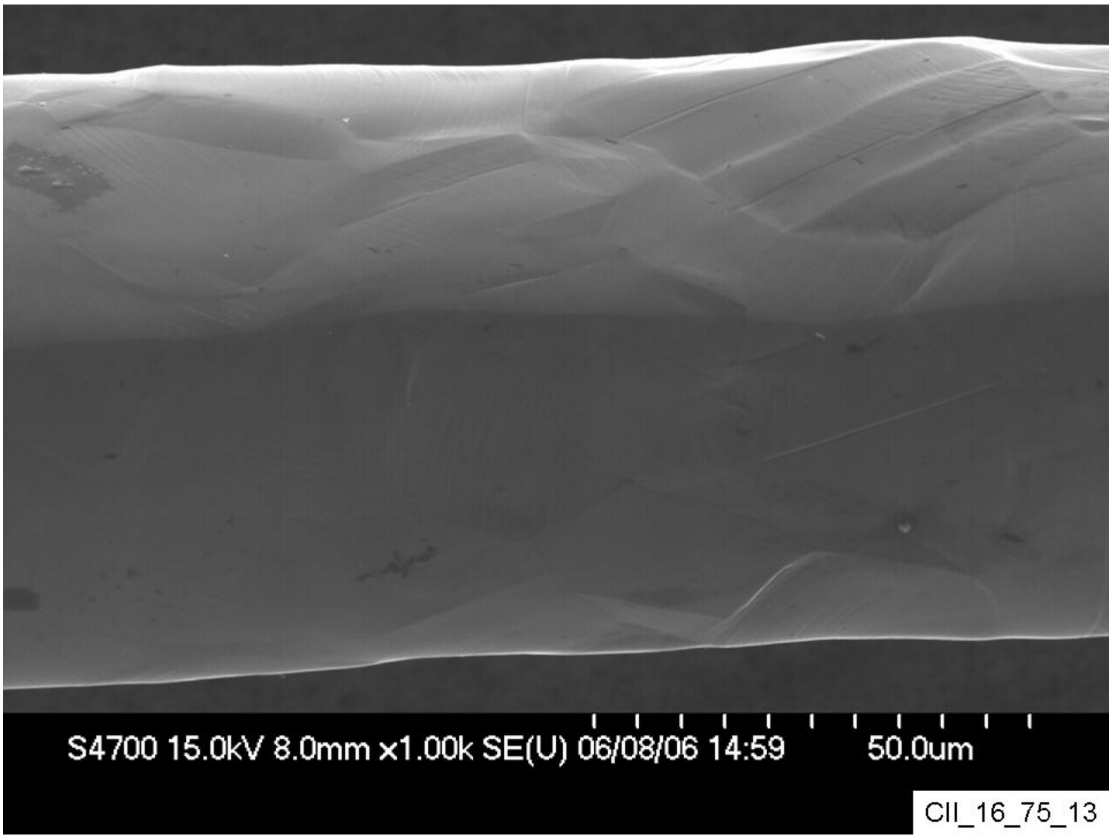
S4700 15.0kV 8.0mm x1.00k SE(U) 06/08/06 14:59
50.0um
CII_16_75_13

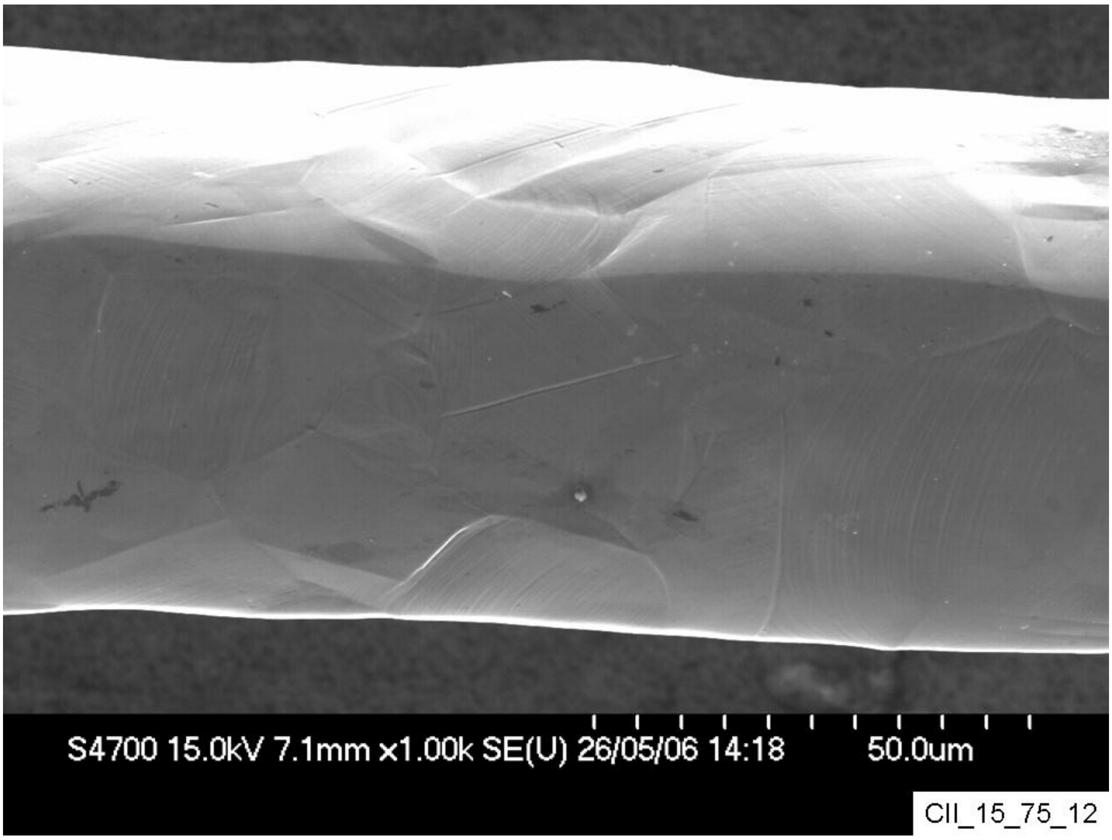
S4700 15.0kV 7.1mm x1.00k SE(U) 26/05/06 14:18
50.0um
CII_15_75_12

D.1.3. 150um specimens

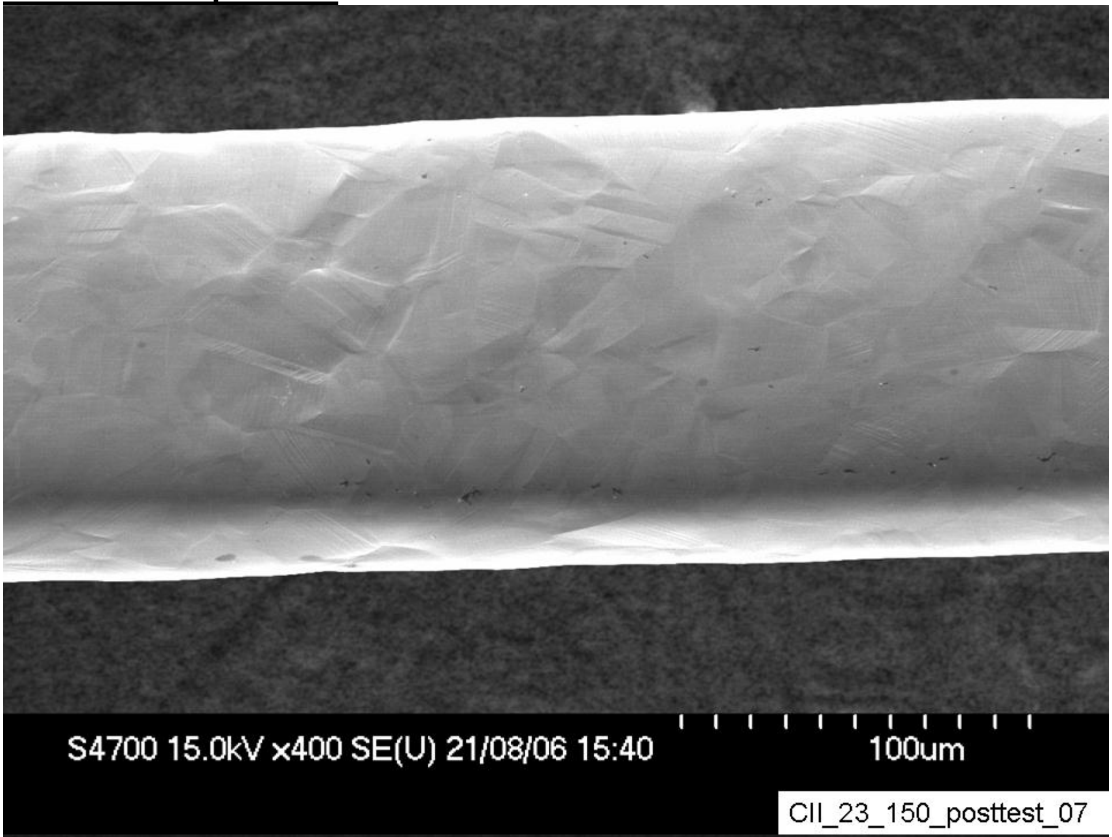

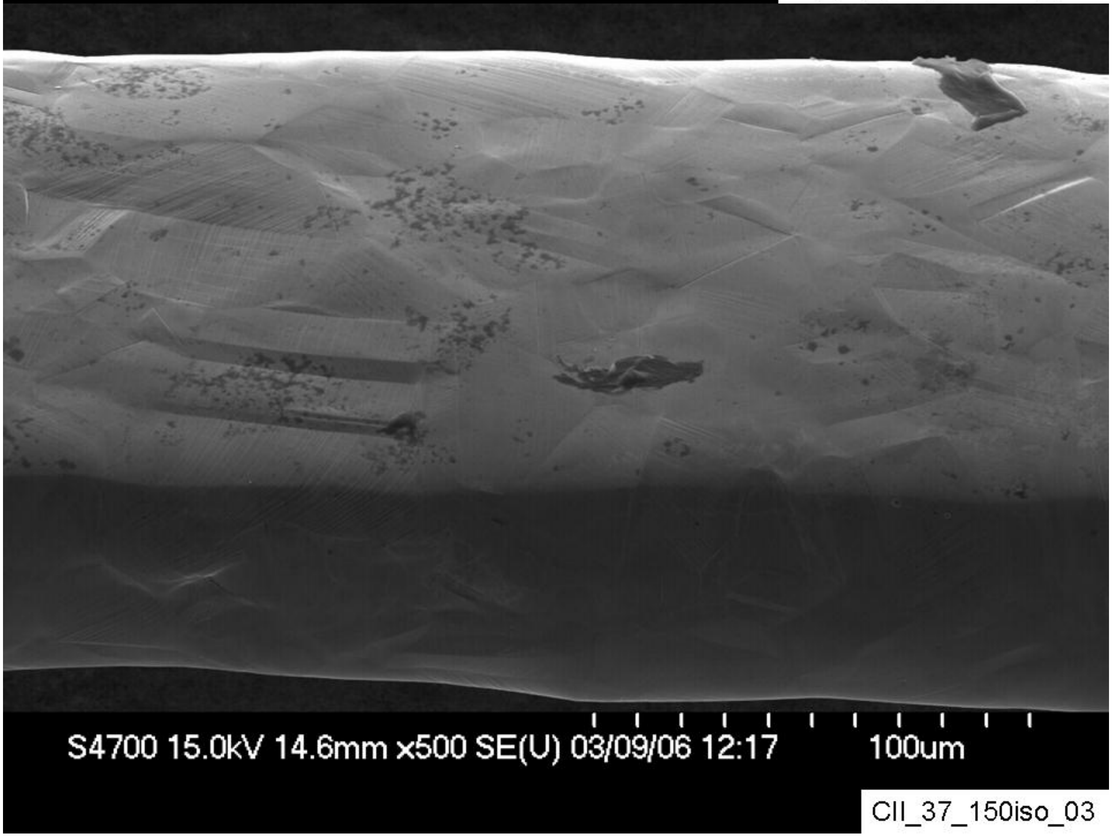

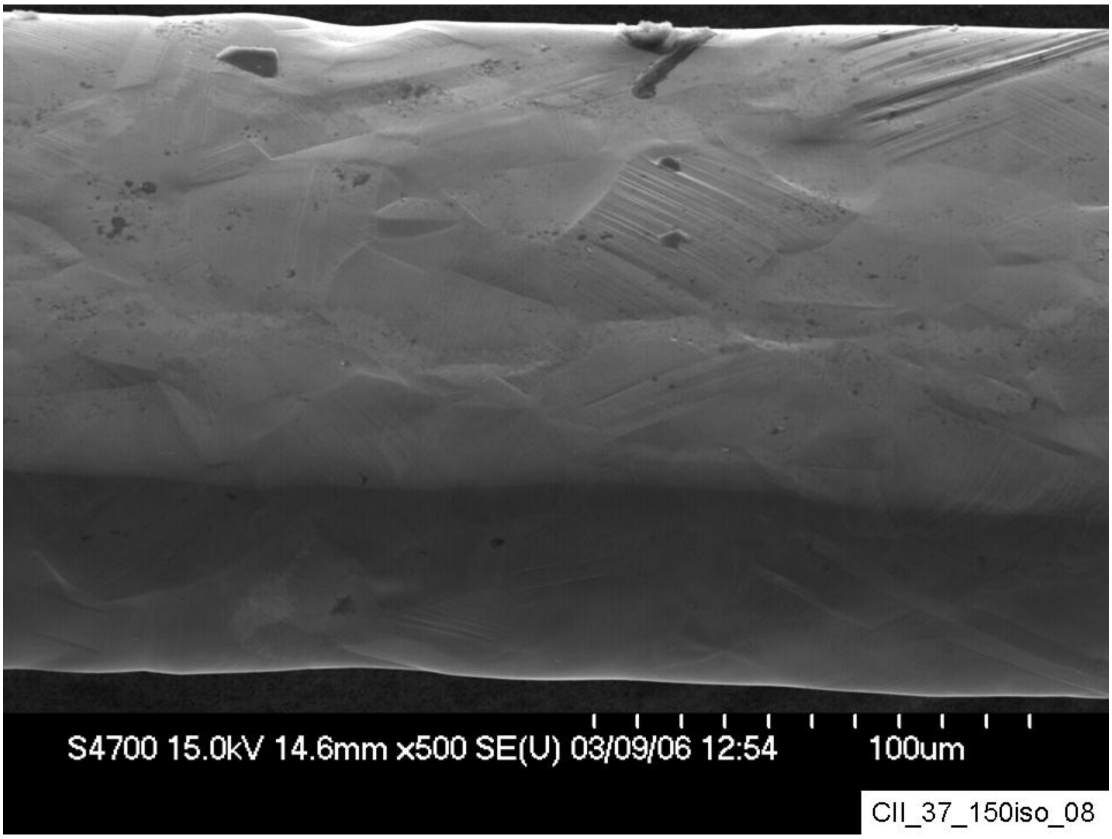
S4700 15.0kV 14.6mm x500 SE(U) 03/09/06 12:54
100um
CII_37_150iso_08

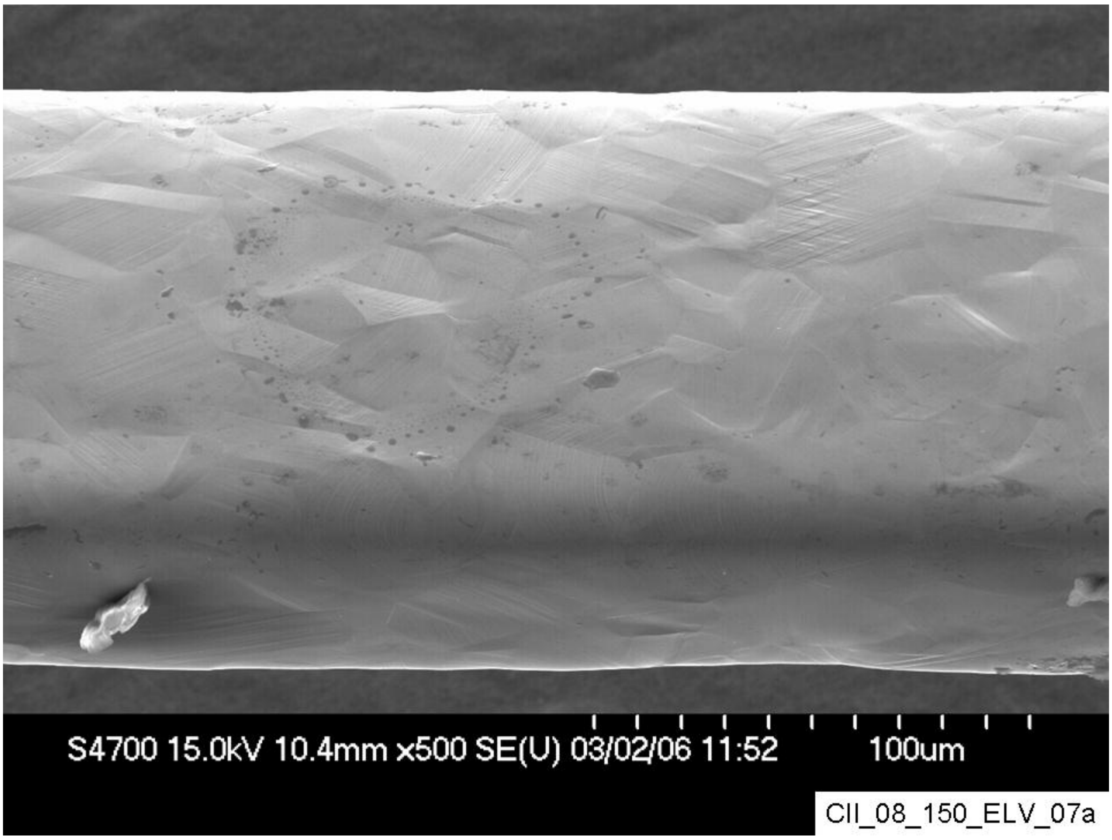
S4700 15.0kV 10.4mm x500 SE(U) 03/02/06 11:52
100um
CII_08_150_ELV_07a

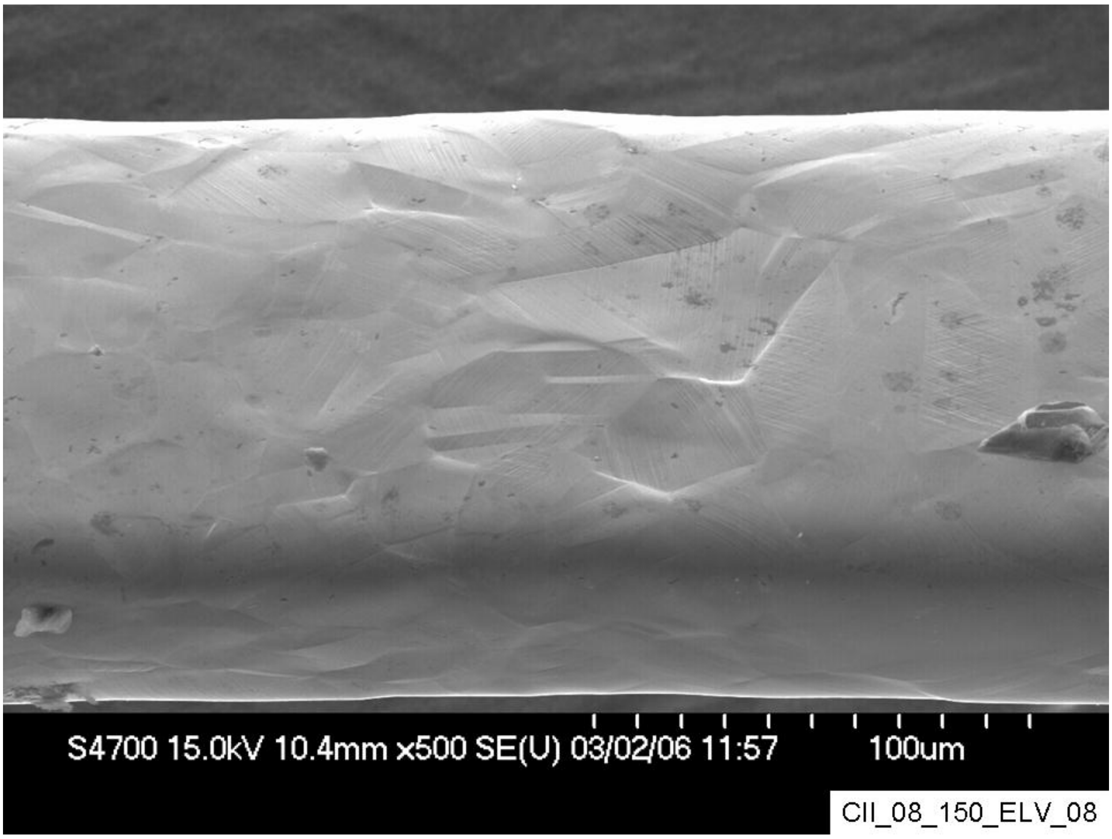
S4700 15.0kV 10.4mm x500 SE(U) 03/02/06 11:57
100um
CII_08_150_ELV_08

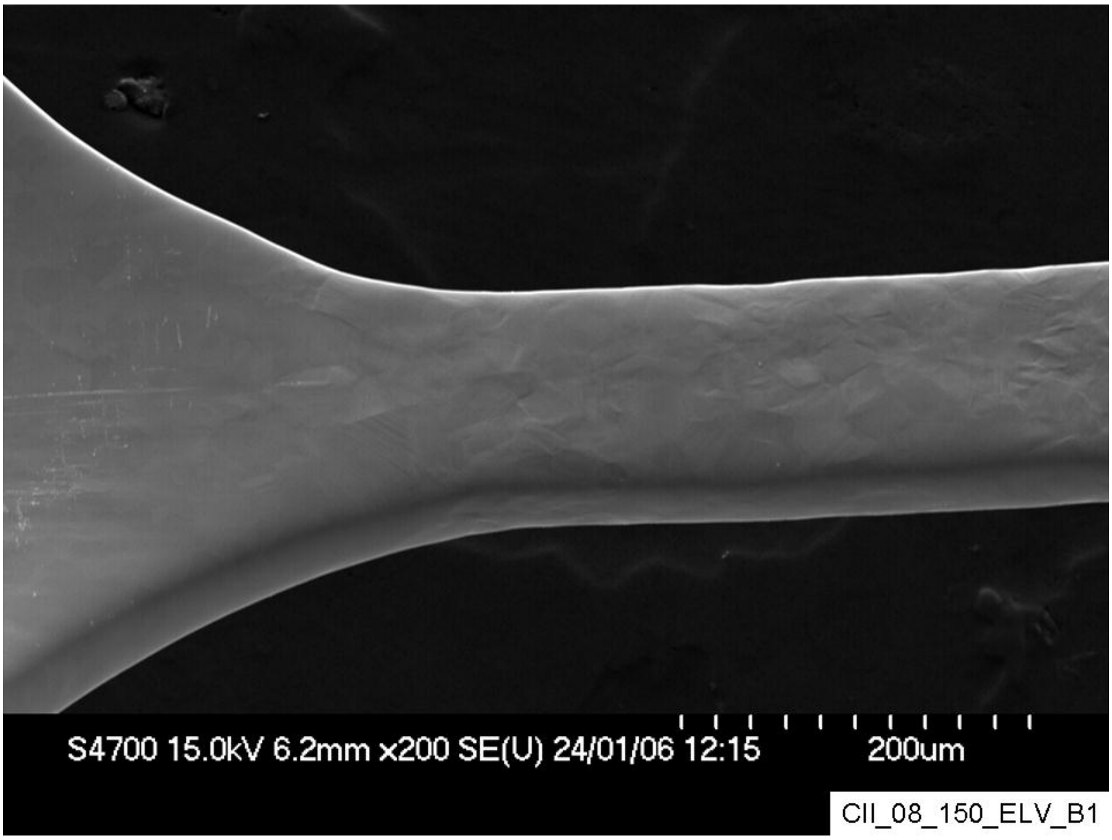
S4700 15.0kV 6.2mm x200 SE(U) 24/01/06 12:15
200um
CII_08_150_ELV_B1

Appendix D.2.

D.2.1. SEM TECHNIQUE FOR FRACTOGRAPHY OF FATIGUE SAMPLES

Accelerating Voltage

Accelerating voltage of 20kV preferable to 15kV. Monitor the emission current, making sure it does not drop.

Working Distance

Move sample closer to the lens, 6mm Z height.

Spot Size

Reduction of spot size also helps to improve image clarity
Go to Column Set up and change Condenser lens 1 (Con Lens 1) setting to 7-5
(Signal to noise ration will be detrimentally affected by this)

Detectors

Use the Upper detector only, this is indicated by the acronym SE(U) which appears on the SEM image.

Image Capture

Capture images at slow capture rate – slow 2 is sufficient
Capture 50um images at magnification of 1.5k.
Use high contrast as it shows up features more clearly.
Take one image of the fracture surface of each side of a sample at the same magnification. This will allow comparison of samples and also help to identify samples that are worth further investigation.

Energy dispersive x-ray microanalysis (EDX)

Use to identify chemical composition of materials.

316L S.S. chemical composition

AISI Type 316L Stainless Steel, annealed sheet
Source: http://www.matweb.com/search/SpecificMaterial.asp?bassnum=Q316N

Component	Wt. %	Component	Wt. %	Component	Wt. %
C	0.03	Mn	2	P	0.045
Cr	17	Mo	2.5	S	0.03
Fe	65	Ni	12	Si	1

Material Notes:
Similar to Type 316 for superior corrosion resistance, but also has superior resistance to intergranular corrosion following welding or stress relieving. Good corrosion resistance to most chemicals, salts, and acids and molybdenum content helps resistance to marine environments. The low carbon content of 316L reduces the possibility of in vivo corrosion for medical implant use. High creep strength at elevated temperatures. 316L has fabrication characteristics similar to Types 302 and 304.

Applications: biomedical implants, chemical processing, food processing, photographic, pharmaceutical, textile finishing, marine exterior trim.

Mounting runout specimens:

Firstly attempted this using the Carbon paste. Paste was rolled into small cylinders and segments of those cylinders were placed on the stub which was covered with a carbon tab. The specimen was then placed atop both “cylinders. In order to further

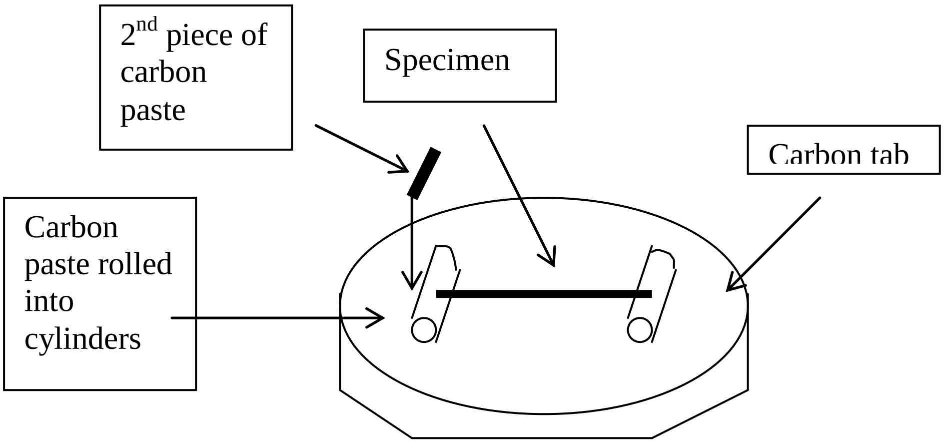

To further improve conductivity an additional piece of carbon paste was placed on top of both the specimen and the carbon paste on which it was placed.

Image quality was very poor with this method, perhaps due to poor conductivity through carbon paste. Replacing the carbon paste with segments of carbon tab lead to an improvement in sample quality thought I couldn’t conclusively say that this was the cause.

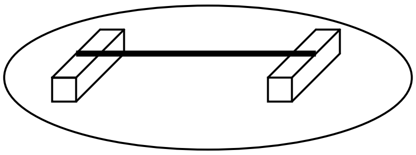

D.2.2. Image Drift

Image drift results in an apparent magnification of the image. Images taken at the same magnification are not at the same magnification when they are stitched together.

Tip:

If the image is drifting, put the instrument into Low Mag [LM] mode, focus on nothing in particular, and wait for 5-10 minutes. The beam may stabilise in this time.

Firstly attempted this using the Carbon paste. Paste was rolled into small cylinders and segments of those cylinders were placed on the stub which was covered with a carbon tab. The specimen was then placed atop both “cylinders. In order to further

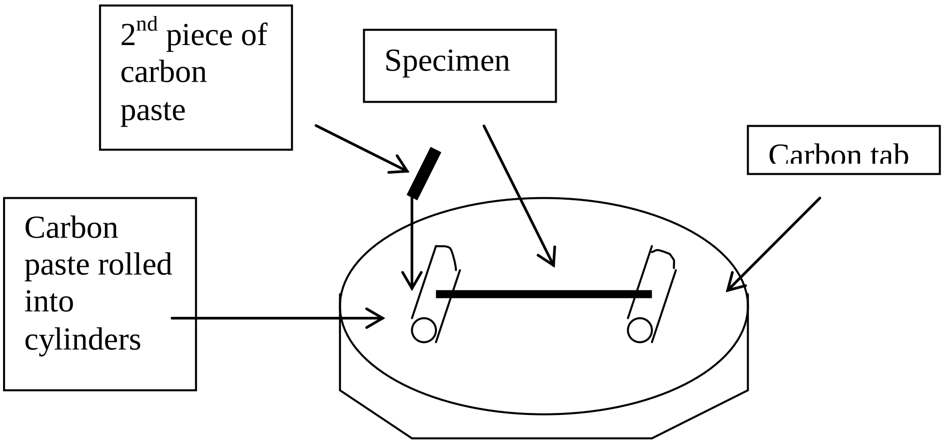

To further improve conductivity an additional piece of carbon paste was placed on top of both the specimen and the carbon paste on which it was placed.

Image quality was very poor with this method, perhaps due to poor conductivity through carbon paste. Replacing the carbon paste with segments of carbon tab lead to an improvement in sample quality thought I couldn’t conclusively say that this was the cause.

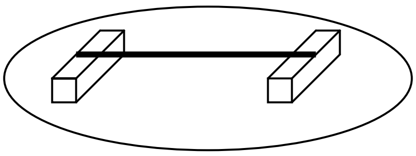

Appendix D.3

D.3.1. Commonly Observed Features

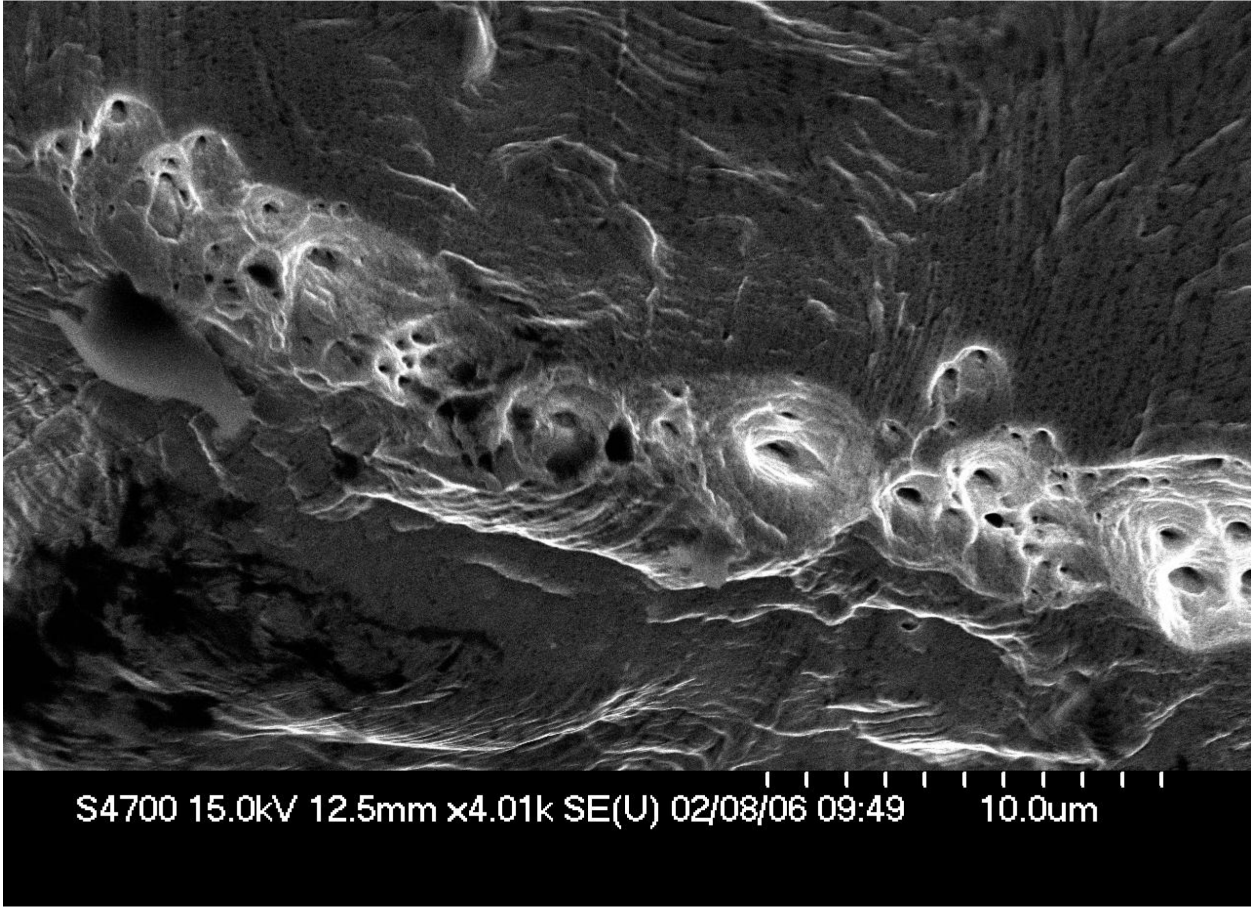

Figure D.3.1. Shear dimples

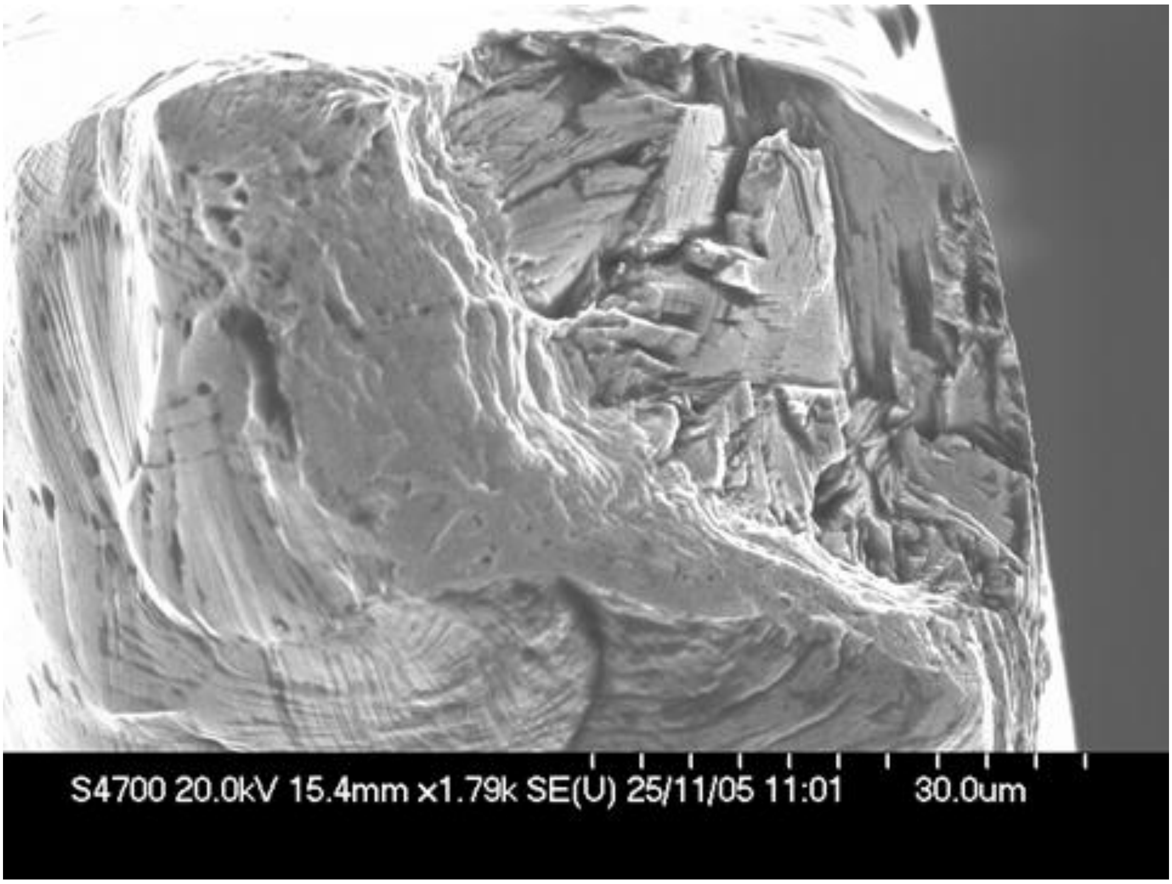

Figure D.3.2. Cleavage-type fracture surface

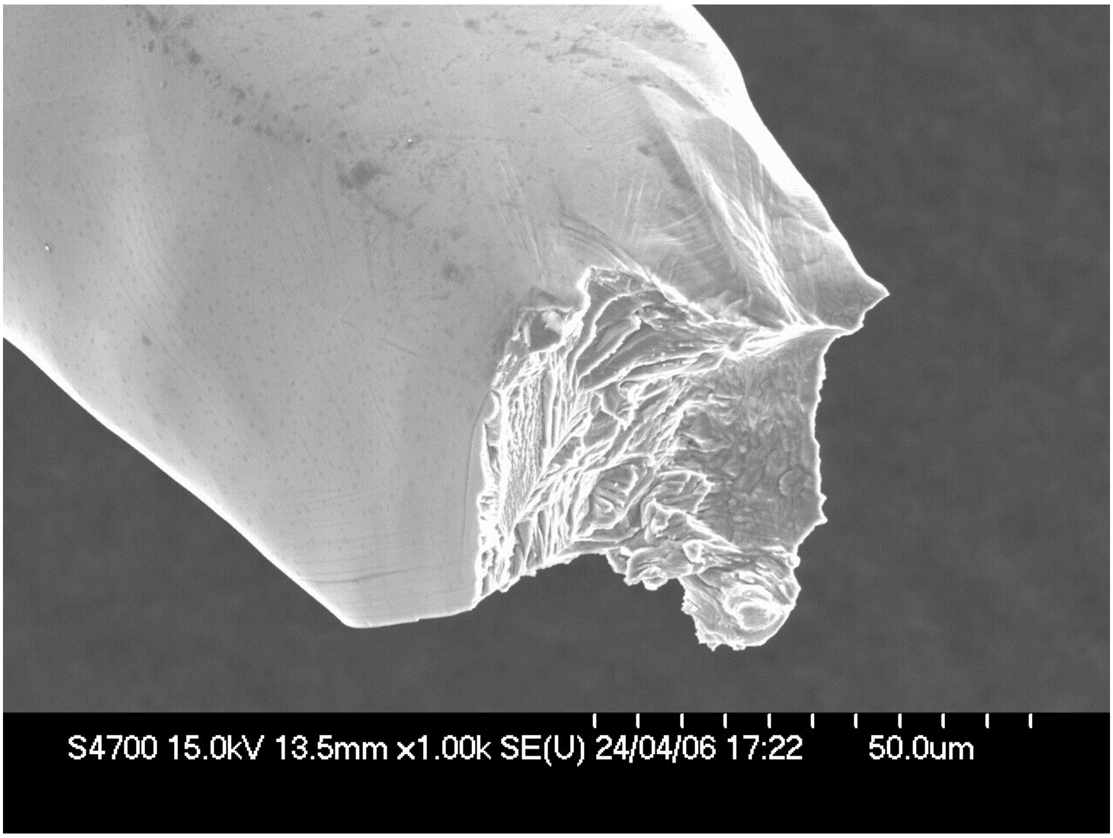

Figure D.3.3. Fractured specimen. 50 μm specimen.

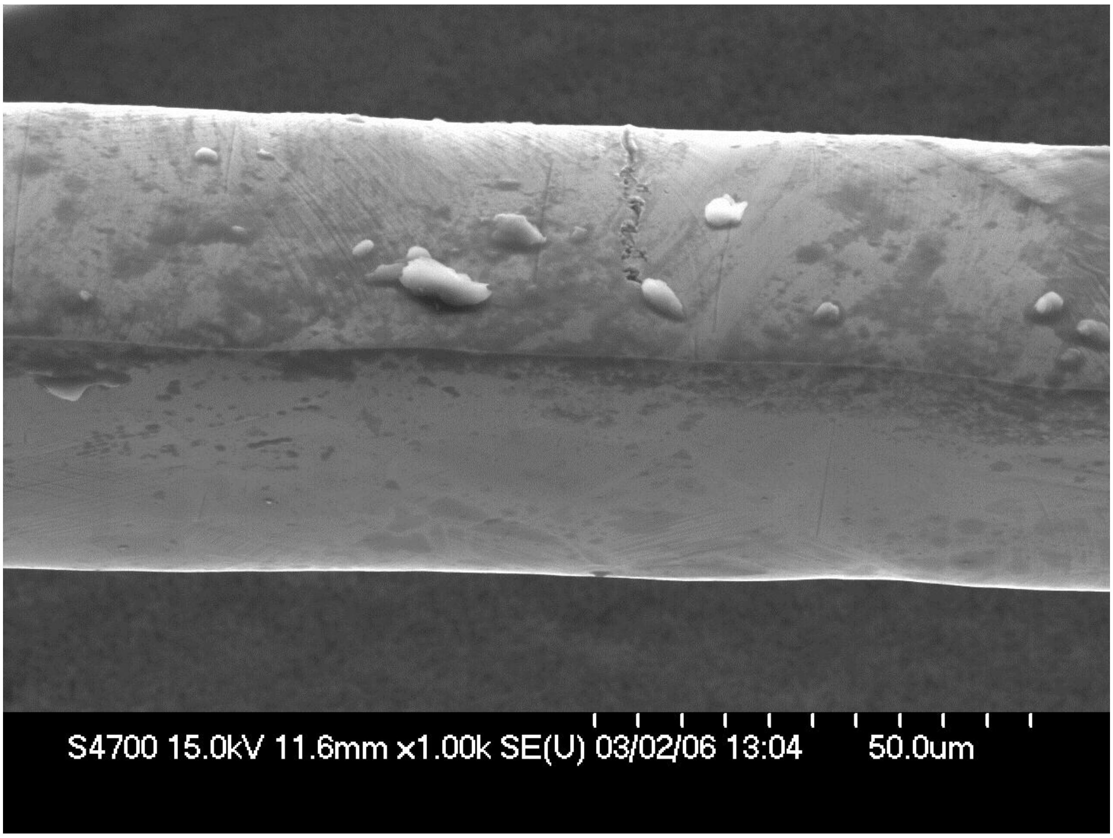

Figure D.3.4. Possible crack. 50 μm specimen.

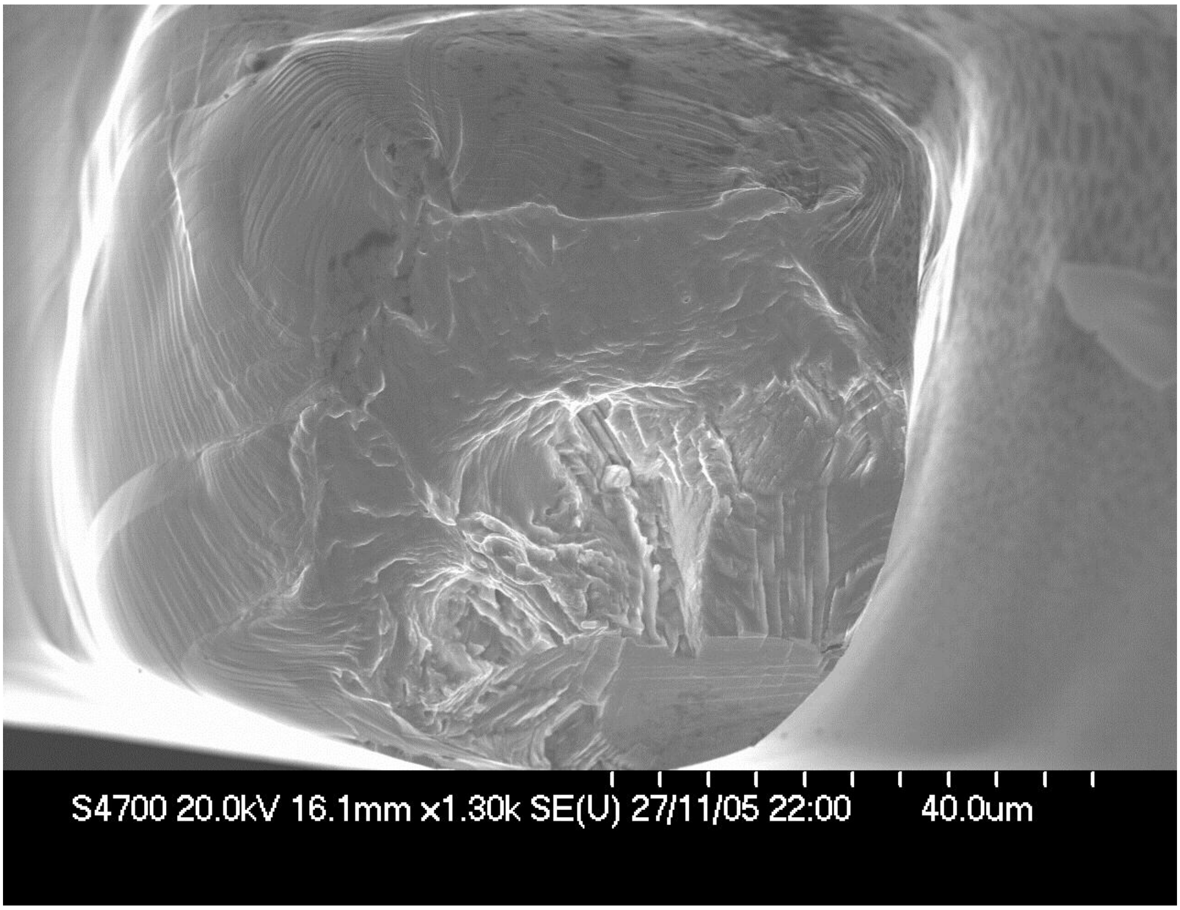

Figure D.3.5. CII_01_75_B. Fatigue and ductile. 75 μm specimen.

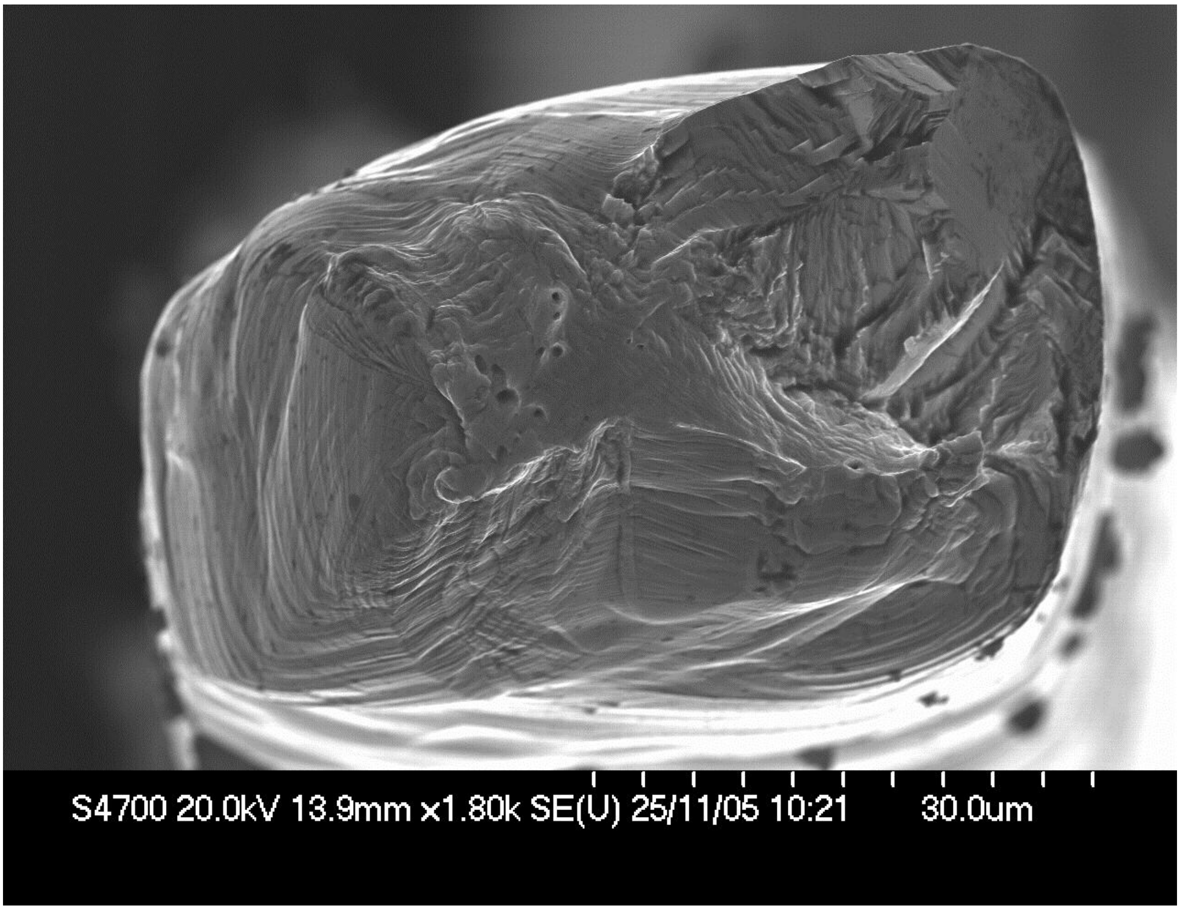

Figure D.3.6. CII_07_50_A. Fatigue and ductile. 50 μm specimen.

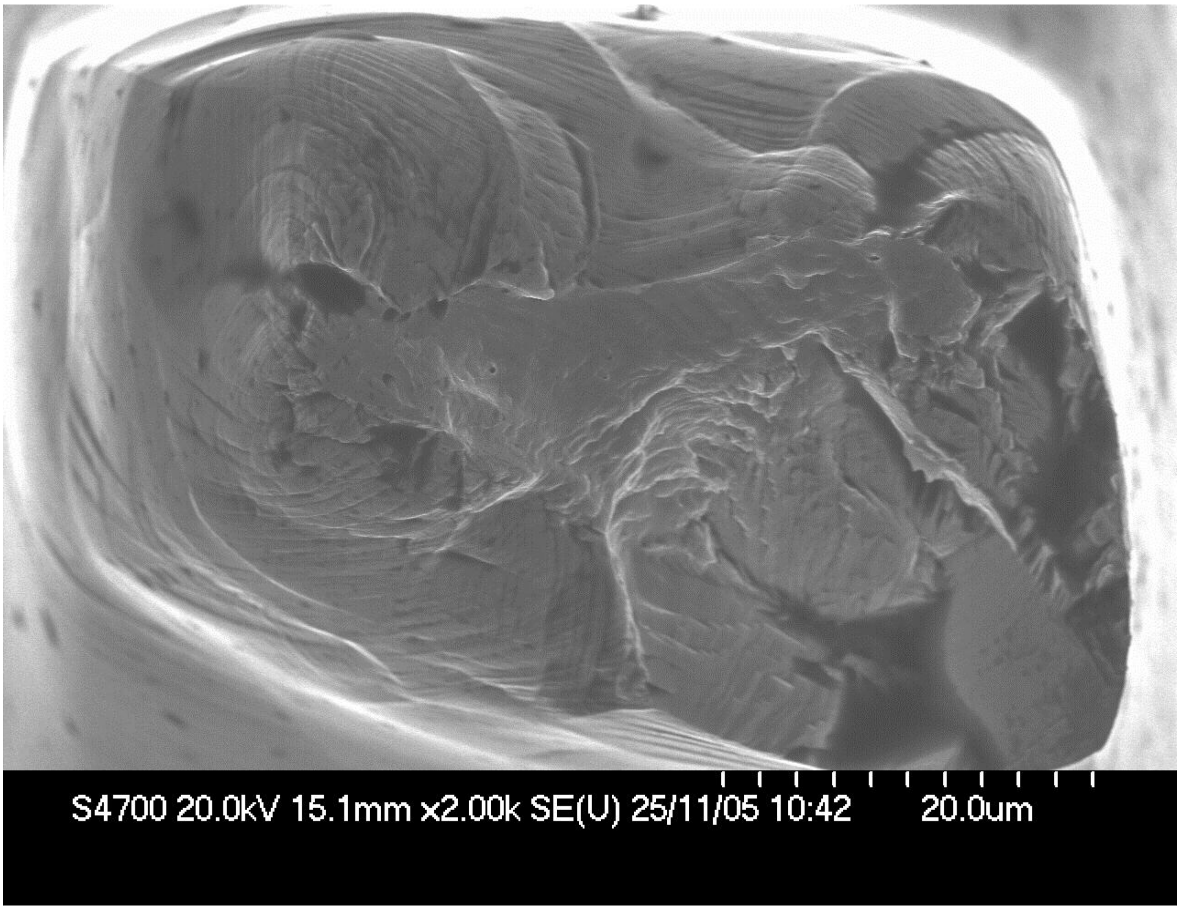

Figure D.3.7. CII_07_50_B. Fatigue and ductile. 50 μm specimen.

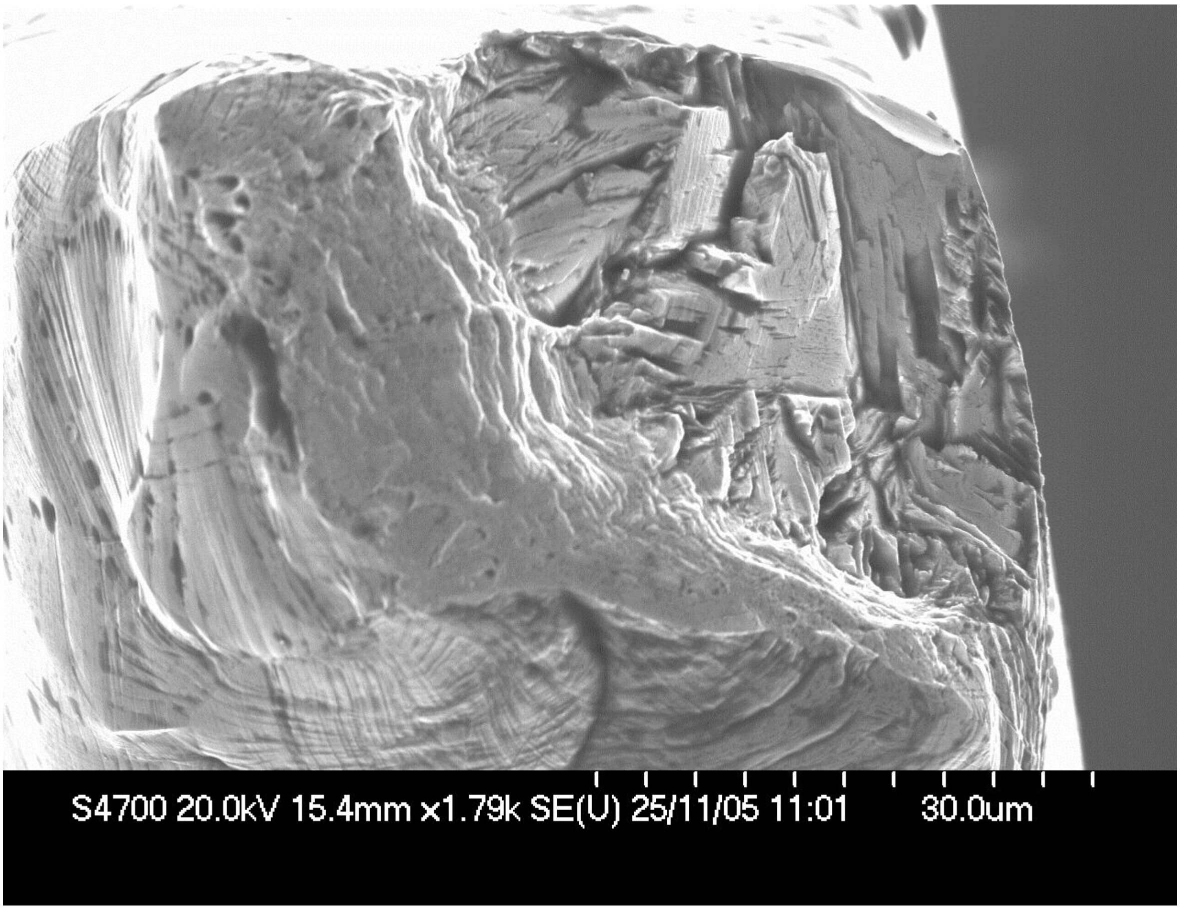

Figure D.3.8. CII_08_50_B. Fatigue and ductile. 50 μm specimen.

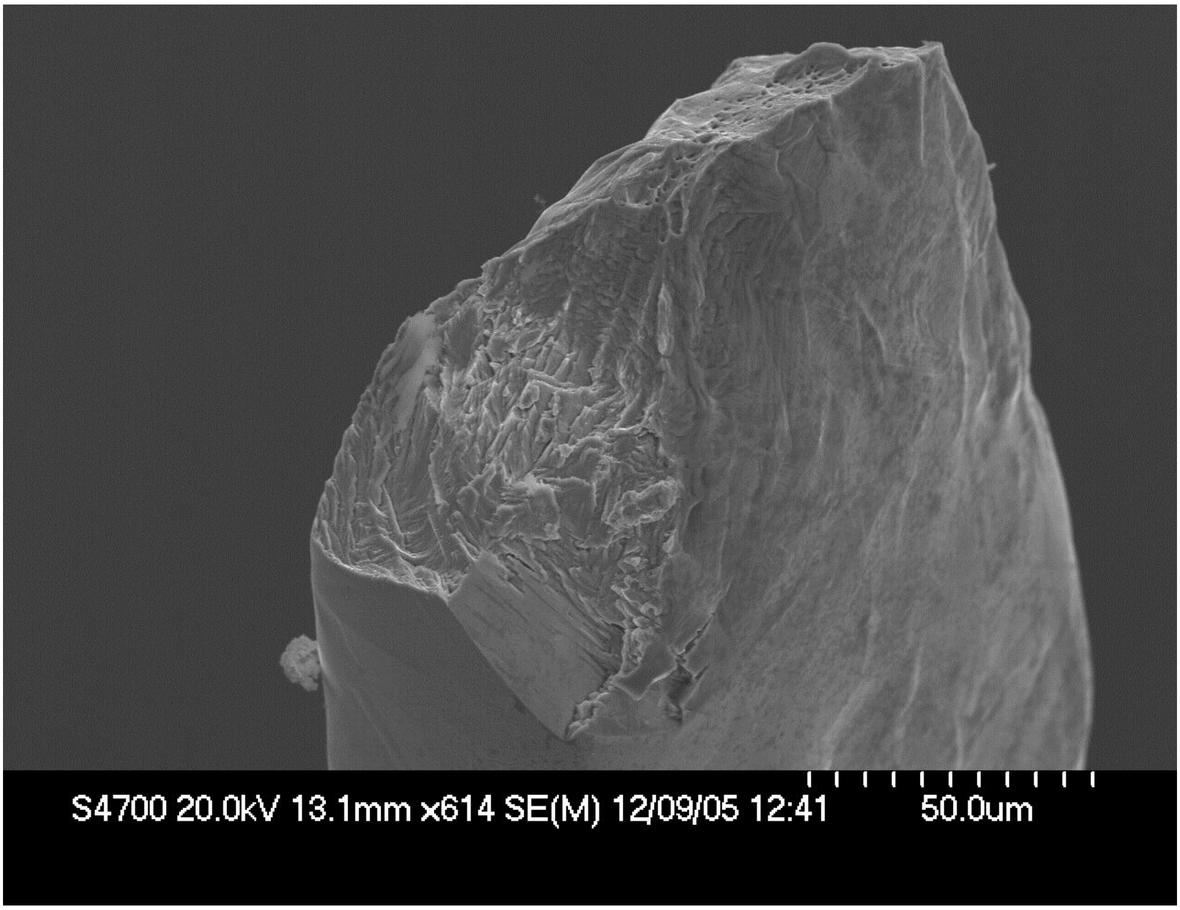

Figure D.3.9. CII_14_150_C1. Fatigue and ductile. 150 μm specimen.

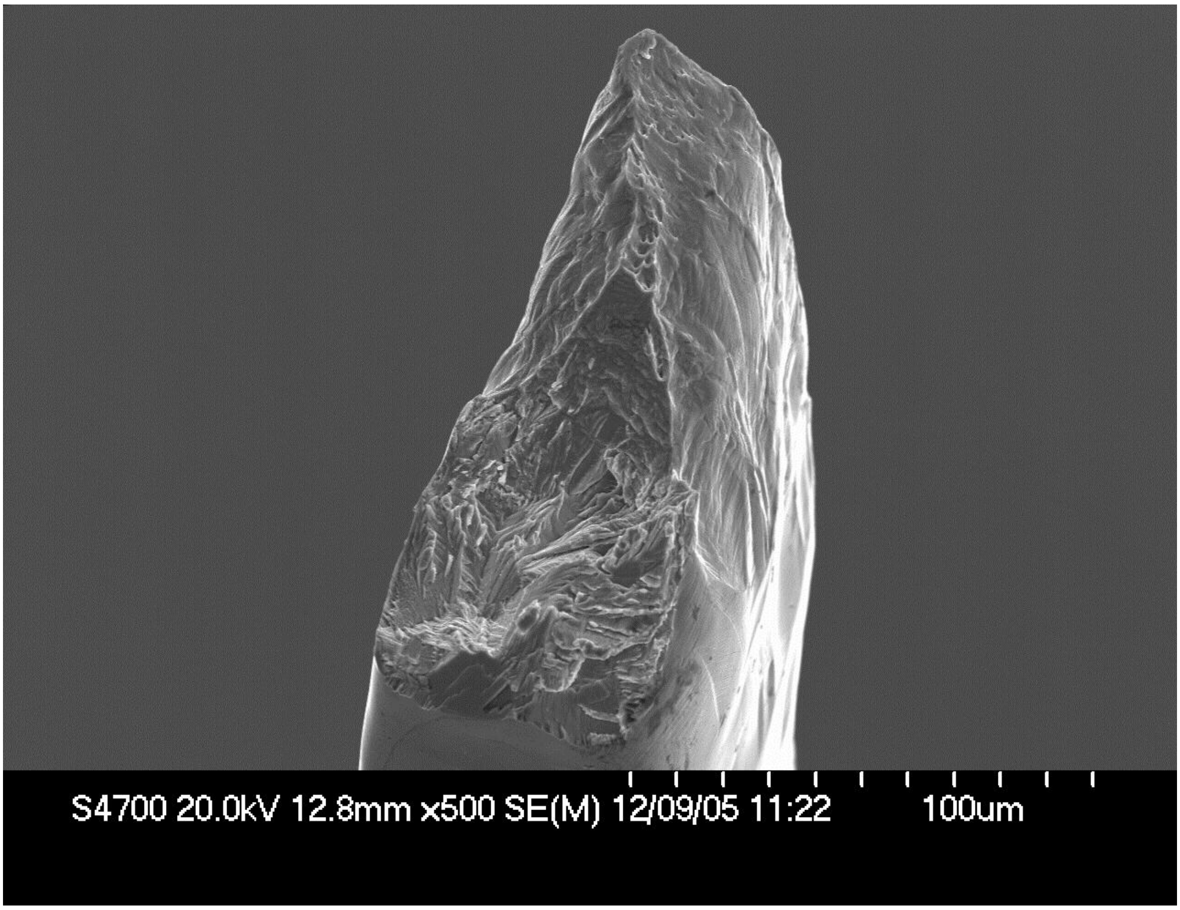

Figure D.3.10. CII_20_150_D1. Fatigue and ductile. Necked down specimen. 150 μm specimen.

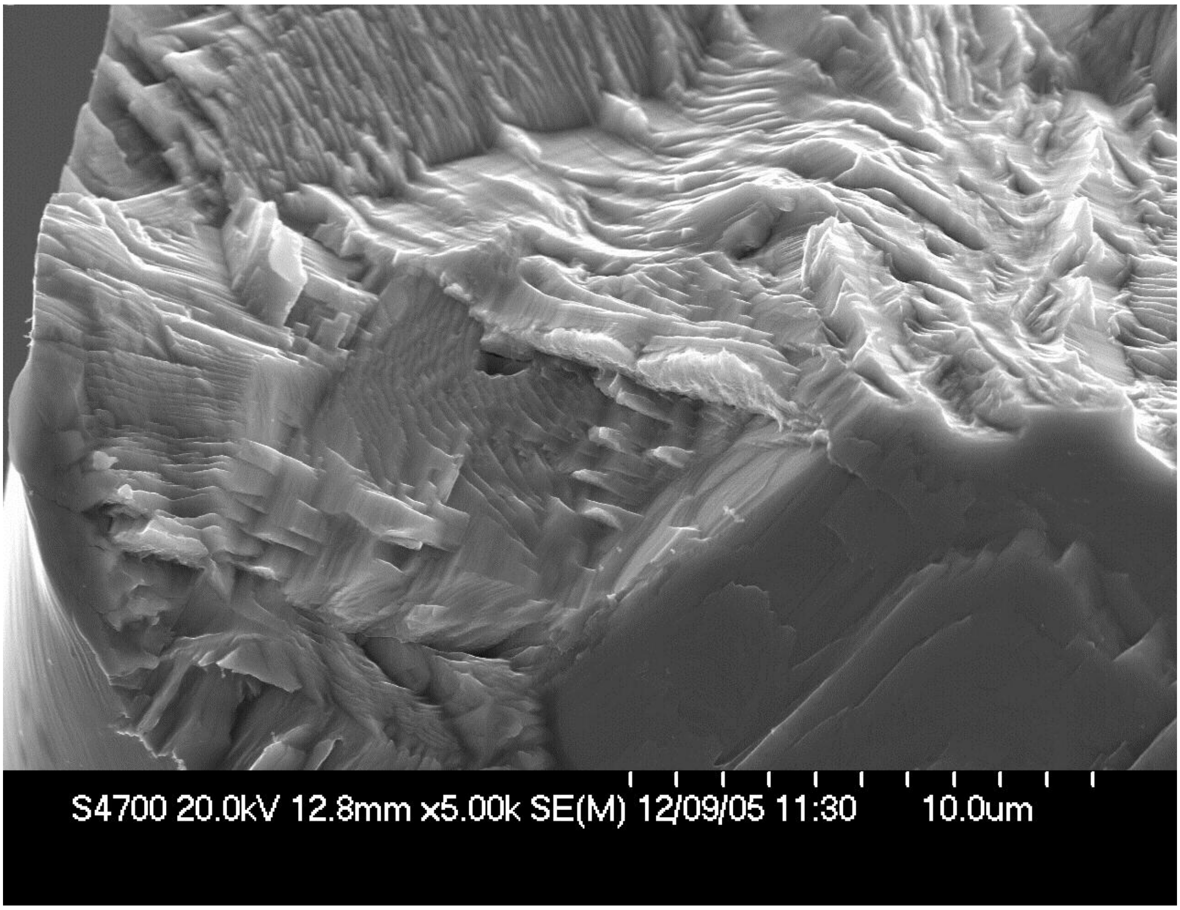

Figure D.3.11. CII_20_150_D2 facetted fracture surface. 150 μm specimen.

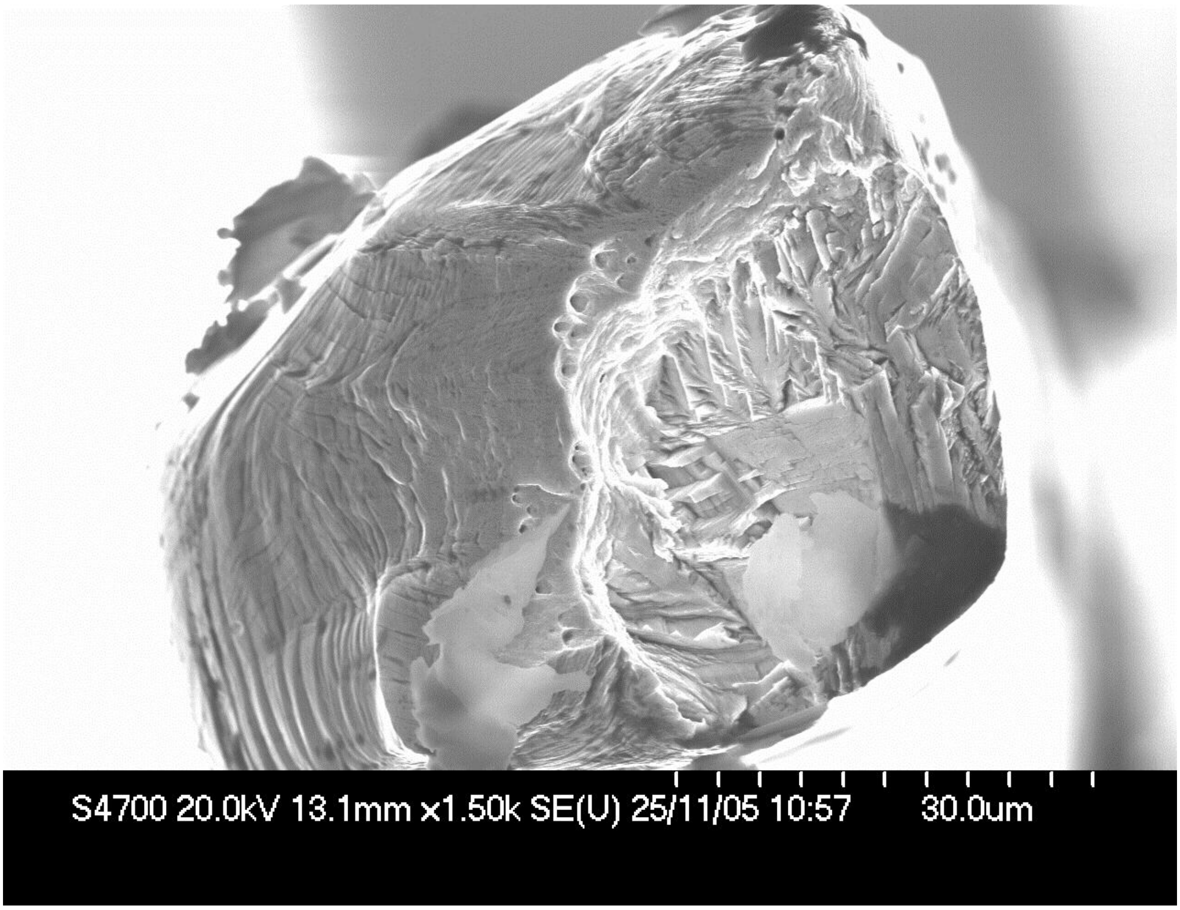

Figure D.3.12. CII_08_50_A HERRINGBONE. 50 μm specimen.

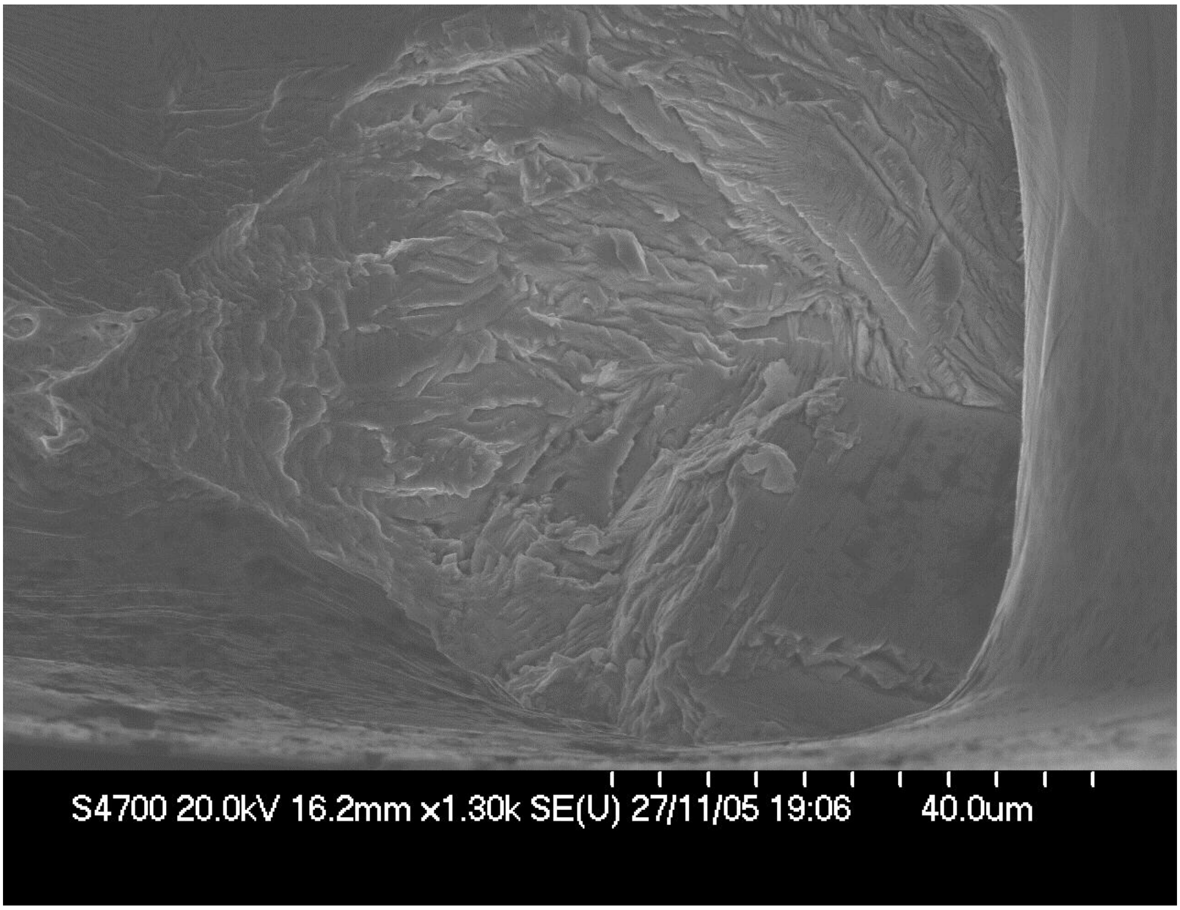

Figure D.3.13. CII_14_150_A1 HERRINGBONE. 150 μm specimen.

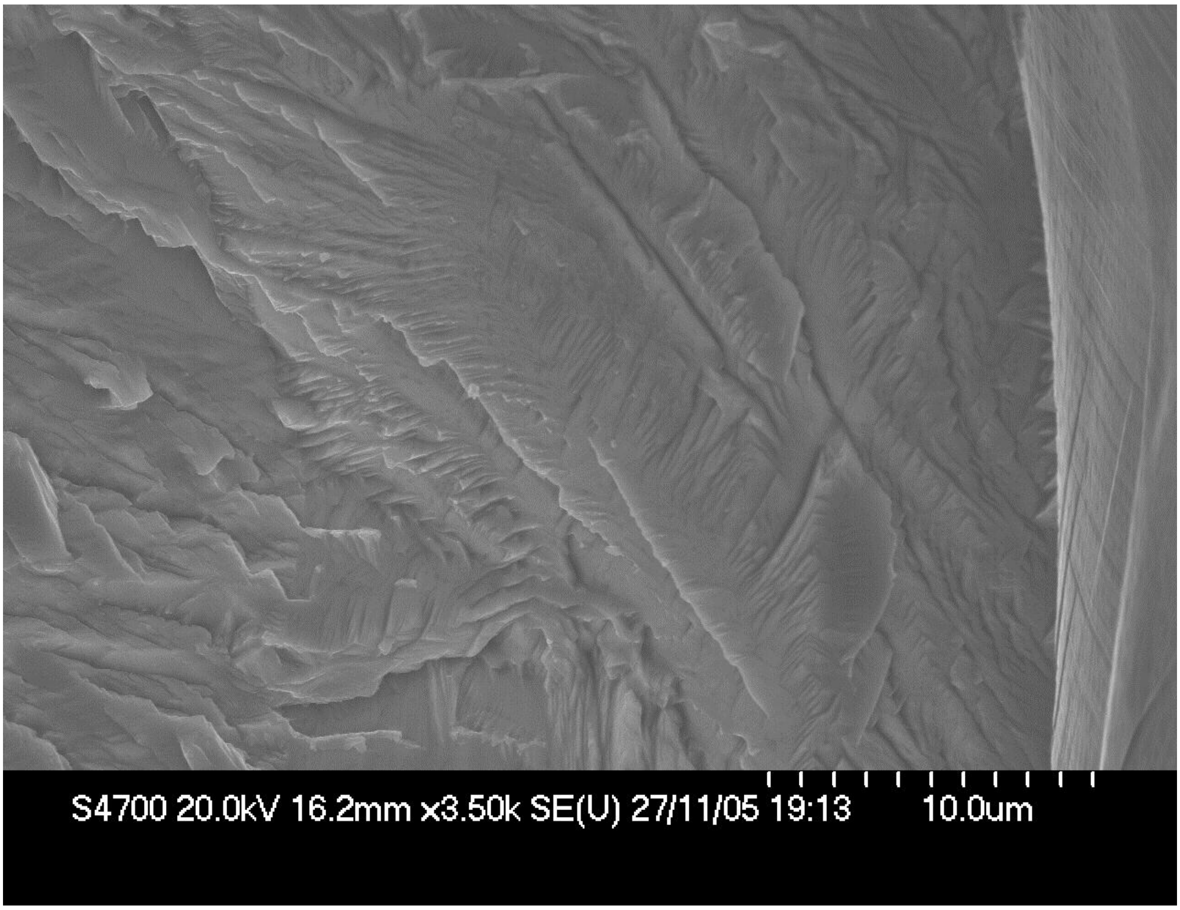

Figure D.3.14. CII_14_150_A3 HERRINGBONE. 150 μm specimen.

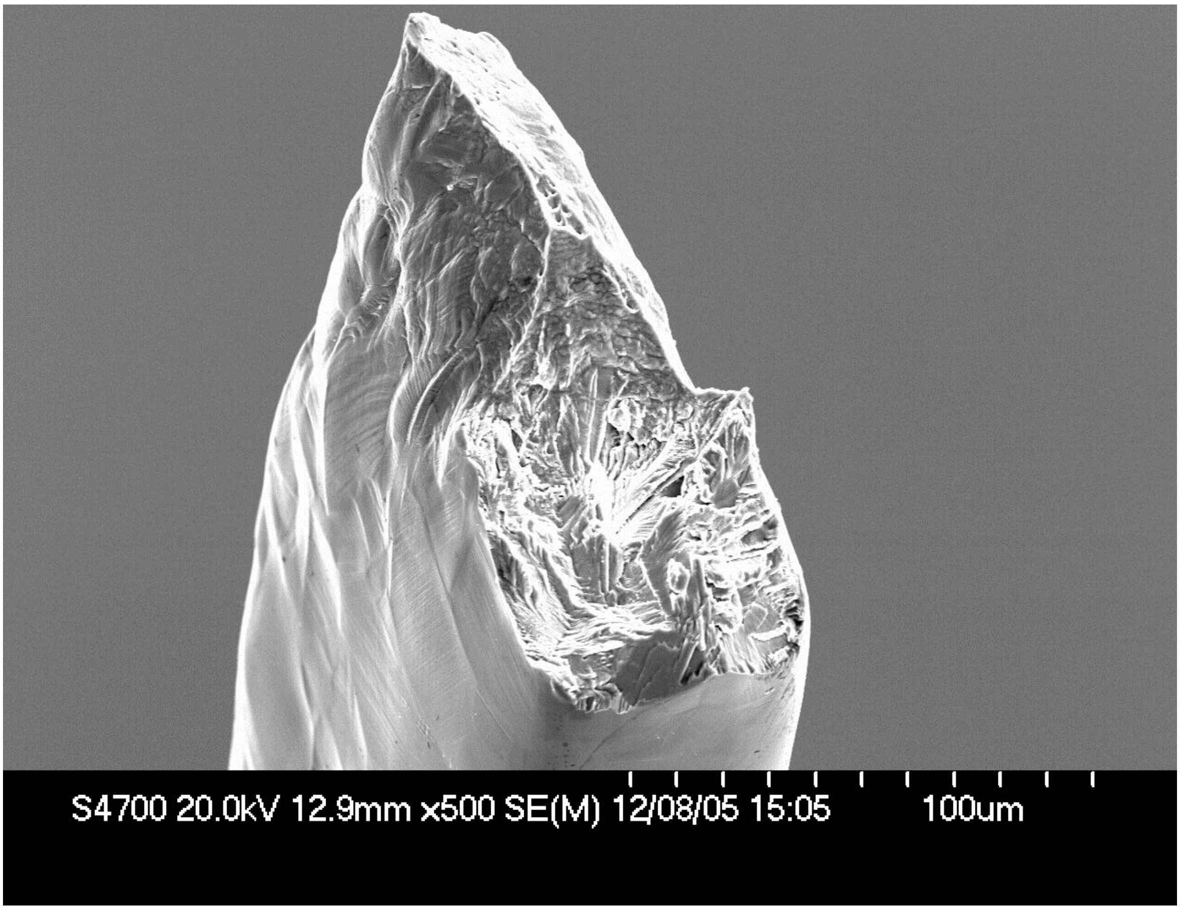

Figure D.3.15. CII_20_150_C5 NECKING. 150 μm specimen.

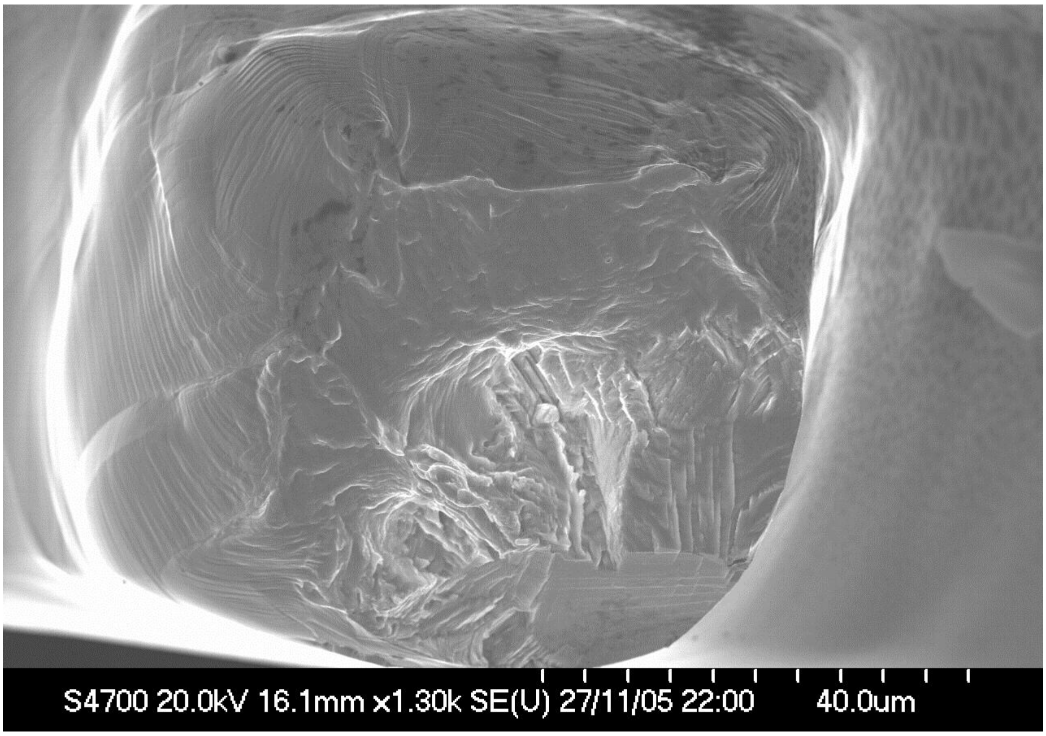

Figure D.3.16. Fracture surface of CII_01_75. Specimen failed at 290,000 cycles. 75 μm specimen.

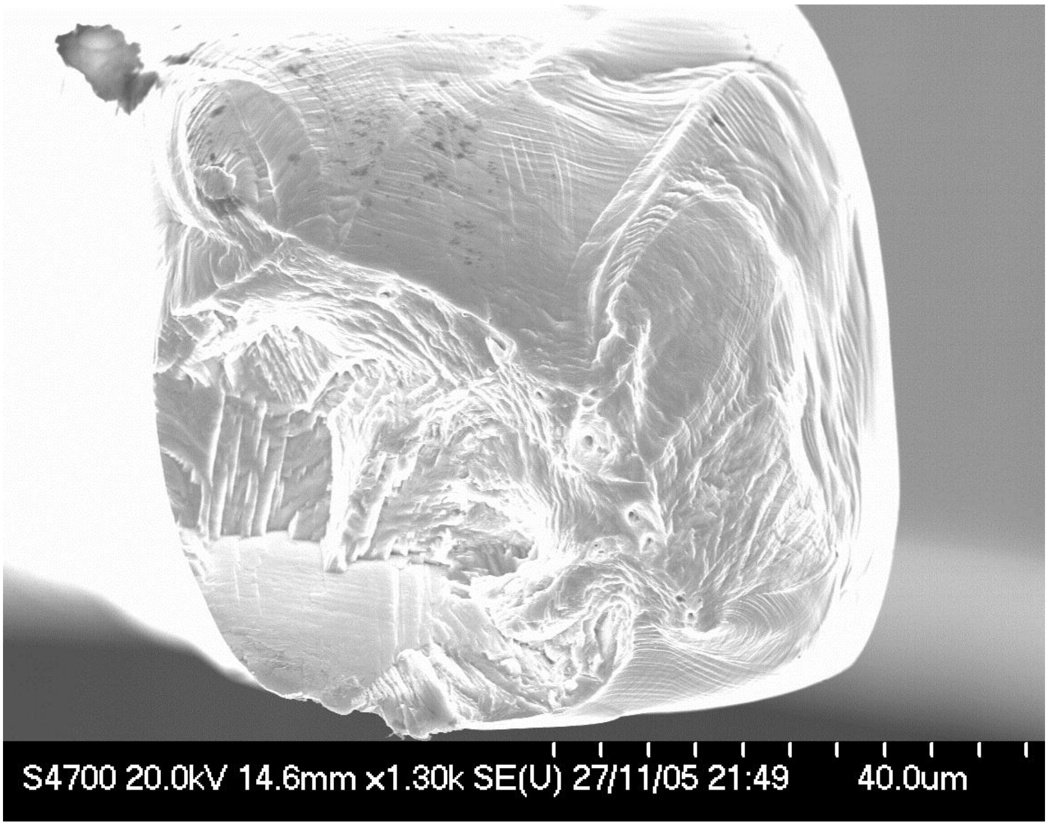

Figure D.3.17. Crack extension on favourable orientated plane. Fracture surface of CII_01_75. Specimen failed at 290,000 cycles. 75 μm specimen.

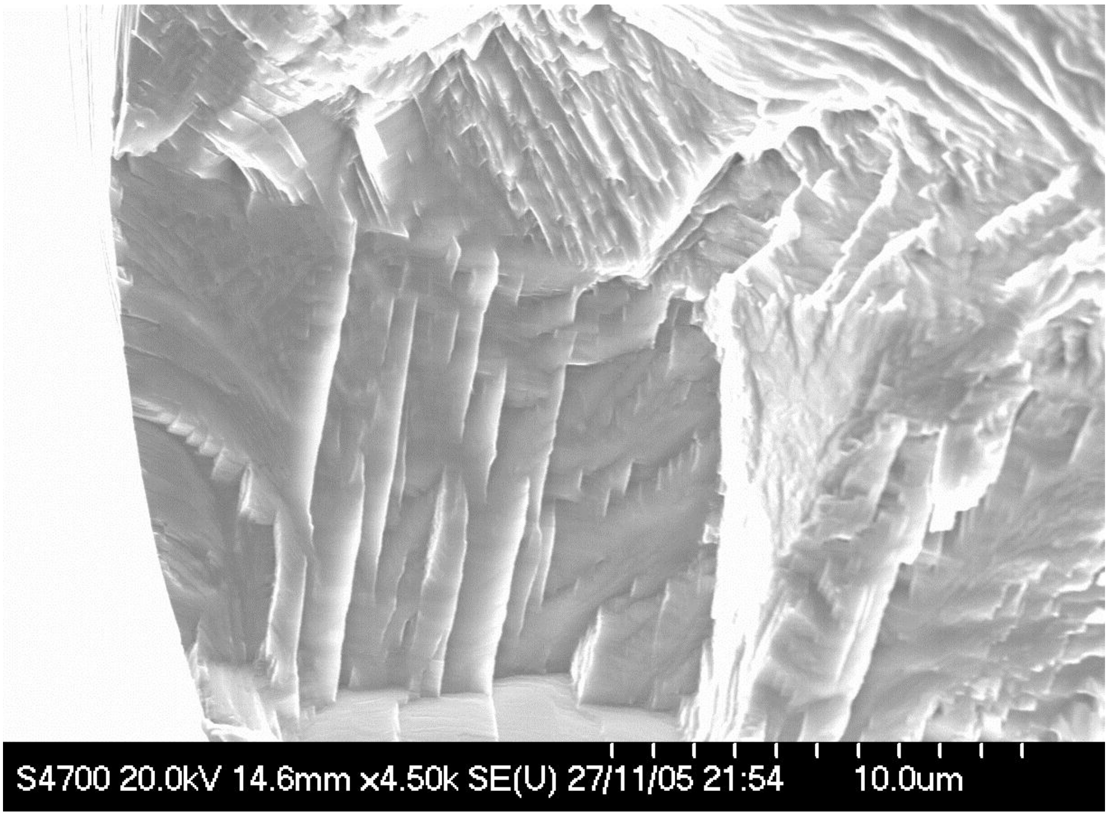

Figure D.3.18. Close-up of facetted fracture surface shown in figure1. 75 μm specimen.

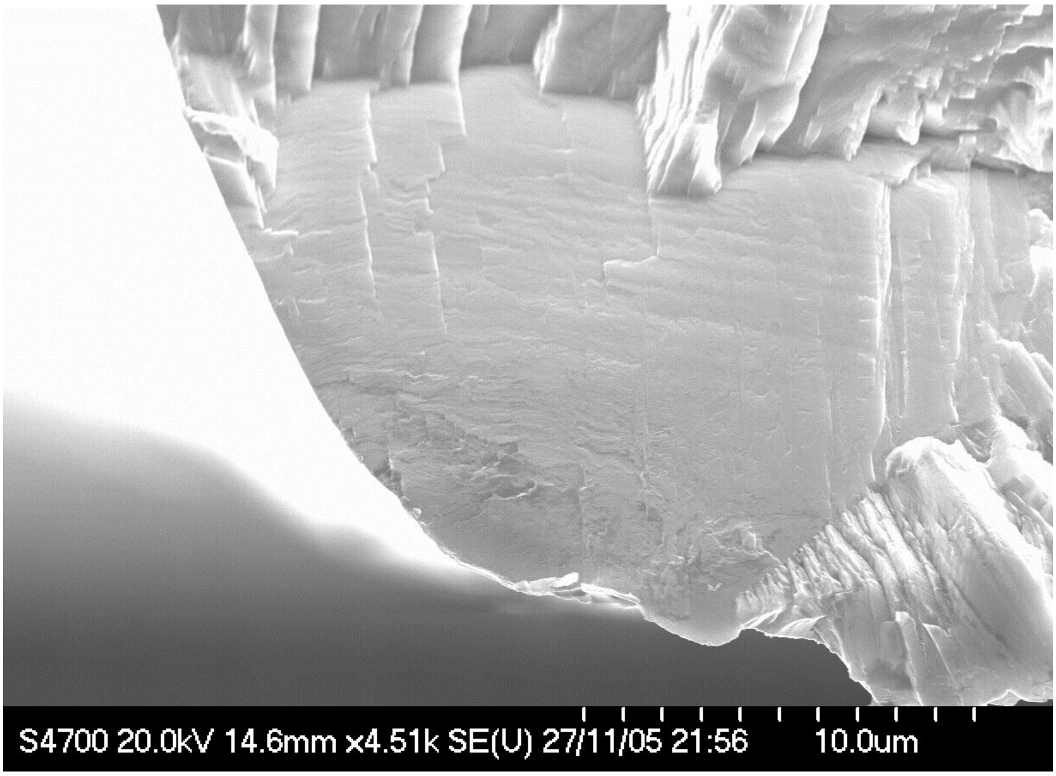

Figure D.3.19. Close–up of relatively large scale, flat area shown in figure 1. 75 μm specimen.